TECTONO-STRATIGRAPHIC ANALYSIS OF A DEEPWATER GROWTH BASIN, AINSA BASIN, NORTHERN SPAIN

by

Matthew R. Hoffman

A thesis submitted to the Faculty and the Board of Trustees of the Colorado School of Mines in partial fulfillment of the requirements for the degree of Master of Science (Geology).

Golden, Colorado

Date _____________

Signed: ____________________________

Matthew R. Hoffman

Signed: ____________________________

Dr. Renaud Bouroullec

Thesis Advisor

Golden, Colorado

Date _____________

Signed: ____________________________

Dr. John D. Humphrey

Professor and Head

Department of Geology and Geological Engineering

ABSTRACT

Growth structures influence coeval deepwater deposition in many of the world's largest hydrocarbon producing regions (i.e., Gulf of Mexico, Indonesia, Nigeria, and Angola). Outcrop studies of analogous basins provide important insights into both the reservoir- and basin-scale stratigraphic architecture. The Ainsa Basin in the Spanish Pyrenees is unique in being one of the few locations in the world where the interaction of deepwater deposits and compressional growth structures can be studied in detail and in three-dimensions. The Middle to Upper Eocene Ainsa Basin fill consists of multiple turbidite systems, including the well-known Ainsa system that exhibit geometries indicative of syn-growth deposition related to large basin-bounding structures (Mediano, Boltaña, and Añisclo Anticlines).

This study focuses on the construction of four syn-growth horizons (base-Ainsa, base-Morillo, base-Guaso, and base-Sobrarbe units) using GoCAD modeling software in a three-dimensional structural model of the basin. A new dip vector projection methodology for 3-D model construction is introduced that constrains the synclinal axes of each syn-growth deepwater system, highlighting shifts in basin depocenter through time. The base of each syn-growth turbidite system (condensed section) is mapped across the basin and used to reconstruct paleo-bathymetry during stages of basin-fill. The construction of syn-growth horizons is constrained by (1) new surface orientation measurements, (2) a balanced cross section, and (3) published sub-surface data. Isopach maps generated from the three-dimensional surfaces reveal thickness trends that show a

strong correlation between basin depocenter and gross sand distribution within the condensed section bounded units, suggesting that paleo-depocenters are a good proxy for reservoir quality sands.

Additionally, this study describes the along-strike geometry of the basin bounding structures and integrates published and newly acquired syn-depositional growth indicators from the stratigraphic record to develop the relative timing of activity on the basin structures. These growth indicators constrain the timing of two phases of growth on the Boltaña Anticline, which consist of an early stage of fault-propagation folding and a second phase of folding from an imbricate detachment fold. The mapping of a canyon within the Morillo stratigraphic unit on the southwestern Mediano Anticline limb suggests a heightened stage of fold growth to the south during Morillo deposition and supports prior interpretations of fold evolution (Poblet *et al.*, 1998). The base-Ainsa and base-Morillo structural surfaces indicate that paleo-lows, created by the Añisclo Anticline, were filled during Ainsa depositional time, suggesting a cessation of local fold growth. Palinspastic restoration of a structural cross section yields 3350 m of shortening (13.6% shortening) in the strata overlying the regional Triassic detachment unit within the basin.

This study can be used as an analog for complex tectono-stratigraphic settings where syn-depositional structures play a major role in the distribution and evolution of deepwater reservoirs.

TABLE OF CONTENTS

ABSTRACT iii

LIST OF FIGURES xi

ACKNOWLEDGMENTS xx

CHAPTER 1 INTRODUCTION 1

1.1 Research Objectives 1

1.2 Location 3

1.3 Regional Geology and Tectonics 3

1.4 Ainsa Basin Geology 6

1.4.1 Ainsa Basin Structural Summary 6

1.4.2 Ainsa Basin Stratigraphic Summary 7

CHAPTER 2 LITERATURE REVIEW 22

2.1 Foreland Basins 22

2.1.1 Piggyback Basins 23

2.1.2 Foreland Fold and Thrust Wedge Mechanics 23

2.2 Compressional Structures 25

2.2.1 Detachment Folds 26

2.2.2 Fault-Propagation Folds 27

2.3 Growth Strata Related to Compressional Structures 29

2.3.1 Large Scale Stratigraphic Patterns 29

2.3.2 Small Scale Stratigraphic Patterns 31

2.3.2.1 Channel/Paleocurrent Deflection 31

2.3.2.2 Mass Transport Complexes 32

2.3.2.3 Clastic Intrusions 33

2.4 Cross Section Balancing and Restoration 33

2.5 3-D Structural Modeling 36

CHAPTER 3 METHODOLOGY 52

3.1 Overall Approach 52

3.2 Field Methods and Data 52

3.2.1 Mapping Methodology 52

3.2.2 Data 54

3.2.2.1 Structural Orientation Measurements 54

3.2.2.2 Three-Point Problem Measurements 55

3.2.2.3 Measured Section 55

3.2.2.4 Seismic Profiles 55

3.2.2.5 Aerial Photo and Digital Elevation Model (DEM) 56

3.2.2.6 Photographs 56

3. 3 3-D Model Construction Methodology 56

3.3.1 Data Import 57

3.3.1.1 Aerial Photo and Digital Elevation Model 57

3.3.1.2 Geologic Contacts 57

3.3.1.3 Structural Orientation Measurements 58

3.3.2 Three-Point Problem Measurement Acquisition 58

3.3.3 Seismic Depth Conversion 60

3.3.4 Dip Vector Conversion 62

3.3.5 Dip Vector Projection 62

3.3.6 System Axis Construction 64

3.3.6.1 X-Y Axis Constraints 64

3.3.6.2 Z-Direction Axis Constraints 64

3.3.7 Surface Interpolation 66

3. 4 Cross Section Construction 67

CHAPTER 4 STRATIGRAPHIC AND STRUCTURAL ANALYSIS 81

4.1 Stratigraphic Analysis 81

4.1.1 Ainsa Stratigraphic Unit 82

4.1.1.1 Ainsa I Sand Interval 82

4.1.1.2 Ainsa II Sand Interval 83

4.1.1.3 Ainsa III Sand Interval 83

4.1.1.4 Base-Ainsa Condensed Section 84

4.1.2 Morillo Stratigraphic Unit 85

4.1.2.1 Morillo I 86

4.1.2.2 Morillo II 86

4.1.2.3 Morillo III 87

4.1.2.4 Base-Morillo Condensed Section 88

4.1.3 Guaso Stratigraphic Unit 89

4.1.3.1 Base-Guaso Condensed Section 90

4.1.4 Sobrarbe Stratigraphic Unit 91

4.2 Structural Analysis 92

4.2.1 Mediano Anticline 92
4.2.2 Boltaña Anticline 95
4.2.2.1 Southern Sector 96
4.2.2.2 Central Sector 97
4.2.2.3 Northern Sector 98
4.2.3 Añisclo Anticline 98
4.2.4 Arcusa Anticline 99
4.3 Oldest Basin-Fill Systems 99
4.4 Seismic Interpretation 102
4.4.1 SP-3 Seismic Profile 102
4.4.2 SP-2 Seismic Profile 104
4.5 3-D Structural Model 105
4.5.1 Structure Contoured Surfaces 105
4.5.1.1 Base-Ainsa Surface 105
4.5.1.2 Base-Morillo Surface 106
4.5.1.3 Base-Guaso Surface 107
4.5.1.4 Base-Sobrarbe Surface 108
4.5.2 Isopach Maps 108
4.5.2.1 Ainsa Isopach Map 108
4.5.2.2 Morillo Isopach Map 109
4.5.2.3 Guaso Isopach Map 110
4.5.3 Dip Contoured Surfaces 110
4.5.4 Shift in System Axes 110

CHAPTER 5 DISCUSSION 159

5.1 Style and Timing of Deformation on the Bounding Anticlines 159

5.1.1 Structural Interpretation 161

5.1.1.1 Mediano Anticline 161

5.1.1.2 Boltaña Anticline 162

5.1.1.3 Añisclo Anticline 165

5.1.2 Timing of Growth 165

5.1.2.1 Timing of Growth on the Mediano Anticline 165

5.1.2.2 Timing of Growth on the Boltaña Anticline 167

5.1.2.3 Timing of Growth on the Añislco Anticline 169

5.1.2.4 Later Tectonic Events 170

5.2 Relationship between Sand Distribution and Depocenter Location in Growth Basins...171

5.2.1 Ainsa Stratigraphic Unit 172

5.2.2 Morillo Stratigraphic Unit 173

5.2.3 Guaso Stratigraphic Unit 174

5.2.4 Isopach Geometries and Depocenter Shifts 174

5.3 3-D Model Construction 175

5.3.1 Lessons Learned 176

5.3.2 Error in Surface Construction 177

5.4 Application to Petroleum Geology 179

5.4.1 3-D Modeling Application and Limitations 179

5.4.2 Ainsa Basin as an Analog 180

5.5 Future Work 182

CHAPTER 6 CONCLUSIONS 192

REFERENCES CITED 195

CD-ROM ....Pocket

LIST OF FIGURES

Figure 1.1 Matrix relating syn-sedimentary growth rate to basin confinement 9

Figure 1.2 Regional location map 10

Figure 1.3 Geological map of Ainsa Basin 11

Figure 1.4 Three-dimensional fault-bend fold models showing the influence of a growing fold surface on deepwater sediment dispersal patterns 12

Figure 1.5 Culture map of study area 13

Figure 1.6 Cross section through the Pyrenees orogeny derived from the ECORS regional seismic profile 14

Figure 1.7 Partial restoration of the ECORS seismic profile through the Pyrenees orogen 15

Figure 1.8 Paleogeographic map of the South Pyrenean Foreland Basin 16

Figure 1.9 Photo-draped digital elevation model (DEM) of Ainsa Basin 17

Figure 1.10 Map and cross sections constructed through the Mediano Anticline 18

Figure 1.11 Stratigraphic cross section through the Tremp, Jaca, and Ainsa Basins ...19

Figure 1.12 Simplified stratigraphic chart of the seven deepwater systems that comprise the Ainsa Basin fill succession 20

Figure 1.13 Chart showing the approximate timing of deposition for the four syn-growth systems that are the focus of this study 21

Figure 1.14 Diagram illustrating the evolution of the Ainsa Basin fill succession 21

Figure 2.1 Schematic model of a typical foreland basin 38

Figure 2.2 Diagram showing the relationship between variables involved in determining the critical taper of a wedge and the force balance on an arbitrary column 39

Figure 2.3 Geometric model of a detachment fold 39

Figure 2.4 Detachment fold kinematic models 40

Figure 2.5 Detachment fold kinematic models 41

Figure 2.6 Growth strata patterns for detachment folds that grow through limb rotation (a) and kink-band migration (b) 42

Figure 2.7 Geometric models of fault-propagation folds 43

Figure 2.8 Growth strata overlying pre-growth stratigraphy causes an upward decrease in fold limb length 44

Figure 2.9 Diagrams demonstrating how a drape sequence can be differentiated from a growth sequence 45

Figure 2.10 Tectono-sedimentary analysis of the Pico de Aguila Anticline 46

Figure 2.11 Experimental results from a flume experiment that documents the effect of topography on turbidity currents 47

Figure 2.12 Diagram of a slump (MTC) 47

Figure 2.13 Three-dimensional diagram of primary features associated with a clastic intrusion 48

Figure 2.14 Example of a balanced cross section restoration from the Orobic Alps ...49

Figure 2.15 Examples of 3-D structural models 50

Figure 2.16 Example of a 3-D dip domain surface construction methodology 51

Figure 3.1 Map of the Ainsa Basin turbidite systems 68

Figure 3.2 Condensed section defining the base of the Sobrarbe system and top of the Guaso system 69

Figure 3.3 Interpreted photo-panel of the Morillo system and the clearly defined ledge stratigraphy 70

Figure 3.4 Regional digital elevation model (DEM) of the Ainsa Basin 71

Figure 3.5 Three-point problem measurements from bedding traces in Gocad 72

Figure 3.6 Diagram illustrating the relationship between the Cartesian coordinates of three separate points and the plane these points define in three-dimensions 73

Figure 3.7 Examples of three-point sets on bedding traces 73

Figure 3.8 Importing seismic profiles into a 3-D Gocad model 74

Figure 3.9 Interval velocities from the SP-2 and SP-3 seismic profiles plotted against two-way travel time (TWTT) 75

Figure 3.10 Checks performed on the seismic profile depth conversion 76

Figure 3.11 Trigonometric relationships used to convert the trend (θ) and plunge (δ) to a unit vector by calculating a measurement's direction cosines 77

Figure 3.12 Dip vector projections to mapped base-Ainsa and base-Morillo condensed section contacts 78

Figure 3.13 Diagrams outlining the steps taken to constrain the plan-view position of each system axis 79

Figure 3.14 Surface interpolation for the base-Ainsa, base-Morillo, base-Guaso, and base-Sobrarbe condensed sections 80

Figure 4.1 Geologic map of the Ainsa Basin 112

Figure 4.1a Northwest quadrant of the geologic map of the Ainsa Basin 113

Figure 4.1b Northeast quadrant of the geologic map of the Ainsa Basin 114

Figure 4.1c Southwest quadrant of the geologic map of the Ainsa Basin 115

Figure 4.1d Southeast quadrant of the geologic map of the Ainsa Basin 116

Figure 4.2 π-axis analysis of the Buil Syncline 117

Figure 4.3 Photodraped digital elevation model (DEM) form the 3-D structural model showing the location and extent of sand body outcrop through the basin axis 118

Figure 4.4 Clastic intrusion located within the Ainsa stratigraphic unit near Rio Sieste 119

Figure 4.5 Growth fault within an upper Banaston sand 119

Figure 4.6 Detailed map of the northern sector of the Boltaña Anticline and its relationship to the syn-tectonic basin-fill 120

Figure 4.7 Map of architectural elements that comprise the Morillo stratigraphic unit 121

Figure 4.8 Map of the lower Sobrarbe unit and the slumps that occur within the lower Sobrarbe deltaic complex along the unit's western margin 122

Figure 4.9 Examples of slumps within the lower Sobrarbe stratigraphic unit 123

Figure 4.10 Detailed map of the southern Mediano Anticline area 124

Figure 4.11 π-analysis of Mediano Anticline pre-growth bedding measurements 125

Figure 4.12 Photo displaying western limb and the northward plunge of the Mediano Anticline 125

Figure 4.13 View toward the north of the southern termination of the Mediano Anticline 126

Figure 4.14 Geometry of the Mediano Anticline pre-growth strata in the vicinity of the Rio Usia 127

Figure 4.15 Triassic shales and evaporites that comprise the regional detachment ...128

Figure 4.16 Volume extracted from the 3-D structural model showing the relationship between the Ainsa, Morillo, Guaso, and Sobrarbe stratigraphic units and the pre-growth strata of the Mediano Anticline 129

Figure 4.17 Submarine canyon that incises into the western limb of the Mediano Anticline in the vicinity of the Mediano Dam 130

Figure 4.18 π-analysis of Boltaña Anticline pre-growth bedding measurements 131

Figure 4.19 Diagram of the Boltaña Anticline in the southern sector 131

Figure 4.20 Volume extracted from the 3-D structural model showing the relationship between the Ainsa, Morillo, Guaso, and Sobrarbe stratigraphic units and the pre-growth strata of the Boltaña Anticline 132

Figure 4.21 A large erosional cut into the fold's western limb that is filled with Late Eocene-Oligocene fluvial strata of the Campodarbe Formation 133

Figure 4.22 Conglomerates rich in cobble-sized carbonate clasts 134

Figure 4.23 Interpreted photopanels of the Boltaña Anticline 135

Figure 4.24 Relationship between Lower Eocene pre-growth carbonates and thinly bedded limestone and mudstone sheets of the Jaca Basin in the fold's northern sector 136

Figure 4.25 Photograph of the Añisclo Anticline 137

Figure 4.26 π-axis analysis of the Buerba Syncline 138

Figure 4.27 Photograph of lower Arro sands within the southwest-verging, recumbent anticline associated with the Las Almazuras Thrust 139

Figure 4.28 View to the southwest from the Peña Montanesa of the Arro and Gerbe deepwater systems and the sub-Arro mudstone sheets and slumps 140

Figure 4.29 View to the north-northeast from the Arro system ledge 140

Figure 4.30 Location map of the SP-2 and SP-3 seismic profiles 141

Figure 4.31 Interpretation of the SP-3 seismic profile 142

Figure 4.32 Interpretation of the SP-2 seismic profile 143

Figure 4.33 Base-Ainsa unit condensed section structural surface 144

Figure 4.34 Base-Morillo unit condensed section structural surface 145

Figure 4.35 Base-Guaso unit condensed section structural surface 146

Figure 4.36 Base-Sobrarbe unit condensed section structural surface 147

Figure 4.37 Ainsa unit isopach displayed on the base-Morillo structural surface 148

Figure 4.38 Morillo unit isopach displayed on the base-Guaso structural surface 149

Figure 4.39 Guaso unit isopach displayed on the base-Sobrarbe structural surface ..150

Figure 4.40 Shaded surface dip values of the base-Ainsa structural surface overlain with structure contours 151

Figure 4.41 Shaded surface dip values of the base-Morillo structural surface overlain with structure contours 152

Figure 4.42 Shaded surface dip values of the base-Guaso structural surface overlain with structure contours 153

Figure 4.43 Shaded surface dip values of the base-Sobrarbe structural surface overlain with structure contours 154

Figure 4.44 Plan-view of the base-Ainsa, Morillo, Guaso, and Sobrarbe constructed system axes 155

Figure 4.45 Structure maps of the base- Ainsa (a), Morillo (b), Guaso (c), and Sobrarbe (d) shown in relation to the deepest point of the base-Ainsa surface axis 156

Figure 4.46 3-D volume extracted from the central portion of Ainsa Basin 157

Figure 4.47 Plot of the deepest point on each syn-growth surface axis 158

Figure 5.1 Location map of the structural cross-section (A-A') 183

Figure 5.2 Palinspastic restoration of the Ainsa Basin and bounding structures 184

Figure 5.3 Stratigraphic units and structures of the Ainsa Basin compared to the geologic time scale of Gradstein *et al*. (2005) 185

Figure 5.4 Distribution of the Ainsa I sand interval (shaded region) overlain on the Ainsa unit isopach map 186

Figure 5.5 Distribution of the Ainsa II sand interval (shaded region) overlain on the Ainsa unit isopach map 187

Figure 5.6 Distribution of the Ainsa III sand interval (shaded region) overlain on the Ainsa unit isopach map 188

Figure 5.7 Paleogeographic map of the Morillo I stratigraphic unit and Morillo I paleocurrent measurements overlain on the Morillo unit isopach map ..189

Figure 5.8 Distribution of the Guaso I and II sand intervals (shaded region) overlain on the Guaso unit isopach map 190

Figure 5.9 Interpreted seismic profile of a piggyback basin from offshore Brunei ..191

ACKNOWLEDGMENTS

I would first like to thank my advisor, Dr. Renaud Bouroullec, for sharing his geologic knowledge, creativity, and passion for research. I am very grateful for his constant support and dedication over the course of this project.

Thanks to Dr. Chris Guzofski of Chevron for sharing his time and knowledge. I greatly appreciate the time he set aside to work with me and share his insights on structural modeling and ways to improve the research.

Thanks to the Chevron Center of Research Excellence (CoRE) research director Dr. David Pyles for sharing his ideas, expertise and enthusiasm.

Thanks to Dr. Julian Clark of Chevron for his dedication to the CoRE program and sharing his expertise both on deepwater systems and the Ainsa Basin.

Thanks to Dr.Bruce Trudgill for his advice and input throughout this project.

A special thanks to Dr. David Hawkins, my undergraduate advisor, for preparing me for the rigors of graduate school.

A very special thanks to CoRE program manager, Charlie Rourke. Her day to day support throughout my time at CoRE was an enormous help. Whether it was trying to secure new software licenses, handling contracts, or giving advice on how to navigate the CSM system, I am greatly indebted to her for all that she's done for me during my graduate education.

Thanks to CoRE for their financial support and making my graduate education possible. The CoRE program has afforded me numerous unique learning and collaborative opportunities for which I am very grateful. I would also like to thank the AAPG Grants-in-Aid program and the contributors to the Kenneth H. Crandall Memorial Grant for additional financial support.

Many thanks to my fellow graduate students and friends at Colorado School of Mines for their friendship and collaboration. In particular, thanks to Han Claringbould for his assistance in the field and to Jessica Matthews for her excellent proof-reading skills and being there for me throughout this process.

A very special thanks to all my fellow CoRE students: Prianto Setiawan, Henri Silalahi, Jeremiah Moody, Amy Moss-Russell, and Alexandra Fleming. It has truly been a privilege to work and collaborate with you.

Last but not least, thanks to my parents, Robert and Cheryl Hoffman, and my siblings, Brad and Corinne Hoffman, for all of the inspiration and love over the years.

CHAPTER 1

INTRODUCTION

1.1 Research Objectives

Deepwater turbidite reservoirs are major targets in some of the world's largest hydrocarbon producing regions (i.e., Gulf of Mexico, North Sea, offshore Nigeria, and offshore Angola). Seismic data from these regions show stratigraphic geometries that are indicative of actively growing structures affecting coeval deepwater depositional systems (Freeth and Ladipo, 1986; Suppe *et al.*, 1992; Vergés *et al.*, 2002; Shaw *et al.*, 2004). Understanding the interaction between growth structures and these depositional systems is crucial for the prediction of reservoir occurrence, geometry, and quality (Fig. 1.1).

The stratigraphic and structural uncertainties present in structurally complex basins can be decreased through the study of outcrop analogs. The Ainsa Basin in the Spanish Pyrenees (Fig. 1.2) is unique in that it is one of the few locations in the world where the interaction of deepwater deposits and growing structures can be studied in detail and in three-dimensions.

The Ainsa Basin (Fig. 1.3) has been the location of numerous studies on turbidite deepwater systems and syn-tectonic stratigraphy (Mutti, 1977; Clark and Pickering, 1996; Poblet *et al.*, 1998; Fernández et al., 2004; Labourdette *et al.*, 2008; Pickering and Bayliss, 2009). To date, structural cross sections and models of the Ainsa Basin have been isolated to individual structures or have been qualitative in nature (Dreyer *et al.*, 1999; Poblet *et al.*, 1998; Fernández *et al.*, 2004). Additionally, the timing of growth on the basin-bounding structures has not been documented in detail. The present study takes into account 1) regional geology, 2) seismic data, 3) structural geometries, 4) detailed stratigraphic architecture of individual syn-growth units, and 5) prior work. A detailed structural model of the basin, coupled with 2-D palinspastic restoration, supports the interpretation of syn-tectonic deepwater deposits by providing insight into the correlation between stratigraphic architecture and active fold growth, as gravity flow deposits are often affected by topography (Fig. 1.4).

The main goals of this research include the following:

1) To define the style and timing of deformation on the Ainsa Basin bounding structures.

2) To constrain the 3-D geometries of the syn-growth deepwater systems and the relationship between sand distribution and depocenters through time.

3) To test new techniques in 3-D structural model construction from surface data.

Prior studies of Ainsa Basin's deepwater systems have focused on the systems' constituent sand bodies, as the sands make up the most prominent reservoir analogs in the basin (i.e. Clark and Pickering, 1996; Fernández *et al.*, 2004; Arbués *et al.*, 2007; Labourdette *et al.*, 2008). This study proposes a new mapping approach based on stratigraphic intervals identified between condensed sections. These condensed section boundaries represent time correlative surfaces that can be correlated from the basin margins to the basin axis. The condensed sections are the surfaces used in the 3-D structural model construction.

An enhanced understanding of Ainsa Basin deepwater fill and its relationship to the bounding structures will make Ainsa Basin an increasingly valuable analog for deepwater reservoirs. Growth structures play a first-order role in influencing the distribution of reservoir facies in a basin (Castelltort *et al.*, 2003). Outcrop studies take into account observations and data on both the seismic and sub-seismic scale, and have important implications for predictive modeling in data-poor environments.

1.2 Location

Ainsa Basin is located in the Huesca Province of northern Spain, approximately 200 km NW of Barcelona (Fig. 1.2). The principal study area is approximately 360 sq. km and covers the Ainsa Basin and its bounding structures (Mediano, Boltaña, and Añisclo Anticlines). The area is bounded to the west by the villages of Campodarbe and Las Bellostas, to the south by the villages of Santa Maria de la Nuez and Liguerre de Cinca, to the east by the village of Palo, and to the north by the village of San Vicente (Fig. 1.5). A secondary study area consists of a corridor through the oldest Ainsa Basin-fill that trends roughly NE-SW, from the town of Gerbe to the southern limit of the Peña Montanesa (Fig. 1.5).

1.3 Regional Geology and Tectonics

The study area is located within the southern Pyrenees, a 400 km long Alpine mountain chain, formed as a result of the N-S collision between the Afro-Iberian and Eurasian plates (Muñoz, 1992; Puigdefábregas *et al*,, 1992; Sibuet *et al.*, 2004). The Pyrenees is a doubly-verging orogen that can be divided into three primary zones: 1) the North Pyrenean Foreland Basin, located in France and characterized by north-verging folds and thrusts, 2) the Axial Zone, characterized by uplifted Hercynian basement, and

3) the South Pyrenean Foreland Basin, located in Spain and characterized by south-verging folds and thrust sheets (Fig. 1.6). The floor thrust of the South Pyrenean Foreland Basin is the sole thrust of the Pyrenean chain, implying subduction of Iberia below Eurasia (Fig. 1.6) (Puigdefábregas *et al.*, 1992).

The Afro-Iberian/Eurasian collision initiated in the Late Cretaceous and is attributed to the northward motion of the African plate (Muñoz, 1992; Puigdefábregas *et al.*, 1992; Sibuet *et al.*, 2004). Plate kinematic reconstructions from offshore paleomagnetic data have demonstrated that the Iberian plate movement was coupled with the African plate from the Cretaceous to Middle Eocene (Srivastava, 1990).

Initial extension, attributed to the rifting of the continental margins in the Late Jurassic and Early Cretaceous, led to the formation of the neo-Tethys and continental basins in southern France and northern Spain (Sibuet *et al.*, 2004). The development of a triple junction to the west of the Bay of Biscay led to the rotation of Iberia and the closure of the neo-Tethys by the early Late Cretaceous through the subduction of its transitional oceanic crust beneath the Eurasian plate (Srivastava, 1990; Sibuet *et al.*, 2004). This phase marked the beginning of the Pyrenean collision event that initiated with the thick-skinned inversion of the Lower Cretaceous rift system, leading to the development of E-W trending elongate basins in front of thrusts (Fig. 1.7) (Muñoz, 1992; Puigdefábregas *et al.*, 2000).

A model incorporating both Pyrenees geology and paleomagnetic data presented by Sibuet *et al.* (2004) demonstrates a major plate boundary rearrangement in the Campanian associated with the end of spreading in the Bay of Biscay. This rearrangement lead to a shift in stress direction between the Afro-Iberian and Eurasian plates from SW-NE to SSE-NNW that was maintained throughout the Pyrenean collision (Sibuet *et al.*, 2004).

By the Paleocene, all major Cretaceous normal faults were inverted and the upper crust regained its pre-rift thickness (Fig. 1.7). At this time, a shift to shallow water facies in the basins occurred, likely as a response to increased crustal thickness related to the inversion (Puigdefábregas, 1992).

The Eocene was marked by a transition to thin-skinned deformation and maximum crustal shortening (Puigdefábregas, 1992; Muñoz *et al.*, 1994; Fitzgerald *et al.*, 1999). In the South Pyrenean Foreland Basin, the emplacement of a southwest-verging imbricate thrust system (Fig. 1.7) led to the formation of structures oblique to the strike of the orogen that partitioned the associated foreland basin into a series of sub-basins (i.e. Tremp-Graus Basin, Ainsa Basin, and Jaca Basin) (Fig. 1.8). By the Middle Eocene, the Ainsa Basin had evolved into a piggy-back basin on the hanging wall of the actively propagating Gavarnie-Sierras Exteriores thrust (Figures 1.2 and 1.6) (Fernández *et al.*, 2004).

A late stage basement-involved thrusting event occurred in the Late Eocene through Early Oligocene that caused movement on the Peña Montanesa Thrust located northeast of the Ainsa Basin. Thrusting propagated southward to later involve thrusts in the Sierras Exteriores (Fig. 1.6) (Farrell *et al.*, 1987). Continuous continental wedging and subduction of the Iberian plate beneath the Eurasian plate continued into the Late Miocene and drove further uplift of the entire region to its present state (Fig. 1.7) (Sibuet *et al.*, 2004).

1.4 Ainsa Basin Geology

The Ainsa Basin is located in the South Pyrenean Foreland Basin and initiated as a foredeep during a period of maximum Pyrenean shortening in the Lower Eocene (Figures 1.2 and 1.6). With the continued southward propagation of the fold and thrust system, the South Pyrenean Foreland Basin became divided into a series of piggy-back basins that lie on the hanging walls of the thrust sheets. Ainsa Basin was incorporated into the hanging wall of the Gavarnie-Sierra Marginales Thrust Sheet and is located on the western margin and in the footwall of of the Montsec Thrust Sheet (Fig. 1.2).

1.4.1 Ainsa Basin Structural Summary

The emplacement of southward propagating thrusts led to the creation of a series of detachment and fault-related folds over a Triassic shale-evaporite layer (Poblet *et al.*, 1998; Fernández *et al.*, 2004). The Ainsa Basin is formed over three synclines related to this folding: 1) the Buil syncline, 2) the Buerba syncline, and 3) the San Vicente syncline (Figures 1.3 and 1.9). The Buil syncline is the largest of the three and is a N-S trending open fold that plunges 7° to the south (Fernández *et al.*, 2004). The northern portion of the Buil syncline is partitioned into the Buerba and San Vicente synclines by the Añislco Anticline, a west-verging fault propagation fold, plunging 10° to the south in the northern portion of the fold and 25° to the south in southern portion of the fold (Fernández *et al.*, 2004; Tavani *et al.*, 2006).

The basin is bounded to the east and west by two large anticlines: 1) the Mediano Anticline (E) and 2) the Boltaña Anticline (W) (Figures 1.3 and 1.9). The Mediano Anticline is a 20 km long, 9 km wide detachment fold that exhibits geometrical variation along strike (Fig. 1.10) (Poblet *et al.*, 1998). The northern portion of the Mediano Anticline is a symmetrical fold with a northwest-southeast striking axis. To the south, the Mediano Anticline transitions to a north-plunging (~10°), tight, east-verging anticline. (Fig. 1.10) (Poblet *et al.*, 1998; Fernández *et al.*, 2004). The Boltaña Anticline is interpreted as a west-verging fault propagation fold (Fernández *et al.*, 2004).

1.4.2 Ainsa Basin Stratigraphic Summary

The pre-tectonic stratigraphy (pre-growth) consists of Triassic through Ypresian (Early Eocene) deposits that show no thickness change in local outcrop. These strata can be divided into two main units: 1) a lower unit that consists of 250 m thick Triassic shales with interbedded evaporites and carbonates, and 2) an upper unit that consists of a 2400 m thick Cenomanian through Ypresian succession of carbonates, calcareous sandstones, and marls (Fig. 1.10) (Poblet *et al.*, 1998). The lower unit serves as the major detachment layer for thrusts and folds throughout the region and is likely highly variable in thickness at the regional scale.

Syn-tectonic deposits consist primarily of siliciclastic turbidites and carbonate platform sediments of the Hecho Group and show clear stratigraphic geometries that display evidence of active growth on the N-S trending basin margin anticlines (e.g., Fig. 1.10) (Mutti *et al.*, 1988; Poblet, 1998; Fernández *et al.*, 2004; Pickering and Corregidor, 2005).

During the evolution of the South Pyrenean Foreland Basin, Ainsa Basin served as an intra-slope basin located between the fluvio-deltaic Tremp-Graus Basin to the east and the deepwater fans of the Jaca Basin to the west (Figures 1.8 and 1.11) (Mutti, 1977;

Seguret *et al.*, 1984; Farrell *et al.*, 1987; Labaume *et al.*, 1987; Muñoz *et al.*, 1994; Fernández *et al.*, 2004).

Ainsa Basin deepwater deposits comprise over 4000 m of strata and are divided into multiple stratigraphic units by past workers. Pickering and Corregidor (2005) identify seven unconformity-bound units deposited over a period of approximately 10 million years, which are, from oldest to youngest: 1) Fosado, 2) Arro, 3) Gerbe, 4) Banaston 5) Ainsa, 6) Morillo, and 7) Guaso units (Fig. 1.12). These unit names are used in this manuscript with the addition of the Sobrarbe unit, a deltaic complex that represents the final stage of Ainsa Basin-fill (Dreyer *et al.*, 1999). The four uppermost systems, the Ainsa, Morillo, Guaso, and Sobrarbe, are the primary focus of this study and based on the timing scenario of Pickering and Bayliss (2009), they were deposited over a period of ~3.5 million years (Fig. 1.13).

Ainsa Basin deepwater systems exhibit a south-southwest shift in the depocenter associated with aggradational stacking through time (Figures 12 and 14) (Pickering and Corregidor, 2005; Heard *et al.*, 2008; Pickering and Bayliss, 2009). This shift is also present within the sand bodies of each system, with the oldest sand body of each system being reset to the east (Pickering and Bayliss, 2009). This shifting and aggradational pattern is attributed to an interplay of glacio-eustatic and tectonic processes, with glacio-eustacy operating at a scale that controls sand input into the basin and tectonics operating at a scale that influences how the systems stack through time (Fig. 1.14) (Heard *et al.*, 2008; Pickering and Bayliss, 2009).

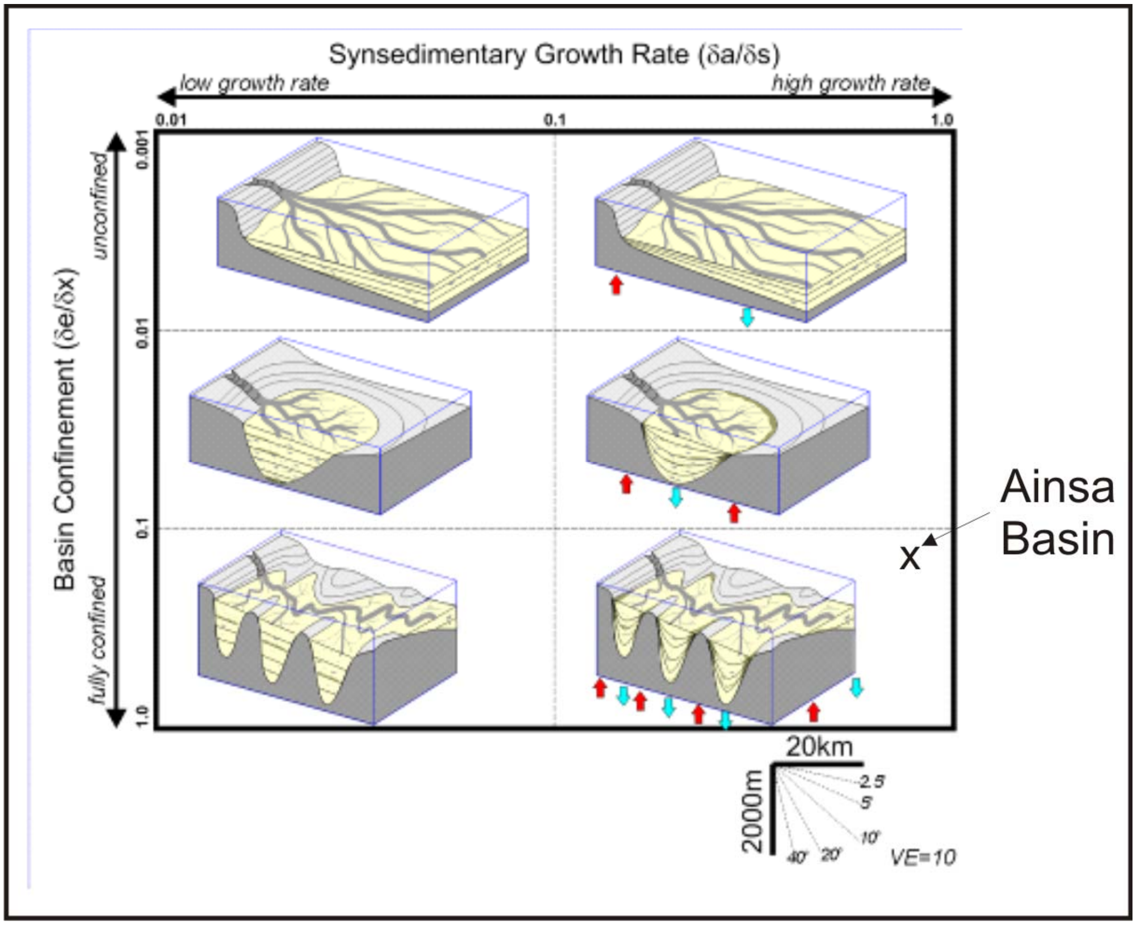

Figure 1.1: Matrix relating synsedimentary growth rate to basin confinement. Ainsa Basin fill geometries are indicative of a highly to moderately confined basin with a high synsedimentary growth rate (from Pyles, 2007).

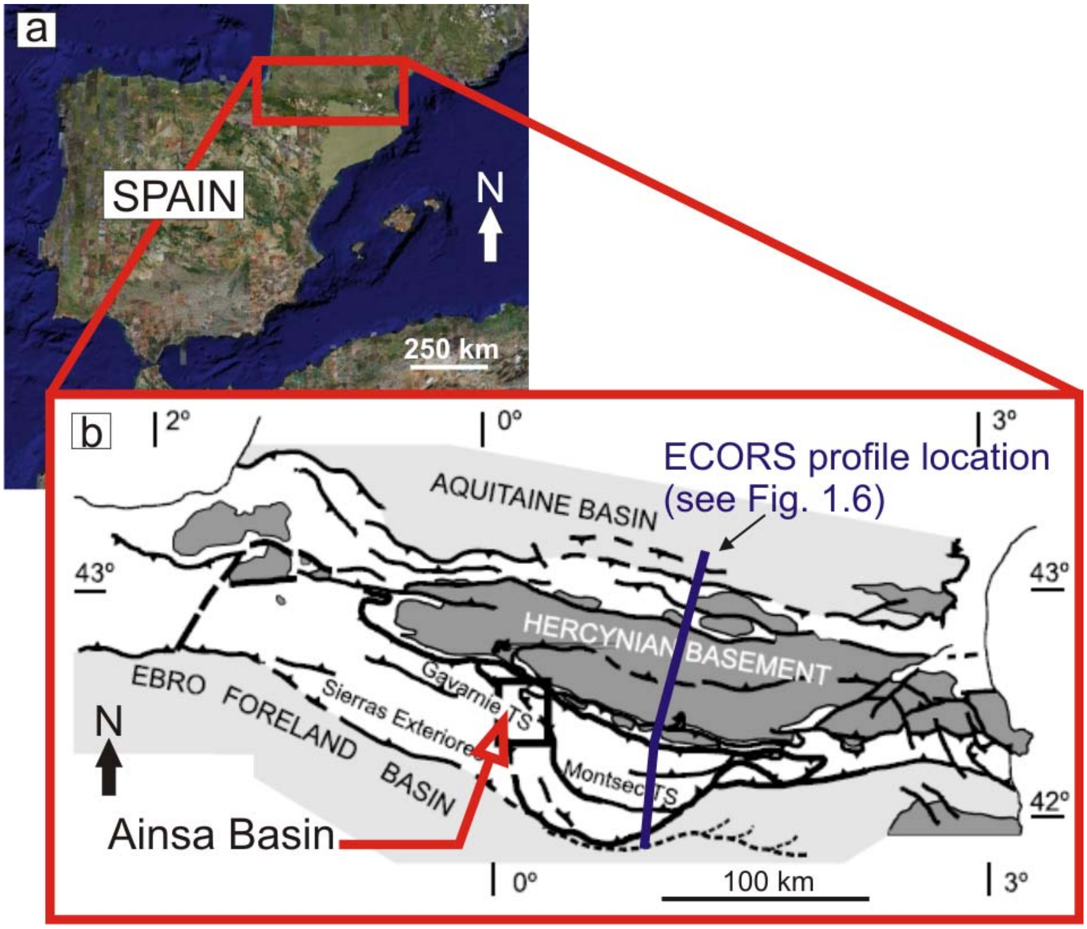

Figure 1.2: Regional location map. a) Location of the Pyrenean orogen. b) General structure of the Pyrenean orogen and location of Ainsa Basin within the southern Pyrenees (modified from Fernández *et al*., 2004; satellite image from GoogleEarth).

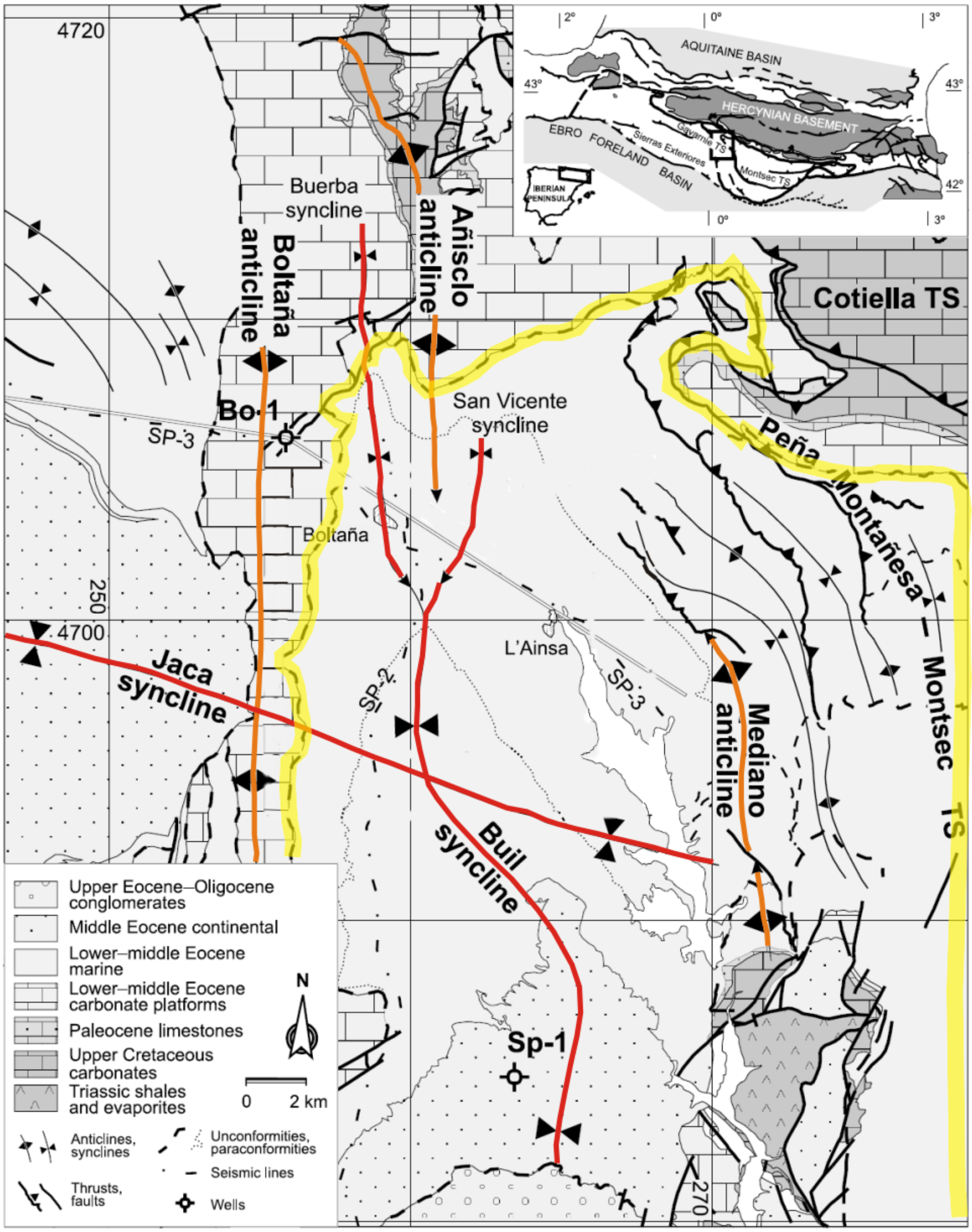

Figure 1.3: Geological map of Ainsa Basin (modified from Fernández *et al.*, 2004). SP-1 and SP-2 are 2-D seismic line locations acquired from the Instituto Geológico y Minero de España (IGME). Bo-1 and Sp-1 mark the location of exploratory wells.

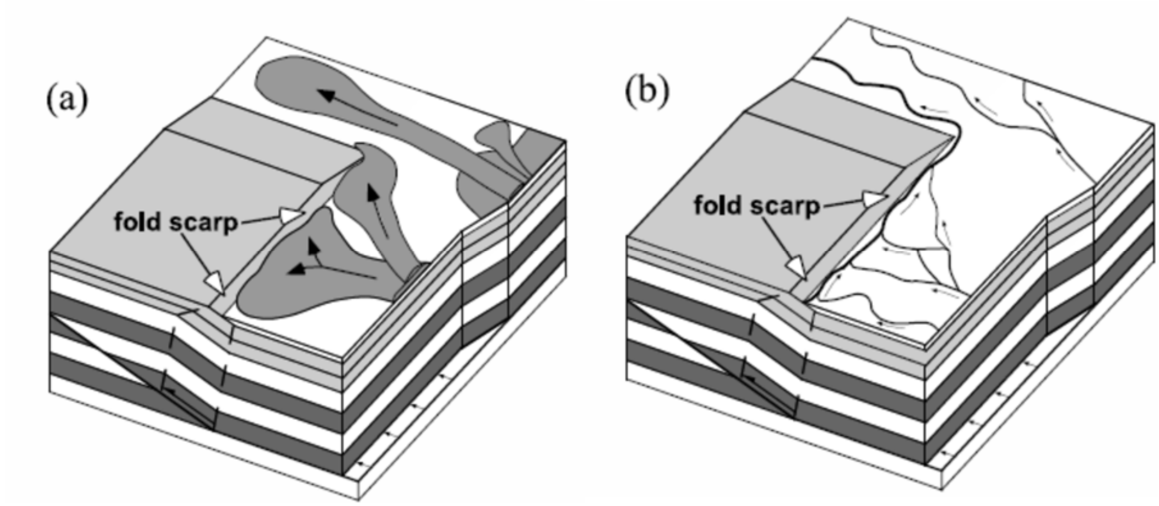

Figure 1.4: Three-dimensional fault-bend fold models showing the influence of a growing fold surface on deep-water sediment dispersal patterns. a) Illustrates the influence on clastic fan deposition. b) Illustrates the influence on channel direction (from Shaw *et al.*, 2004).

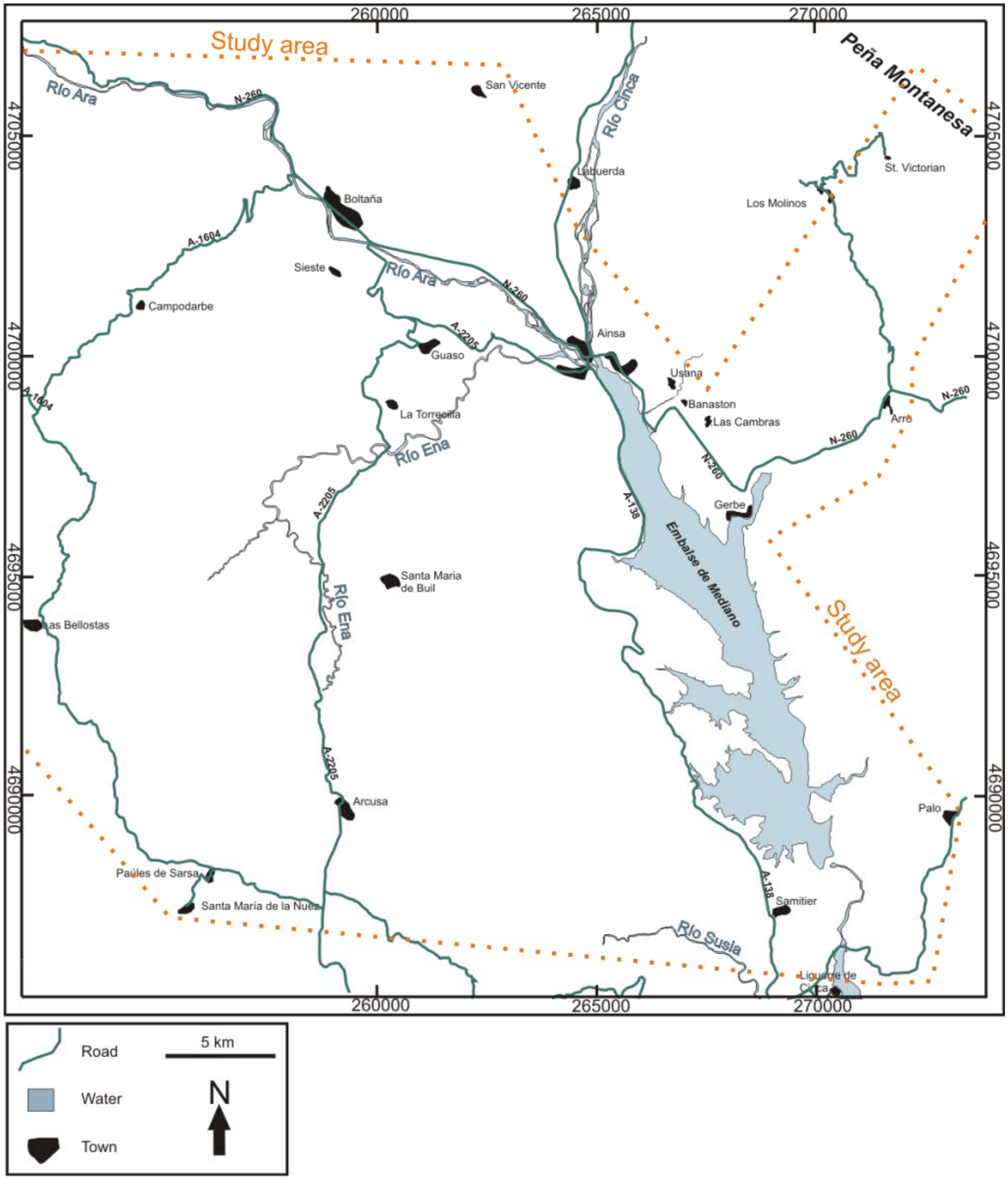

Figure 1.5: Culture map of study area. Units along outer border are UTM coordinates.

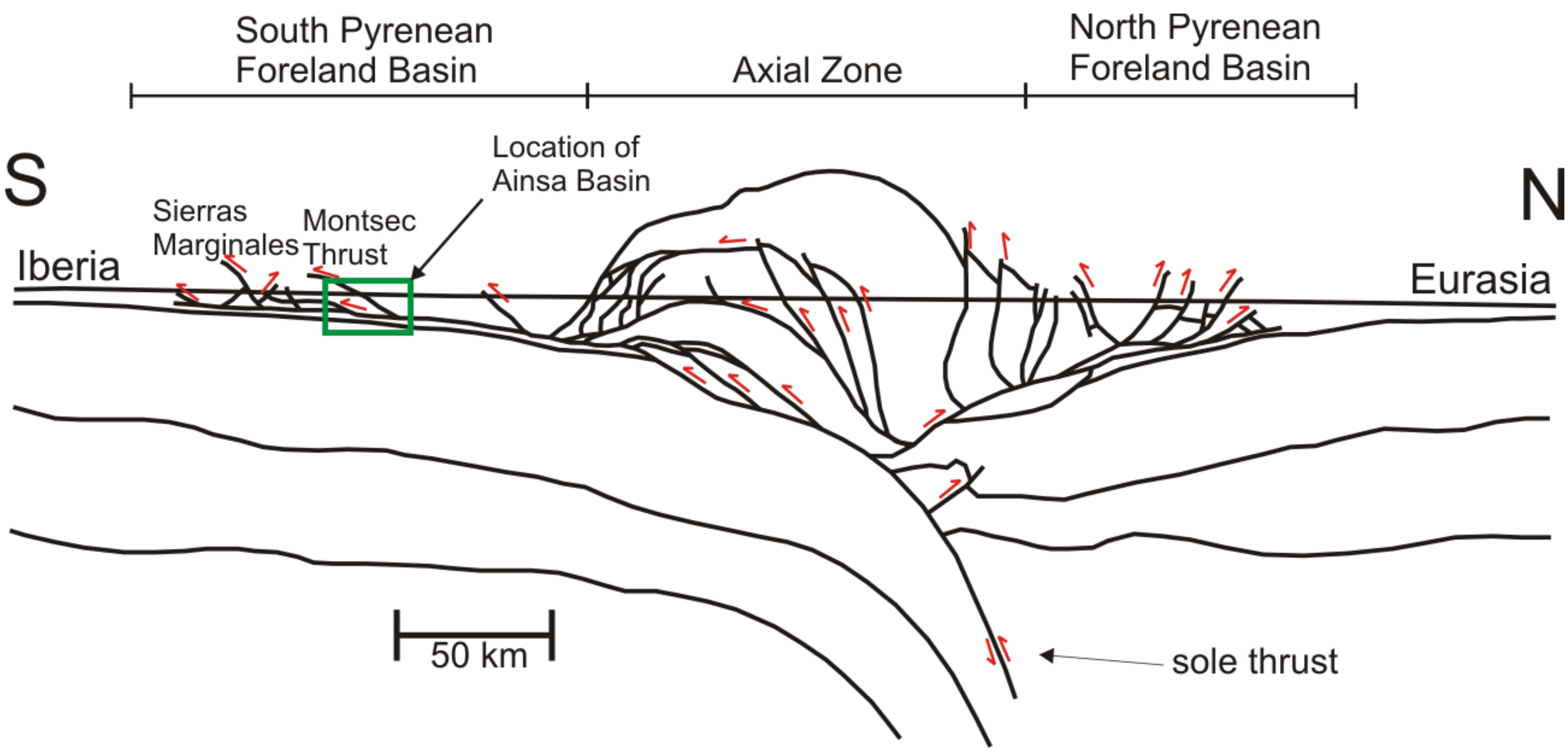

Figure 1.6: Cross section through the Pyrenees orogeny derived from the ECORS regional seismic profile (see Fig. 1.2 for location) (modified from Puigdefábregas *et al.*, 1992).

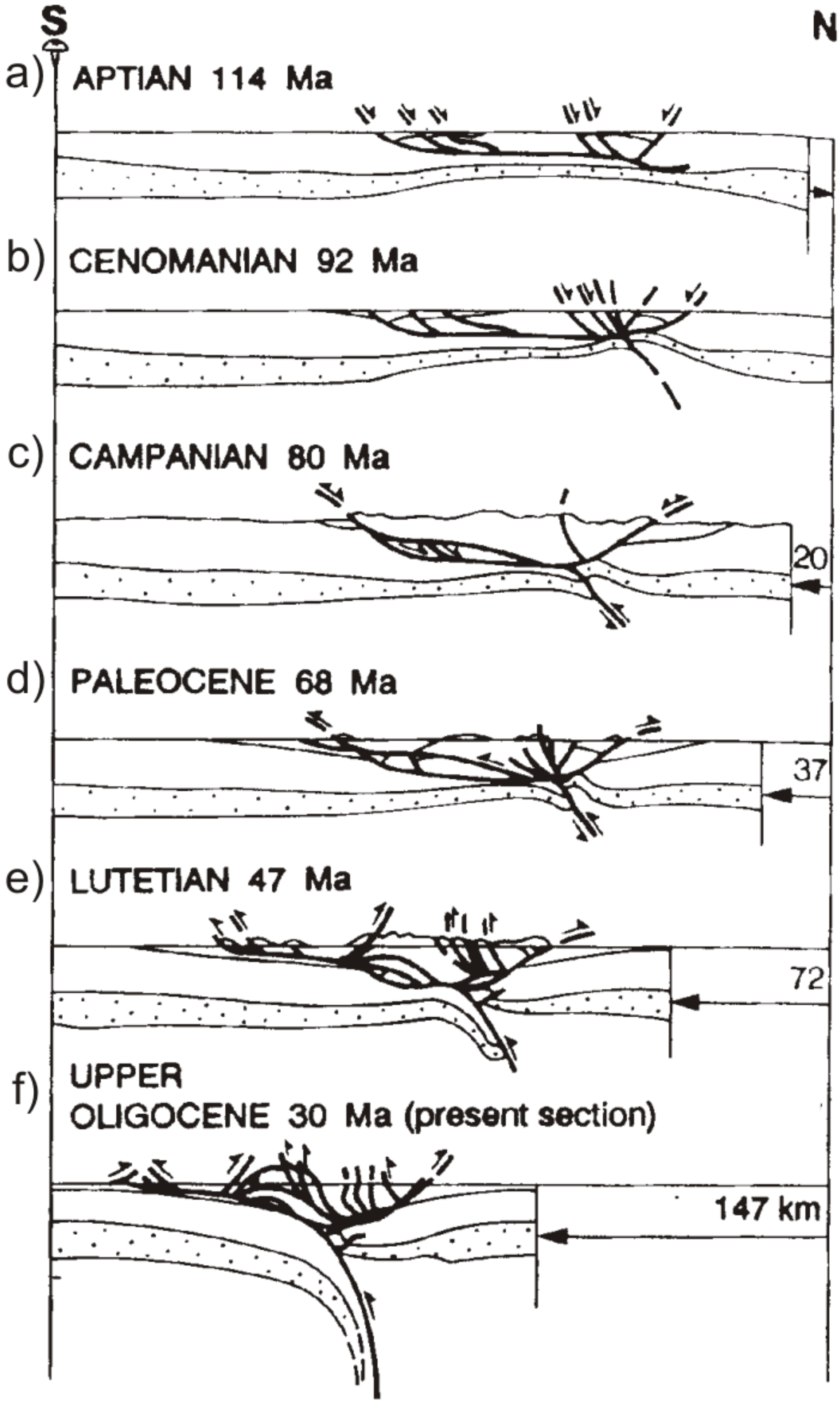

Figure 1.7: Partial restoration of the ECORS seismic profile through the Pyrenees orogen (from Puigdefábregas *et al.*, 1992).

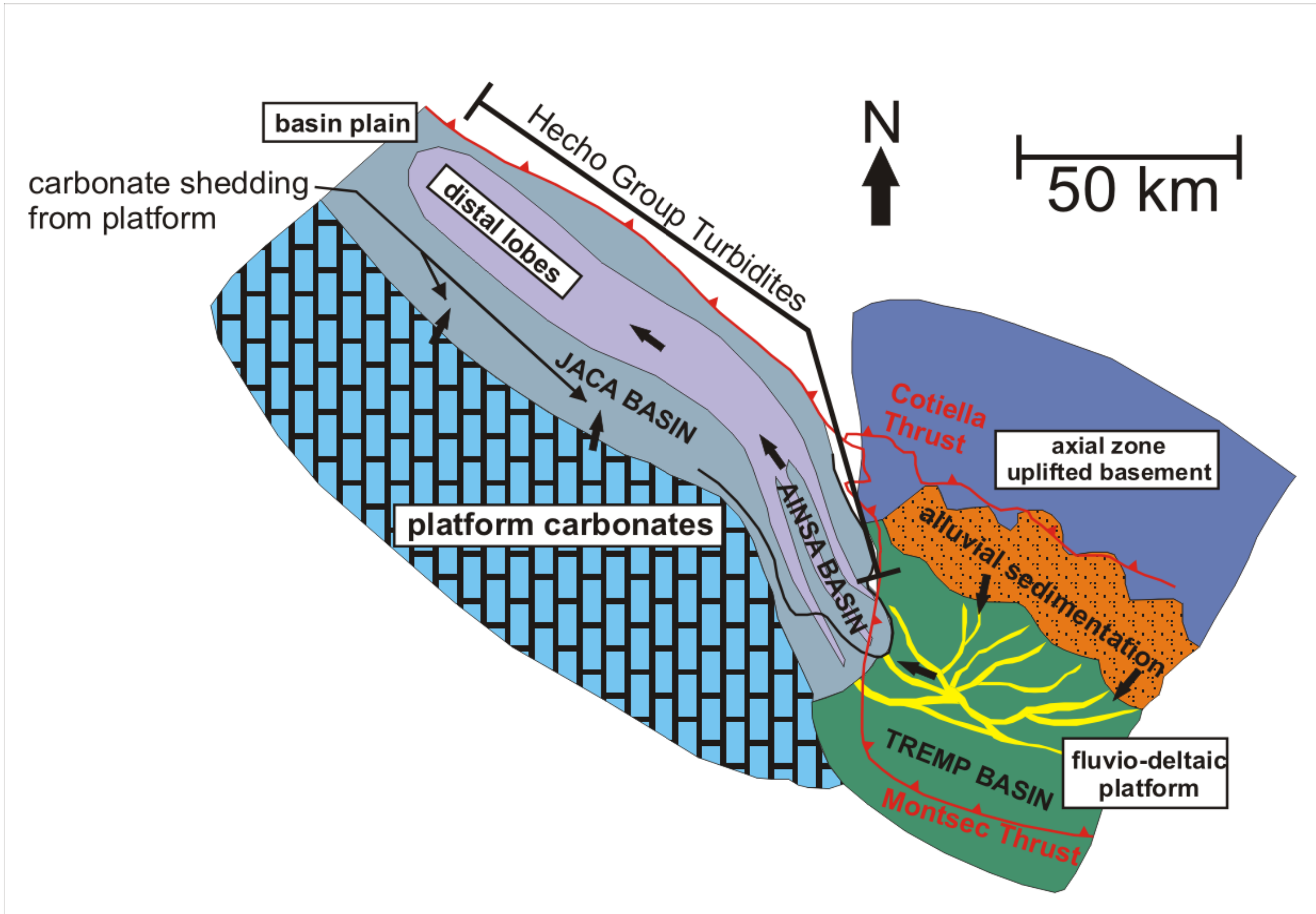

Figure 1.8: Paleogeographic map of the Middle Eocene South Pyrenean Foreland Basin (modified from Muñoz *et al.*, 1998).

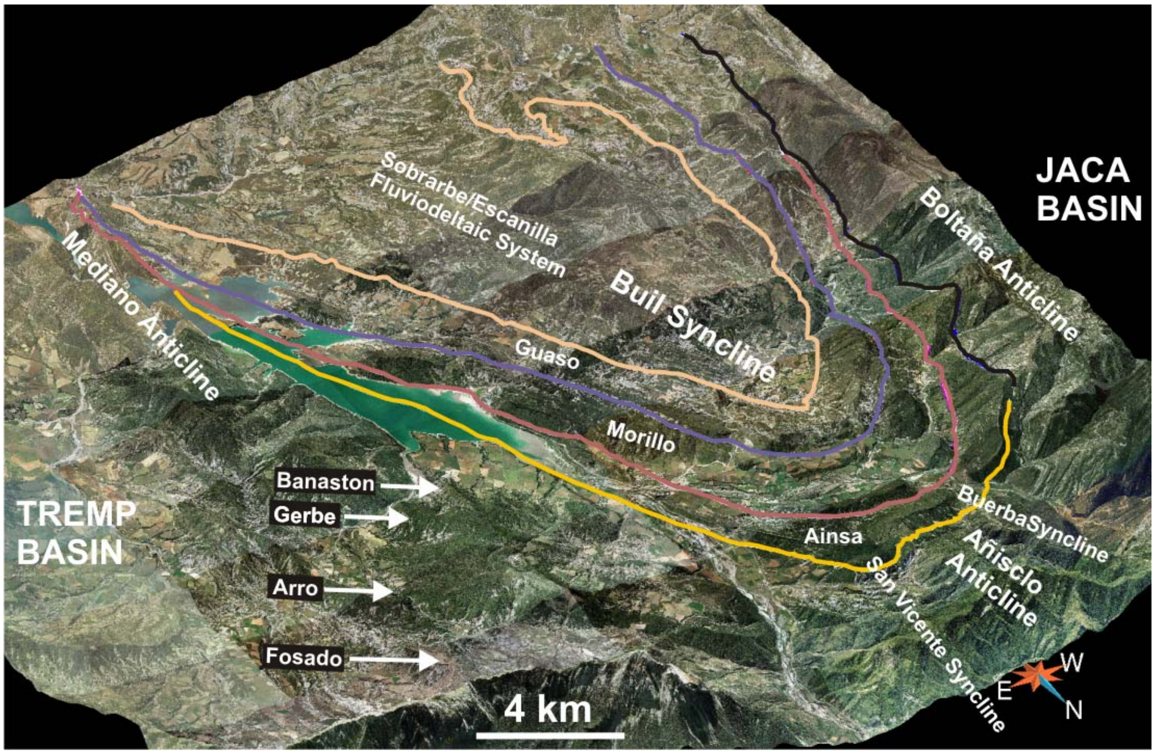

Figure 1.9: Photo-draped digital elevation model (DEM) of Ainsa Basin. View is to the southwest. Major basin structures and the eight primary deepwater stratigraphic units are labeled. The Ainsa, Morillo, Guaso and Sobrarbe units are mapped as condensed section bound units in this study.

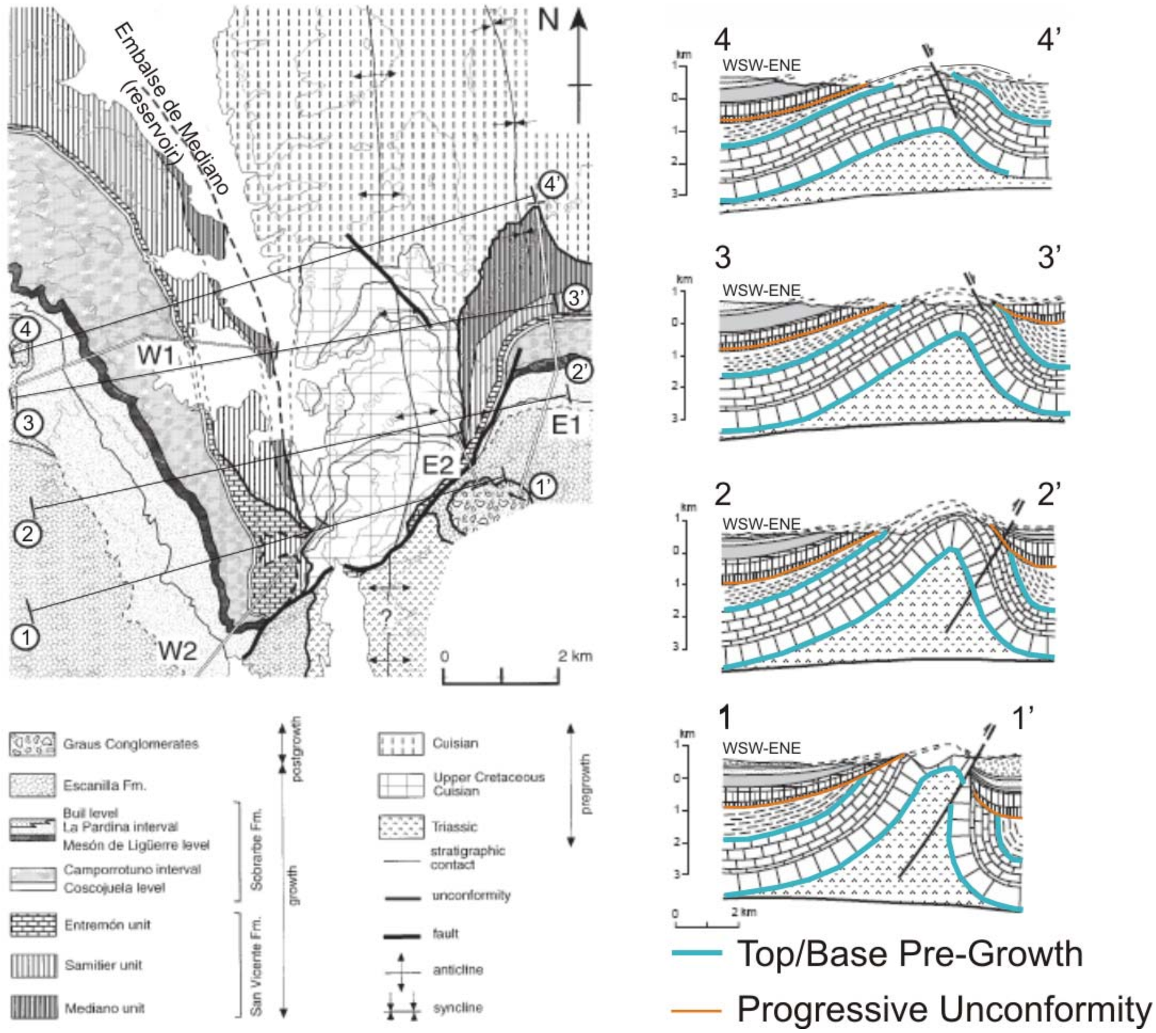

Figure 1.10: Map and cross sections constructed through the Mediano Anticline. Note the intra-growth strata progressive unconformity and wedging onlap geometries which are indicative of synsedimentary fold growth (modified from Poblet *et al*., 1998).

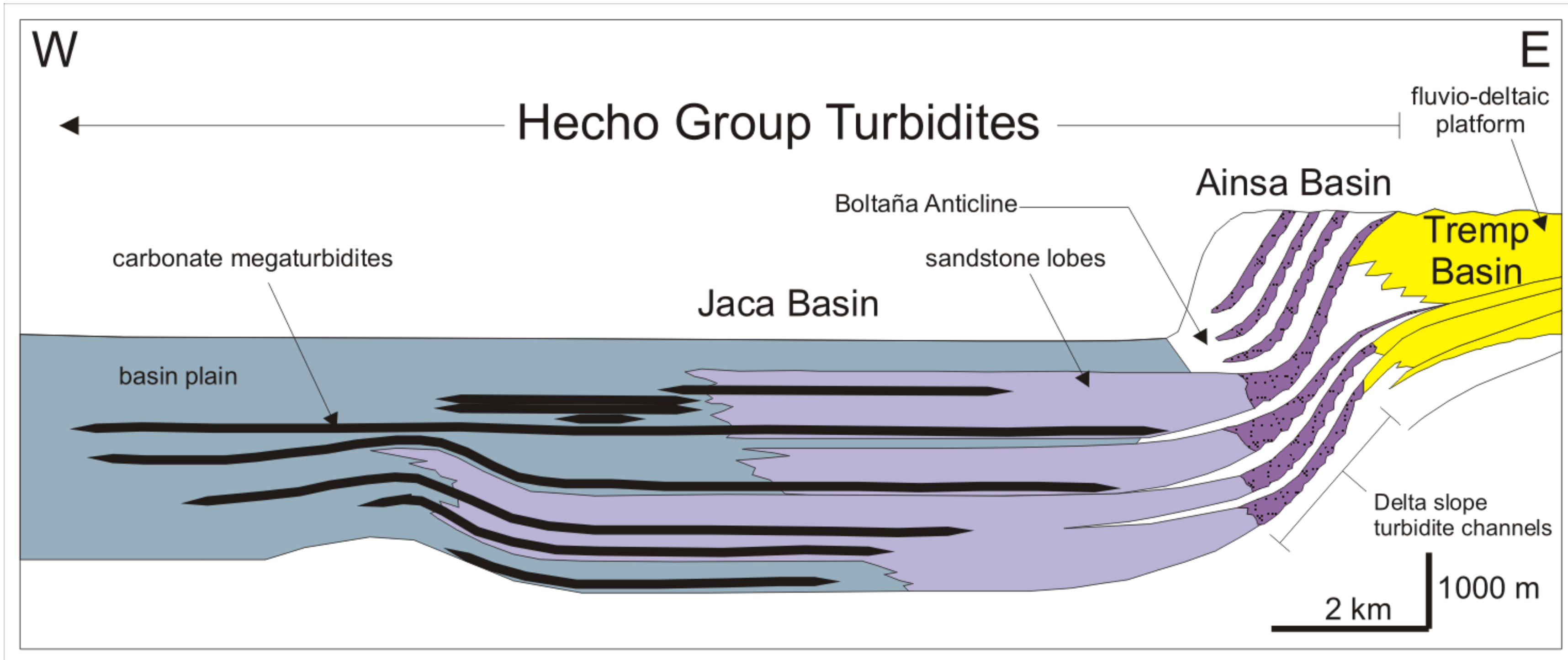

Figure 1.11: Stratigraphic cross section through the Tremp, Jaca, and Ainsa Basins. Ainsa Basin served as an intra-slope mini-basin between fluvio-deltaic systems in the Tremp Basin and deepwater lobes of the Jaca Basin. Note the lack of outcrop correlation between the upper turbidite deposits of Ainsa Basin and deepwater lobe deposits of Jaca Basin (modified from Labaume *et al*., 1987).

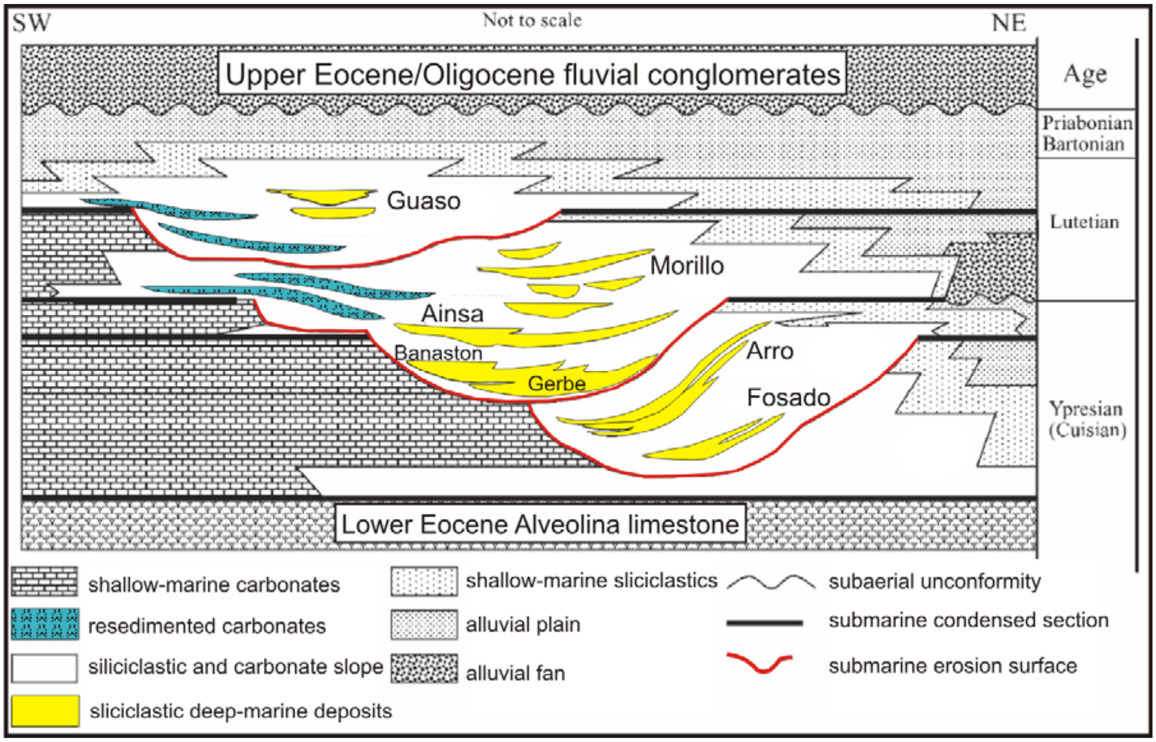

Figure 1.12: Simplified stratigraphic chart of the seven deepwater systems that comprise the Ainsa Basin fill succession. Absent is the Sobrarbe system which directly overlies the Guaso system, making up the final stage of Ainsa Basin fill (modified from Pickering and Corregidor, 2005).

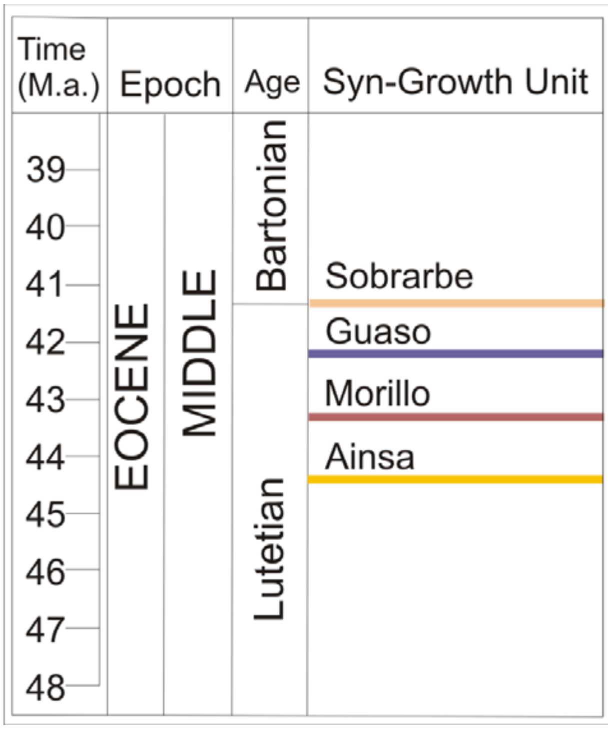

Figure 1.13: Chart showing the approximate timing of deposition for the four syn-growth systems that are the focus of this study. Timing is based on Pickering and Bayliss (2009).

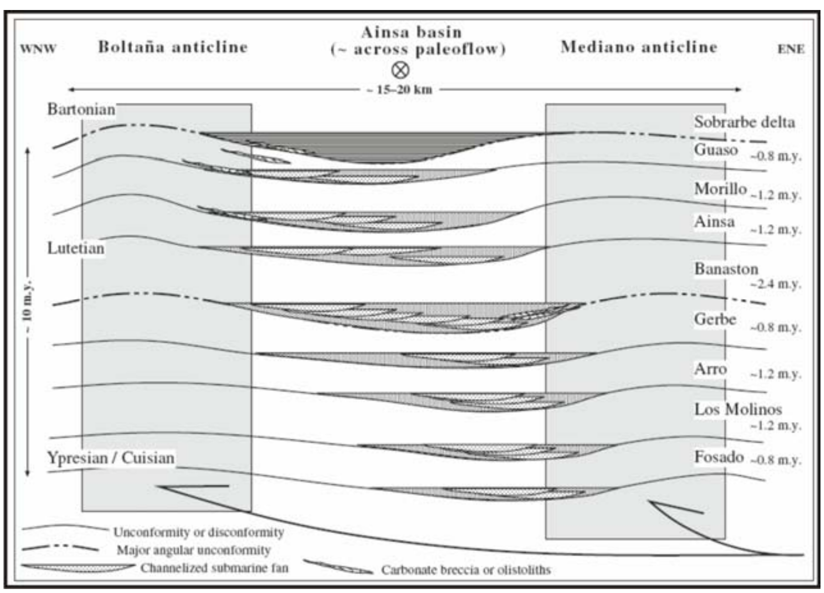

Figure 1.14: Diagram illustrating the evolution of the Ainsa Basin fill succession. System timing is based on ~400 k.y. glacio-eustatic cyclicity. Note the overall westward shift of the systems through time and the westward intra-system shift of sand bodies (modified from Pickering and Bayliss, 2009).

CHAPTER 2

LITERATURE REVIEW

This chapter summarizes current knowledge for 1) foreland basins, 2) detachment folds and fault-propagation folds, 3) stratigraphic response to compressional structural growth, 4) structural cross section construction and restoration, and 5) 3-D structural modeling.

2.1 Foreland Basins

Foreland basins are defined as elongate troughs that develop between a contractional orogenic belt and a stable craton, as a result of flexural subsidence created by orogenic thrust sheet loading (Fig. 2.1a) (Decelles and Giles, 1996). Foreland basins are usually wedge-shaped in transverse cross section and thickest adjacent to the orogenic belt (Fig. 2.1b). The dominant source of sediment for the basin-fill is from the associated orogen; however, minor contributions may come from the craton side of the basin (Dickinson and Suczek, 1979). General characteristics of a foreland basin include a foredeep, forebulge, and a back-bulge (Fig. 2.1c), which forms in isostatic response to thrust sheet loading in the hinterland (Decelles and Giles, 1996). The following two sections describe piggyback basins and the mechanics that govern the structural evolution of foreland basins.

2.1.1 Piggyback Basins

In an active orogen with continued propagation of the orogenic wedge towards the foreland, the foreland basin may become partitioned by thrust sheets and evolve into a series of piggyback basins (Fig. 2.1c) (Ori and Friend, 1984; Decelles and Giles, 1996). Piggyback basins are defined as all sedimentary basins formed on active thrust sheets (Ori and Friend, 1984; Clevis *et al*., 2004). The foreland extent of piggyback basins is defined by the frontal thrust of the foreland fold and thrust belt (Decelles and Giles, 1996). Piggyback basin deposits typically consist of alluvial and fluvial sediments in the sub-aerial setting and sediment gravity flows and fine-grained shelf sediments in the sub-aqueous setting (Decelles and Giles, 1996). One of the distinctive characteristics of piggyback basins is the prevalence of growth strata, indicating that sediment was deposited and deformed at or near the syn-tectonic surface (Riba, 1976; Burbank *et al.*, 1992, Coney *et al.*, 1996; Decelles and Giles, 1996; Poblet *et al.*, 1998).

2.1.2 Foreland Fold and Thrust Wedge Mechanics

The development of critical-taper theory, as applied to tectonics, in the early 1980s provided a broad mechanical model for the comparison of macroscopic structure and mechanics between individual wedges found in natural orogens. Davis *et al.*, (1983) first described the theory quantitatively in a geologic context.

Critical-taper theory can be applied to both fold-and-thrust belts and accretionary wedges. This is due to the commonalities these features share in cross section: 1) a hinterland dipping detachment surface below which there is little to no deformation, 2) a large degree of horizontal shortening above a detachment surface, 3) a wedge-shaped geometry that tapers toward the distal regions of the orogen, and 4) the presence of a back-stop against which the relative movement of geologic bodies drives deformation (Chapple, 1978; Davis *et al.*, 1983).

To conceptualize wedge deformation, fold-and-thrust belt and accretionary wedge development is compared to the wedge of snow or soil that forms in front of a moving bulldozer (Fig. 2.2) (Chapple, 1978; Davis and Suppe, 1980). The bulldozer is analogous to the overlying lithospheric plate in the accretionary wedge setting or the inner thickest part of a mountain range in a fold-and-thrust belt setting. With movement over the detachment surface, the overlying material deforms internally until a critical taper is achieved. Once the critical taper is attained and the wedge no longer accretes material, the wedge slides without internal deformation and represents the thinnest body of material that can be thrust over the underlying detachment surface (Davis *et al.*, 1983; Boyer, 1995). If material continues to be actively accreted, the wedge continuously deforms internally to maintain critical taper.

Evolution of the critically-tapered wedge model is based on pressure-dependent, time-independent Coulomb failure, which describes the conditions under which brittle deformation occur (brittle fracture or frictional sliding). This is defined by the Coulomb criterion for shear traction at failure:

$$\left|\tau\right| = S_0 + \mu(\sigma_n - p_f)$$

, where τ is shear traction, S_0 is cohesion, μ is the coeffiecient of friction, σ_n is the normal traction, and p_f is pore fluid pressure. The role of cohesion (S_0) is considered negligible relative to the role of pore fluid pressure (p_f), which has been empirically demonstrated to significantly decrease a siliciclastic rock's ultimate strength, rupture strength, and ductility when elevated above the hydrostatic gradient (Handin *et al.*, 1963).

Figure 2.2 shows all parameters involved with the critically-tapered-wedge model: α represents the local angle of topographic relief, β represents the local dip angle of the fixed detachment surface, D represents the water burden measured along the angle of gravity, and dx represents an artificial column within the wedge. Internal deformation within the wedge and movement of the wedge itself is dependent on a balance of forces in the x direction. These include: 1) the x component of the gravitational body force ($-\rho g H\, dx \sin \beta$), 2) the x component of the water overburden in the case of a sub-sea wedge ($-\rho_w g D\, dx \sin(\alpha+\beta)$), 3) the frictional resistance to sliding ($-\tau_b\, dx$), and 4) the normal traction acting across a face perpendicular to the x axis, which is positive under a compressional regime.

Ultimately, wedge deformation can be described by two driving forces: 1) gravity acting on the sloping top surface of the wedge and 2) the horizontal push from the rear of the wedge that is dependent on the taper or the sum of the angles of the detachment surface and the topographic relief (α+β) (Davis *et al.*, 1983). The horizontal push is considered to be the dominant force, at four to five times greater than the gravitational force (Davis *et al.*, 1983).

2.2 Compressional Structures

The Ainsa Basin is bounded to the east, west, and north by growth anticlines that are interpreted as detachment and fault-propagation folds (Poblet *et al.*, 1998; Fernández *et al,*. 2004; Tavani *et al*., 2006). The following section describes the geometric and kinematic models for such compressional structures.

2.2.1 Detachment Folds

Detachment folds form above bedding-parallel detachment faults related to distributive deformation in the overlying hanging-wall strata (Epard and Groshong, 1995; Poblet and Hardy, 1995; Storti and Poblet, 1997; Poblet *et al.*, 1997; Shaw *et al.*, 2005). The detachment fault is generally associated with an incompetent and ductile unit, such as salt or shale, which thickens into the core of the overlying fold (Fig. 2.3) (Wallace and Homza, 2004). The fold itself is not related to a thrust ramp, however, detachment folds have been documented to evolve into thrust-breakthrough and fault-propagation geometries (i.e. Tavani *et al.*, 2006).

Detachment folds can be identified by geometry alone. Sufficient evidence includes thickening of an underlying incompetent unit and the lack of a ramp (Wallace and Homza, 2004). However, this requires knowledge of the geometries of both the incompetent and competent units. Without detailed knowledge of the unit geometries, growth strata must be used as the diagnostic element (Poblet *et al.*, 1997; Wallace and Homza, 2004).

Multiple kinematic models have been developed for detachment folds (Dahlstrom, 1990; Epard and Groshong, 1995; Storti and Poblet, 1995; Poblet *et al.*, 1997). Dahlstrom (1990) discusses the implications of a model predicting depth-to-detachment using the stratigraphic elevation of a reference horizon above the detachment surface and the area uplifted above a pre-folded level. This predictive method was deemed problematic due to disproportionately large areas lifted above regional with relatively little shortening on shallow anticlinal limb dips. Epard and Groshong (1995) presented an area balanced fold model that grows by limb rotation and requires layer parallel strain to accommodate changes in bed-length. Two kinematic evolutions are presented: 1) a fixed hinge model, and 2) a migrating hinge model (Fig. 2.4).

Poblet *et al.* (1997) introduce two end-member models: 1) folds that grow primarily through limb rotation and 2) folds that grow primarily though limb lengthening (kink-band migration) (Fig. 2.5). A third model is presented wherein the detachment fold growth occurs through both limb rotation and limb-lengthening (Fig. 2.5). While multiple kinematic models have been documented, the most prevalent and best-supported model is a fixed anticlinal hinge with rotating limbs (Wallace and Homza, 2004).

The kinematic evolution of a given detachment fold can be determined by growth strata geometries (Fig. 2.6) (Poblet and Hardy, 1995; Poblet *et al.*, 1997). Folds that grow through limb rotation create growth strata geometries with fanned limb dips (Fig. 2.6a) while folds that grow through limb lengthening create growth strata geometries with dips that are concordant with pre-growth strata (Fig. 2.6b) (Poblet and Hardy, 1995; Poblet *et al.*, 1997; Castelltort *et al.*, 2003). Assuming kink-band migration models for fault-related folds, only detachment folds should show evidence of significant limb rotation (Wallace and Homza, 2004).

2.2.2 Fault-Propagation Folds

Fault-propagation folds occur when a thrust ramp propagates gradually so that at any moment during active faulting, slip dies out to zero at the fault tip (Suppe and

Medwedeff, 1990; Mitra, 1990; Saffar, 1993; Wallace and Homza, 2004). The fault-propagation fold grows at the ramp tip, consuming slip on the underlying ramp. Common characteristics of fault propagation folds include: 1) an asymmetric fold geometry with a steeply dipping forelimb and gentler dipping backlimb with vergence in the direction of transport, 2) an adjacent syncline pinned to the fault tip, and 3) fold geometries that generally tighten with depth (Shaw *et al.*, 2005).

Three main models of folding have been documented in the literature: 1) a constant thickness model (Fig. 2.7a) (Suppe and Medwedeff, 1990), 2) a fixed axis model (Fig. 2.7b) (Suppe and Medwedeff, 1990) and 3) trishear folding described by Erslev (1991) (Fig. 2.7c).

Constant thickness fault-propagation folds assume angular fold hinges and preservation of bed length. Limbs are assumed not to rotate with fold growth and the fold hinges migrate with the rock (Fig. 2.7a) (Wallace and Homza, 2004).

Fixed-axis fault-propagation fold models account for bed thickening or thinning in the forelimb, the magnitude of which is controlled by the cut-off angle values and changes in fault dip (Fig. 2.7c) (Suppe and Medwedeff, 1990).

Trishear fold models develop through the distributed shear in a triangular zone anchored at the fault tip. Trishear fold geometries are dependent on the propagation to slip ratio, the angle between the surfaces defining the trishear zone (apical angle), and fault orientation (Fig. 2.7c) (Erslev, 1991; Shaw *et al.*, 2005).

Fault-propagation folds must meet the kinematic condition of forming at and being genetically related to propagation at the tip of a fault ramp. The interpretation of a fault-propagation fold cannot be based on geometry alone, as a preexisting fold can be modified by the later propagation of a ramp tip (Wallace and Homza, 2004). Ideally, knowledge of the fold core can serve as a diagnostic indicator of a fault-propagation fold, however, poor outcrop and limited resolution of seismic imaging make interpreting fold core geometries difficult. In general, fault-propagation folds can be assumed to maintain a constant forelimb and backlimb dip (Mitra, 1990; Suppe and Medwedeff, 1990; Saffar, 1993; Wallace and Homza, 2004). Additionally, they are more likely to form in homogenous strata with anisotropic mechanical stratigraphy (Wallace and Homza, 2004).

2.3 Growth Strata Related to Compressional Structures

The following sections describe patterns observed in the stratigraphic record that are indicators of syn-depositional structural growth.

2.3.1 Large Scale Stratigraphic Patterns

Growth strata are important indicators of the timing and kinematics of faults and folds, serving as a passive marker that records tectonic activity. Growth geometries are most easily recognizable and studied in seismic data (Fig. 2.8b) (i.e. Suppe *et al.*, 1992; Morley and Leong, 2007). Assuming a kink-band migration folding mechanism, where beds change dip by rolling through axial surfaces (Suppe *et al.*, 1992), sedimentation during active fold growth causes an upward decrease in limb length through the growth strata and a narrowing of the axial surfaces (Fig. 2.8) (Medwedeff, 1992; Suppe *et al.*, 1992; Shaw *et al.*, 2005). Growth strata can also reflect which axial surfaces were active or remained fixed during fold growth (Fig. 2.8a) (Suppe *et al.*, 1992). Consequently, it is possible to distinguish between strata deposited synchronously with tectonic deformation and strata deposited over stationary paleo-topography (Fig. 2.9).

Basin-fill not only records the history and kinematics of deformation, but other external controls such as climate change or eustatic sea-level changes as well. These factors combine to influence two main variables: 1) sediment supply (S) and 2) accommodation (A) (Castelltort *et al.*, 2003). Varying rates of deformation and eustatic sea-level change, the rates of sediment supply, and accommodation creation or destruction are directly affected (Gupta and Cowie, 2000; Castelltort *et al.*, 2003). The relationship between accommodation and sediment supply (A/S) is manifested in growth strata geometries (Poblet *et al.*, 1997; Castelltort *et al.*, 2003; Tavani *et al*., 2007).

Castelltort *et al.* (2003) use biostratigraphic and magnetostratigraphic data to calculate variation of accommodation space and sediment supply and document the changes in growth rate of the Pico de Aguila Anticline, a detachment fold in the southern Pyrenees (also see Poblet and Hardy, 1995). This study identifies three primary controls that fold growth has on the stratigraphic record: 1) thickness variation, 2) modification of the depositional profile, and 3) the progradational/retrogradational (P/R) thickness ratio changes within sequences. The Pico de Aquila Anticline is shown to affect the stratigraphic record in the following ways: 1) sequence thicknesses are greatest in the synclinal hinges adjacent to anticline crest, 2) shallow water facies were deposited on the anticline crest and deeper water facies deposited in the synclinal hinges, indicating syn-depositional structural relief, and 3) growth on the structure creates spatial variation in subsidence at the local scale, altering A/S ratios, and favoring increased thickness in retrogradational units relative to progradational units (Fig. 2.10). These stratigraphic patterns are not necessarily specific to the Pico de Aguila Anticline and can potentially be found associated with any structure in a where accommodation space is actively being created or destroyed during sedimentation.

2.3.2 Small Scale Stratigraphic Patterns

The following sections describe patterns observed at the outcrop scale that are indicators of syn-depositional structural growth.

2.3.2.1 Channel/Paleocurrent Deflection

Depending on A/S ratios, paleocurrents may be deflected parallel to a fold axis if a significant paleo-high is developed along an anticlinal hinge (Fig. 2.11) (Castelltort *et al.*, 2003; Moody, 2009).

Multiple studies document the mechanics of sediment gravity flows as they interact with structural topography. Clayton (1993) describes a method to distinguish between paleocurrent deflection caused by the Coriolis Effect and deflection caused by topography. The amount of flow deflection possible by the Coriolis Effect can be predicted through knowledge of flow thickness, velocity, and paleo-latitude. Structural topography can create flow non-uniformity in turbidity currents, which describes the spatial variability in flow velocity, and which triggers the rapid deposition of suspended sand (Kneller and Branney, 1995; Kneller, 1998). Tank experiments involving turbidity currents and a wedge shaped obstacle indicate that topography can cause a thickening of the flow up-current from the obstacle, which corresponds to an abrupt increase in thickness of deposit in the region of the thickened flow (Morris and Alexander, 2003).

Additionally, flume experiments indicate that turbidity current deflection off of an obstacle (i.e. basin margin slopes, faults surfaces) can generate sedimentary structures that indicate secondary current directions orthogonal to oblique to the obstacle (Kneller *et al.*, 1991). These results have implications for reconstructing basin paleo-physiography and tectonic configurations through time.

2.3.2.2 Mass Transport Complexes

The presence of mass transport complexes (MTCs) in the stratigraphic record can potentially record tectonic activity (Martinsen *et al.*, 2003). MTCs are closely related to margins that may steepen with structural growth. While MTCs may occur at any time during a basin's evolution, they are commonly found in the early phases of basin-fill during lowstand phases when the sedimentation at the shelf edge is at its peak (Moscardelli, 2006). This is the case in the Ainsa Basin, where MTCs within the earliest deepwater basin-fill systems are attributed to slope instabilities triggered by thrust activity and played a role in shaping the basin-floor morphology (Arbués et al., 2007).

MTC geometry can vary extensively, ranging from a few meters to two hundred meters in thickness, and hundreds of square meters to tens of thousands of square kilometers in area (Moscardelli, 2006). MTCs are divided into two sub-categories: slumps and slides. Slides define a translational movement with little internal deformation, whereas slumps define translational movement coupled with a high degree of internal bed deformation (Cook and Mullins, 1983). Analysis of minor, syn-sedimentary fold axes within slumps provides clues as to the direction of transport and orientation of the paleo-slope (Fig. 2.12) (Bradley and Hanson, 1998).

Ultimately, original lithology dictates the MTC type, with thinly laminated, muddier material more likely to experience internal deformation, and more cohesive material (i.e. massive carbonates and lithified blocks) likely to remain undeformed. Both slumps and slides are bounded upslope by a related basal scarp or shear plane that has a few to hundreds of meters of relief (Cook and Mullins, 1983; Tripsanas *et al*., 2007).

2.3.2.3 Clastic Intrusions

Another potential indicator of structural growth is the presence of clastic intrusions or sedimentary dykes and sills. Intrusion networks are most commonly documented in tectonically active settings where sedimentation rates are high and tectonic stresses facilitate the development of high fluid pressures within unconsolidated sediments (Winslow, 1983; Jolly and Lonergan, 2002). Clastic intrusions form from the injection of pressurized fluids with entrained grains into overlying substrate (Fig. 2.13). Structures consist of dish and pillar structures, convolute lamination, load structures, and flames (Jolly and Lonergan, 2002).

2.4 Cross Section Balancing and Restoration

Cross section restoration and balancing places geometric and temporal constraints on structural interpretations. In addition to aiding academic studies, restoration plays a major role in determining the evolution of hydrocarbon systems through time and thus has become a critical tool used in the hydrocarbon industry (Wickham and Moeckel, 1997). Current balancing and restoration techniques originated from early methods in calculating deformational shortening. Fundamentally, section balancing relies on the concept of compatibility: a deforming rock mass remains coherent can be restored to its original geometry without unexplained gaps and overlaps (Coward, 1992).

Methods in cross section restoration and balancing have undergone significant evolution since early studies. Oertel (1974) first applied the concept of measured strain to structural restoration, but limited the application to an individual layer within a single fold. Oertel and Ernst (1978) applied strain data to the restoration of a multi-layered fold. Strain from layer to layer was accounted for by dividing a fold into zones of homogeneous strain. Inconsistencies were identified with this method, largely associated with the assumption of homogeneous strain and incompatibilities between strain zones. Attempts to correct these inconsistencies were made with the application of finite elements and strain trajectories to restoration (i.e. Cobbold, 1979; Cobbold and Percevault, 1983; Gratier *et al.*, 1991). Elliott (1983) established a hierarchy for cross section construction confidence and created guidelines for defining a truly balanced and restorable cross section.

Two main types of balancing may be performed: line-length balancing and area balancing. Line-length balancing involves the restoration of lines measured from bedding lengths across a section and matching them to a plotted, restored state. Area-balancing involves matching areas of fault blocks to a pre-deformed state. This method is particularly applicable to blocks that have been internally strained. While both methods assume plane-strain, area loss or gain in the area-balancing method may be accounted for by adjusting areas in the pre-deformed state. However, problems arise when variable bed thicknesses exist, making this method most applicable to layer-cake sections (Coward, 1992).

For a cross section to be considered balanced and restorable, assumptions must be made and sections must adhere to a specific set of criteria. 2-D balancing techniques assume plane strain, meaning that no material has moved in nor out of the plane of the cross section. Therefore, balanced cross sections must be drawn parallel to the transport direction because oblique sections will not maintain constant area throughout deformation. However, methods have been developed for the measurement of strain in oblique sections through defined correction curves based on the degree of obliqueness to the deformational transport direction (Fernández *et al.*, 2003). This is particularly applicable to studies wherein limited outcrop data prevent cross section construction parallel to transport direction (Cooper, 1983).

To gain a sense of deformation in three-dimensions, multiple sections can be built. These sections must be compatible, lacking unexplained discrepancies between fault displacements and stratigraphic thicknesses along strike. In thrust systems in particular, all hanging wall cutoffs must match footwall cutoffs, and all faults must be geologically reasonable (Cooper and Trayner, 1986; Zoetemeijer and Sassi, 1992). Faults and folds are restored sequentially in the reverse order by which they formed, so that the last fault to form is the first to be restored (Fig. 2.14).

Balanced cross section construction problems often arise from natural geologic complexities that include: 1) variable stratigraphic thicknesses, 2) sedimentary compaction, and 3) three-dimensional variation between sections. In contractional growth settings, major stratigraphic thickness variations can occur relative to the proximity of growth structures because stratal geometries are highly dependent on fold growth rate and sedimentation rate (Suppe *et al.*, 1992; Poblet *et al.*, 1997). Determining these thickness variations is a major objective of the present study; however, thickness variation rules out the use any area-balancing techniques due to the required assumption of layer-cake stratigraphy.

Problems in cross section balancing arise when sedimentary compaction is not taken into account. Sediment compaction is attributed to unconsolidated deposits undergoing significant volume loss as younger, overlying deposits are successively deposited. When performing a restoration, these deposits must be back-stripped (inverted differential compaction) to restore original thicknesses and dips. Finally, when considering the viability of cross sections, variation in fault geometries, displacement, and stratigraphic thickness variation must be considered.

2.5 3-D Structural Modeling

3-D structural models serve as powerful interpretative tools in understanding both the structural evolution and the syn-tectonic stratigraphic architecture of a basin (Fig. 2.15). Visualization of these dynamic systems in three-dimensions facilitates the identification of stratigraphic thickness variations and their temporal and spatial relationship to local growth structures.

Variation exists in methodology for the construction of 3-D structural models. Some studies utilize the construction of 2-D cross sections and interpolate structural horizons between these sections (Fig. 2.15a) (e.g. De Donatis, 2001; Paton *et al.*, 2007, Guillaume *et al.*, 2008). This method is particularly applicable in the interpretation of 3-D seismic volumes wherein the creation of closely spaced sections is possible (e.g., Rowan, 1997; Hennings *et al.*, 2000). Other studies avoid the integration of 2-D sections in order to negate error associated with the projection of 3-D data onto a two-dimensional plane (de Kemp 1998, 2000; Maerten *et al.*, 2001; Fernández *et al.*, 2004). A hybrid of these two methods is used in Husson and Mugnier (2003), wherein two balanced cross sections used to constrain structural geometry and kinematics are coupled with reference horizons generated from the projection of surface data in three-dimensions. This method avoids the error associated with interpolation between 2-D sections through the three-dimensional construction of folded strata.

Fernández *et al.* (2004) describe a 3-D dip domain method to model the turbidite systems in the Ainsa Basin. Domains of uniform dip were identified from surface data (2.16a) and surfaces for each dip domain were constructed that matched assigned dip and contact orientation (Fig. 2.16b). These surfaces were merged together and smoothed to create the basal surfaces of the turbidite systems (Fig. 2.16c).

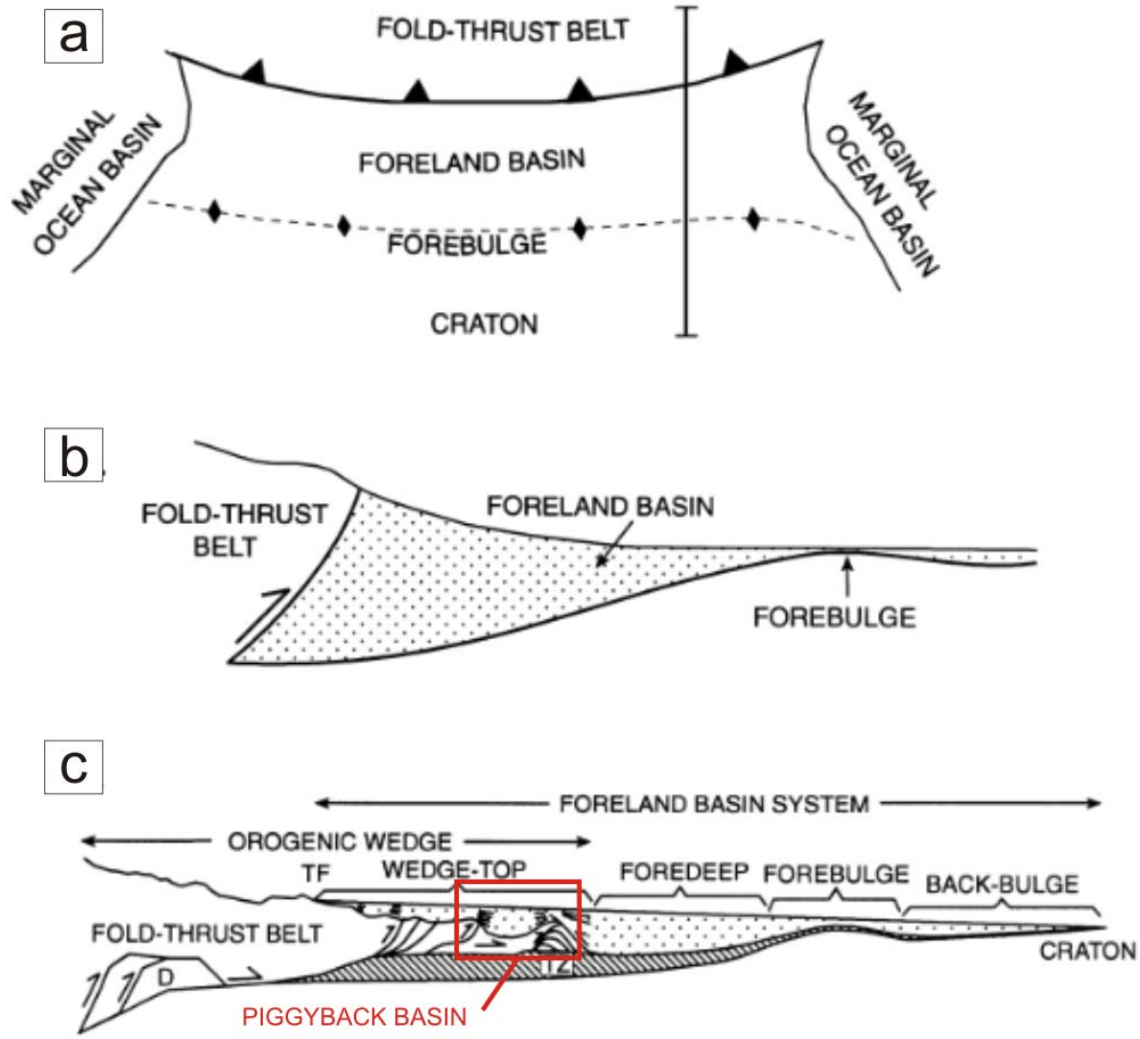

Figure 2.1: Schematic model of a typical foreland basin. a) Foreland basin in map view bounded by marginal ocean basins. Vertical line denotes position of cross-section shown below. b) Standard foreland basin geometry in cross-section with vertical exaggeration more than 10x. c) Detailed cross-section diagram of foreland basin components (modified from Decelles and Giles, 1996).

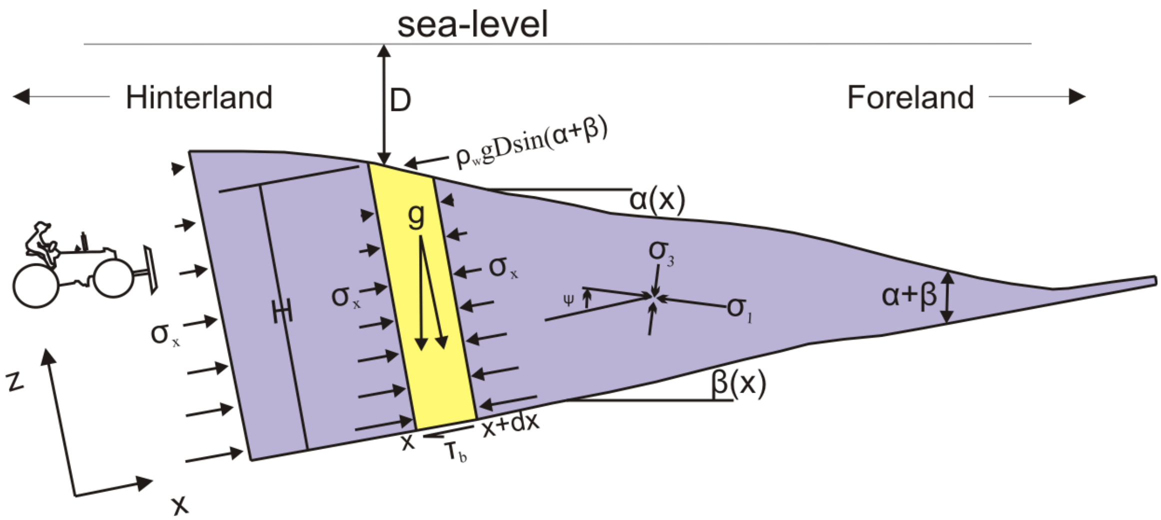

Figure 2.2: Diagram showing the relationship between variables involved in determining the critical taper of a wedge and the force balance on an arbitrary column with a width dx (modified from Davis *et al*., 1983).

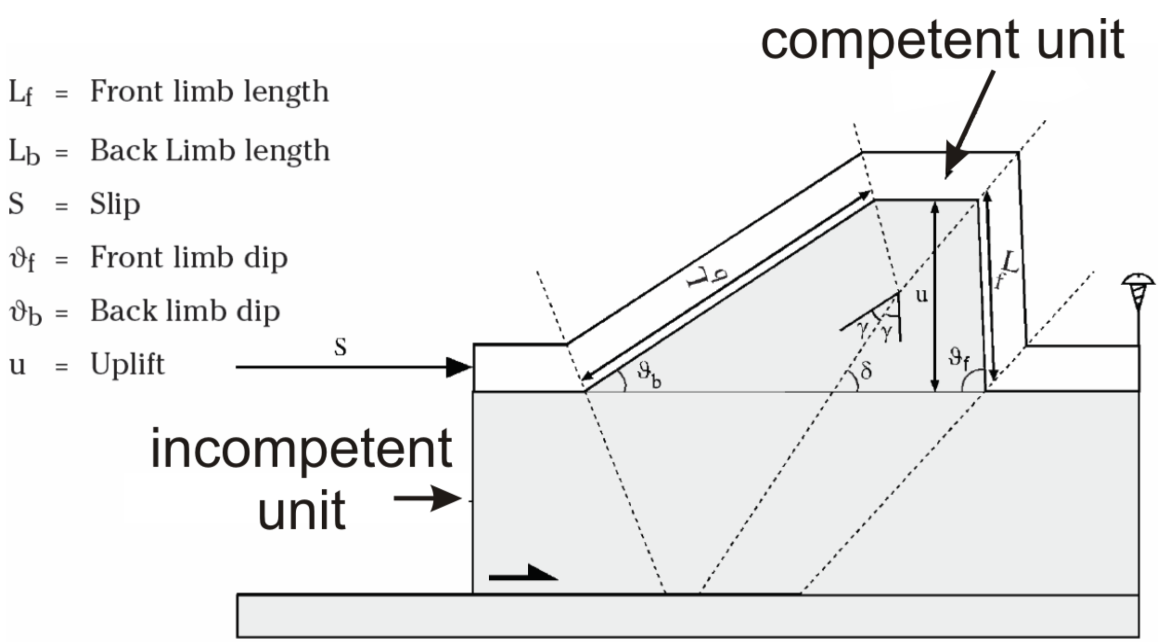

Figure 2.3: Geometric model of a detachment fold after Poblet and McClay (1996) (modified from Shaw *et al.*, 2005).

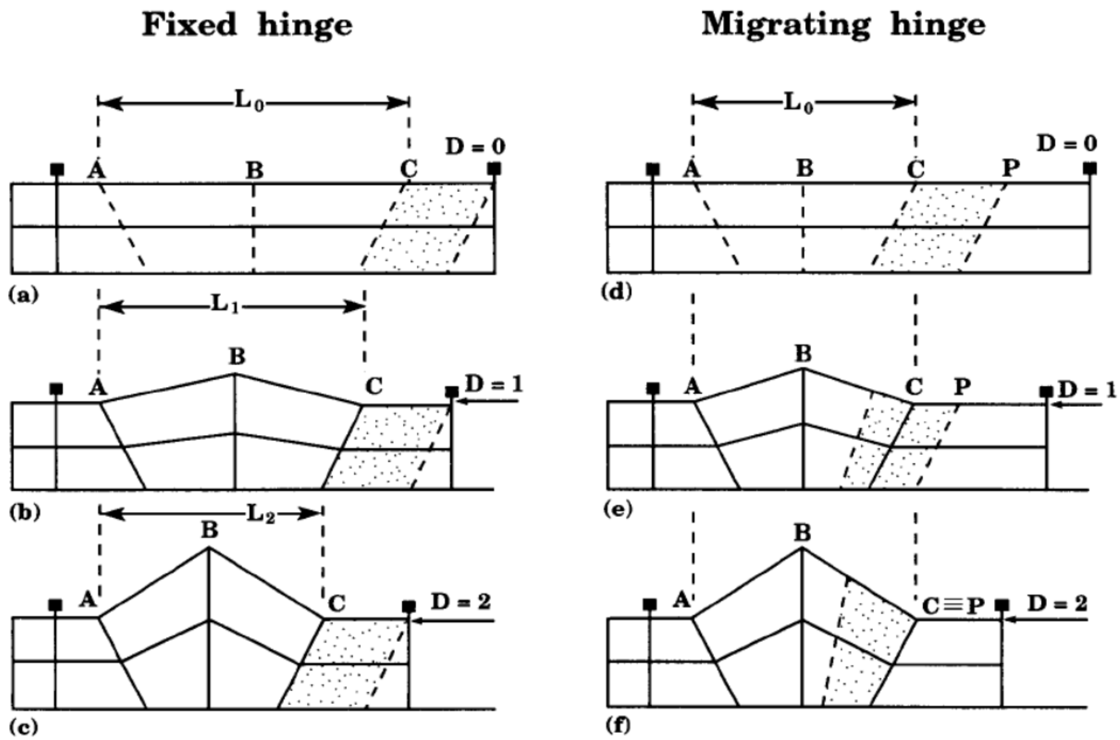

Figure 2.4: Detachment fold kinematic models. Diagram shows two possible kinematic evolutions: 1) folding with a fixed hinge (a, b, and c) and 2) folding with a partially migrating-hinge. The stippled region represents an area that is fixed with respect to the layers (from Ephard and Groshong, 1995).

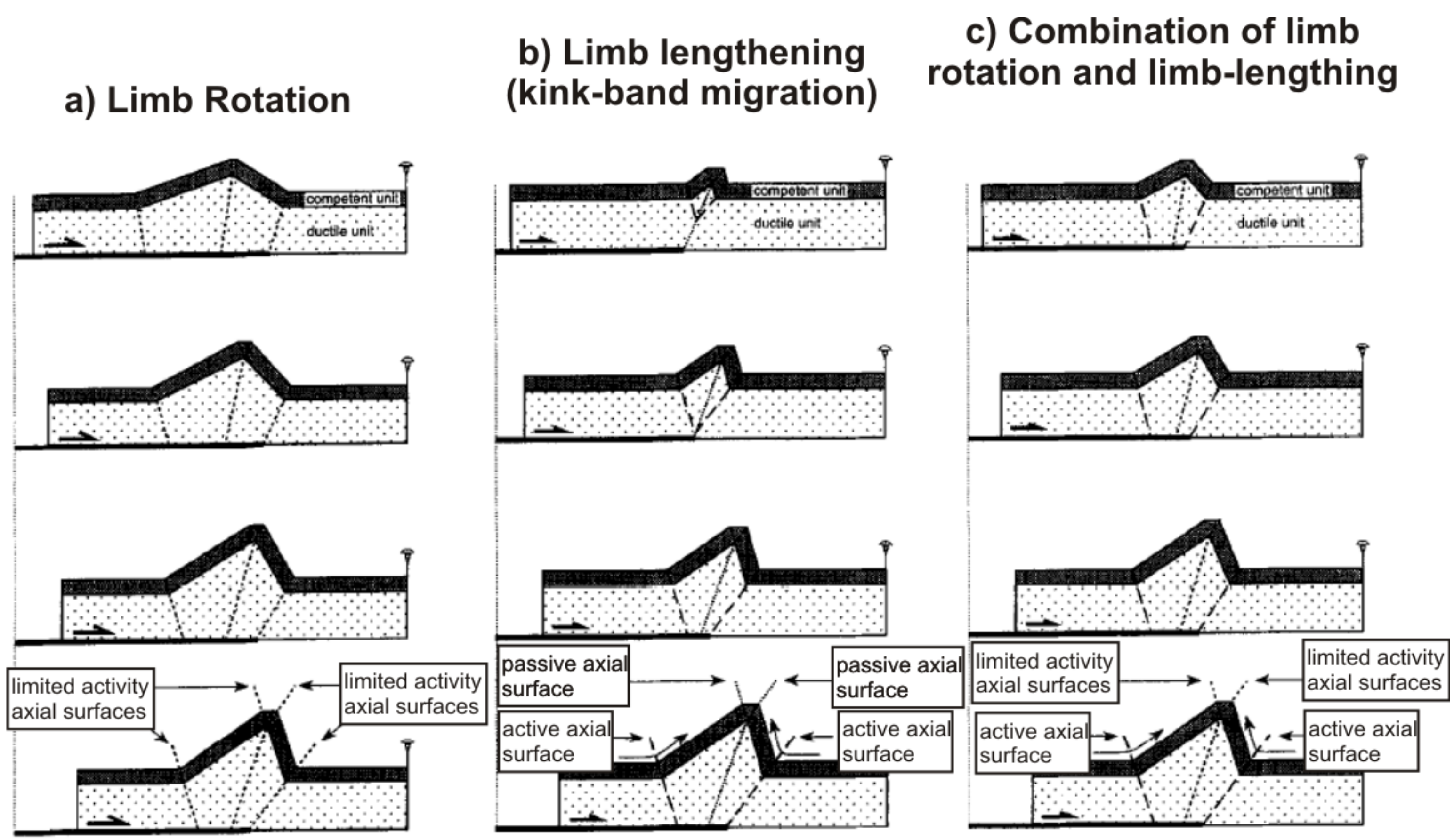

Figure 2.5: Detachment fold kinematic models proposed by Poblet *et al*. (1997). a) Fold growth through limb-rotation. b) Fold growth through limb-lengthening (kink-band migration). c) Fold growth through a combination of limb rotation and limb lengthening (modified from Poblet *et al*., 1997).

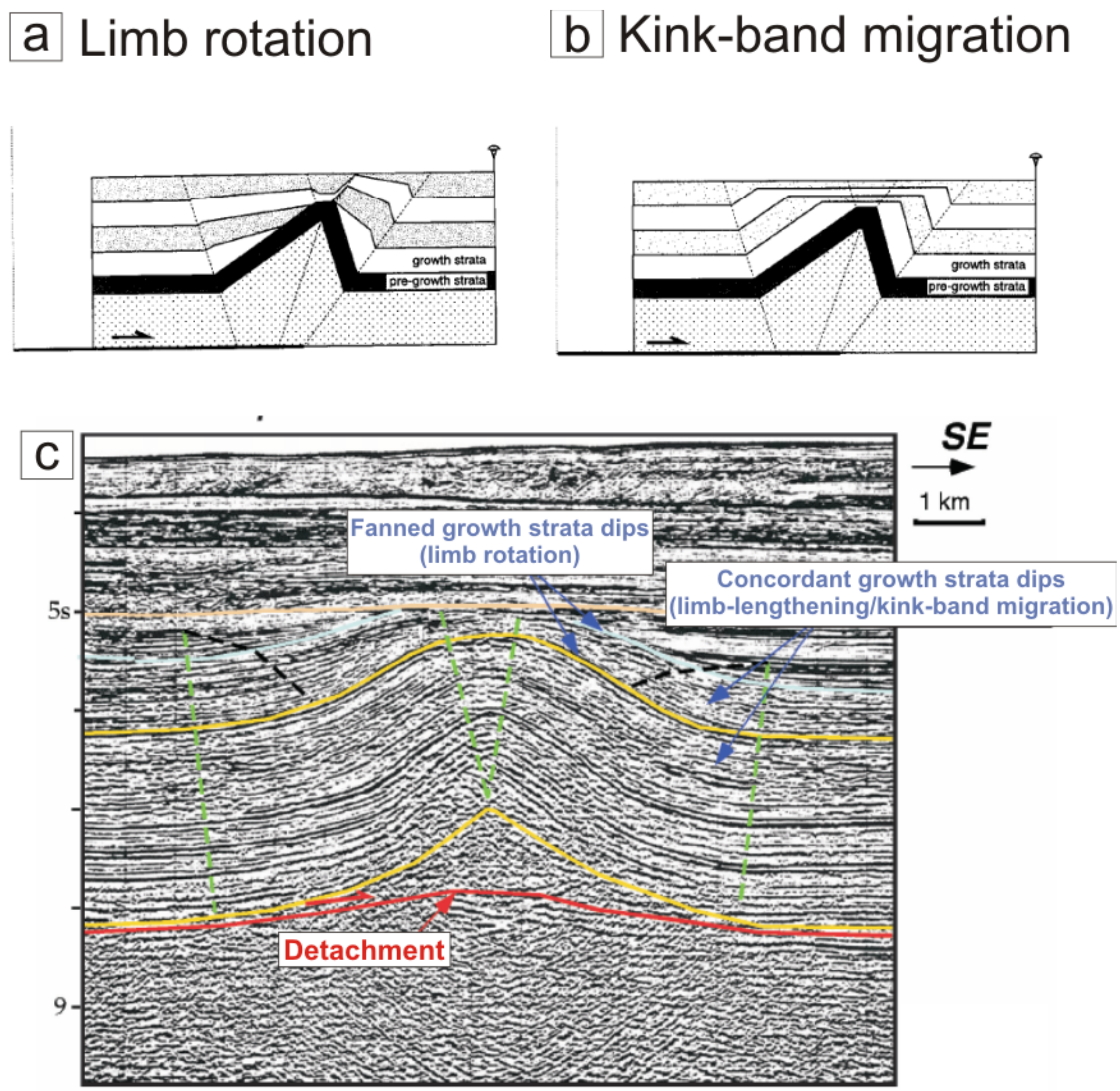

Figure 2.6: Growth strata patterns for detachment folds that grow through limb rotation (a) and kink-band migration (b). Seismic profile of a detachment fold in the Mississippi Fan Fold Belt from Rowan (1997). Note that older growth strata show concordant dips, but younger growth strata show fanned dips, indicating that this fold grew through an early phases of limb-lengthening (modified from Poblet *et al.*, 1997 (a,b) and Shaw *et al.*, 2005 (c)).

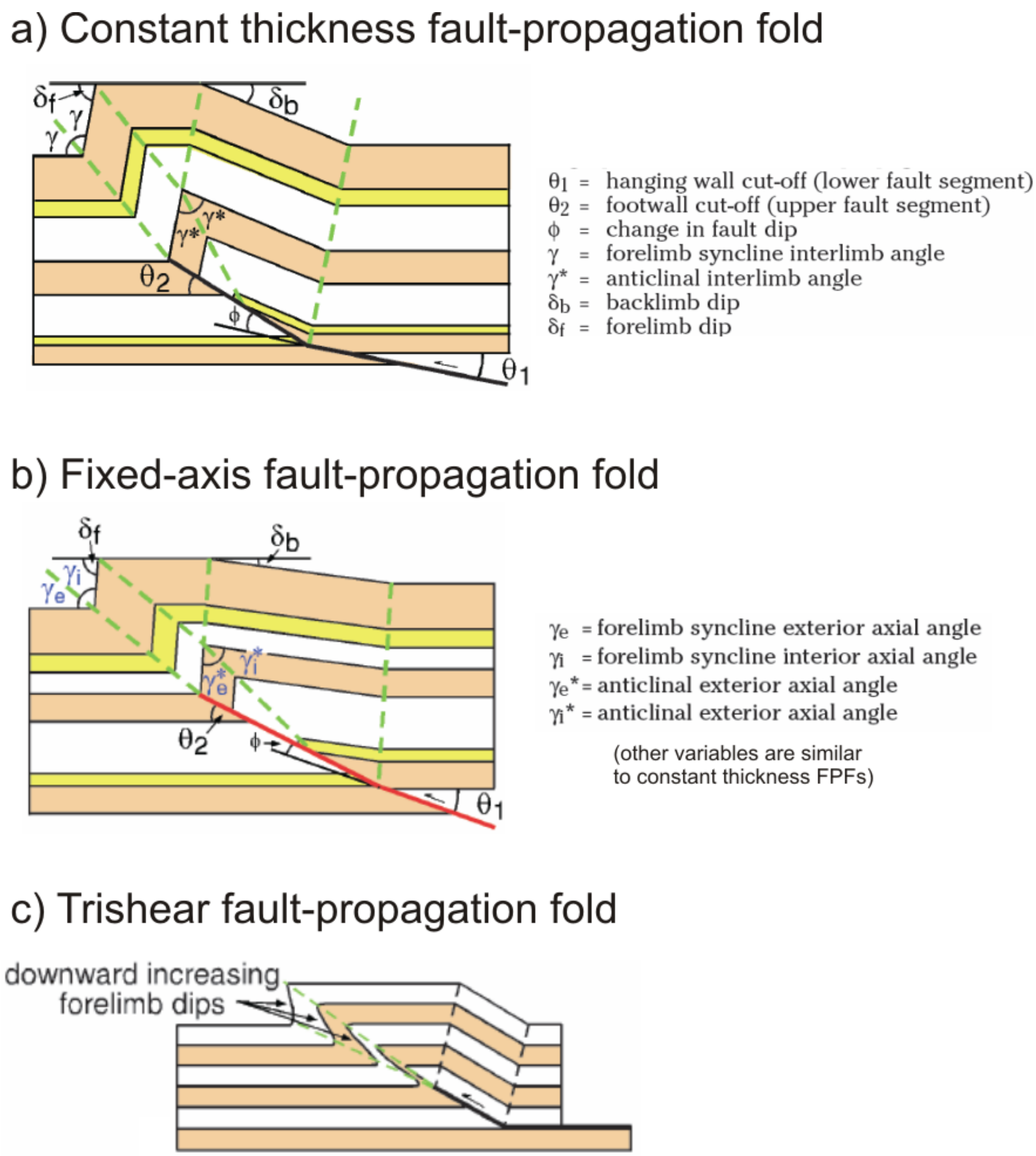

Figure 2.7: Geometric models of fault-propagation folds (modified from Shaw *et al.*, 2005).

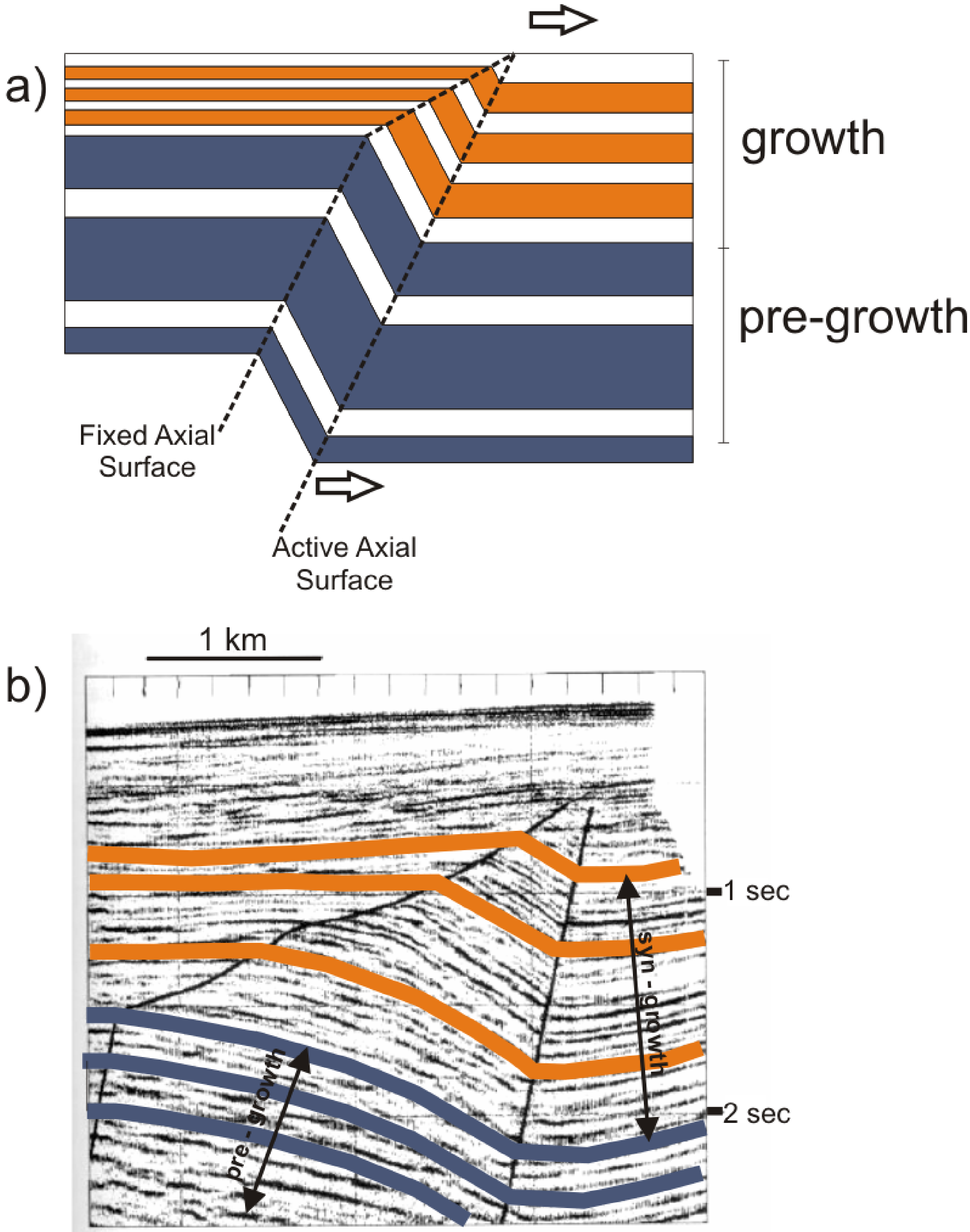

Figure 2.8: Growth strata overlying pre-growth stratigraphy causes an upward decrease in fold limb length. a) Geometric model of a fold limb and growth strata pinned between an active axial surface and fixed axial surface. b) Seismic example of a growth triangle (modified from Suppe *et al.*, 1992).

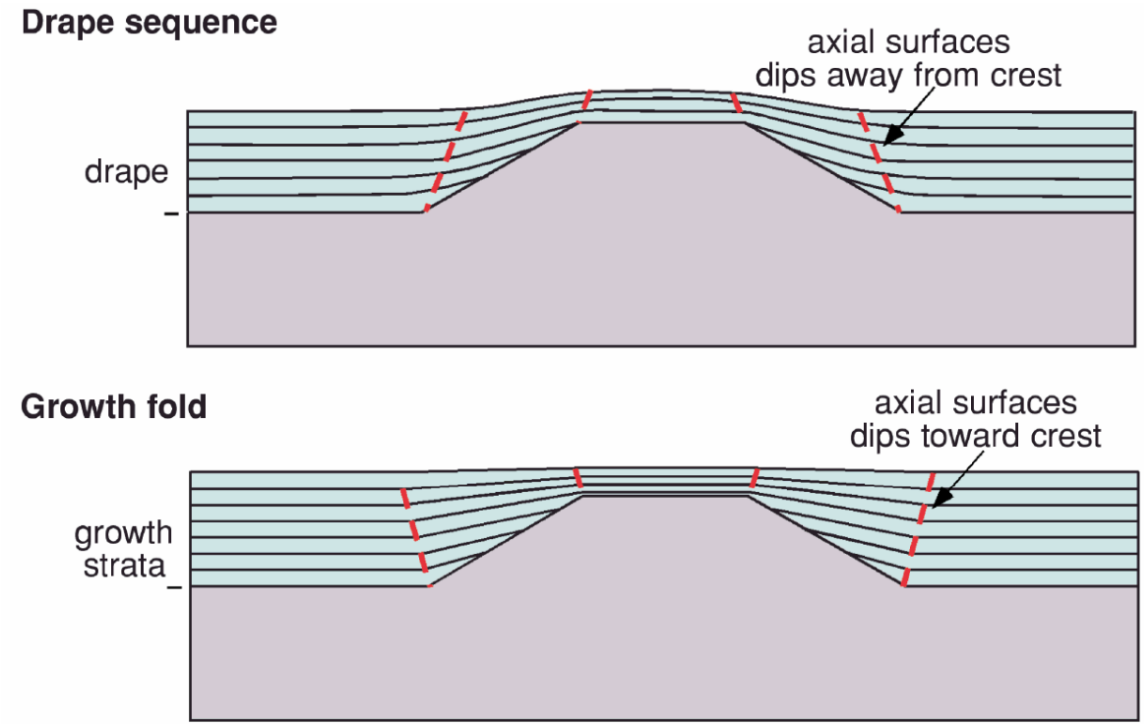

Figure 2.9: Diagrams demonstrating how a drape sequence can be differentiated from a growth sequence based on the orientation of axial surfaces relative to a fold crest (from Shaw *et al*., 2005).

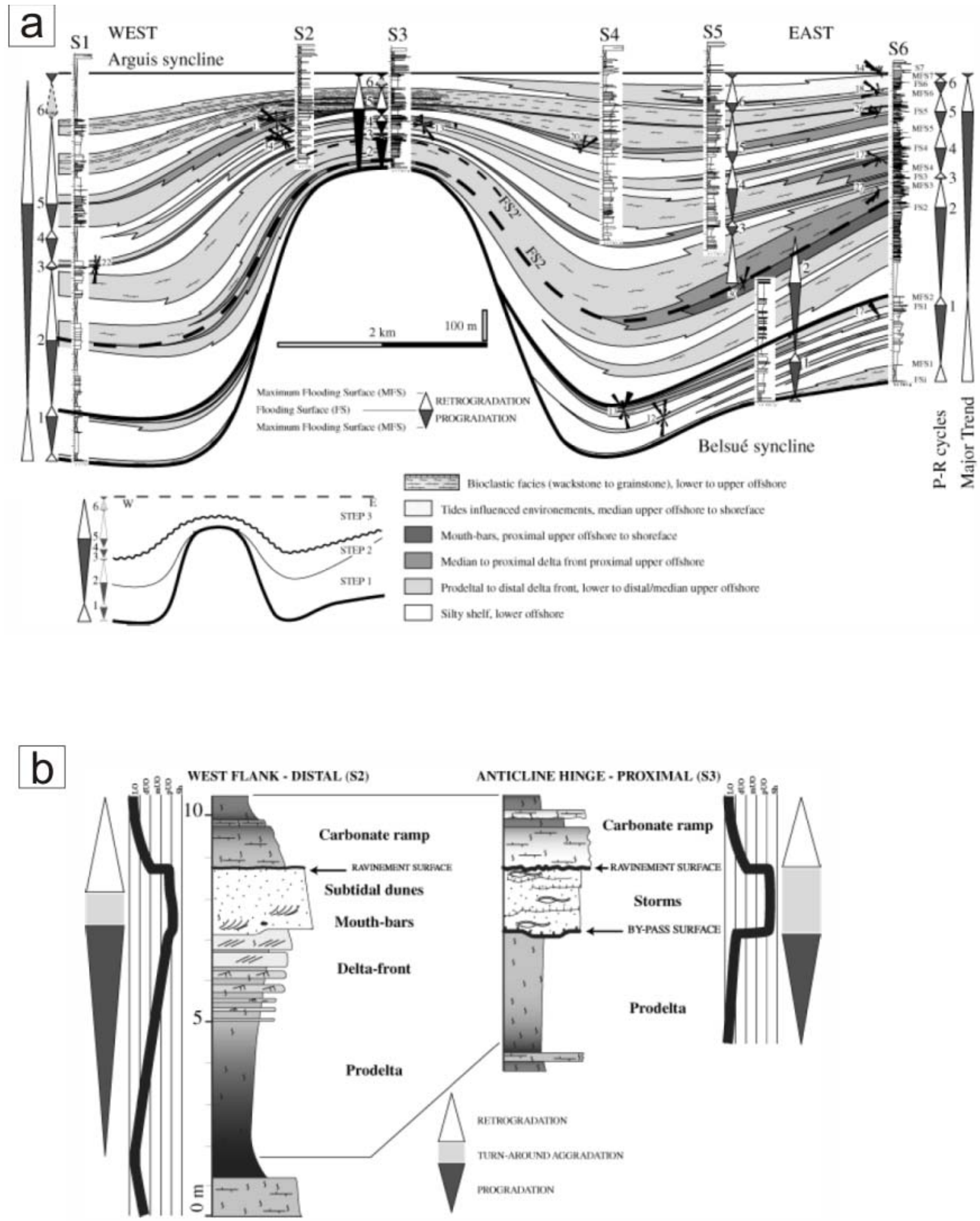

Figure 2.10: Tectono-sedimentary analysis of the Pico de Aguila Anticline. a) Cross section through the Pico de Aguila Anticline showing facies distributions and three main steps of fold growth. b) Intra-sequence comparison between deposits on the anticlinal hinge and western limb of the anticline. Paleoenvironment abbreviations include: LO, lower offshore; dUO, distal upper offshore; mUO, median upper offshore; pUO, proximal upper offshore; Sh, shoreface (from Castelltort *et al.*, 2005).

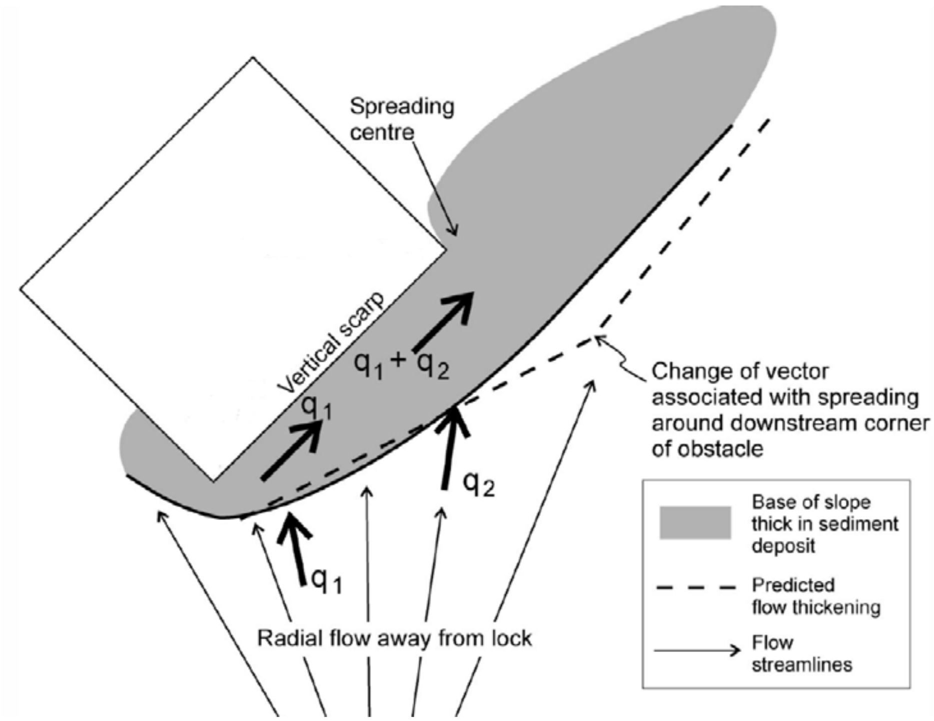

Figure 2.11: Experimental results from a flume experiment that documents the effect of topography on turbidity currents. Note that flow streamlines encounter the obstacle at an oblique angle to obstacle's strike. In addition to flow thickening, flow streamlines are diverted parallel to the obstacles strike (from Morris and Alexander, 2003).

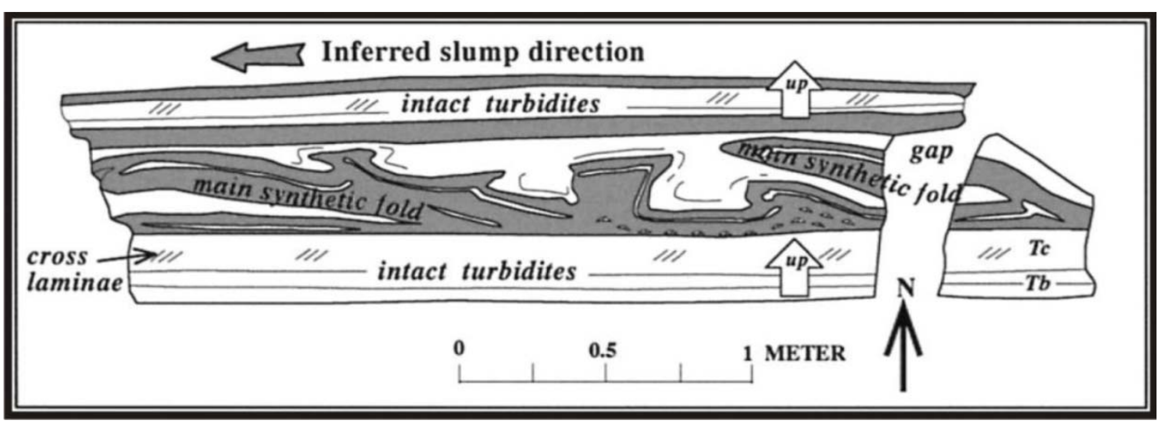

Figure 2.12: Diagram of a slump (MTC). Analysis of the intra-slump fold axes gives an indication of slump transport direction and paleoslope orientation (from Bradley and Hanson, 1998).

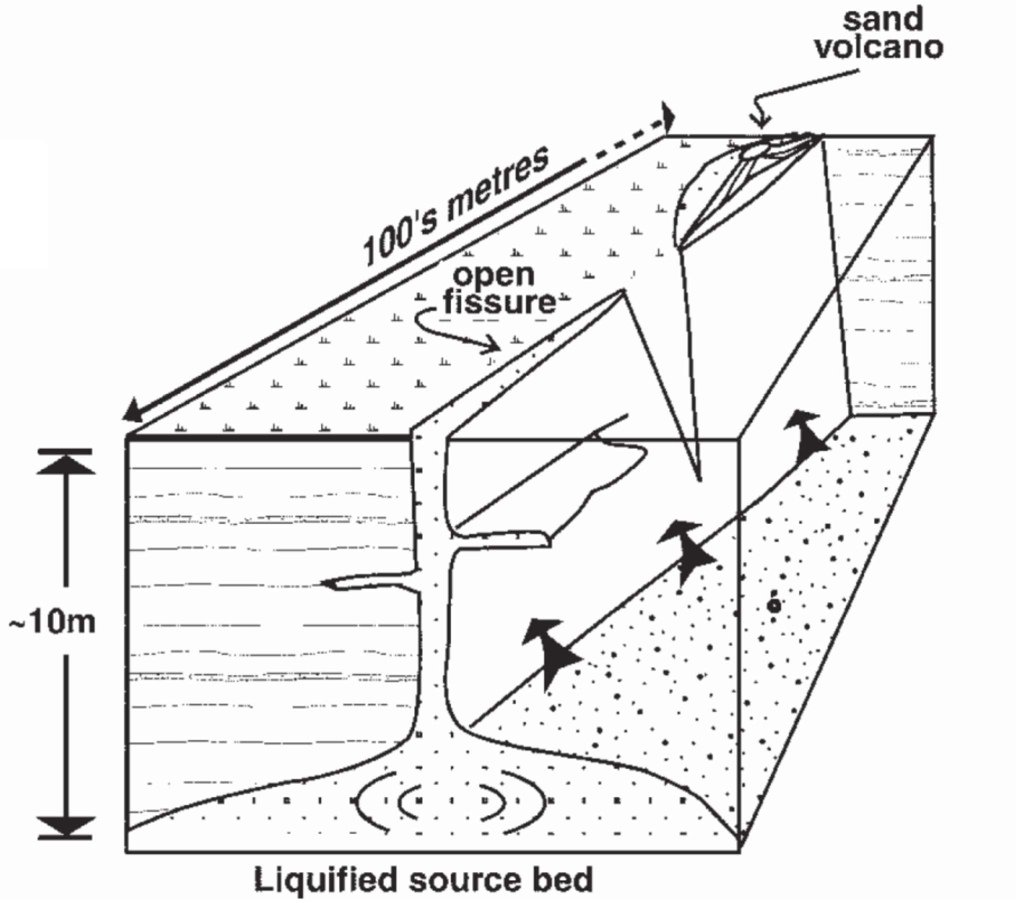

Figure 2.13: Three-dimensional diagram of primary features associated with a clastic intrusion. Fissures, particularly ones triggered by tectonic activity, can extend hundreds of meters in length. Sand volcanoes have small height to diameter ratios and are typically less than 40 m in diameter (from Jolly and Lonergan, 2002).

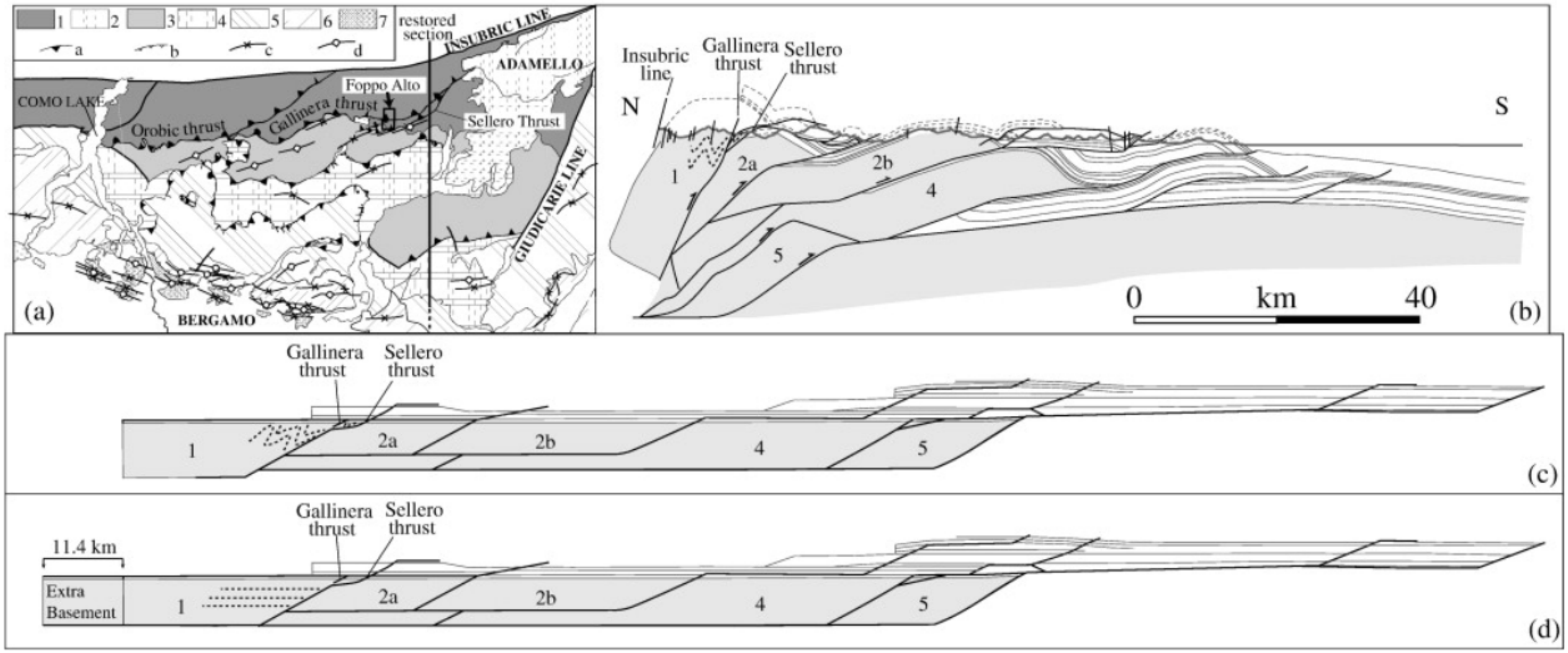

Figure 2.14: Example of a balanced cross section restoration from the Orobic Alps. a) Map showing the position of the restored section. 1: crystalline basement, 2: Tertiary magmatic body, 3: Permian clastics, 4: Lower Triassic carbonates, 5: Upper Triassic rocks, 6: Jurassic to Cretaceous pelagic deposits, 7: Cretaceous turbidite system, a: major thrust faults, b: minor thrust faults, c: synclines, d: anticlines. b-d) Steps of section restoration (from Carminati, 2008).

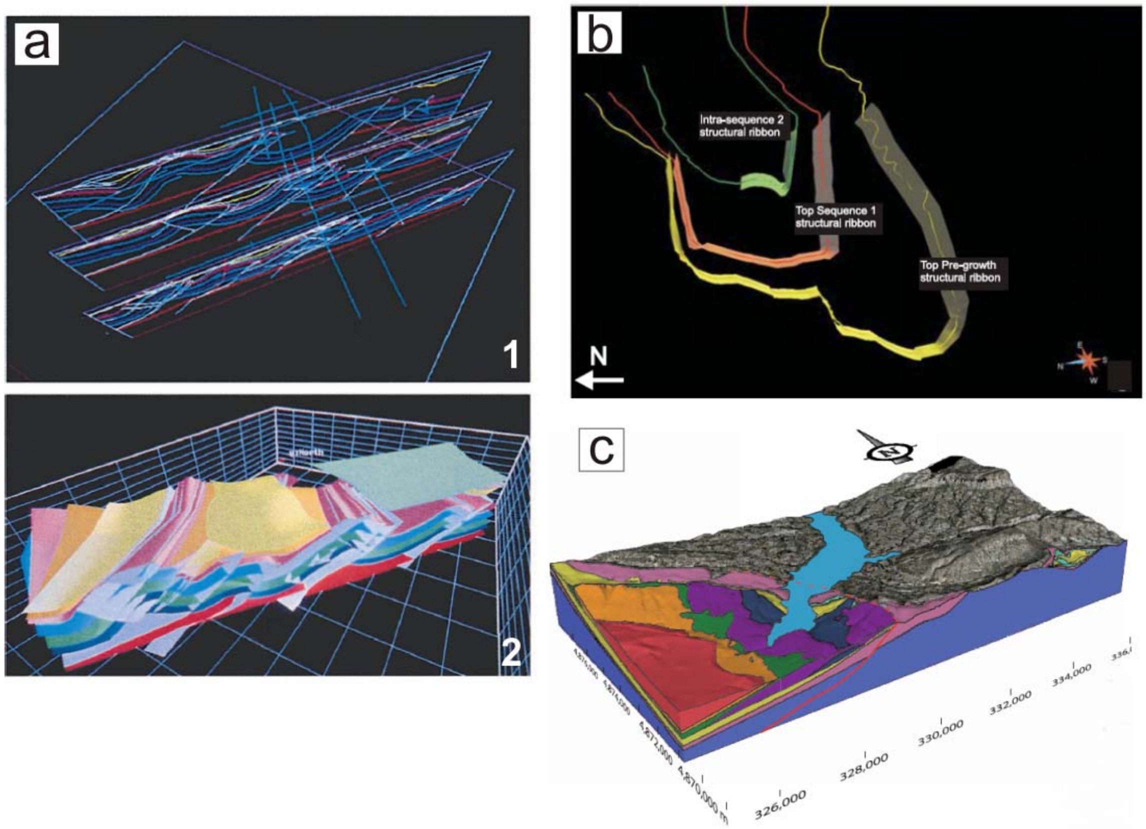

Figure 2.15: Examples of 3-D structural models. a) The use of balanced cross sections (1) and seismic data in 3-D horizon construction (2) (from De Donatis, 2001). b) The building of structural ribbons for later extrapolation into 3-D horizons (from Paton *et al.*, 2007). c) 3-D geologic visualization of strata from the Tremp Basin (from Guillaume *et al.*, 2008).

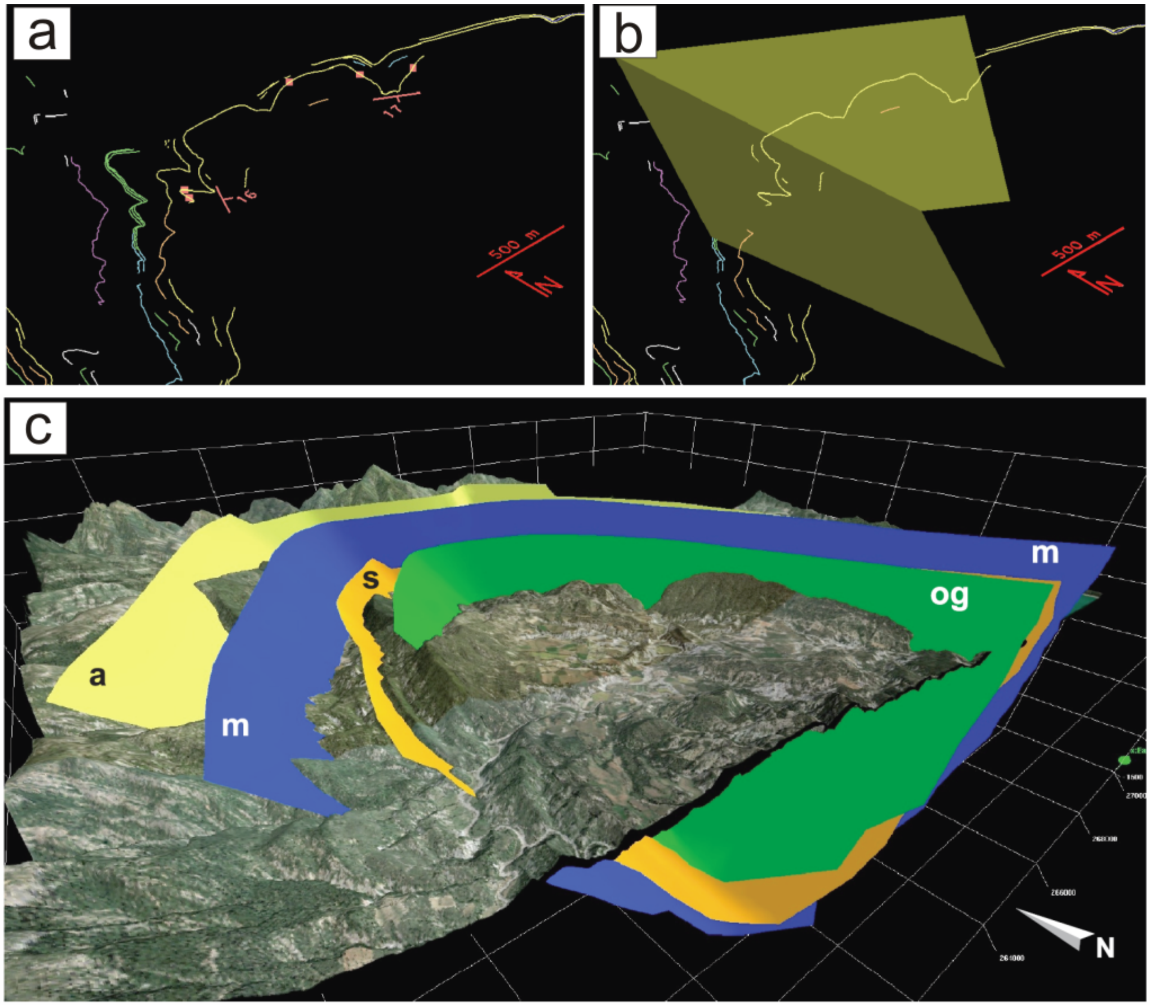

Figure 2.16: Example of a 3-D dip domain surface construction methodology. a) Two domains are interpreted from surface measurements. b) Merged dip domain surfaces in three-dimensions c) Reconstructed basal horizons from smoothed dip domains of the O Grao (og), Sieste (s), Morillo (m), and Ainsa turbidite systems (modified from Fernández *et al.*, 2004).

CHAPTER 3

METHODOLOGY

3.1 Overall Approach

The methodology developed for this study focused on meeting the primary research objectives: 1) to constrain the three-dimensional geometries of the syn-growth deepwater intervals, and 2) to define the timing and style of deformation on the bounding growth structures. This chapter describes the steps taken to meet these objectives, which include 1) field methods and data, 2) 3-D model construction, and 3) cross section construction.

3.2 Field Methods and Data

The following sections describe the methods used and data collected during field work in the Ainsa Basin.

3.2.1 Mapping Methodology

Prior work on the Ainsa Basin deepwater fill largely focused on the turbidite sandstones (Clark and Pickering, 1996; Pickering and Corregidor, 2000; Fernández *et al*., 2004; Labourdette *et al*., 2008). In these publications, system boundaries are defined as the unconformities at the base of major sandy channel complexes (Fig. 3.1). This study proposes mapping the Ainsa Basin deepwater systems on the basis of condensed section bounding surfaces. This approach has been applied in studies on other deepwater outcrops, such as the Lewis Shale (Pyles and Slatt, 2007) and the Ross Sandstone (Pyles, 2008).

Condensed sections in the Ainsa Basin are represented by extensive mudstone sheets that are dark gray in color, slightly shiny in luster, and range in thickness from 2 to 4 meters (Fig. 3.2). They are interpreted to record periods of low sediment supply into the basin possibly associated with maximum flooding surfaces. For this study, the most shale-rich and often darkest portion of the condensed sections is used to define correlatable horizons.

The use of condensed sections as correlation horizons rather than diachronous unconformities permits the correlation of syn-growth systems on a chronostratigraphic basis from the basin margins to axis. Additionally, the condensed sections are typically topographically recessive in nature and form valleys between sand-supported ridges (Fig. 3.3).

Two main advantages come from mapping condensed sections:

1) Condensed sections drape paleo-bathymetry and provide a general shape of the basin or "container" at a given time.

2) Condensed section mapping establishes a chronostratigraphic datum for the detailed intra-system correlation of architectural elements.

The four youngest systems of Ainsa Basin fill (Ainsa, Morillo, Guaso, and Sobrarbe systems) are mapped based on condensed sections (Fig. 1.9). Older systems, which have poorer outcrop exposure, exhibit significantly more deformation that makes correlation of condensed sections problematic. Additionally, the study of the four youngest systems benefits from the numerous studies of their stratigraphic architectures

(Pickering and Corregidor, 2000; Arbués *et al.*, 2007; Labourdette *et al*., 2008; Moody, 2009; Setiawan, 2009; Silalahi, 2009).

3.2.2 Data

The following section describes the data collected and analyzed in this study. They include: 1) structural orientation measurements, 2) three-point problem measurements, 3) measured sections, 4) aerial photos, and 5) photographs.

3.2.2.1 Structural Orientation Measurements

More than 600 structural orientation measurements were collected in the field. The majority of measurements were obtained on bedding planes; however, measurements were also collected on fault planes and minor fold axes. All of the measurements were marked on a map and recorded with a handheld Magellan GPS. Measurements were recorded in Right-Hand-Rule (RHR) format.

These measurements served to 1) constrain the along-strike variation of the basin bounding anticlines, and 2) constrain the three-dimensional geometries of the four upper syn-growth deepwater systems (Ainsa, Morillo, Guaso, and Sobrarbe).

These measurements were used to 1) model fold axes in both the pre-growth and syn-growth stratigraphy, 2) construct syn-growth condensed section surfaces in a 3-D model, and 3) construct a basin-scale structural cross section perpendicular to major basin structures.

3.2.2.2 Three-Point Problem Measurements

Additional data were obtained through solving three-point problems from bedding traces on a photo-draped digital elevation model (DEM) imported into GoCAD modeling software. A total of 70 three-point problems were calculated and were critical in filling in gaps where field measurements were not obtained, particularly in areas of inaccessible terrain. Additionally, three-point problem measurements have the advantage of providing a more regional sample of bedding attitude, avoiding errors associated with obtaining a field measurement on local bedding undulations or irregularities.

3.2.2.3 Measured Section

Field mapping was supported by more than 3200 m of measured sections obtained by Setiawan (2009). These measured sections were collected within the Morillo depositional system.

3.2.2.4 Seismic Profiles

Two seismic profiles (SP-2 & SP-3) were acquired from the Instituto Geológico y Minero de España (IGME). The SP-2 line is 23 km in length and trends roughly N-S through the central-western portion of the Ainsa Basin. The SP-3 line is 29 km in length and trends roughly WNW-ESE through the northern portion of the basin (Fig. 1.3).

The SP-2 and SP-3 seismic data were recorded in 1979 by Prakla-Seismos with a two millisecond sampling rate and a five second record length. The profile was shot in 48 groups spaced at 110 m with 36 receivers per group. The highcut frequency was 125 Hz and the lowcut frequency was 12.5 Hz.

3.2.2.5 Aerial-Photo and Digital Elevation Model (DEM)

Broad structural mapping was aided by a georeferenced aerial photomosaic acquired from Spain's Ministerio de Medio Ambiente, y Medio Rural y Marino, draped over a 90 m resolution regional digital elevation model (DEM).

3.2.2.6 Photographs

More than 1000 photographs were taken throughout the field mapping process and interpreted in order to document key stratigraphic relationships, architectural elements, and structural geometries.

3.3 3-D Model Construction Methodology

In order to constrain the three-dimensional geometries of the upper four systems of the Ainsa Basin fill, a 3-D structural model of the upper four deepwater systems was constructed. Methodology was developed to accurately construct the base of each deepwater system. This method was developed to answer two key questions:

1) How to construct stratigraphic surfaces in a growth basin where thickness changes are prevalent?

2) How to constrain the 3-D variation of basin axes through time using a limited dataset?

Data used in the construction of the 3-D model consisted of: 1) a digital elevation model (DEM) (Fig. 3.4), 2) mapped geologic contacts, 3) structural orientation measurements, and 4) two depth-converted seismic profiles that run roughly north-south and east-west. All modeling was conducted using GoCAD modeling software with Chevron proprietary plug-ins.

The following section describes the data and steps taken in model construction in this study, including: 1) data import, 2) three-point problem measurement acquisition, 3) seismic depth conversion, 4) dip vector conversion, 5) dip vector projection, 6) system axis construction, and 7) surface interpolation.

3.3.1 Data Import

The following sections describe the data imported into the 3-D model to be used in surface construction.

3.3.1.1 Aerial-Photo and Digital Elevation Model (DEM)

A regional DEM was imported into GoCAD as a surface. The aerial photomosaic was imported as a voxet, georeferenced, and draped over the DEM surface (Fig. 3.4).

3.3.1.2 Geologic Contacts

All contacts were digitized in OziExplorer mapping software. Topographic maps of Ainsa Basin were imported and georeferenced. Geologic contacts were traced directly from hand-drawn maps created in the field onto the imported topographic maps in OziExplorer. The coordinates of each contact were then converted to text files for import into GoCAD. Once imported, the contacts were projected onto the surface defined by the DEM (Fig. 3.4b).

3.3.1.3 Structural Orientation Measurements

The UTM coordinates of each structural orientation measurement recorded by GPS was imported into GoCAD as a point. All points were projected onto the topographic surface defined by the DEM. Elevation coordinates recorded by GPS were discarded because of the lack of accuracy in handheld GPS elevation readings and so that all data imported into the model could be referenced to the resolution of the DEM.

3.3.2 Three-Point Problem Measurement Acquisition

Curves were created on each discernible bedding trace (Figures 3.5a and 3.5b). On each bedding trace curve, three points were created that covered the entirety of the curve (Fig. 3.5c). The Cartesian coordinates of each point were then used to calculate the orientation of the plane formed by each three point group using the method described by Vacher (2000) (Fig. 3.6).

This method uses Cramer's rule, a linear algebra technique, to compute the equation of the plane defined by the three specified points. The full derivation of the equations is described in detail in Vacher (2000).

In each three-point problem calculation, the Cartesian coordinates of each point in the three-point set are first defined as a system of linear equations:

$$
\begin{aligned}
&ax + by + cz + d = 0\\
&ax_1 + by_1 + cz_1 + d = 0\\
&ax_2 + by_2 + cz_2 + d = 0\\
&ax_3 + by_3 + cz_3 + d = 0
\end{aligned}
$$

, where *a*, *b*, *c*, and *d* are unknown linear coefficients and x_n, y_n, and z_n are the Cartesian coordinates of the three-point set. The equation of the plane through a given three-point set is:

$$\begin{vmatrix} x & y & z & 1 \\ x_1 & y_1 & z_1 & 1 \\ x_2 & y_2 & z_2 & 1 \\ x_3 & y_3 & z_3 & 1 \end{vmatrix} = 0$$

and can be expanded by its cofactors in order to solve for the unknown linear coefficients:

$$a = \begin{vmatrix} y_1 & z_1 & 1 \\ y_2 & z_2 & 1 \\ y_3 & z_3 & 1 \end{vmatrix} = -\begin{vmatrix} z_1 & y_1 & 1 \\ z_2 & y_2 & 1 \\ z_3 & y_3 & 1 \end{vmatrix}$$

$$b = -\begin{vmatrix} x_1 & z_1 & 1 \\ x_2 & z_2 & 1 \\ x_3 & z_3 & 1 \end{vmatrix}$$

$$c = \begin{vmatrix} x_1 & y_1 & 1 \\ x_2 & y_2 & 1 \\ x_3 & y_3 & 1 \end{vmatrix}$$

After solving for the linear coefficients, the strike azimuth and dip angle can then be calculated with the following equations:

$$\theta_{strike} = \arctan(-b/a)$$

$$\theta_{dip} = \arctan\left(\sqrt{\left(\frac{a^2+b^2}{c^2}\right)}\right)$$

Using these equations, a spreadsheet was written to calculate structural orientation measurements from multiple three-point sets.

Potential error involved with the three-point method is largely based on the resolution of the DEM and sampling of the bedding trace. It is important that the bedding trace sampled exhibit near uniform dip. If any significant change in bedding attitude occurs along the length of a bedding trace, the resulting three-point calculation may result in exaggerated dip values (Fig. 3.7). This error was minimalized by obtaining multiple measurements on different bedding traces in close proximity to one another. In all cases where three-point problem measurements were in dispute with measurements collected in the field, the field measurements were honored and the three-point problem measurements were discarded.

3.3.3 Seismic Profile Depth Conversion

The shot point coordinates for each line were imported into GoCAD as a curve marking the location of each profile (Fig. 3.8a). These curves were then shifted to the specified datum elevation of 450 m above sea level. Vertical surfaces were created with the top of the surfaces bounded by the datum curve, on which the seismic profiles were draped (Fig. 3.8b).

Seismic profiles were depth-converted using a modification of the method described by Suss and Shaw (2003). Stacking velocities provided on the lines themselves were converted to interval velocities using Dix's Law:

$$V_{1\text{-}2}= [(v^2_{RMS2}(t_2-v^2_{RMS1})t_1)/(t_2-t_1)]^{1/2}$$

wherein $V_{1\text{-}2}$ is the interval velocity, v_{RMS} is the upper and lower RMS velocity, and t is the upper and lower time values bounding the interval. Interval velocities deeper than two seconds two-way travel time (TWTT) were discarded to avoid anomalous values from Paleozoic basement rock. The remaining interval velocities were plotted against TWTT, from which a simple linear regression function was derived (Fig. 3.9). The linear regression function:

$$y = 1.5304x - 7.5996$$

was used for the time-depth conversion. The seismic profile was clipped at two seconds TWTT and was flexed on the vertical surface to fit the depth conversion (Fig. 3.8c).

Without well control, a robust velocity model is not attainable; however, two checks were performed to ensure that the depth-conversion was reasonable. First, the dip of major seismic reflectors was compared to the dip of surface outcrops. For example, the top of platform carbonates that crop out in the Boltaña Anticline could be correlated to an easily recognizable reflector on the SP-3 profile. Their respective dips were compared by projecting the surface dips into the subsurface and comparing these dips to seismic dip (Fig. 3.10b). Second, because the SP-2 and SP-3 profiles intersect each other, they can be compared for consistency in the depth conversion. Key reflectors were traced from one profile to the other to ensure that the depth-conversion was consistent between the two lines.

3.3.4 Dip Vector Conversion

Structural orientation measurements were converted from RHR strike and dip format to dip vectors by defining the measurements' direction cosines (Fig. 3.11). This method, described by Groshong (1999), calculates a unit vector in X-Y-Z space. Converting measurements to dip vector served two main purposes: 1) all data was converted to a format compatible with GoCAD modeling software, and 2) the dip vectors themselves are a critical component to surface construction.

A spreadsheet was written that took the Cartesian coordinates (Easting, Northing, and elevation) of the measurement location and the RHR strike and dip, and calculated a second point that marked the unit vector of the measurement. This vector is anchored at the site of the measurement location and can be multiplied by a given factor and extended to various lengths.

3.3.5 Dip Vector Projection

Due to the large data density required to construct surfaces in three-dimensions, data must be used from multiple stratigraphic surfaces to construct an individual surface (Fernández *et al.*, 2004). Therefore, data must be projected onto the mapped contacts that are the basis for 3-D surface construction. Individual dip vectors were orthogonally projected to their intersection with a nearby contact (Fig. 3.12). At the orthogonal intersection point, the dip vectors were recalculated using the method described in section 3.4.4., with the intersection point taking the place of the original measurement location and serving as the dip vector anchor along the mapped contact.

A series of criteria was established to minimize error associated with data projection:

1) Data points projected to a particular surface contact must be acquired in one of the adjacent systems. As a result of the growth geometries of the basin-fill systems, measurements reflect a shallowing or steepening relative to their position to the basin axis. Therefore, projecting data across multiple units with varying growth geometries will likely not represent real bedding attitudes at the contact.

2) The measurement itself must not be collected on an irregular surface. Irregular surfaces include: erosional channel cuts, MTC bedding surfaces, slump scars, and bar forms.

3) In an area of relatively high contact rugosity, projected dip vectors must not conflict with vector projections closer to the contact (3.12b). In other words, contact rugosity increases the error in projection and therefore the closer the measurement is to the contact itself, the greater the likelihood the measurement reflects the true attitude of the surface along the contact.

Condensed sections often exist as relatively smooth, continuous surfaces and therefore vectors can be projected with high confidence and without the error involved with a rugose contact.

With the dip vectors projected to the contacts, the individual measurements were compared with one another and their relationship to the contact itself. Erroneous data was easily recognized and discarded.

3.3.6 System Axis Construction

The dip vectors anchored at the contacts serve as the initial framework for surface construction. The next step defined how the surfaces close in the subsurface. This was done by constructing the axis of each syn-growth system at depth. Axis construction was performed by first defining the location of 1) the axis in plan-view or X-Y space (easting and northing) and 2) constraining it in the third dimension ("Z" or vertical direction).

3.3.6.1 X-Y Axis Constraints

Dip vectors were extended from the contacts into the subsurface to their plan-view intersection with a vector in a similar position on the opposite fold limb (3.13a). With a robust data set, the dip vectors define a distinct zone of intersection (3.13b). A best fit curve was constructed through this zone of intersection for each of the four syn-growth surfaces (base-Ainsa, base-Morillo, base-Guaso, and base-Sobrarbe). A vertical surface was constructed through each best fit curve. This surface marks the plan-view location of each system axis, on which the vertical location can vary (3.13c).

In some cases, structural complexity can cause axis to split into two separate axes. The presence of an axis split is clearly indicated by the dip vector intersection pattern and the secondary axes are constrained in the same manner as the primary axes (3.13c).

3.3.6.2 Z-Direction Axis Constraints

The system axes were constrained in the vertical or "Z" direction by four separate methods. The following methods serve as individual controls on the vertical position of each system axis along-strike. The final axes are represented by a curve constructed on each system’s axis plane that meets all controls established by the following four methods:

1) The dip vectors themselves represent the steepest possible path to a system's axis. Due to the bowl-shaped geometry of the basin, the surface dip can only shallow from the limbs towards the axis. The dip vectors extended from the surface to their intersection with the axis plane marking a lower boundary for Z-position of each system axis.

2) The SP-2 seismic profile runs roughly parallel to the strike of the system axes. While the profile's resolution is too low for discernible surfaces within the syn-growth stratigraphy to be traced for any considerable distance, the reflections provide constraints on the overall shape of the system axes along-strike. By extending dip vectors into the subsurface, the surface contacts can be correlated to individual reflections in the subsurface. Curves are constructed throughout the length of SP-2 profile using the correlation reflector as an anchor point and, honoring seismic dip, picking the curve throughout the entire profile length. The curves generated for each system were projected from the seismic profile onto the axis planes and reconciled with the dip vector described in the first method.

3) The curve representing each axis must be anchored at the surface axial trace intersection with the contact. This intersection serves as a point where the axes must intersect the surface. Structural orientation measurements taken on or near these points of intersection measure the axis itself in proximity to the surface contact.

4) Data projected to the system contacts was partitioned into zones and system axes modeled on stereonets using the π-axis technique. Bedding orientations taken from

the fold limbs in each zone are plotted as poles on a stereonet and a common great circle is fitted to the data. The pole to this great circle represents the "π-axis," a stereographic expression of the trend and plunge of the local system axis.

The "π-axis" orientation for each zone was imported into GoCAD as a curve and used as a fourth constraint on the Z-position of the system axes.

3.3.7 Surface Interpolation

Dip vectors were extended 300 m to 1000 m into the subsurface from the surface contacts. This step was interpretive, as the extension distance for each vector largely depended on its proximity to the system axis and the rate of dip change from the limb to axis. For example, if a dip vector was in close proximity to a system axis, it likely intersects the axis over a relatively short distance. Additionally, if a dip vector extension crossed into a shallower region of dip in plan-view, the vector must be clipped.

Following the subsurface extension of the dip vectors, curves were created for each dip vector connecting it to the system axes. These connecting curves represent the shortest path from the dip vectors' subsurface extension to the system axis, and in plan-view, they appear as straight extensions of the dip vector to the system axis. These connecting curves, the dip vectors, the system axis curves, and the surface contacts all serve as guides in surface interpolation (3.14a).

Surface interpolation was conducted using GoCAD's Discreet Smooth Interpolation (D.S.I.) algorithm (Lévy and Mallet, 1999). The dip vectors, surface contacts, and system axes were set as hard controls in the interpolation, with D.S.I.

creating smooth triangulated surfaces for each condensed section that honor all established controls (Figures 3.14b and 3.14c).

3.4 Cross Section Construction

The line of section for a basin scale structural cross-section was chosen to run approximately perpendicular to the basin-bounding Mediano and Boltaña Anticlines. A dip domain construction method was used (Groshong, 1999), which simplified the section into planar segments of roughly uniform dip separated by hinges. Axial surfaces connect hinge lines in folded layers and bisect the angles between adjacent dip domains in units of constant thickness.

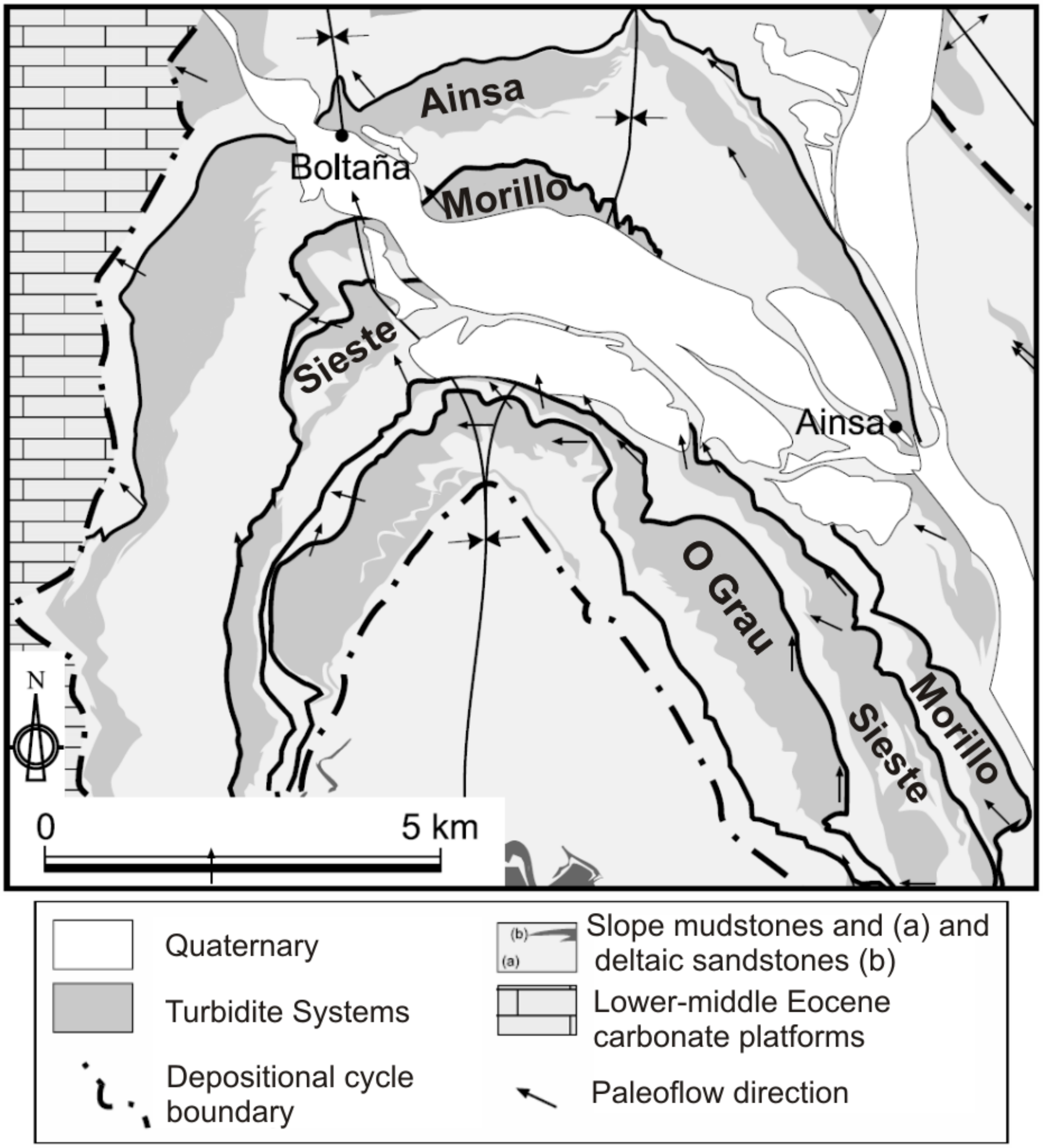

Figure 3.1: Map of the Ainsa Basin turbidite systems from Fernández *et al.* (2004). Note that the systems are defined by unconformities at the base of the turbidite channel complexes.

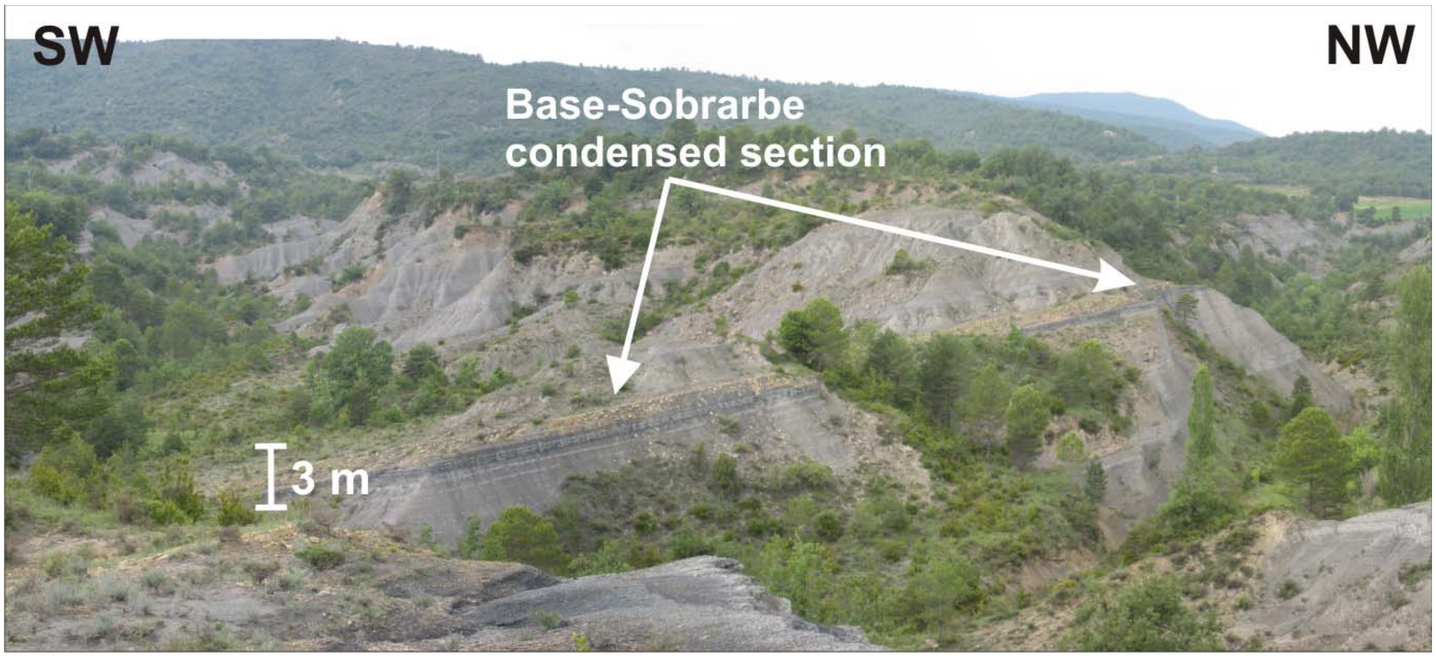

Figure 3.2: Condensed section defining the base of the Sobrarbe system and top of the Guaso system.

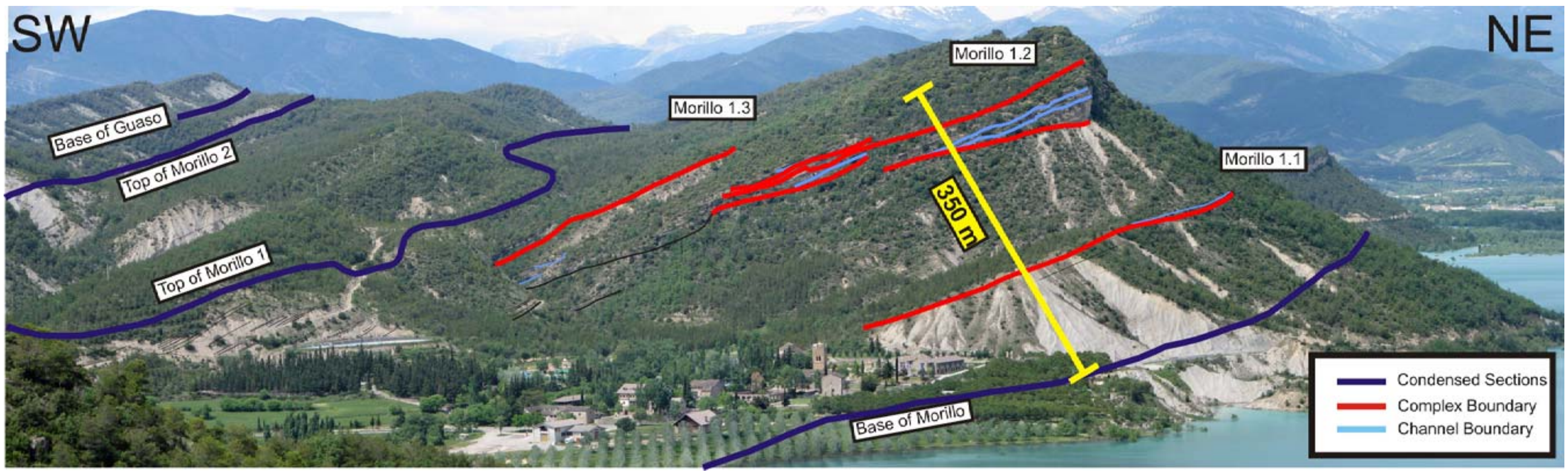

Figure 3.3: Interpreted photo-panel of the Morillo system and the clearly defined ledge stratigraphy. Sandy channel complexes form the ledges while recessive shale-rich units form valleys. The condensed sections that bound the Morillo system and define internal divisions (Morillo 1, 2, and 3) are shown in dark blue lines (modified from Moody, 2009).

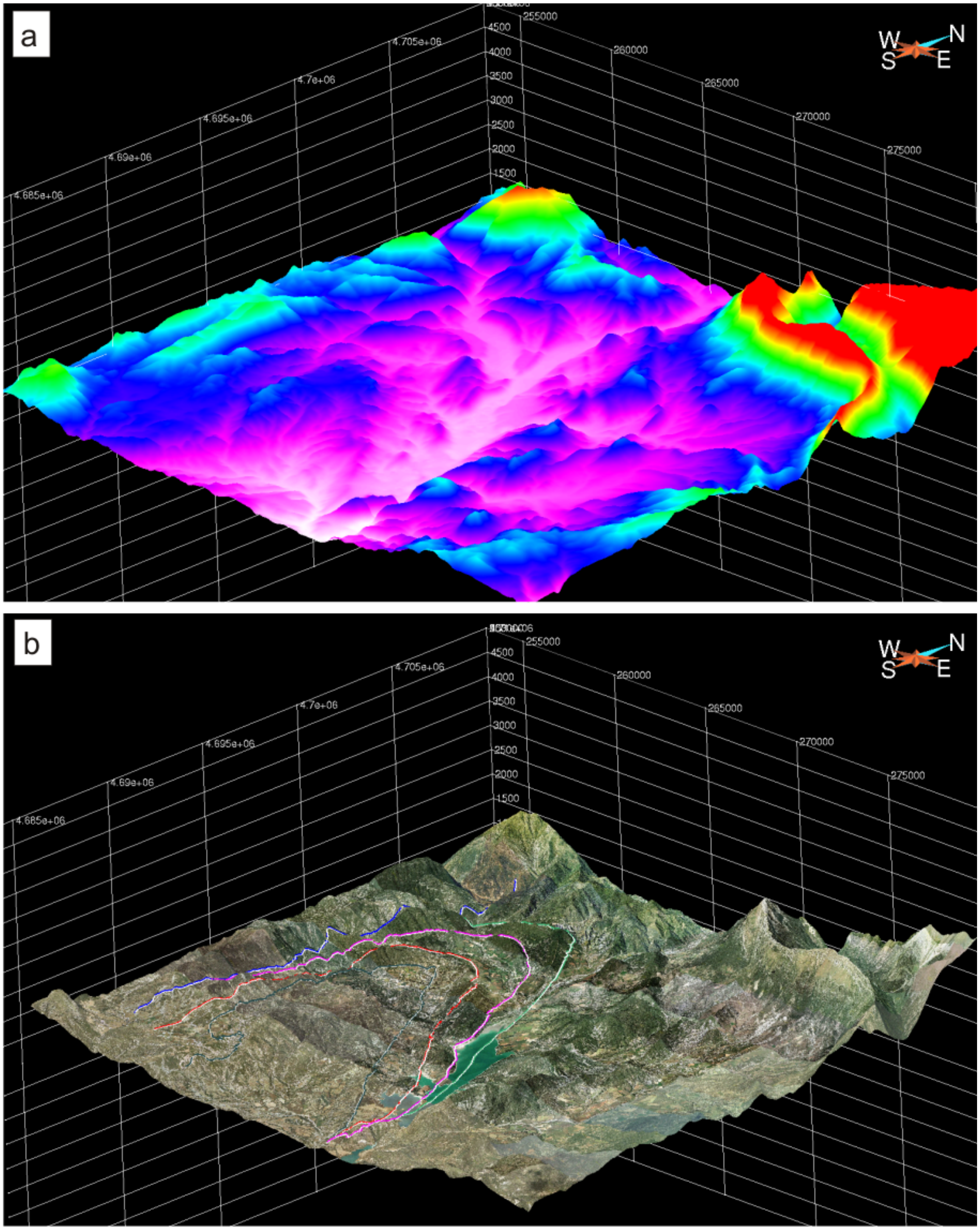

Figure 3.4: Regional digital elevation model (DEM) of the Ainsa Basin. a) DEM surface without a photo-drape. b) DEM draped with an aerial-photo mosaic. Also shown are the mapped condensed sections as curves projected onto the DEM.

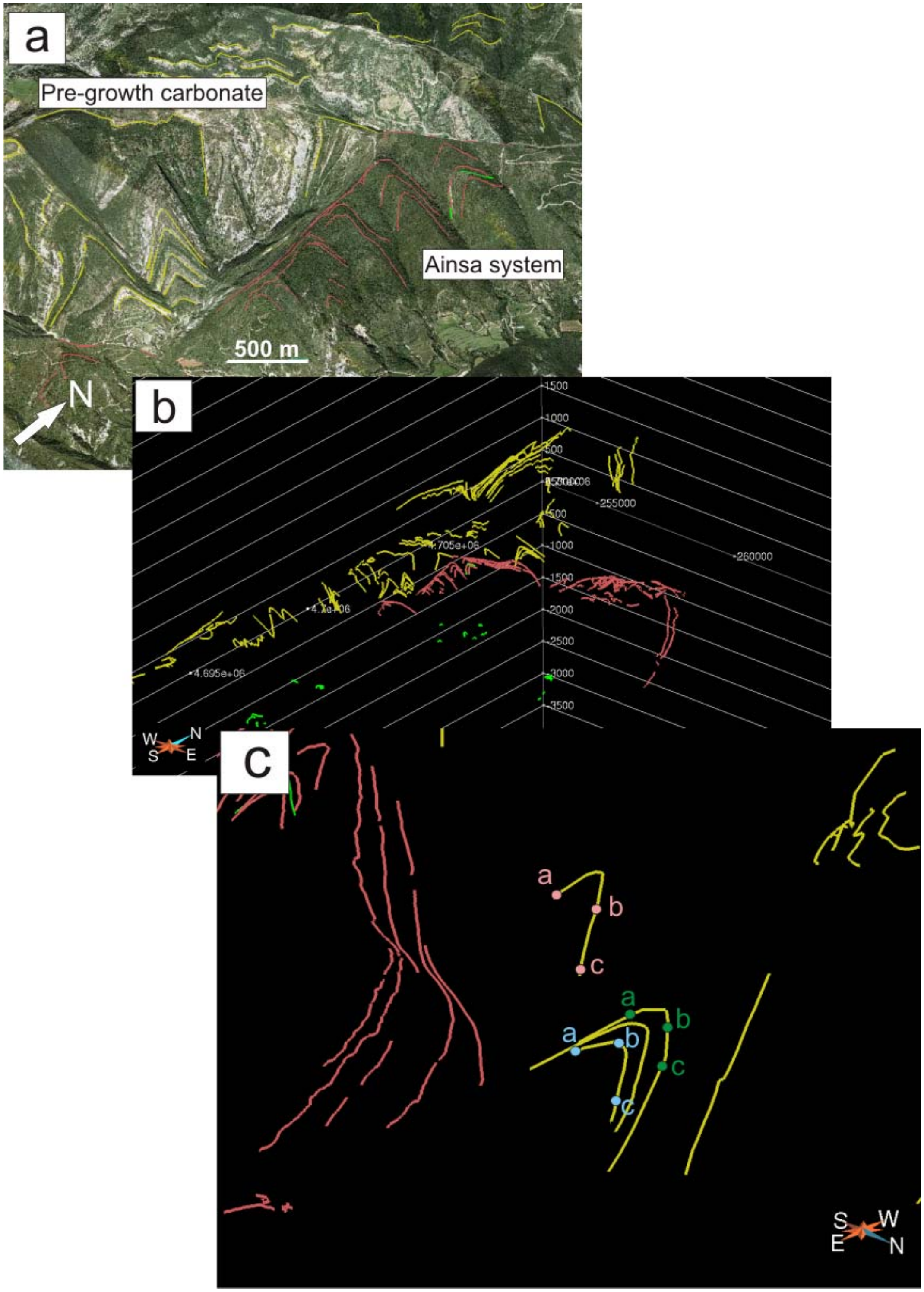

Figure 3.5: Three-point problem measurements from bedding traces in GoCAD. a) Clearly defined bedding traces in the Ainsa system and the pre-growth carbonate that outcrops on the Boltaña Anticline. b) The collection of bedding traces used in the three-point problem analysis. c) Individual three-point sets on pre-growth carbonates that define individual structural orientation measurements.

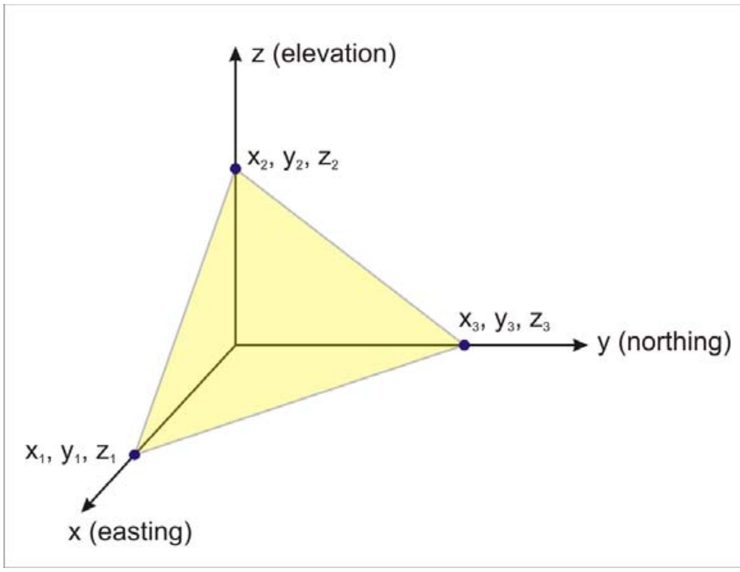

Figure 3.6: Diagram illustrating the relationship between the Cartesian coordinates of three separate points and the plane these points define in three-dimensions (modified from Vacher, 2000).

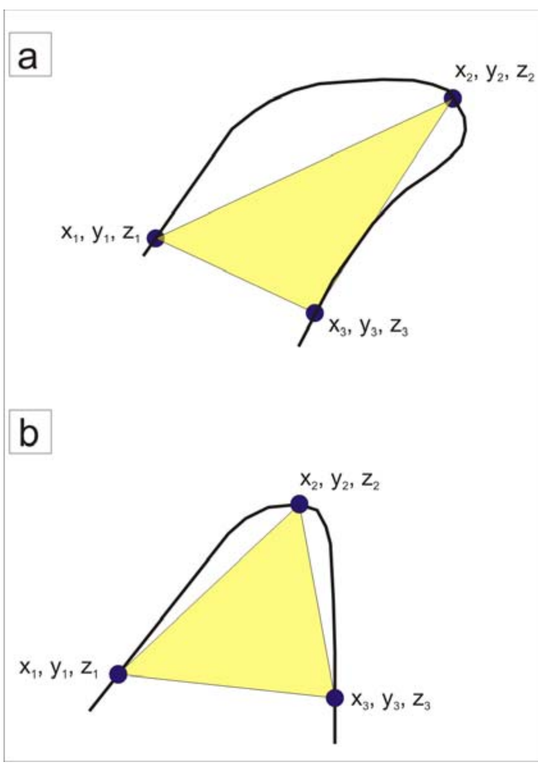

Figure 3.7: Examples of three-point sets on bedding traces. a) A bedding trace with variable dip. Note that the plane formed by the three-point set does not reflect the true bedding attitude. b) A bedding trace with uniform strike and dip. Note that the plane formed by the three-point set accurately reflects the true bedding attitude.

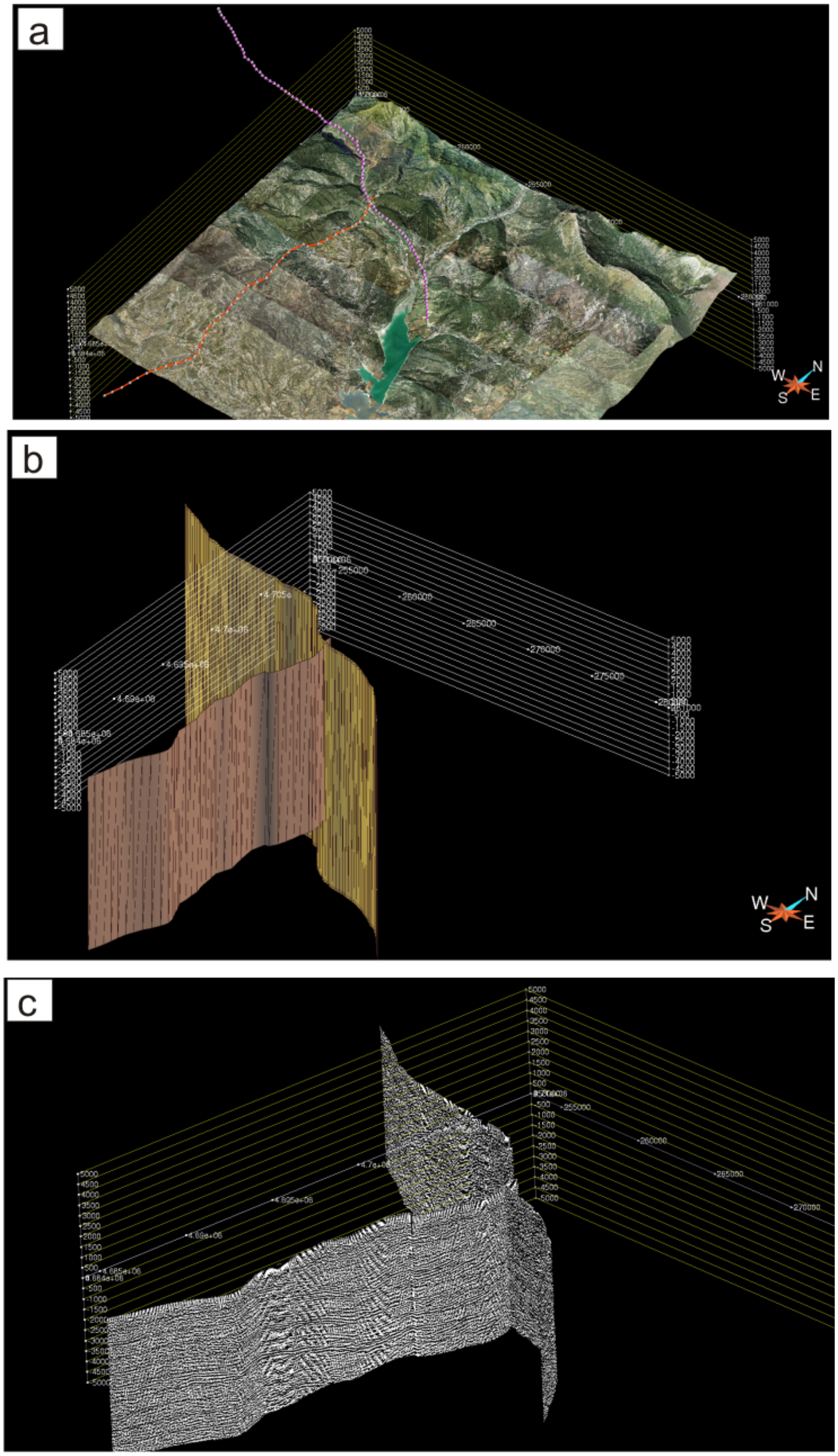

Figure 3.8: Importing seismic profiles into a 3-D GoCAD model. a) Shot-point locations from the Sp-2 and SP-3 lines defined as curves. b) Vertical surfaces constrained by the shot-point curves on which the SP-2 and SP-3 seismic profiles are draped. c) Depth-converted SP-2 and SP-3 seismic profile voxets draped on the vertical surfaces.

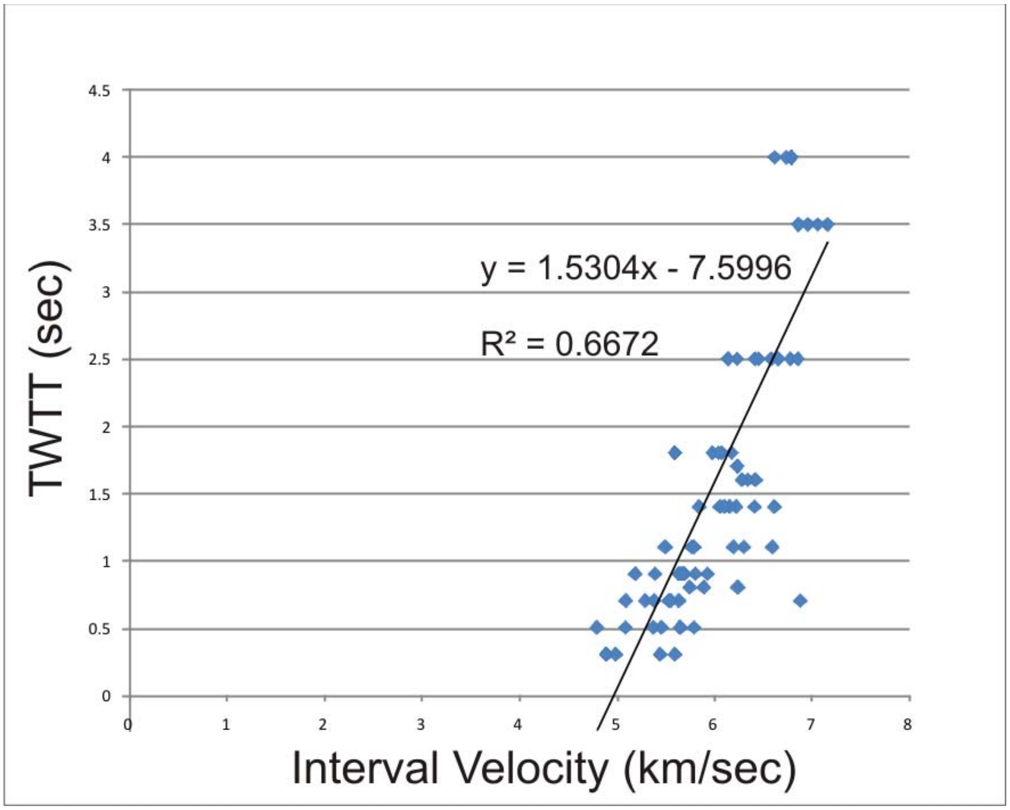

Figure 3.9: Interval velocities from the SP-2 and SP-3 seismic profiles plotted against two-way travel time (TWTT). Stacking velocities were converted to interval velocities using Dix's Law (as described in section 3.3.3).

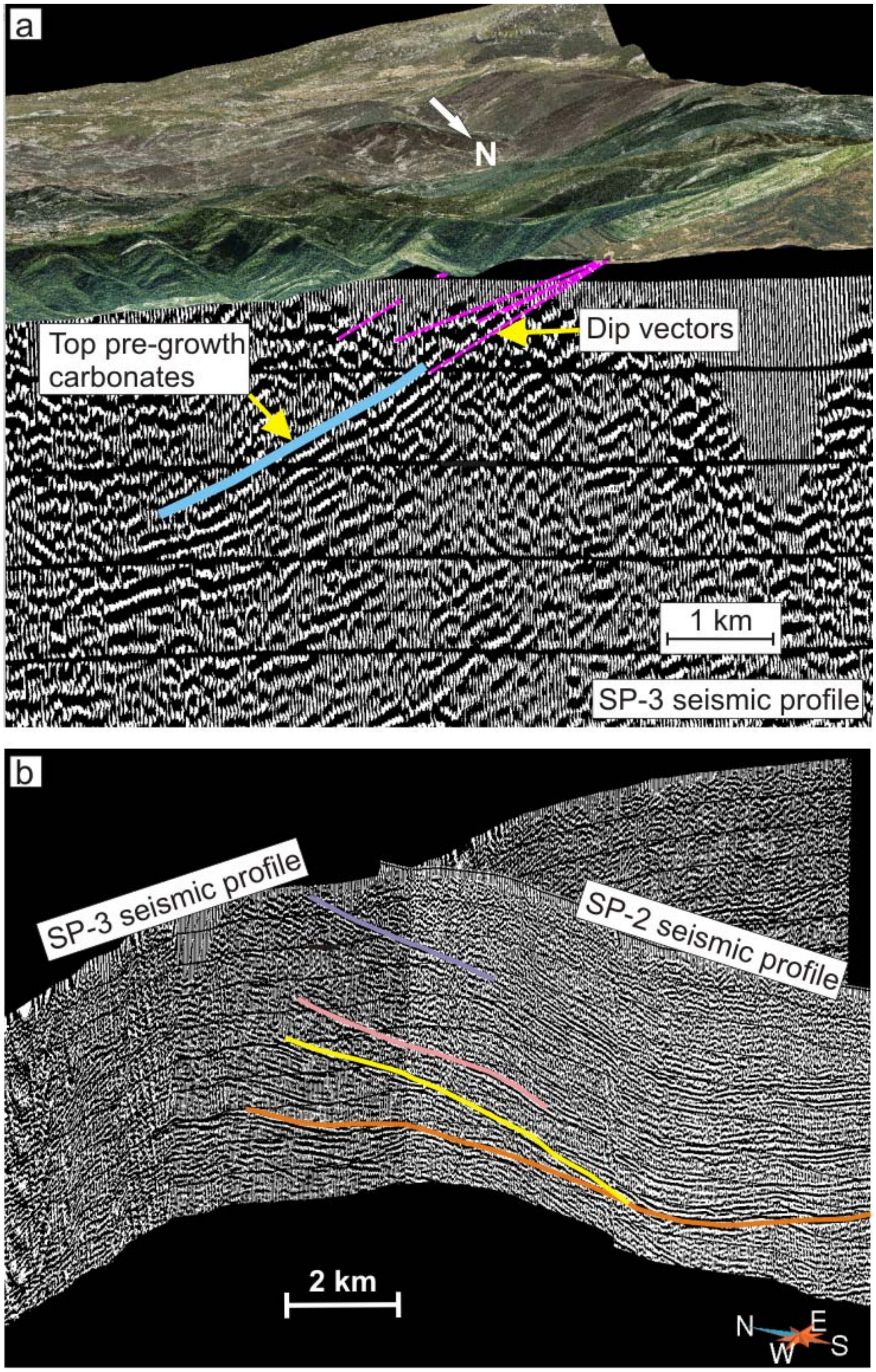

Figure 3.10: Checks performed on the seismic profile depth conversion. a) Surface measurements from the top of pre-growth carbonates on the backlimb of the Boltaña Anticline align with the interpreted top of pre-growth carbonates on the SP-3 seismic profile. b) Key reflectors align at the intersection of the SP-2 and SP-3 profiles indicating consistency in the depth conversion.

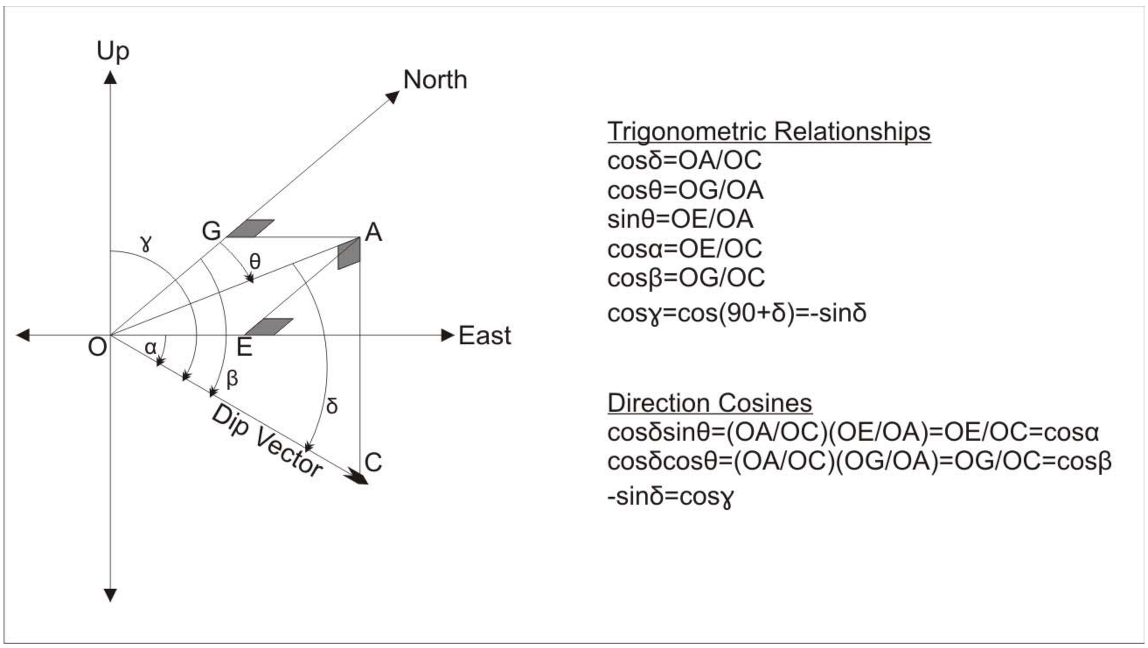

Figure 3.11: Trigonometric relationships used to convert the trend (θ) and plunge (δ) to a unit vector by calculating a measurement's direction cosines (modified from Groshong, 1999).

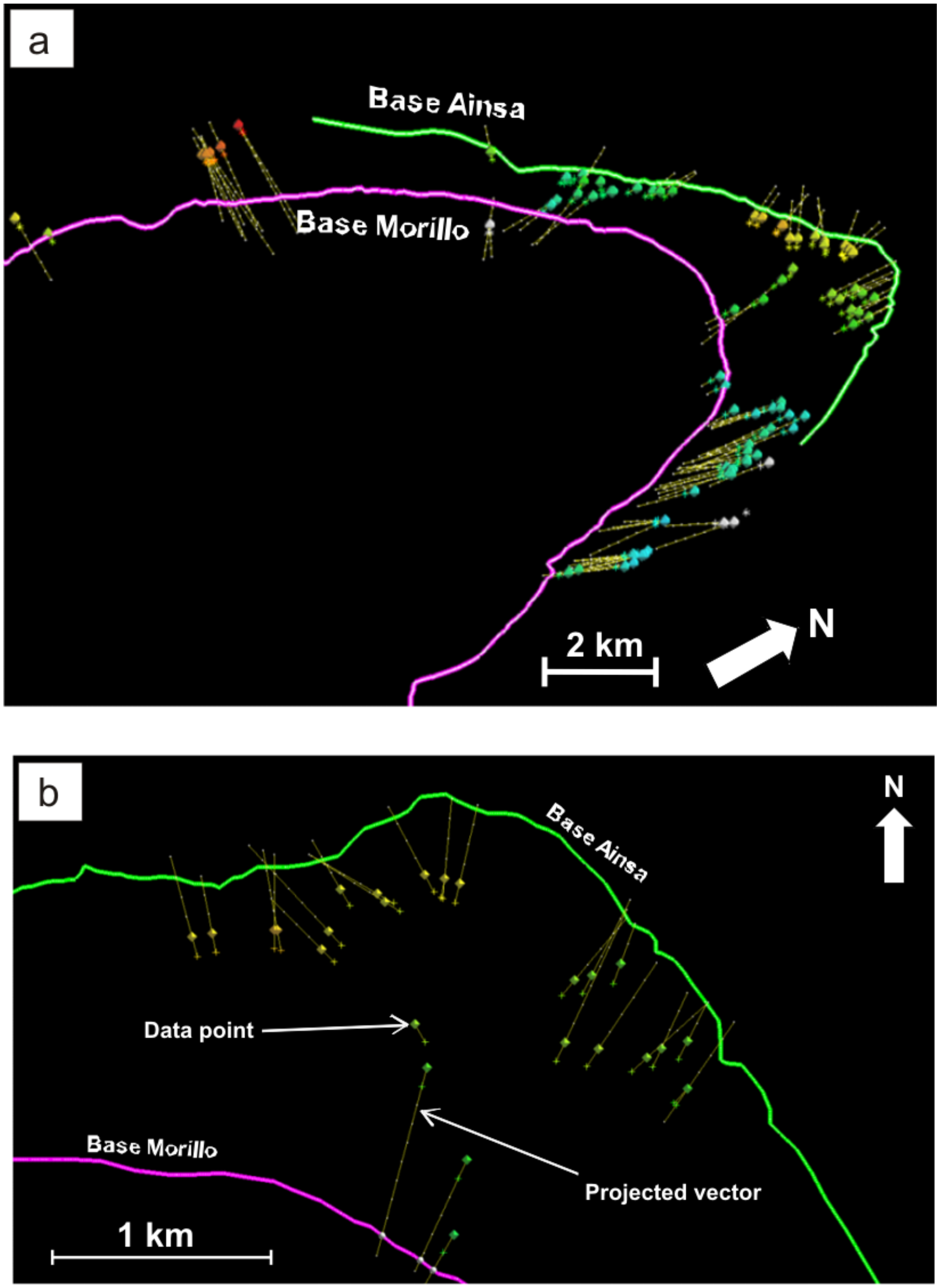

Figure 3.12: Dip vector projections to mapped base-Ainsa and base-Morillo condensed section contacts. a) Series of structural orientation measurements taken within the Ainsa system. b) The site of structural orientation measurements are represented by points. Individual lines show the projection of each measurement to the nearby contact. Note the overlap in vector projections onto the relatively rugose base-Ainsa contact, likely due to bad or erroneous data. After projecting the data, erroneous data can be recognized and discarded.

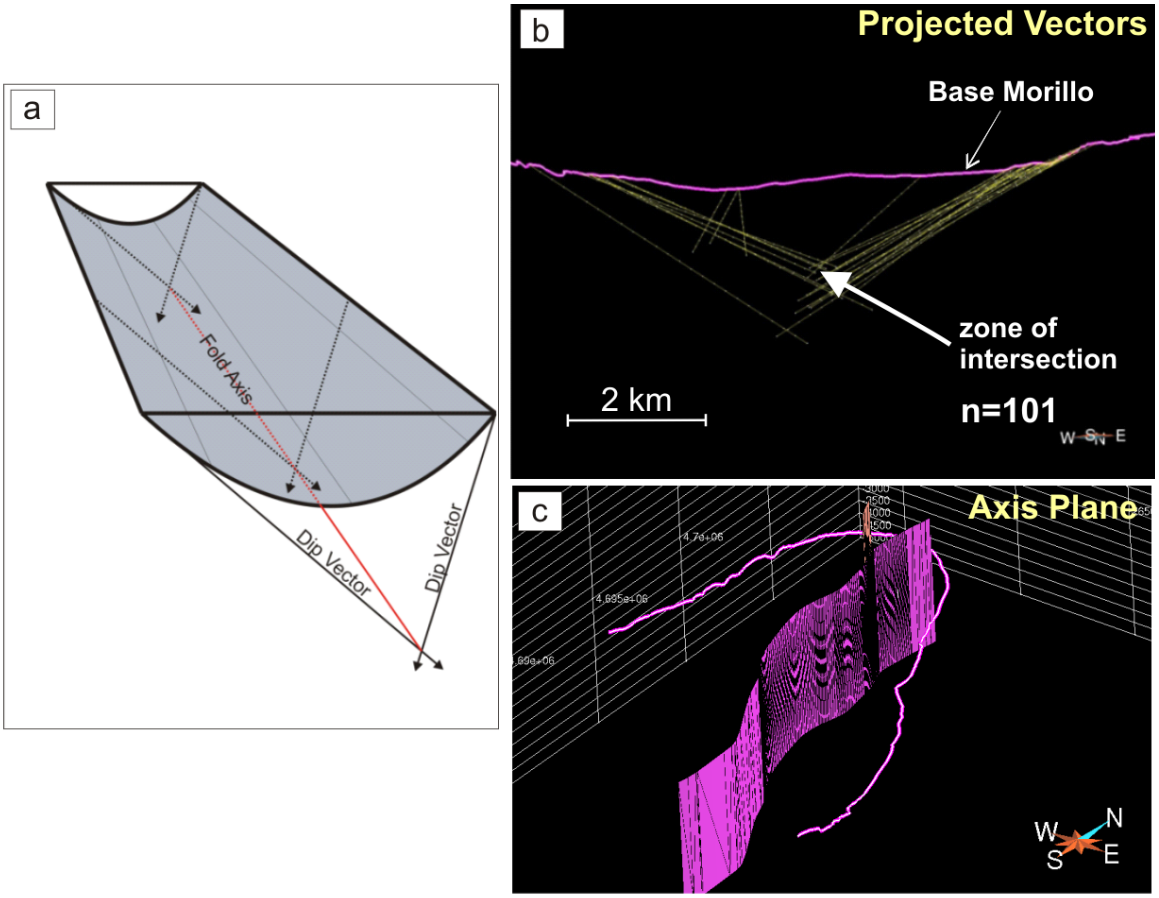

Figure 3.13: Diagrams outlining the steps taken to constrain the plan-view position of each system axis. a) Dip vectors from similar positions on opposite limbs of a fold, projected into the subsurface, define a zone of intersection that constrains the plan-view location of a fold axis along-strike. b) The subsurface zone of intersection from 101 dip vectors projected to the Morillo contact. A best-fit curve was constructed through this zone of intersection to define the along-strike variation of the Morillo system axis. c) Vertical axis plane constructed through the best-curve that constrains the plan-view location of the Morillo system axis.

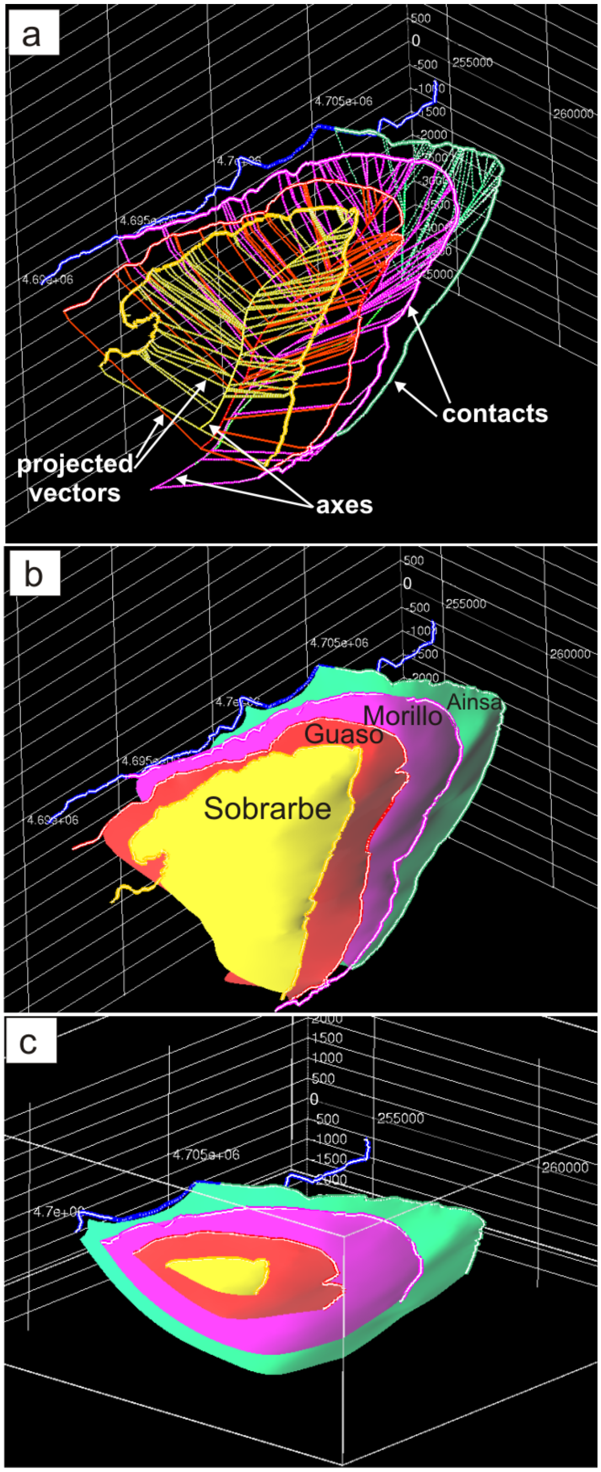

Figure 3.14: Surface interpolation for the base-Ainsa, Morillo, Guaso, and Sobrarbe condensed sections. a) Controls used in the surface interpolation, which include: 1) the condensed section surface contacts; 2) the projected dip vectors; 3) connecting curves that join the dip vectors to their respective system axis; and 4) the system axes constrained in three-dimensions. b) The resulting syn-growth condensed section surfaces. c) 3-D slice through the syn-growth condensed section surfaces.

CHAPTER 4

STRATIGRAPHIC AND STRUCTURAL ANALYSIS

The following sections summarize the observations and results from the field mapping, seismic interpretation, and 3-D structural modeling components of this research. The approach to field mapping was largely based on redefining the upper deepwater basin-fill systems (Ainsa to Sobrarbe) as condensed section bound units and on characterizing the along-strike geometries and internal complexities of the basin's bounding structures. Field mapping was partially informed by multiple studies on the Ainsa Basin deepwater systems and bounding structures.

The seismic interpretation section of this chapter describes the basin-scale stratigraphic and structural observations made from two seismic profiles located in the basin. The 3-D modeling section describes geometries and trends observed in structure, isopach, and dip maps generated from the model.

4.1 Stratigraphic Analysis

A primary method of this research involved mapping the four upper deepwater systems as condensed section bound units. The base-Ainsa, base-Morillo, base-Guaso, and base-Sobrarbe condensed sections were mapped around the basin (Fig. 4.1). The axis of the basin is the Buil Syncline, which plunges 10° to the south-southwest (Fig. 4.2). The locations of the base-Morillo and base-Guaso condensed sections were tested against stratigraphic correlations of the Morillo unit by Setiawan (2009). The following section describes the sand interval distribution, general paleocurrent trends, and position of condensed section unit boundaries of the Ainsa, Morillo, Guaso, and Sobrarbe systems.

4.1.1 Ainsa Stratigraphic Unit

The Ainsa stratigraphic unit is characterized by three main channelized sand intervals (Ainsa I, II, and III) interpreted as lower slope and axial basin floor submarine fans (Clark and Pickering 1996; Pickering and Corregidor, 2005; Pickering and Bayliss, 2009). Ainsa system sediment input entered Ainsa Basin from the east and reached base of slope in the approximate location of the Embalse de Mediano (Mediano Reservoir). Deepwater sediment gravity flows are interpreted to have exited the basin across a wide zone in the northern and northwestern parts study area between the San Vicente Syncline to the east and the eastern limb of the Boltaña Anticline to the west (Fig. 4.1a). The stratigraphy of the Ainsa I, II, and III is described briefly below.

4.1.1.1 Ainsa I Sand Interval

The easternmost and most proximal outcrop of the Ainsa I sand interval is located at the Ainsa Quarry (A, Fig. 4.3), 1 km southeast of the town of Ainsa and visible from the A-138 road. The Ainsa I sand interval is a channel complex 40 meters thick and 750 m wide (Clark and Pickering, 1996; Arbués *et al*., 2007). The outcrop is located oriented oblique to the mean paleoflow direction of 290° at the quarry (Clark and Pickering, 1996; Pickering and Corregidor, 2000). The Ainsa I sand interval is also observed to the north (B, Fig. 4.3) and forms the lowermost ridge 1 km south of the town of San Vicente. Mean paleoflow direction at this location is 320° (Pickering and Corregidor, 2000). The

Ainsa I sand interval thins rapidly west of this location and terminates 1 km west of the San Vicente Syncline (C, Fig. 4.3). Levee deposits that are correlative to the channel complex are observed cropping out along the road between Ainsa and Labuerda (Clark and Pickering, 1996) (D, Fig. 4.3).

4.1.1.2 Ainsa II Sand Interval

The easternmost and most proximal outcrop of the Ainsa II sand interval is also located at the Ainsa Quarry where mean paleoflow is 255° (Pickering and Corregidor, 2000). This sand is correlated northwards to the major ledge-forming sand (D, Fig. 4.3) on which the town of Ainsa is constructed and reaches a maximum thickness of 50 m (Clark and Pickering, 1996). Mean paleoflow at this location takes on a more northwestern trend to 320° (Fig. 4.3) (Pickering and Corregidor, 2000). Outcrop of the Ainsa II sand interval continues northwards through the San Vicente Syncline (E, Fig. 4.3) to its exposure in the Barranco de San Martin, immediately east of the Boltaña castle. This more distal outcrop is characterized by a 55 m thick succession of thin bedded sandstones that display significantly less channelization and is interpreted as the channel-lobe transition area for the Ainsa II interval (Clark and Pickering, 1996) (F, Fig. 4.3).

4.1.1.3 Ainsa III Sand Interval

The Ainsa III sand interval is only a few meters in thickness at its most eastern and proximal exposure at the Ainsa Quarry (A, Fig. 4.3). Mean paleoflow direction at this location is 330° (Pickering and Corregidor, 2000). The distal portion of the Ainsa III sand interval is largely limited to the northwestern extent of the Ainsa unit, supporting a major ledge that extends from immediately east of the San Vicente Syncline (F, Fig. 5.3), to the west where it correlates beneath the Boltaña castle and eventually runs parallel to the strike of the Lower Eocene pre-growth carbonates that form the eastern limb of the Boltaña Anticline (G, Fig. 4.3). Ainsa III sand interval thickness is 15-20 m thick at this western location and gradually thins to the southwest to its termination approximately 1.5 km northwest of the Morcat ruins (Figures 4.1 and 4.3). Mean paleoflow in the vicinity of the town of Boltaña is 345° however measurements collected to the southwest (G, Fig. 4.3), along the Ainsa III ledge are 320° (Pickering and Corregidor, 2000).

A clastic intrusion is observed within the mudstone sheets below the Ainsa III sand interval at its intersection with Rio Sieste. This feature is 3-4 meters wide and is composed of an intrusion of mudstone that was injected upwards, disrupting the surrounding carbonate-rich strata that have a rounded appearance in outcrop (Fig. 4.4).

4.1.1.4 Base-Ainsa Condensed Section

The base-Ainsa condensed section crops out west of the town of Labuerda (Fig. 4.1b). It is covered by Quaternary river gravels of the Rio Cinca and the Embalse de Mediano to the south and east of Labuerda (Figures 4.1 and 4.3). The method used to correlate the condensed section through this covered region is based on: 1) maintaining reasonable stratigraphic thickness of the Ainsa unit, 2) maintaining structural trends observed in outcrop of the overlying Morillo unit, and 3) reconciling its position relative to known outcrop of the underlying Banaston stratigraphic unit.

The base-Ainsa condensed section is characterized by a 4 m thick package of dark gray, thinly bedded mudstone found approximately 30 m below the base of the Ainsa I sand interval in the San Vicente syncline. This package, entirely free of sand beds, underlies interbedded mudstones and sandstones of the lower Ainsa unit, and overlies thin interbedded mudstones and sandstones of the upper Banaston unit. This relationship is more apparent to the west, approximately 1.3 km northeast of the town of Boltaña, where the condensed section is observed overlying an upper Banaston sand interval that displays growth fault geometries (Fig. 4.5). The base-Ainsa condensed section is correlated to the southwest across the Rio Ara to the Ainsa III ridge where it onlaps the pre-growth, Lower Eocene carbonates of the eastern Boltaña fold limb (A, Fig. 4.6).

4.1.2 Morillo Stratigraphic Unit

The Morillo stratigraphic unit is characterized by three main intervals (Morillo I, II, and III) that are separated by condensed sections (Figures 4.3 and 4.7). Setiawan (2009) correlated these intervals around the basin and identified two stratigraphic domains: a northern, axial siliciclastic- dominated domain and a southern marginal carbonate-dominated domain. The siliciclastic-dominated domain primarily consists of mudstone sheets with channelized sand intervals composed of debris flows and turbidite sands and is generally limited to a more axial position (Fig. 4.7). In contrast, the carbonate-dominated domain is in a more basin marginal position relative to the siliciclastic domain and is primarily composed of carbonate rich mudstone sheets, carbonate-filled channels, carbonate debris flows, and platform carbonate (Fig. 4.7).

These domains are present in the Ainsa, Guaso, and Sobrarbe units, but have only been mapped in the Morillo unit (Setiawan, 2009).

4.1.2.1 Morillo I

Along the eastern limb of the Buil syncline, the transition from siliciclastic- to carbonate- dominated domains within the Morillo I occurs approximately 1.5 km west of Camporrotuno (Fig. 4.7). On the western margin this transition occurs approximately 2 km east of the Morcat ruins. At this location the Morillo I contains limestone sheets interbedded with numerous MTCs, primarily consisting of carbonate debris flows and slumps (Fig. 4.7) (Setiawan, 2009).

The proximal portion of the Morillo I sand interval crops out between Morillo de Tou and Sierra de Morillo and is characterized by sand filled channel complexes that stack laterally and vertically to form a 75 m thick channel complex set (Figures 4.3 and 4.7). Paleocurrent direction ranges from 200° to 350° (Setiawan, 2009).

The distal portion of the Morillo I sand interval crops out near Rio Sieste and Rio Ara (Figures 4.3 and 4.7). Channel complexes stack vertically in this more axial and distal position. Mean paleocurrent is 315°. Paleocurrents exhibit a clockwise rotation upwards within the sandy interval to a northward trend of 005° (Fig. 4.7) (Moody, 2009; Setiawan, 2009).

4.1.2.2 Morillo II

The Morillo II stratigraphic unit contains a lower proportion of siliciclastic strata relative to Morillo I. As in the Morillo I, transition from the carbonate- to siliciclastic-dominated domain in the Morillo II occurs 1.5 km west of Camporrotuno (Fig. 4.7). On the western margin, transition to the southern carbonate dominated domain occurs 1.2 km northwest of the village of Urriales (Fig. 4.7). However, numerous carbonate debris flows, likely sourced from the Boltaña Anticline to the west, that are interbedded with siliciclastic mudstone sheets. The carbonate strata in the western basin margin is forms aggrading and prograding limestone sheets (Setiawan, 2009). The carbonate strata of the eastern margin are characterized by the presence of carbonate filled channels that indicate a southeastern carbonate source. These features are described in more detail in section 4.3.1.

In the eastern, proximal part of the system, the Morillo II sandy channel complexes are observed in a more southern position relative to the Morillo I sandy axis. The Morillo II channel complexes are spread over a 2 km wide zone between the villages of Coscojuelo de Sobrarbe and Morillo de Tou and reach thicknesses of up to 11 m (Figures 4.3 and 4.7) (Setiawan, 2009). Channels exhibit lateral-stacking patterns and a mean paleocurrent direction of 270° (Setiawan 2009). In the more distal and axial position at Rio Sieste, correlative Morillo II sandy channel complex thicknesses reach 35 m and exhibit a mean paleoflow of 340° (Clark and Pickering, 1996; Setiawan, 2009).

4.1.2.3 Morillo III

The Morillo III stratigraphic unit continues the upward decreasing trend of sandy strata relative to the Morillo I and II units and is dominated by thinly bedded mudstone sheets, with maximum Morillo III sand channel thicknesses on the scale of only a few meters (Setiawan, 2009). Carbonate debris flows on the western margin indicate continuous sediment sourcing from the Boltaña Anticline to the west (Fig. 4.7). These carbonate debris flows are most abundant in vicinity of Rio Eña and decrease to the south towards the village of Castellazo where the western margin is almost entirely dominated by limestone sheets (Fig. 4.7).

4.1.2.4 Base-Morillo Condensed Section

The base-Morillo condensed section is contains 3 to 4 m of thinly laminated, dark gray mudstone sheets with a distinctive silvery appearance.

Along the eastern syncline limb the condensed section is mappable below the major channel complexes of Morillo I north of the village of Morillo de Tou and can be correlated to the south below the Embalse de Mediano and cropping out again along the reservoir's bank immediately west of Coscojuela de Sobrarbe (Figures 4.1, 4.3, and 4.7). At the Mediano Dam, the base-Morillo condensed section merges with the progressive unconformity on the Mediano Anticline's western limb (Poblet *et al.*, 1998). Only Morillo II and younger strata crop out on the western limb exposure south of the Mediano Dam (Fig. 4.7).

The condensed section north of Morillo de Tou correlates to the west of the Ainsa III ledges where outcrop becomes covered by Quaternary river gravels (Figures 4.1 and 4.3). The condensed section is next observed in the synclinal axis in the valley between the Ainsa III and Morillo I ledges west of the town of Boltaña (Fig. 4.3).

From the town of Boltaña, the condensed section is correlated to the southwest, outcropping along the western edge of the Rio Sieste valley near the base of the Ainsa III ledge dip slope (Fig. 4.7). West of the Morcat ruins, the Morillo transitions to carbonate-rich mudstones and outcrop quality and abundance becomes poor (Fig. 4.6). Outcrops in stream valleys allows for the correlation of the base-Morillo condensed section southwards with good confidence to where it onlaps the pre-growth Lower Eocene carbonates of the eastern Boltaña Anticline limb, approximately 2 km northwest of the village of Castellazo (Fig. 4.1d).

4.1.3 Guaso Stratigraphic Unit

The Guaso stratigraphic unit contains two main sand intervals: 1) an older eastern sand interval (Guaso I), and 2) a younger western sand interval (Guaso II) (Sutcliffe and Pickering, 2009). These sand intervals are interpreted as laterally extensive lobes (Sutcliffe and Pickering, 2009). The Guaso I sand extends from its southeastern termination located 1.5 km south of Morillo de Tou to the north, forming a prominent ledge (Fig. 4.3). At Rio Eña, the Guaso I sand interval begins to thin towards the west and terminates beneath Quaternary river gravels north of the town of Guaso. The Guaso II sand interval extends from the town of Guaso to the southwest and terminates westward 2 km south of Rio Eña (Fig 4.3).

Seven paleocurrent measurements (3 grooves, 3 flutes, and 1 ripple set) were collected as part of the present study within the Guaso I sand interval in the vicinity of Rio Eña indicate a mean paleocurrent trend of 353° (range from 340° to 025°). This north-northwest paleocurrent trend indicates a more south-southeast sediment source relative to the older units and is consistent with the trend documented in Sutcliffe and Pickering (2009) for both the Guaso I and Guaso II sand intervals.

4.1.3.1 Base-Guaso Condensed Section

The base-Guaso condensed section is very similar to the base-Morillo condensed section, characterized by a 5 m thick, thinly laminated mudstone sheet with a distinctive silvery appearance.

Along the eastern Buil Syncline limb, the base-Guaso condensed section is identifiable approximately 30 m below the Guaso ledge northwest of Morillo de Tou (Figures 4.1 and 4.3). It is also observed southward, 500 m west of the town of Coscojuelo de Sobrarbe, overlying debrites of the Morillo III stratigraphic unit (Figures 4.1 and 4.7). The condensed section continues southwards where it crops out along the shore of the Embalse de Mediano, 1 km west of the town of Camporrotuno. The exposure at is located underwater to the south of this point. The condensed section correlates to the base of limestone sheets that crop out and trend laterally into platform carbonates on the Mediano Anticline's western limb between the villages of Mediano and Samitier (Fig. 4.1d).

The condensed section is correlated from Morillo de Tou to the north and west through the syncline axis, forming the base of the Guaso I ledge until just west of its intersection with Rio Eña at El Grado (Figures 4.1a and 4.3). At this location it becomes covered by Quaternary river gravels.

Along the western side of the Buil Syncline, the base-Guaso condensed section can be correlated to the south from Rio Sieste. It crops out continuously at the base of the Guaso II ledge, near the unit's intersection with the Rio Eña (Fig. 4.1a). The condensed section follows this ledge along the eastern side of the Rio Eña valley for 1.5 km where it can be tracked to 800 m west of the village of Castellazo (Fig. 4.1c). In the vicinity of the village of Castellazo, numerous carbonate blocks of reworked platform carbonate ranging in diameter from a few to tens of meters, crop out within a limestone sheet interval that overlies the condensed section. These blocks are part of debris flows shed from an early Boltana Anticline.

Outcrop of the base-Guaso condensed section is not observed south of the village of Castellazo and at no point can an onlap relationship be directly observed along the pre-growth strata of the Boltaña Anticline's eastern limb (Fig. 4.1). However, as in the Morillo unit, the Guaso unit exhibits a transition to carbonate-dominated facies in this southwestern portion of the basin.

4.1.4 Sobrarbe Stratigraphic Unit

The youngest strata of the Ainsa basin-fill consists is the Sobrarbe stratigraphic unit, a fluvio-deltaic complex that prograded into the basin from the south-southeast (Dreyer *et al.*, 1999). This progradational event is consistent with the more southerly source for basin sedimentation identified in the Guaso unit, relative to the underlying Morillo and Ainsa systems that exhibit a more northern and easterly source. Dreyer *et al.* (1999) identified four composite sequences that comprise the fluvio-deltaic complex that are bounded by regressive unconformities. Strata on the western margin of the system contain numerous slumps that juxtapose deltaic and fluvial sands adjacent to pro-delta mudstones (Fig. 4.8) (Dreyer *et al.*, 1999; Silalahi, 2009). Large slump scars are observed in the southwestern part of the Buil Syncline and penetrate as low as the deepwater mudstones of the uppermost Guaso unit. These slumps serve to overthicken the lowest strata of the Sobrarbe stratigraphic unit (Fig. 4.9).

This study establishes the base-Sobrarbe as a regional condensed section that can be mapped throughout the entire basin. The base-Sobrarbe condensed section is characterized by a 2.5 m thick black mudstone sheet that is easily recognized (Fig. 3.2). This condensed section is often associated with a bright orange, 5 cm thick siderite crust.

At its northernmost extent at the axis of the Buil Syncline axis, the condensed section separates Guaso turbidite sands from Sobrarbe prodelta mudstones. On the western margin it can be mapped through the Arcusa Anticline (Fig. 4.8) to the south beyond the study area. (Moss-Russell, 2009; Silalahi, 2009). South of Urriales (Fig. 4.8), the condensed section is locally structurally repeated by the large slumps of the overlying deltaic complex (Fig. 4.9a). On the eastern side of the basin, the condensed section can be mapped to the south, ~3 km northwest from the village of Mediano, where it becomes covered (Fig. 4.1d).

4.2 Structural Analysis

The following sections describe the along-strike variation and internal complexities of the major basin structures.

4.2.1 Mediano Anticline

The Mediano Anticline is located along the eastern side of Ainsa Basin. The fold is 15 km long and its axis trends roughly north-south, with minor deviations from this orientation (Figures 4.1b and 4.10). The northern termination of the fold is marked by its truncation by the Las Almazuras Thrust, a structure related to a shallow imbricate thrust system located in the northeast region of Ainsa Basin (Fig. 4.1b). In this area, the axial trace takes on a more NW-SE trend of 135°. The southern termination of the fold is in the vicinity of northernmost portion of the Embalse de Grado (reservoir) (Fig. 4.10). In this location the axial trace deviates from its dominantly north-south trend to a more SSW- NNE orientation to 195° (Fig. 4.10). The paleo-extent of the Mediano Anticline to the south is undefined due to limited outcrop and a post-folding, cross-cutting deformational event that involved a series of steeply dipping normal and strike-slip faults.

The Mediano anticline plunges 7° to the north (Figures 4.11 and 4.12) and displays significant variation in geometry along-strike. The southern region of the fold exhibits the greatest structural relief and exhibits the greatest amount of shortening (Poblet *et al.*, 1998). The fold is tight and asymmetric with a minimum interlimb angle of 45°. The eastern fold limb is overturned, dips approximately 60° to the northwest, and is cut by a steep northeast-southwest oriented, northwest dipping thrust fault (Fig. 4.13).

In the vicinity of Rio Usia (Fig. 4.10), the fold transitions to a symmetrical, open fold with an interlimb angle of >120°. The eastern limb is cut by a northwest-southeast trending normal fault (D, Fig. 4.10). Through correlation of the Paleocene-Lower Eocene contact across the fault, the maximum slip is estimated to be less than 100 meters (Fig. 4.14)

Due to the maximum amount of structural relief to the south and the northward plunge of the fold, the southern exposure of the Mediano Anticline exhibits a near complete pre-growth through syn-growth stratigraphic section, from the oldest Triassic shales and evaporites (Fig. 4.15) to the final stage of syn-growth basin fill: the Sobrarbe Formation (cropping out along road A-138, (A, Fig. 4.10). This southern exposure is the only location on the Mediano Anticline where the relationship between the syn-growth Ainsa Basin-fill systems and the pre-growth stratigraphy is observed (Fig. 4.16).

The Ainsa system is the oldest system to display thickness changes related to the Mediano Anticline. Older systems (i.e. Bansaston, Gerbe, Arro, & Fosado systems) show no thickness or facies changes relative to the structure (Poblet *et al.*, 1998). The base of the Ainsa system is covered by the Embalse de Mediano (reservoir), however the top of the Ainsa unit is observed near the reservoir. The Ainsa unit crops out on a peninsula 2 km NE of the town of Mediano. At this location the Ainsa unit is characterized by carbonate-rich mudstone sheets, 120 m in thickness. Further south the base of the Morillo unit crops out along the road to the Mediano dam (immediately east of the town of Mediano). No Ainsa strata are interpreted at this location. Therefore, the unit thins to zero via onlap onto the pre-growth strata of the anticline's western limb (B, Fig. 4.10).

The Morillo stratigraphic unit also thins towards the anticline's western limb. The Morillo unit's thickness on the peninsula located 2 km north-northwest of the town of Mediano is approximately 340 m in thickness and consists primarily of carbonate rich mudstone (Figures 4.1 and 4.7). Farther south along the road to the Mediano dam (immediately east of the town of Mediano) the Morillo thins to approximately 200 m and is also dominated by carbonate rich mudstone sheets. In the vicinity of the Castillo de Samitier (C, Fig. 4.10), the Morillo unit thins to 25 m and is composed of platform carbonates, carbonate filled channels, and large carbonate clasts (up to 20 m in diameter) within carbonate mudstones.

A Morillo age submarine canyon that erodes into pre-growth strata is present within the Morillo stratigraphic unit on the Mediano Anticline's western limb (Fig. 4.17).

Canyon-fill consists of carbonate rich mudstone sheets, limestone channels, and debris flow deposits (Setiawan, 2009). Blocks of platform carbonate ranging in size from 3 to 15 meters in diameter outcrop within the debris flow deposits. The base of this canyon is correlated to the north to the base of the Morillo II stratigraphic sub-unit, 1.5 km from the Castillo de Samitier (Setiawan, 2009).

The overlying Guaso and Sobrarbe units have similar trends to the Morillo unit. They transition from carbonate rich mudstone sheets to platform carbonate southwards toward the western Mediano Anticline limb. However, platform carbonates of the Guaso unit are well-developed and intact, lacking erosional channels or canyon cuts. Outcrop of platform carbonate coeval with the Sobrarbe system is not present due to the present day erosional surface and the fold's truncation by later structures. Additionally, the Sobrarbe system laterally transitions from mudstone to limestone sheets as it approaches the western limb of the Mediano Anticline. Limestone sheets of the Sobrarbe system outcrop in a road cut along A-138 approximately 1 km north of Meson de Liguerre (A, Fig. 4.10).

4.2.2 Boltaña Anticline

The Boltaña Anticline is a major regional topographic feature and is cored by Lower Eocene platform carbonates interbedded with marls and calcareous sands. The Boltaña Anticline trends north-south and extends for over 22 km along the western margin of Ainsa Basin, forming a topographic high extending from its southern termination at the southwestern-most limit of Ainsa Basin to the north where it extends beyond the study area. The fold's axial trace maintains a N-S trend throughout its entire length and continues this trend to the north where it runs parallel to the Añisclo Anticline towards the Pyrenean axial zone (Fig. 4.1a). At the Boltaña Anticline's southern termination, the fold plunges 8° to the south. However, a π-axis analysis of all pre-growth bedding shows a near horizontal axis along the majority of the fold's extent, with an axis trend and plunge of approximately 01°/360 (Fig. 4.18). This value represents an average of all bedding dips acquired throughout the anticline's entire exposure in the basin. Minor local variations in plunge of less than a few degrees can be observed along the fold's strike.

The Boltaña Anticline exhibits considerable geometric variation along strike. For descriptive purposes, the fold can be divided into three sectors: 1) a southern sector, 2) a central sector, and 3) a northern sector.

4.2.2.1 Southern Sector

The southern sector of the Boltaña Anticline is defined as the area between the town of Las Bellostas and the southern extent of the study area (Fig. 4.1c). In this region, the Boltaña Anticline plunges 8° to the south and is partitioned into two folds, each characterized by steeply dipping western limb and gentler dipping eastern limb (Fig. 4.1c). The eastern limb on the eastern fold dips approximately 22° to the east and the western limb dips between 70° and 80° to the west. The eastern limb of the western fold dips approximately 40° to the east and the western limb is 70° to the west.

Lower Eocene platform carbonates crop out in the core of each fold and syn-growth carbonate-rich mudstone sheets that are coeval to the siliciclastic deepwater systems of the upper basin-fill (Morillo and Guaso) crop out on the folds' limbs. While not directly observed, a thrust fault is inferred to juxtapose the vertical limb of the western fold directly over the eastward dipping limb of the western fold, accounting for the major changes in observed bedding dips over distances on the scale of 10s of meters from east to west (Fig. 4.19).

4.2.2.2 Central Sector

The central sector of the Boltaña Anticline is defined as the area between the town of Las Bellostas to the south and the town of Campodarbe to the north (Fig. 4.1). This region of the fold is characterized by a near horizontal fold axis and a large erosional cut into the fold's western limb. The fold's eastern limb is steepest in the central sector, reaching dips upwards of 40° to the east (Fig. 4.20). The geometry of the western limb is obscured by an erosional surface that cut into the Lower Eocene pre-growth carbonates. This erosional surface extends for 6 km along the anticline's western limb and forms a broad synclinal geometry (Figures 4.1 and 4.21). This surface is estimated to have eroded upwards of 400 m into the Lower Eocene pre-growth carbonate.

This erosional cut is filled by Late Eocene-Oligocene fluvial strata that thicken to the west towards the Jaca Basin. The strata immediately overlying the erosional surface are composed of conglomerates containing cobble-sized carbonate clasts (up to 30 cm in diameter), suggesting some reworking of the underlying carbonate facies into the fluvial deposits (Fig. 4.22). Grain size fines upwards through the succession, decreasing to medium- to coarse-grained channel sands and interbedded siltstone-mudstone red beds (paleosols).

4.2.2.3 Northern Sector

The northern sector of the Boltaña Anticline is defined as the area of the fold between the village of Campodarbe and the northern limit of the study area. The northern sector contains the present day Boltaña Canyon, formed from Rio Ara incision, and exhibits the most complete section (>500m) of Lower Eocene pre-growth carbonates in the basin (Fig. 4.23a). The fold's eastern limb dips approximately 20° to the east and the western limb is nearly vertical, dipping 80° to the west.

On the eastern limb, a clear onlap relationship is observed between the Lower Eocene pre-growth carbonates and the Banaston and Ainsa systems. The Banaston thins and pinches out completely against Lower Eocene platform carbonates along the A-1604 road between the towns of Boltaña and the village of Campodarbe (A, Fig. 4.6 and Fig. 4.23). At the point of the upper-Banaston pinch out, the base Ainsa condensed section subcrops as Ainsa onlaps and thins onto the Lower Eocene platform carbonates of the eastern limb.

Thinly bedded limestone and mudstone sheets of the Jaca Basin crop out along the fold's vertical western limb (Fig. 4.24). Bedding dips are similar to the pre-growth carbonates at vertical to overturned, however display highly variable strikes. Multiple small-scale folds are present (wavelengths < 100m) with vertical axes that imply a N-S σ_1 direction; perpendicular to that of the Boltaña Anticline (Fig. 4.24b).

4.2.3 Añisclo Anticline

The southern termination of the Añisclo Anticline plunges southwards steeply below Ainsa Basin to the north at an angle of 26° (Fig. 4.1a). Pre-growth Cretaceous-

Paleocene carbonates crop out several kilometers to the north of the study area (Fig. 4.25) and, while a detailed analysis of this structure was not performed, the Añislco Anticline affects Ainsa deepwater deposits by partitioning the Buil syncline into two smaller synclines: the Buerba (located west of the Añisclo Anticline) and San Vicente (east of the Añisclo Anticline) Synclines. π-axis stereonet analysis of the these synclines indicate that the Buerba Syncline axis plunges 19° and trends to 150°, and the San Vicente Syncline plunges 24° and trends to 183° (Fig. 4.26).

4.2.4 Arcusa Anticline

The Arcusa Anticline is 4 km long and is located in the southwestern region of the study area, immediately southeast of the town of Arcusa (Fig. 4.1c). The fold is open and plunges to the north-northwest at 8°. The eastern limb dips 20° to 25° to the east. The western limb dips ~10° to the west in the northern portion of the fold, near the town of Arcusa, and becomes nearly flat lying approximately 1.5 km to the south. The lower strata of the Sobrarbe unit exhibit no thickness changes relative to proximity of the Arcusa Anticline (Moss-Russell, 2009; Silalahi, 2009). However, Dreyer *et al.* (1999) recognized wedge geometries in the upper Sobrarbe sequences that thin towards the Arucsa Anticline axis and interpreted them to be deposited coeval with the onset of Arcusa Anticline growth.

4.3 Oldest Basin-Fill Systems

An approximately 4 km wide corridor was mapped through the northeast portion of the basin, between the village of Gerbe and the San Victorian monastery. This corridor runs roughly perpendicular to a series of small, northwest-southeast trending thrusts and folds known as the Arro fold system (Casas *et al.*, 2002) or the Peña Montanesa imbricate fan (Farrell *et al.*, 1987). These structures deform the oldest deepwater basin-fill systems of Ainsa Basin, which include the Banaston, Gerbe, Arro, and Fosado Systems.

The Banaston system consists of a series of erosive lower-slope, sand-filled channels in the proximal, northeast portion of the basin (Pickering and Bayliss, 2009). Bedding dips are 30° to 35° to the west-southwest as it crops out along the eastern limb of the Mediano Anticline (Fig. 4.1b). This portion of the system is nearly 500 m thick and correlates to a nearly 700 m thick section of laterally-offset stacked basin-floor sands to the NW that lie beyond the study area (Pickering and Bayliss, 2009).

The Gerbe system consists of two sand intervals (Gerbe I and II) that are interpreted as lower slope erosive channel complexes that form a major topographic ledge (Fig. 4.1b) (Clark and Pickering, 1996; Pickering and Bayliss, 2009). In the vicinity of the town of Gerbe, the Gerbe I sand interval is 45 m in thickness and 2750 m in width (Clark and Pickering, 1996). The Gerbe II sand interval is 30 m in thickness and 1500 m wide (Clark and Pickering, 1996). The Gerbe II sand interval is documented to thicken considerably to the northwest in the San Vicente Syncline to over 200 m (Pickering and Bayliss, 2009). The main Gerbe ledge dips 20° to the southwest near N-260 and steepens to the northwest reaching dips of 40° to the southwest. The Gerbe system is correlated across the Mediano Anticline fold axis (Arbués *et al.*, 2007) and does not display growth geometries related to this structure.

The Arro system crops out within a syncline immediately adjacent to and northeast of the Mediano Anticline axis. The Mediano Anticline dies out in this northeastern region of the basin and is overridden by the Las Almazuras Thrust that deforms the lower Arro system. Sand intervals of the of the lower Arro system are deformed in a tight, recumbent, southwest verging anticline associated with the Las Almazuras Thrust.

The Arro system is interpreted as an unconfined sand interval related to the mouth of the Charo Canyon, located to the east beyond the study area (Milligan and Clark, 1995; Clark and Pickering, 1996). Maximum Arro sand interval thickness is 210 m. Lower Arro sands are observed cropping out within the anticline immediately adjacent to and northeast of the Arro syncline. The best exposure of the Arro system is at the Los Molinos-Arro road cut (C, Fig. 4.1b), as other portions of the system are obscured by vegetation.

The strata underlying the Arro sand interval are dominated by mudstone sheets and mudstone dominated slumps with very little sand present in the system (Figures 4.28 and 4.29). The sand intervals of the Fosado system crop out as discrete sand intervals that range in thickness from a few to up to 30 m in thickness and are interpreted as lower to base of slope channel complexes (Pickering and Bayliss, 2009).

The slump and mudstone sheet dominated strata that surround these lowermost sands are deformed by the Los Molinos Thrust. This thrust dips to the northeast at 8 to 15° degrees and is often associated with a several meter thick zone of small scale deformation characterized by tight folds and slickenlined fault and bedding surfaces.

To the northeast is the massive Peña Montanesa (Fig. 4.29) which is composed of Creteaceous-Paleocene carbonate that was thrust over the oldest basin-fill systems by the Peña Montanesa Thrust. This structure is also referred to in the literature as the Sierra Ferrara Thrust (Casas *et al.*, 2002).

4.4 Seismic Interpretation

The SP-2 and SP-3 seismic profiles were interpreted as part of this study in order to constrain subsurface structural geometries and aid in 3-D model construction (see section 3.3.6.2). The SP-2 profile trends roughly N-S through the central-western portion of the Ainsa Basin and continues to the south beyond the study area (Fig. 4.30). The SP-3 profile trends west-northwest to east-southeast through the northern portion of the basin and continues to the west beyond the study area (Fig. 4.30). Details on the position, acquisition, and depth conversion of these two profiles are described in sections 3.2.2.4 and 3.3.3. The profiles are used in the present study to distinguish the detachment, pre-growth, and syn-growth stratal geometries observed in the seismic at the basin scale. The following sections describe the general structural geometries observed in the original time profiles.

4.4.1 SP-3 Seismic Profile

The SP-3 seismic profile was originally published in Soto *et al.* (2002) as part of a regional cross-section through the Tremp and Ainsa Basins. The present study uses the main seismic horizon picks identified in Soto *et al.* (2002), however does not attempt to interpret the profile with the same Tremp Basin formation terminology applied in the study. Additionally, Soto *et al.* (2002) incorrectly references the profile in their cross-section, leading to the misinterpretation of Ainsa Basin structures. Picks made on the SP-3 profile were correlated to the SP-2 profile following the depth conversion in GoCAD (section 3.3.3).

The SP-3 seismic profile images the western limb of the Mediano Anticline (A, Fig. 4.31), the Buil Syncline, and the eastern limb of the Boltaña Anticline (B, Fig. 4.31). The regional Triassic detachment unit (shales and evaporites) is easily discernible as a reflector-poor zone that immediately overlies a strong reflector that separates the detachment from the basement, and underlies coherent reflectors within the overlying pre-growth Cretaceous-Paleocene carbonates. The overlying deepwater basin-fill is marked by discontinuous reflectors that cannot be traced at the basin scale. The seismic data do not resolve channel complexes and condensed sections.

On the western Boltaña Anticline limb, strong reflections overlying the Cretaceous-Paleocene pre-growth carbonates are interpreted to be the Lower Eocene platform carbonates that outcrop in the core of the anticline. These reflections terminate to the east at what is interpreted to be a diachronous and unconformable surface that separates the Lower Eocene platform carbonates from the deepwater basin-fill (B, Fig. 4.31).

The western limb of the Boltaña Anticline is poorly imaged due to near vertical bedding dips. A deeper structure is recognizable that is interpreted to be a ramp extending upwards from the lower regional detachment (C, Fig. 4.31). This ramp dips to the east and can be traced into the core of the Boltaña Anticline where imaging becomes poor and the ramp reflector is lost. This ramp structure is correlative to the ramp structure identified in the northern portion of the SP-2 profile (C, Fig. 4.32). The footwall strata below the ramp appear to be slightly folded above the regional detachment layer (D, 4.31). However, it is possible that this geometry is a result of a velocity pull up.

4.4.2 SP-2 Seismic Profile

The SP-2 seismic profile images the Ainsa Basin parallel to the Buil Syncline axis. From north to south the overall geometry is characterized by climbing reflectors in the northern portion of the profile that shallow and then climb again to the south. The profile runs 1-2 km west of the Arcusa Anticline and therefore the climbing geometry in the south can be partially attributed to this structure. However, considering the transition to shallow-water, carbonate-dominated facies that occurs to the southern portions of the basin-fill units, this geometry is likely in part reflecting paleo-basin physiography (A, Fig. 4.32).

Similar to the SP-3 profile, the regional Triassic detachment unit (shales and evaporites) is easily discernible as a reflection-poor zone that immediately overlies a pronounced basement reflector. Coherent reflectors, traceable at the regional scale, characterize the overlying pre-growth Cretaceous-Paleocene carbonates. The diachronous and unconformable surface that separates the Lower Eocene platform carbonates from the deepwater basin-fill is correlated from the SP-3 line, however tracing this surface to the south is not straightforward, as a single reflector is not identifiable at the regional scale. However, as in the SP-3 line, the deepwater fill is characterized by more discontinuous reflections, which provide some constraint on the location of the unconformity through the SP-2 profile (B, Fig. 4.32).

The Boltaña Anticline ramp identified in the SP-3 profile is present in the northern portion of the SP-2 line (C, Fig. 4.32). This ramp dips and shallows to the south as it merges with the lower detachment.

4.5 3-D Structural Model

Three-dimensional surfaces were constructed for the base- Ainsa, Morillo, Guaso, and Sobrarbe condensed sections using the methodology described in section 3.3 (3-D model construction methodology). From these surfaces structure, isopach, and dip maps were generated. The following sections describe the trends and geometries observed in these maps.

4.5.1 Structure Contoured Surfaces

Contour values displayed on the structure surfaces represent the surfaces' position relative to sea level. Therefore, negative values are below sea-level (BSL) whereas positive values are above sea level (ASL) contours. All structure contoured surfaces were generated using GoCAD modeling software.

4.5.1.1 Base-Ainsa Surface

The base-Ainsa surface displays a bowl-shaped geometry (Fig. 4.33). The deepest portion of the surface is 3.5 km southwest of the town of Ainsa and reaches a maximum depth of 1300 m BSL (A, Fig. 4.33). The surface climbs in all directions from this location, most gradually to the south along the Buil Syncline axis. The highest point of the base-Ainsa surface reaches 1040 m ASL (B, Fig. 4.33).

The northern portion of the surface exhibits two synclines branching off the main Buil syncline. These are the San Vicente (eastern) and Buerba (western) Synclines (Fig. 4.33). The synclinal geometries shown in this surface extend and broaden from their topographic intersection into the subsurface where they merge with the larger Buil Syncline to the south.

On the western side of the basin, west of the town of Boltaña, the base-Ainsa surface onlaps the pre-growth carbonates of the Boltaña Anticline and therefore the surface subcrops to the south (Fig. 4.33). Continuation of this surface to the south is speculative and construction is based on maintaining a gradual thinning of the Ainsa stratigraphic unit to its pinchout against a diachronous and unconformable pre-growth surface constrained by the pre-growth / syn-growth contact along the Boltaña Anticline's eastern limb.

4.5.1.2 Base-Morillo Surface

The base-Morillo surface displays a similar bowl-shaped geometry (Fig. 4.34). The deepest portion of the surface is 4.5 km southwest of the town of Ainsa and reaches a maximum depth of 850 m BSL (A, Fig. 4.34). The surface climbs in all directions from this location, most gradually to the south along the Buil Syncline axis. The highest point of the base-Morillo surface reaches 970 m ASL (B, Fig. 4.34).

The northern portion of the surface does not display synclinal geometries present in the base-Ainsa surface. Slight undulations in the surface are present in these areas, but are likely reflecting the projection of data from the underlying Ainsa unit onto the base-

Morillo surface, as the mapped base-Morillo condensed section does not exhibit the presence of the San Buerba and San Vicente synclines.

The surface is clipped in the southwest region of the study area, south of the point where base-Morillo surface onlaps the pre-growth carbonates of the Boltaña Anticline. To the east of the onlap point, the surface is likely affected by the Arcusa Anticline. The lack of exposure of Morillo strata through this region makes constraining the geometry of the surface impossible. On the eastern Buil syncline limb, the surface is constructed to its southeast termination on the western limb of the Mediano anticline.

4.5.1.3 Base-Guaso Surface

The base-Guaso surface exhibits a more elongate axial geometry than the base-Ainsa and base-Morillo surfaces (Fig. 4.35). The surface reaches a maximum depth of 300 m BSL 5.5 km southwest of the town of Ainsa (A, Fig. 4.35) The highest point of the base-Guaso surface reaches 970 m ASL (B, Fig. 4.35).

No evidence exists of the Buerba and San Vicente Synclines affecting this surface, as it is entirely contained within the Buil Syncline. Continuous exposure of the base-Guaso condensed section on both syncline limbs permits construction of the surface throughout the entire study area. The lack of exposure of the base-Guaso surface in the Arcusa Anticline makes subsurface construction of the surface through fold in the subsurface unconstrained. The fold is reflected in a shallowing of surface dips in the vicinity of the Arcusa anticline, but no fold axis is distinguishable (Fig. 4.35).

4.5.1.4 Base-Sobrarbe Surface

The base-Sobrarbe surface is the youngest surface constructed and displays a similar elongate axial geometry to the base-Guaso surface (Fig. 4.36). The surface reaches a maximum depth of 200 m ASL, 5.5 km southwest of the town of Ainsa (A, Fig. 4.35). The highest point of the base-Sobrarbe surface reaches 880 m ASL (B, Fig. 4.35)

The Arcusa Anticline is observed in the southwest region of the study area. The presence of the Arcusa Anticline this creates a broad synclinal geometry immediately to the west-northwest of the anticline axis in the vicinity of the village of Arcusa.

4.5.2 Isopach Maps

Isopach maps were created for the Ainsa, Morillo, and Guaso stratigraphic units. The contoured thickness values were generated at each surface node by measuring the orthogonal distance between the upper and lower bounding surfaces for each stratigraphic unit. Each unit's isopach contours are displayed on the upper bounding surfaces. All isopach contoured surfaces were generated using GoCAD modeling software.

4.5.2.1 Ainsa Isopach Map

The Ainsa stratigraphic unit reaches a maximum thickness of 700 m in the axis of the San Vicente Syncline (A, Fig. 4.37). This zone of maximum thickness merges with an extended thick of ~ 500 m that extends to the south-southeast along the eastern Buil Syncline limb. The Ainsa thins to the south and where it onlaps the Mediano and Boltaña Anticlines.

A thin occurs on the western limb of the Buerba Syncline where the Ainsa unit thins to 300 m (E, Fig. 4.37). This thin corresponds to a region in the axial part of the surface where only the Ainsa III sand interval is present.

A thick occurs along the western Buil Syncline limb (D, Fig. 4.37) where the Ainsa unit thickens to over 500 m. This thick corresponds with a recess in the pre-growth carbonates of the Boltaña Anticline. This recess is filled with carbonate rich mudstones with very little sand present. It is important to note, as described in section 4.1.5.1, that the southern continuation of the base-Ainsa beyond the surface expression of the onlap is speculative. Therefore, thickness anomalies may exist along this western syncline limb resulting from a lack of constraints on the base-Ainsa surface.

4.5.2.2 Morillo Isopach Map

The Morillo stratigraphic unit reaches a maximum thickness of 900 m immediately west of the town of Ainsa (A, Fig. 4.38). This zone of maximum thickness is part of a broad isopach thick that trends south-southeast to north-northwest across the northern portion of the unit. The eastern syncline limb displays a gradual thinning trend to the southeast towards the Morillo unit's point of pre-growth onlap in the southeastern portion of the study area. At this point of onlap, an elongate thick is observed that trends north-northwest, forming a canyon geometry (B, Fig. 4.38).

Two anomalous thicks occur along the western Buil Syncline limb (C,D, Fig. 4.38). However, they appear to be localized and limited to less than 2 km in extent. They seem to correspond with off-axis Morillo sand intervals that crop out on the western Buil Syncline limb (A, Fig. 4.1c).

4.5.2.3 Guaso Isopach Map

The Guaso stratigraphic unit reaches a maximum thickness of 600 m in the axis of the Buil Syncline 5 km southwest of the town of Ainsa (A, Fig. 4.39). This thick has a "C" shape and extends from the northeast to the south where it turns to the east. The Guaso unit exhibits similar thinning trends to the southeast and southwest along the eastern and western Buil Syncline limbs as the Morillo and Ainsa units. The Guaso unit thins to less than 50 m on the southern part of the Mediano Anticline.

4.5.3 Dip Contoured Surfaces

Dip contours were created for the base-Ainsa, base-Morillo, base-Guaso, and base-Sobrarbe surfaces to highlight changes in surface dip. Dip contours are shaded on the surfaces and are overlain with structure contours (Figures 4.40 to 4.43). The shaded dip contours a reflect a clear shallowing of limb dip upwards in the basin-fill succession, with the base-Ainsa surface (Fig. 4.40) showing the greatest structural dip and the base-Guaso and base-Sobrarbe surfaces showing the shallowest structural dip. Additionally, anomalously high dip values ranging from 45 to 55° are observed on the base-Ainsa and base-Morillo surfaces along the western Buil Syncline limb (Figures 4.40 and 4.41).

4.5.4 Shift in System Axes

The construction of each system axis using a dip-vector projection 3-D model construction methodology (as described in section 3.3) constrains the position of each syn-growth system axis in three dimensions. Prior to surface construction, this shift was apparent in the 3-D model by comparing the plan-view pattern of the constructed axes

(Fig. 4.44). The axes show a south-southwest shift with each younger system. The shift between the Ainsa and Morillo system axes, on the scale of a few hundred meters, is relatively minor compared to the shift that occurs between the Morillo and Guaso systems, which can exceed 1.5 km along the axes' strike. The axis shift between the Guaso and Sobrarbe systems is also less than the Morillo-Guaso system shift, not exceeding 1 km along the axes' strike.

This shift is also apparent in the 3-D structural surfaces (Figures 4.45 and 4.46). Figure 4.45 compares the deepest portion of the base-Ainsa system axis (marked by the star) to the overlying base-Morillo, base-Guaso, and base-Sobrarbe surfaces. Using the star as a reference point, the southwest shift in axes of the 3-D structural surfaces is clearly visualized.

The deepest point of each system axis was compared in the context of magnitude and direction of shift (Fig. 4.47). The shift between the deepest point of the base-Ainsa axis to the base-Morillo axis is 700 m at 214°. The shift between the deepest point of the base-Morillo axis the base-Guaso axis is 1400 m at 201°. The shift between the deepest point of the base-Guaso and the base-Morillo axis is 1400 m 182°. The overall trend in shift direction rotates from a south-southwest azimuth to a more north-south azimuth with each successive system.

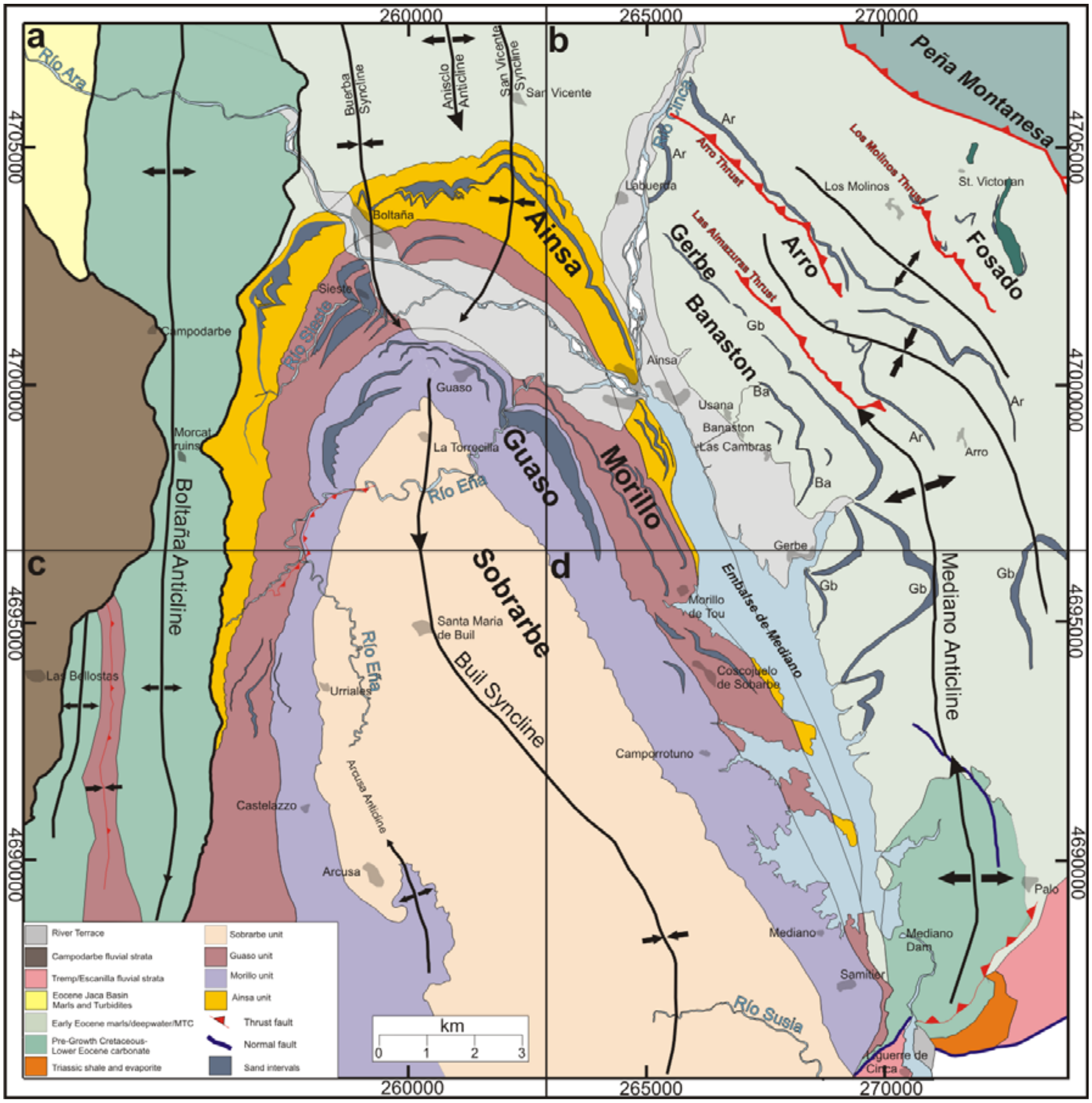

Figure 4.1: Geologic map of the Ainsa Basin. Sand intervals are labeled as follows: Ar: Arro sand intervals, Gb: Gerbe sand intervals, Ba: Banaston sand intervals. The four quadrants (a,b,c, and d) are presented in figures 4.1a, 4.1b, 4.1c, and 4.1d.

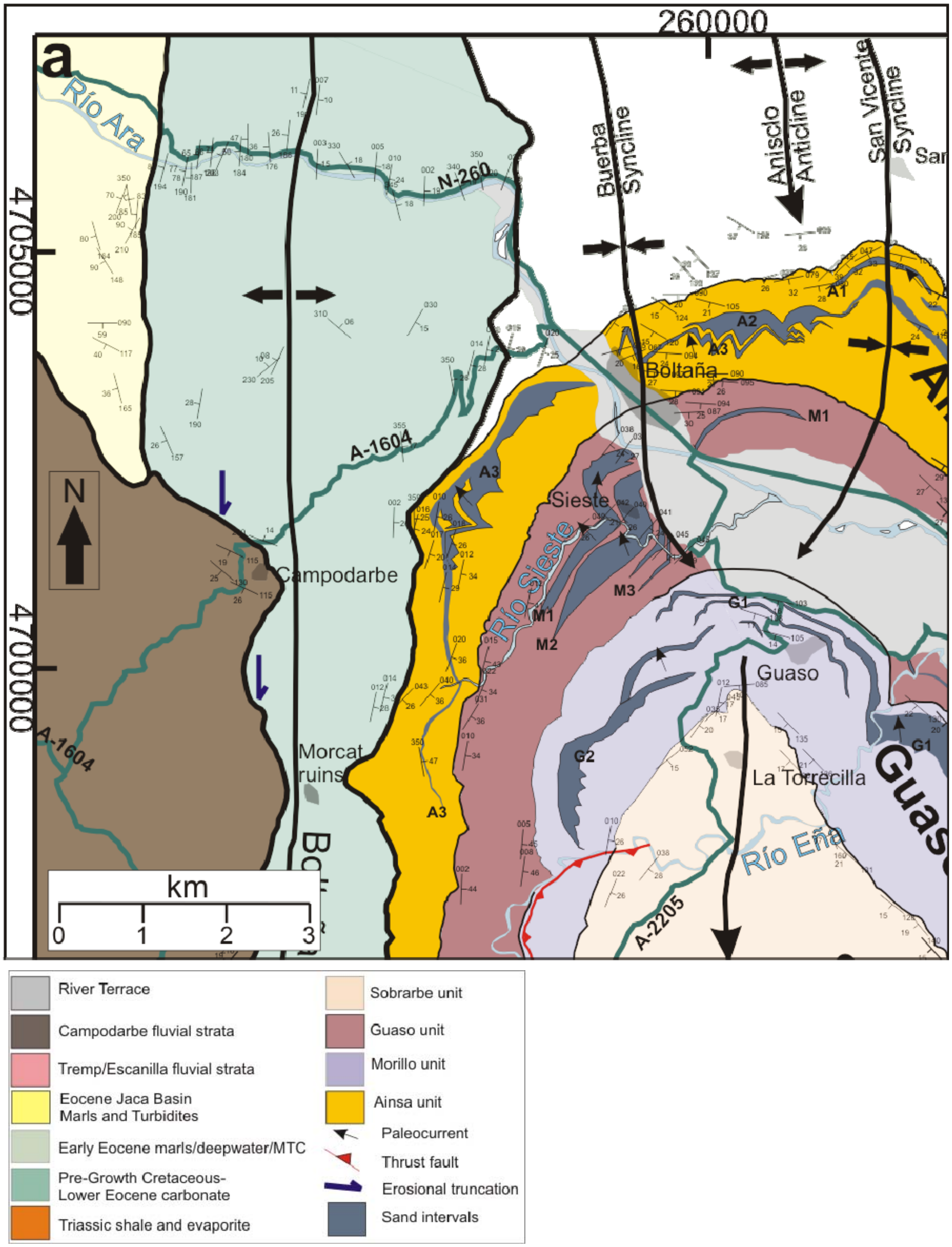

Figure 4.1a: Northwest quadrant of the geologic map of the Ainsa Basin. Sand intervals are labeled as follows: A: Ainsa sand intervals, M: Morillo sand intervals, G: Guaso sand intervals.

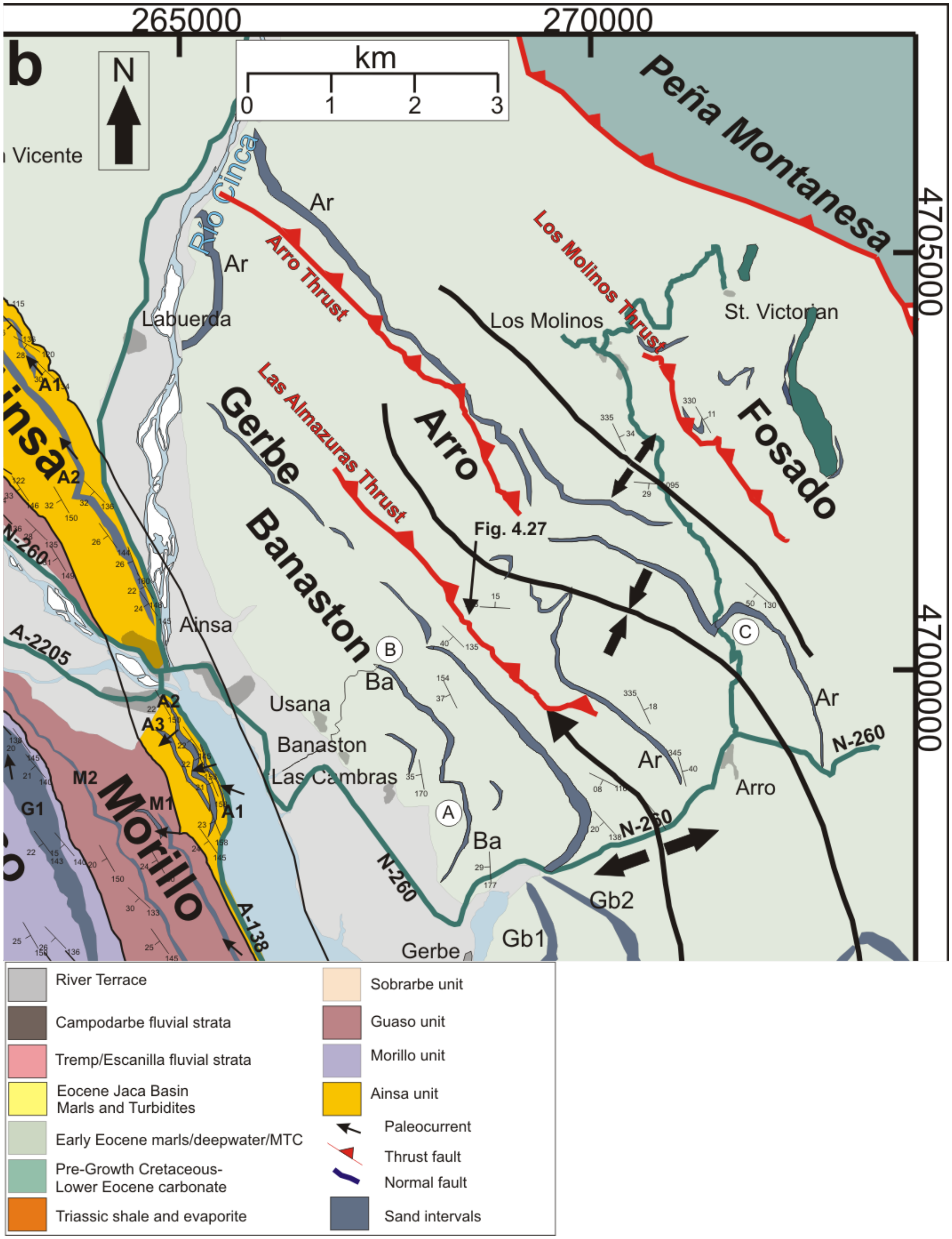

Figure 4.1b: Northeast quadrant of the geologic map of the Ainsa Basin. Sand intervals are labeled as follows: Ar: Arro sand intervals, Gb: Gerbe sand intervals, Ba: Banaston sand intervals, A: Ainsa sand intervals, M: Morillo sand intervals, G: Guaso sand intervals. Letters A-C mark references in the text.

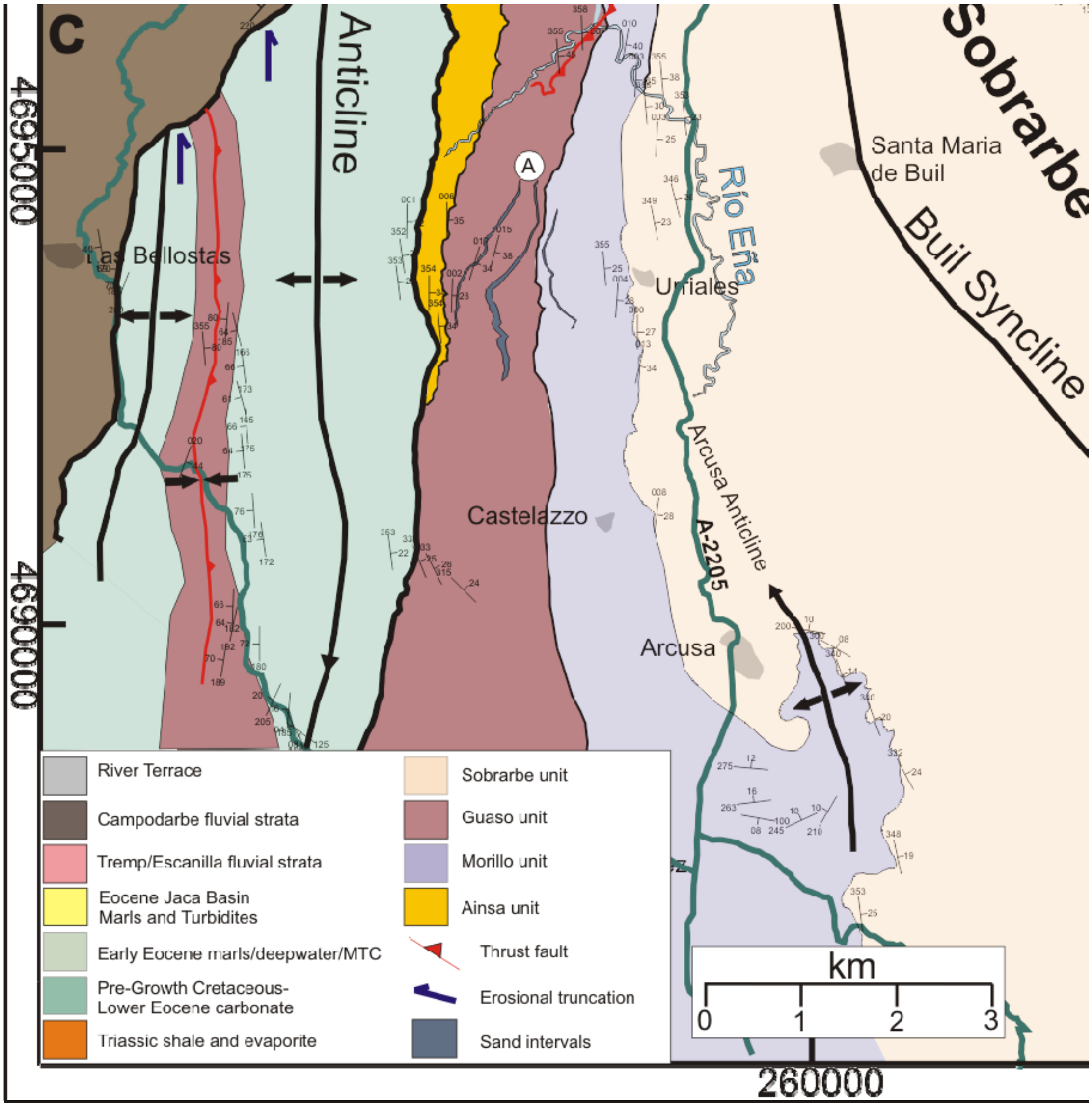

Figure 4.1c: Southwest quadrant of the geologic map of the Ainsa Basin. Letter A marks a reference in the text.

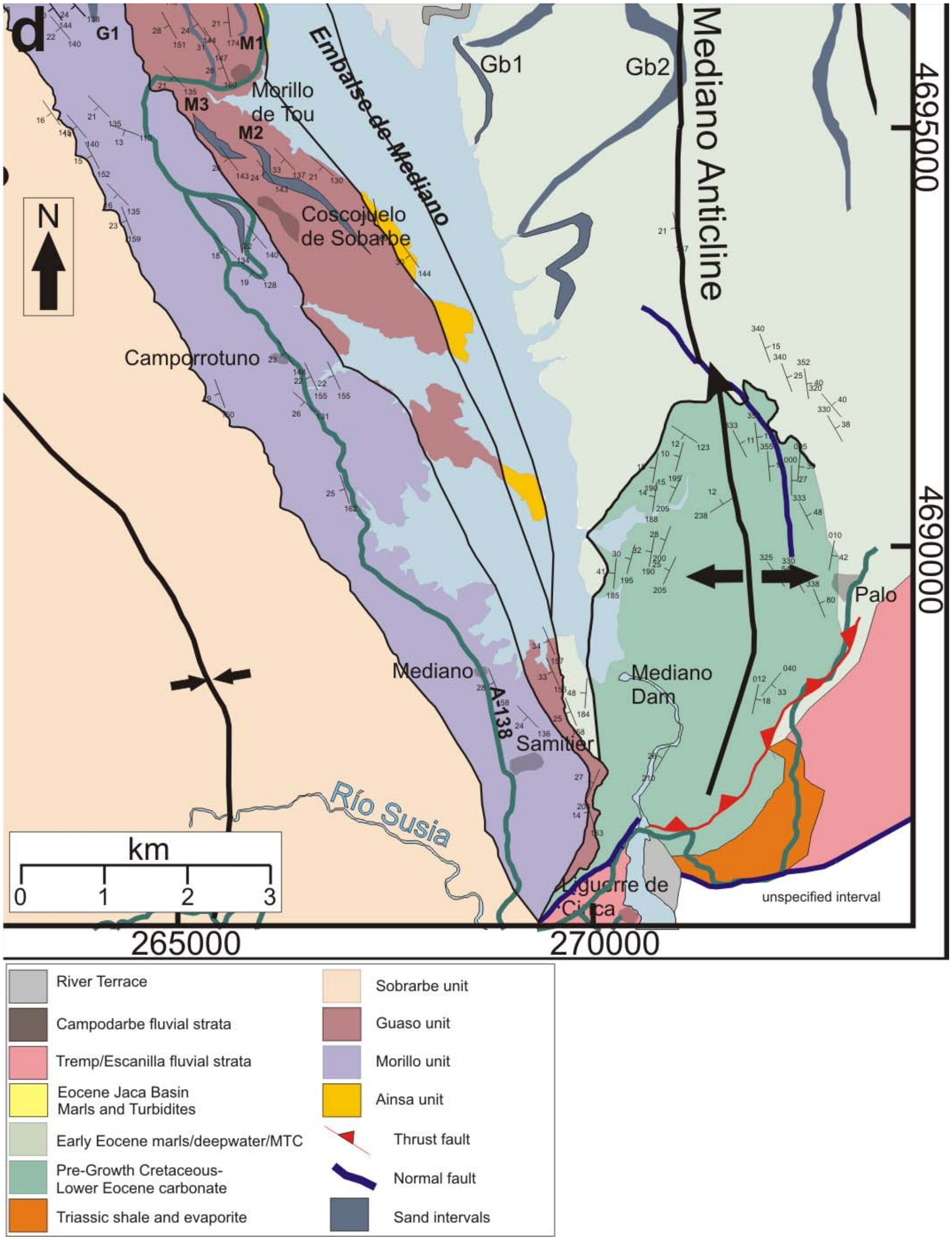

Figure 4.1d: Southeast quadrant of the geologic map of the Ainsa Basin. Sand intervals are labeled as follows: Ar: Arro sand intervals, Gb: Gerbe sand intervals A: Ainsa sand intervals, M: Morillo sand intervals, G: Guaso sand intervals.

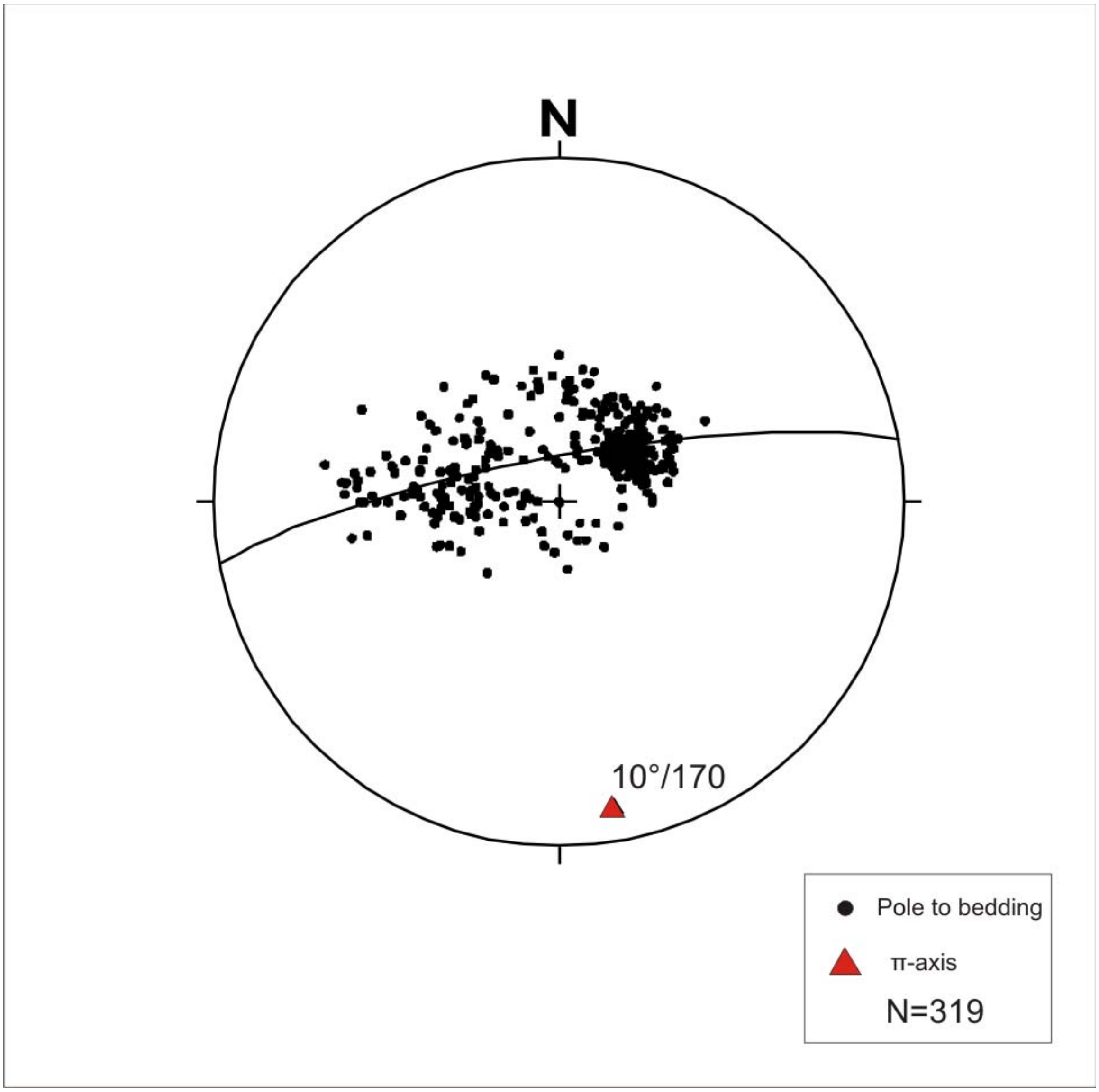

Figure 4.2: π-axis analysis of the Buil Syncline. Data points consist of all syn-growth strata measurements. The data were plotted and fold axis calculated using StereoNet© (Geological Software).

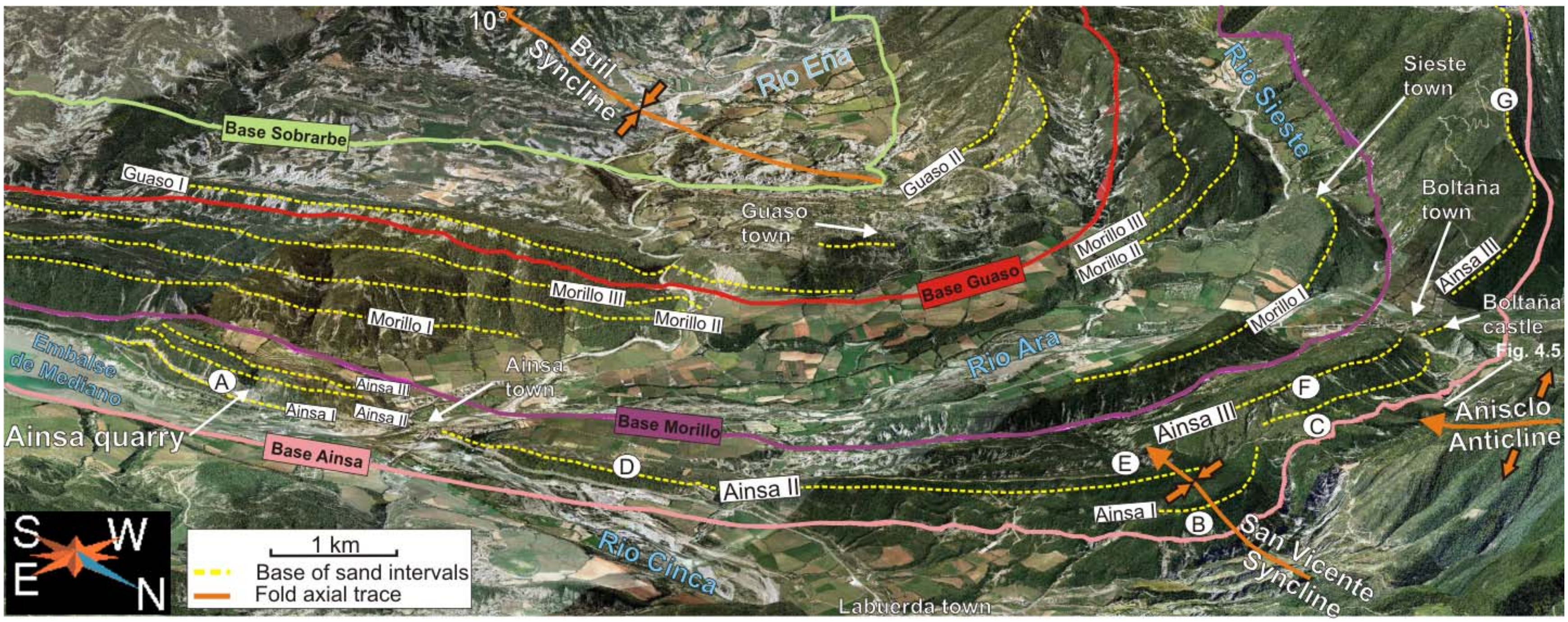

Fig. 4.3: Photodraped digital elevation model (DEM) forms the 3-D structural model showing the location and extent of sand interval outcrop, condensed sections, and fold axes through the basin axis. Letters A-G mark references in the text.

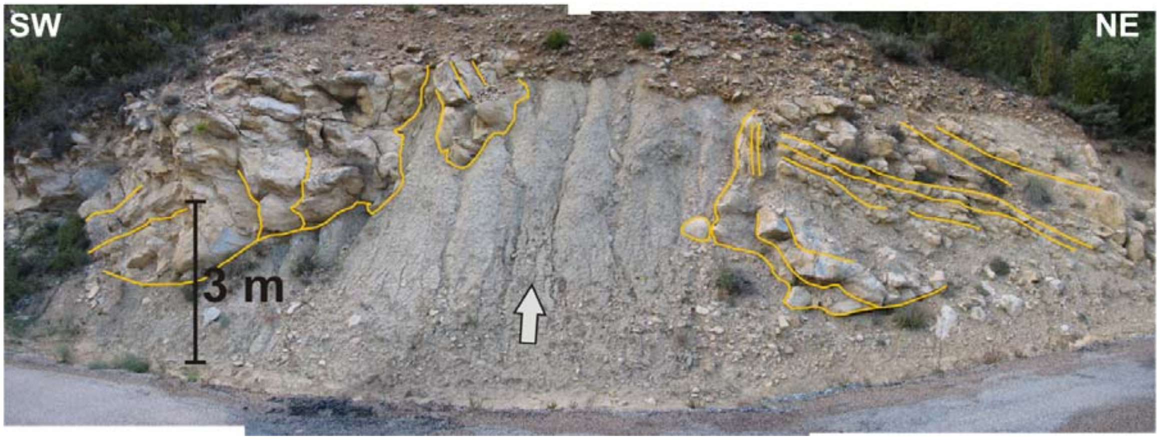

Figure 4.4: Clastic intrusion located within the Ainsa stratigraphic unit near Rio Sieste (see Fig. 4.6 for location).

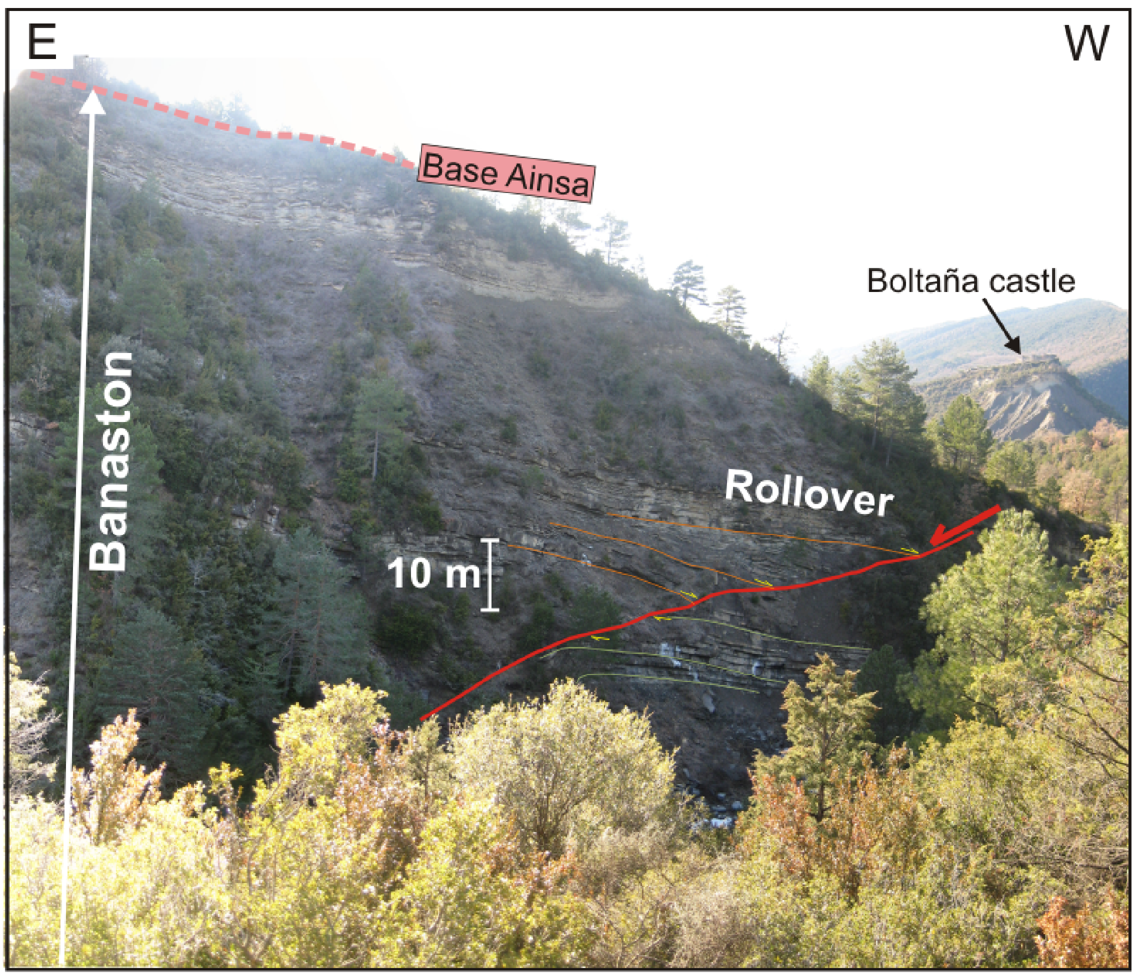

Figure 4.5: Growth fault within an upper Banaston sand. The base-Ainsa condensed section directly overlies the pictured ledge (see Fig. 4.6 for location).

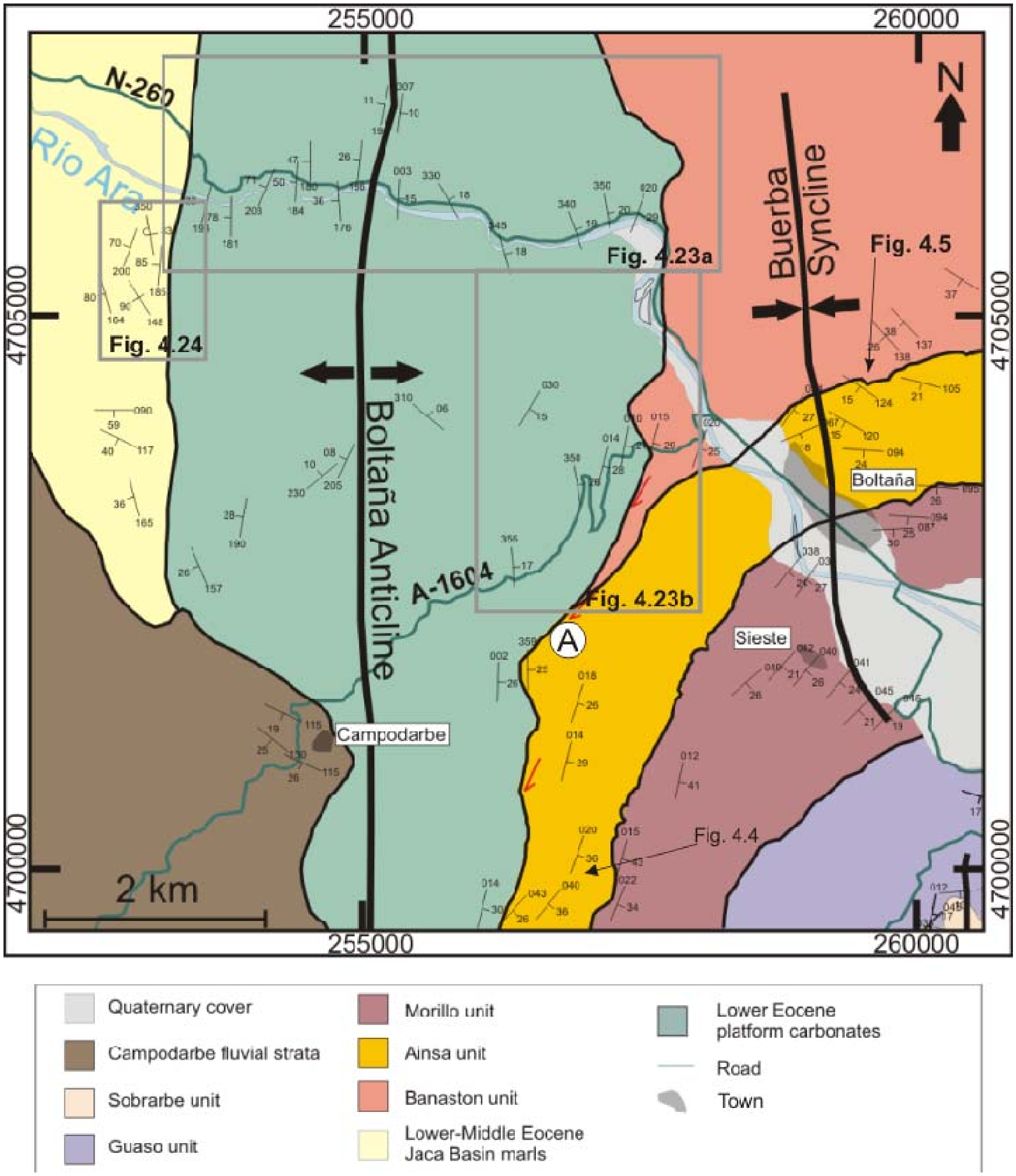

Figure 4.6: Detailed map of the northern sector of the Boltaña Anticline and its relationship to the syn-tectonic basin-fill. Letter A marks a reference in the text.

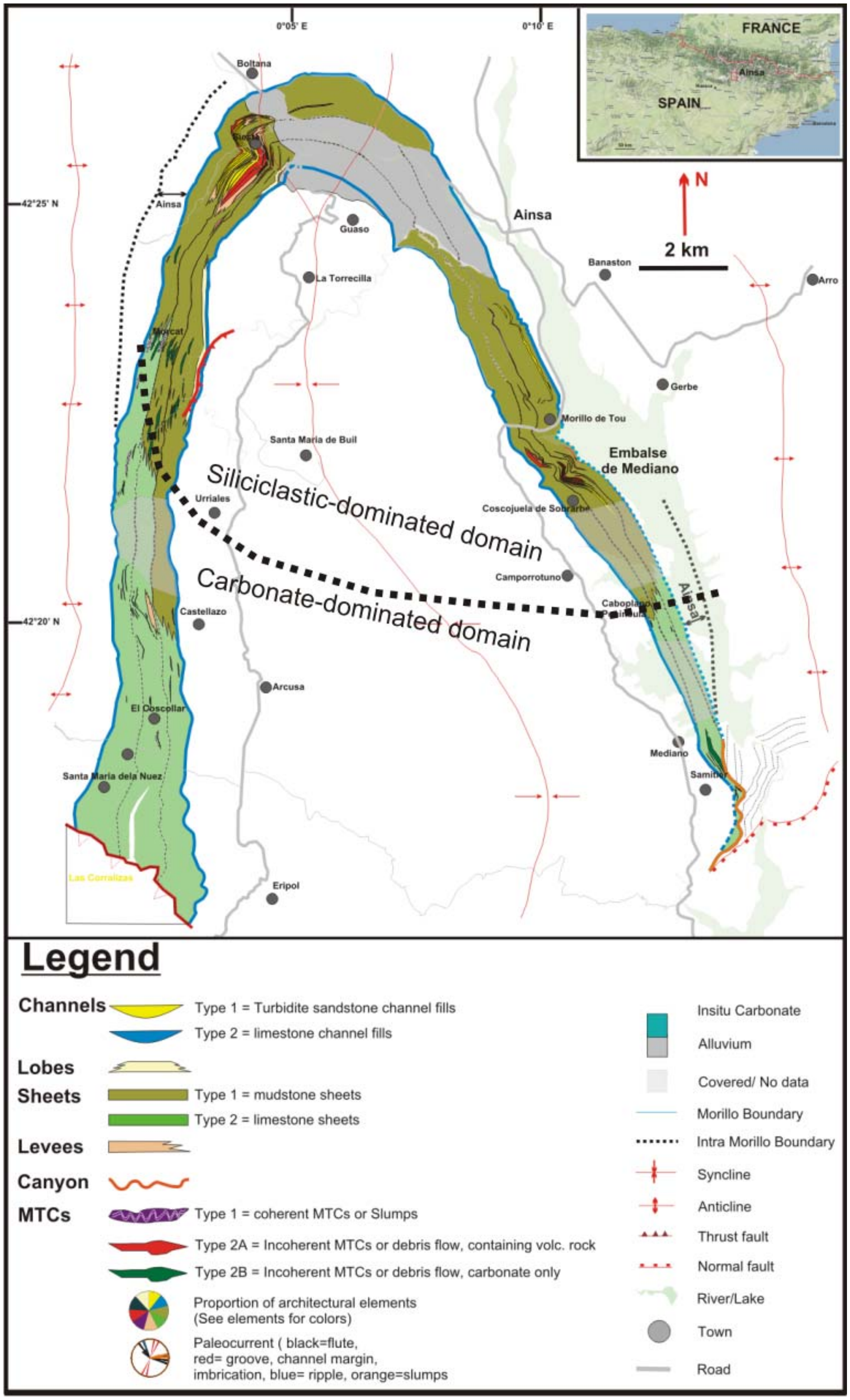

Figure 4.7: Map of architectural elements that comprise the Morillo stratigraphic unit (modified from Setiawan, 2009).

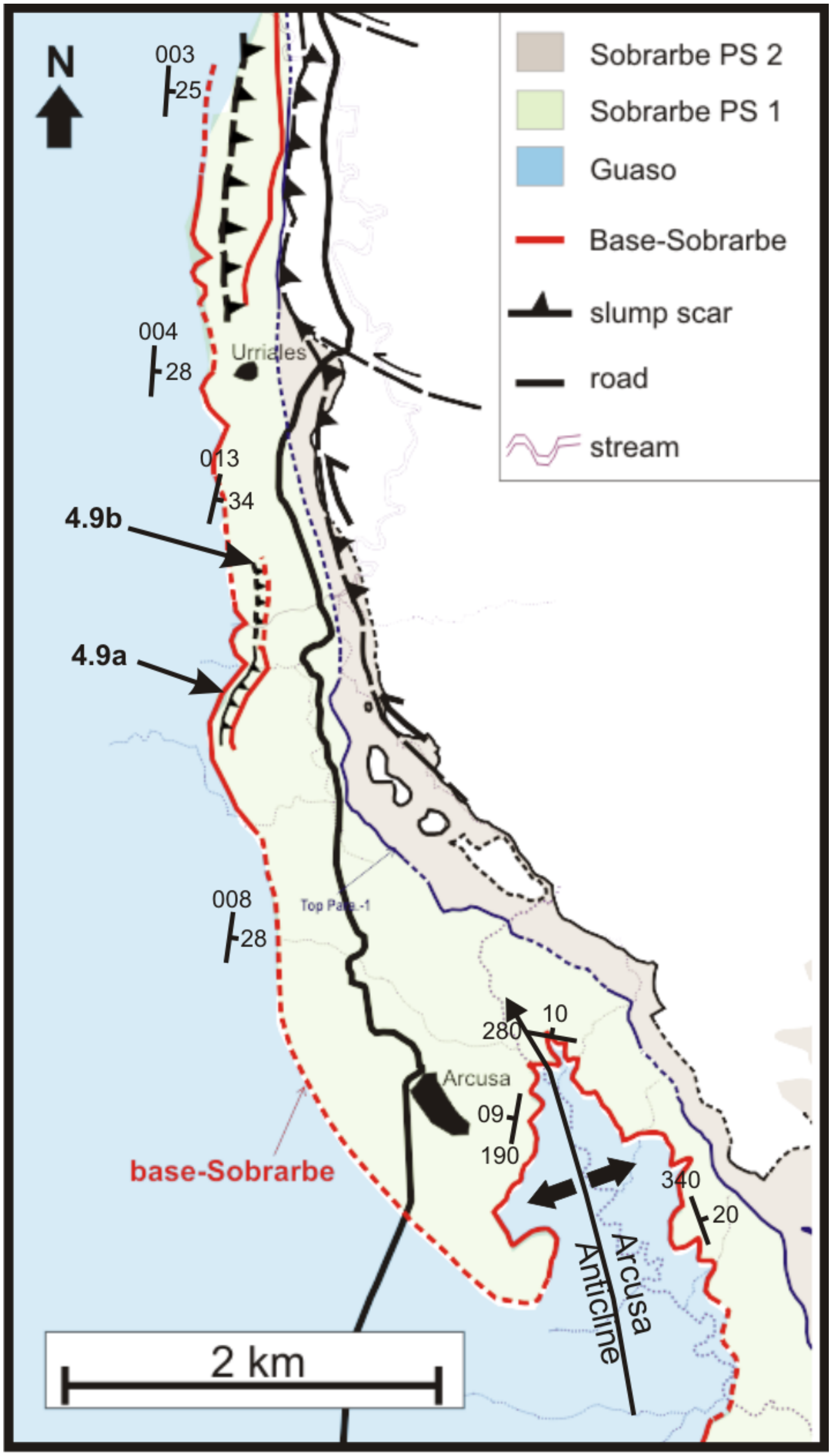

Figure 4.8: Map of the lower Sobrarbe unit and the slumps that occur within the lower Sobrarbe deltaic complex along the unit's western margin (modified from Silalahi, 2009).

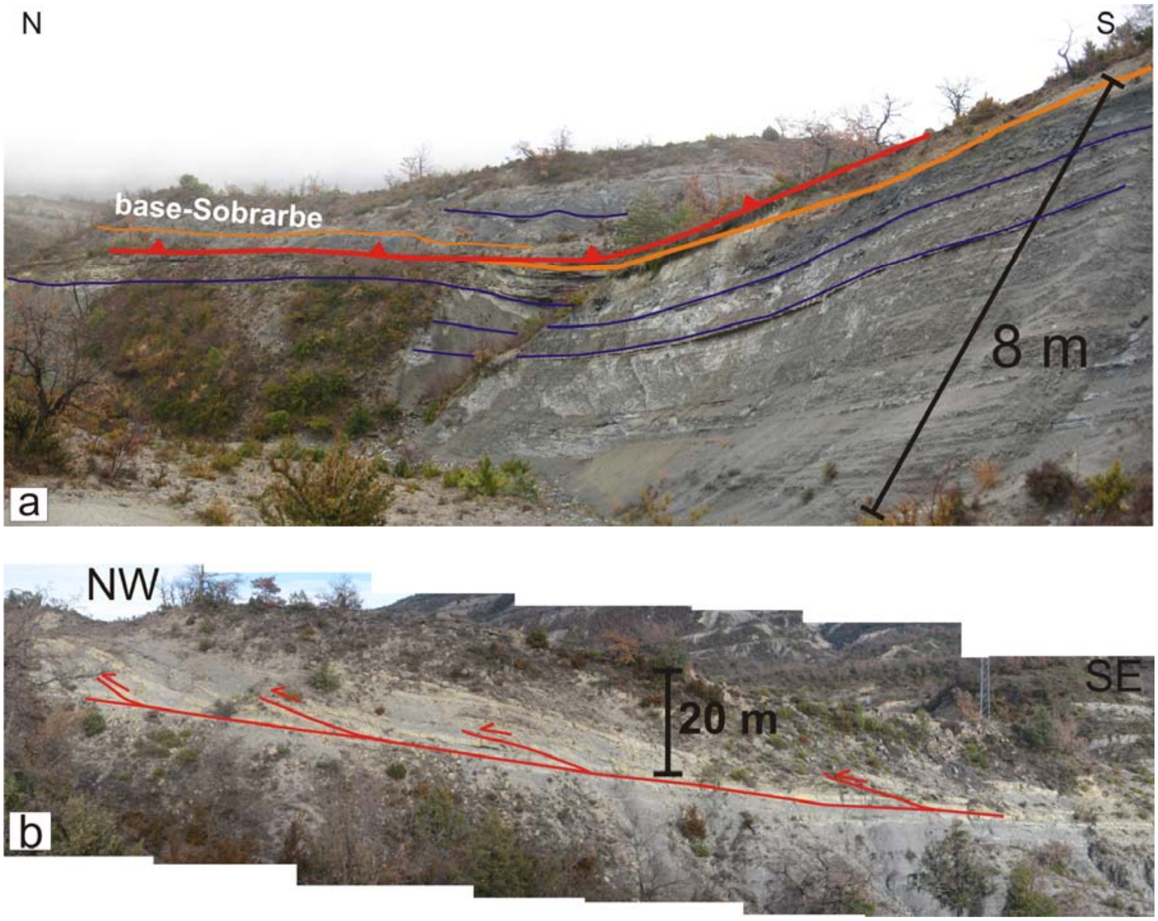

Figure 4.9: Examples of slumps within the lower Sobrarbe stratigraphic unit. a) The base-Sobrarbe condensed section is repeated as the result of a cross-cutting thrust, thickening the unit by approximately 10 m. Transport direction is E to W. b) A series of repeated mudstone beds from the propagation of thrusts from a lower detachment surface (see Fig. 4.8 for locations).

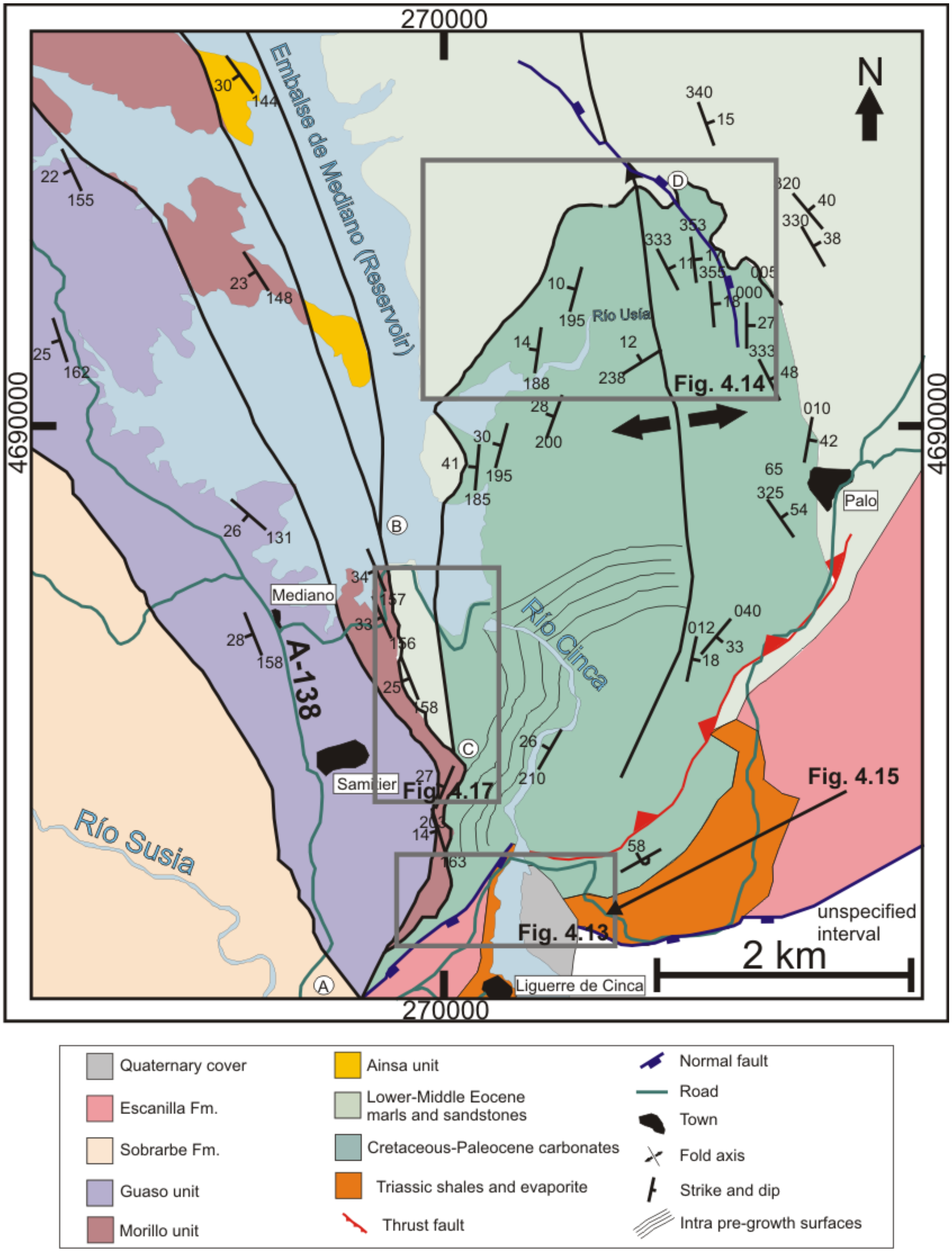

Figure 4.10: Detailed map of the southern Mediano Anticline area. Letters A-D mark references made in the text.

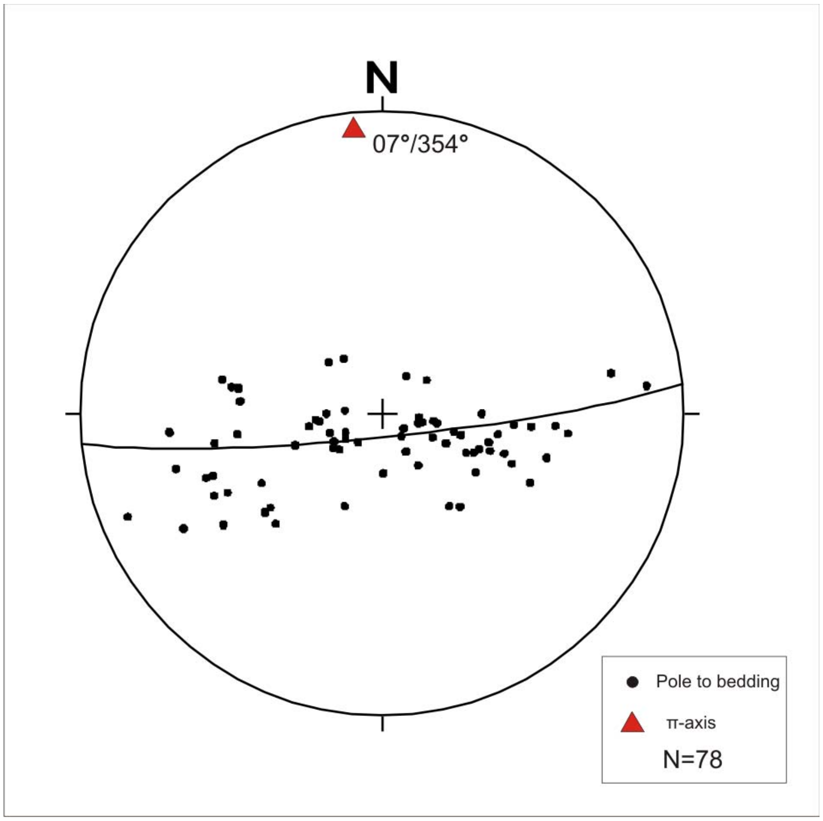

Figure 4.11: π-analysis of Mediano Anticline pre-growth bedding measurements.

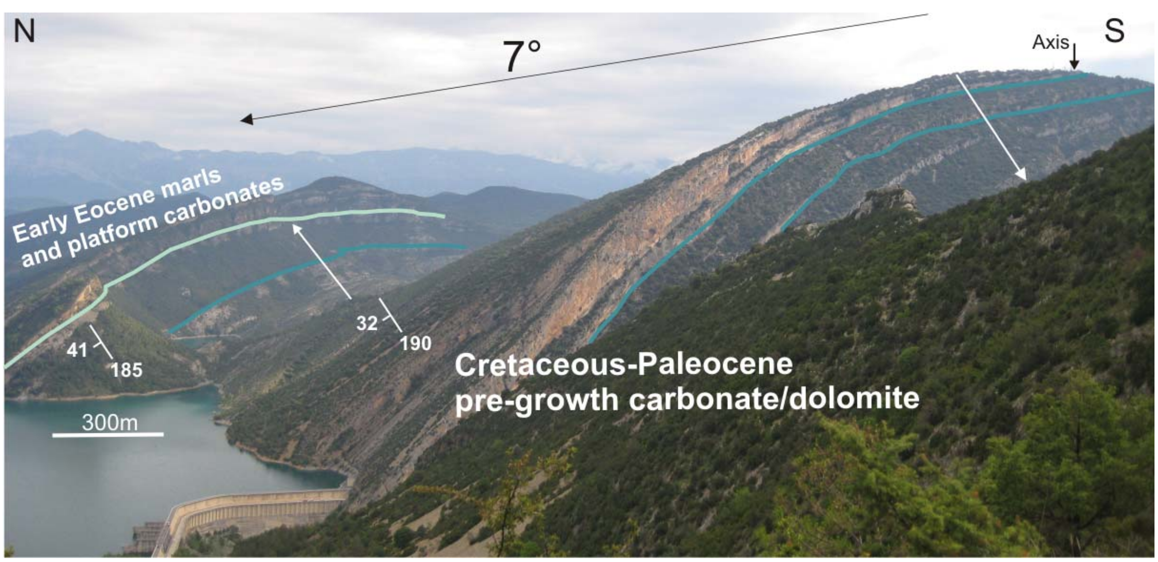

Figure 4.12: Photo displaying western limb and the northward plunge of the Mediano Anticline. Note the northward shallowing of limb dips.

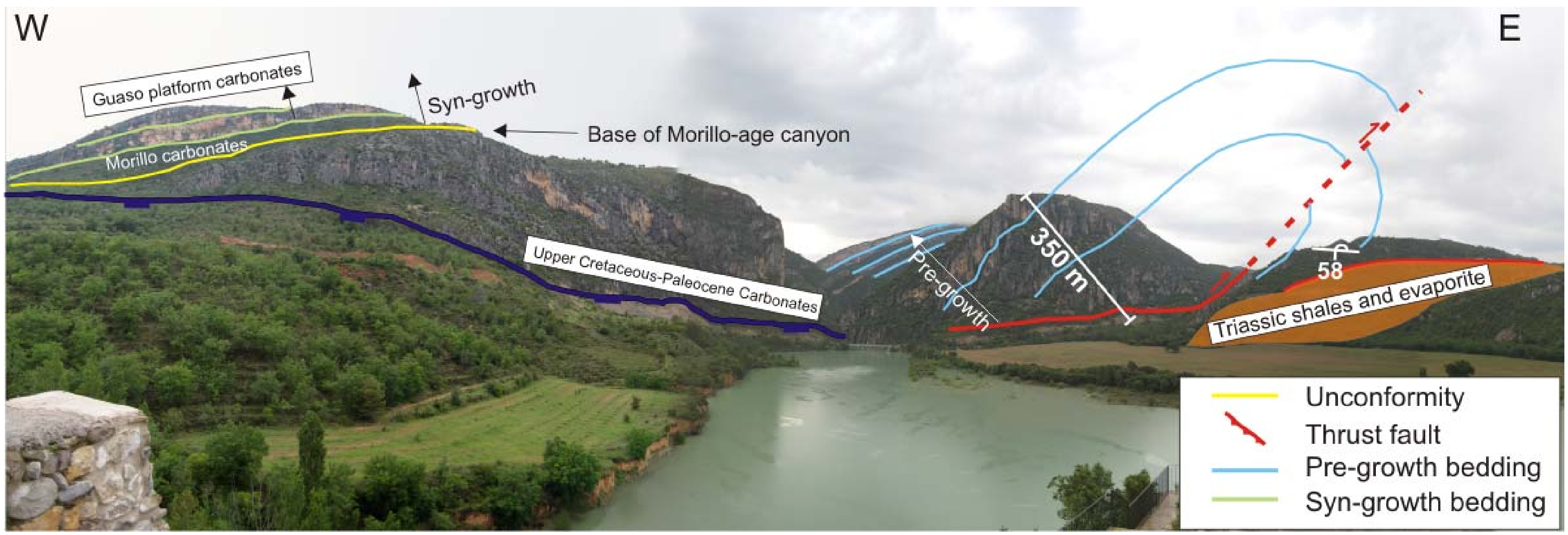

4.13: View toward the north of the southern termination of the Mediano Anticline. The geometry of the fold axis projected into the air is speculative and does not represent the correlation of marker beds across the fault (see Fig. 4.10 for location).

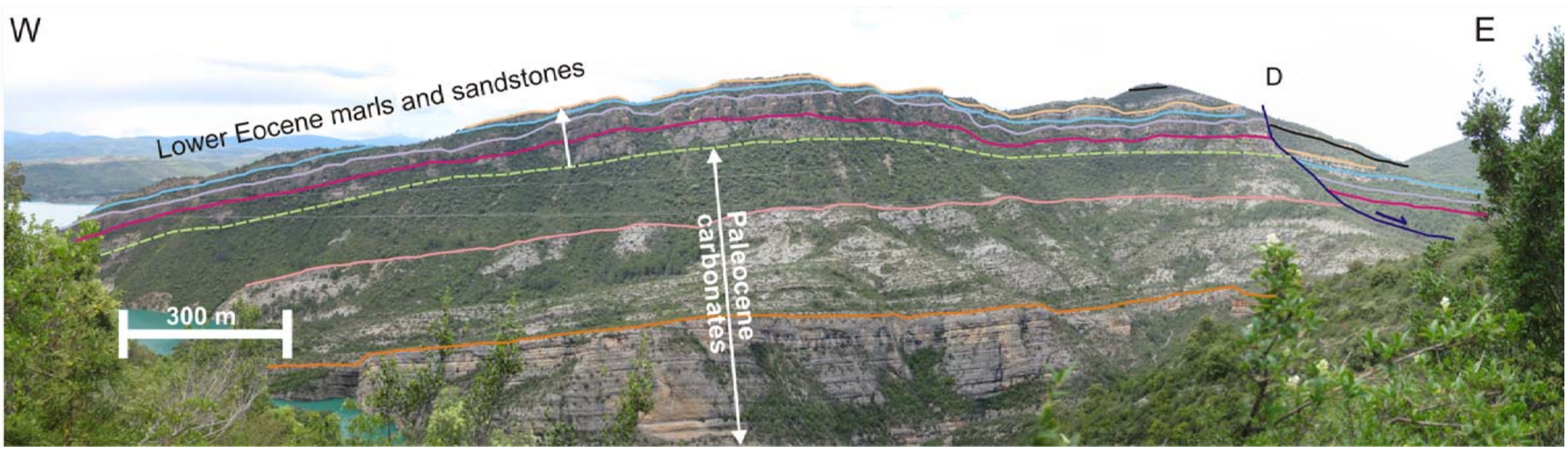

Figure 4.14: Geometry of the Mediano Anticline pre-growth strata in the vicinity of the Rio Usia. Note the open fold geometry and shallow limb dips (see Fig. 4.10 for location).

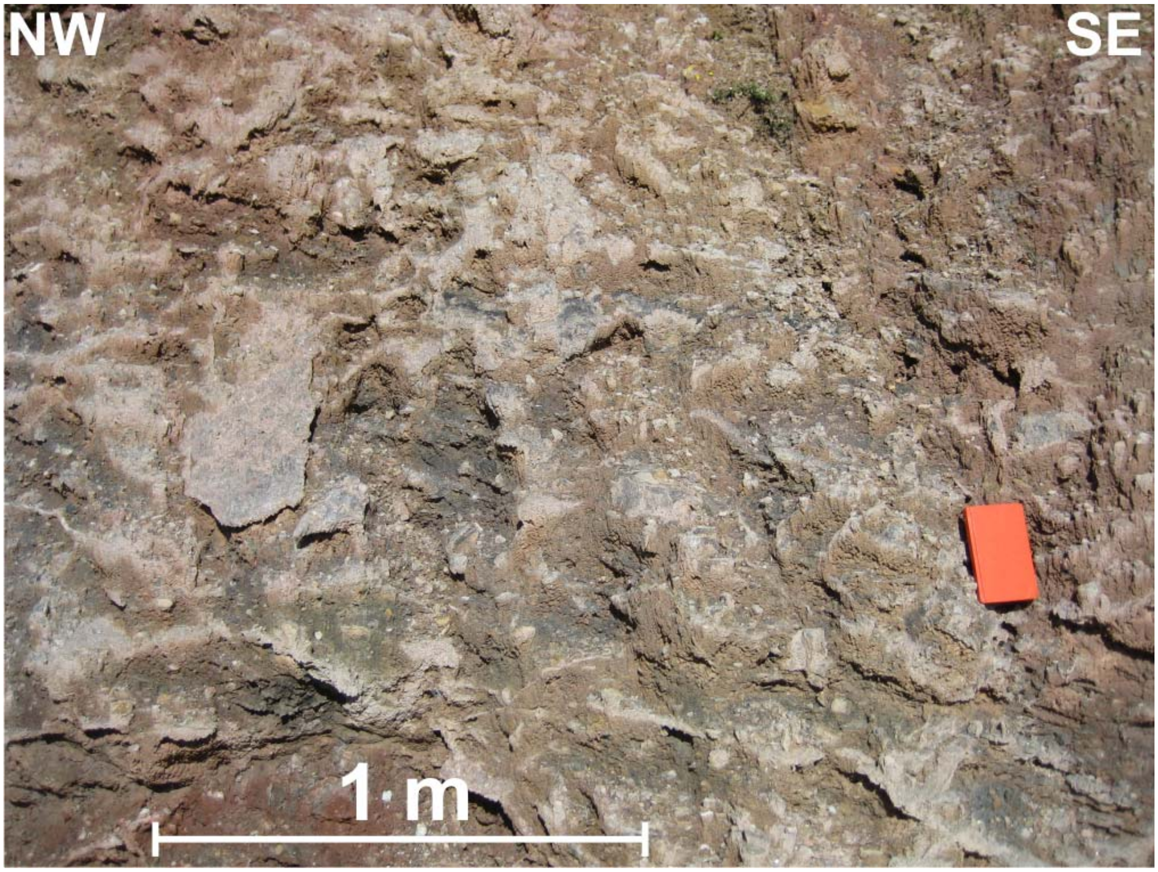

Figure 4.15: Triassic shales and evaporites that comprise the regional detachment. Note lack of bedding and chaotic nature of the strata (see Fig. 4.10 for location).

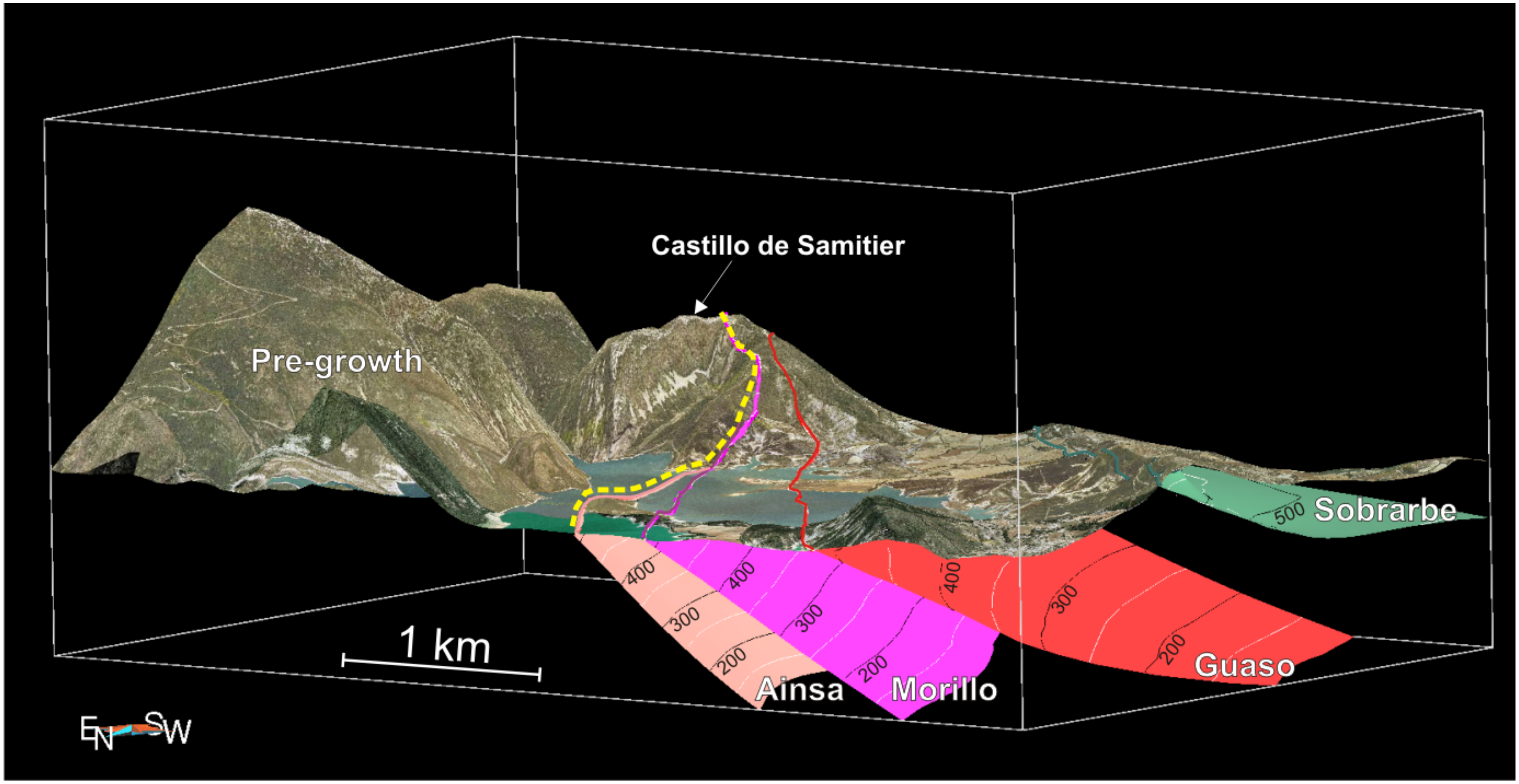

Figure 4.16: Volume extracted from the 3-D structural model showing the relationship between the Ainsa, Morillo, Guaso, and Sobrarbe stratigraphic units and the pre-growth strata of the Mediano Anticline. V.E. = 2x.

Figure 4.17: Submarine canyon that incises into the western limb of the Mediano Anticline in the vicinity of the Mediano Dam (see Fig. 4.10 for location). a) View to the northwest (from Setiawan, 2009). b) View to the south-southwest (modified from Setiawan, 2009). Note position of carbonate blocks.

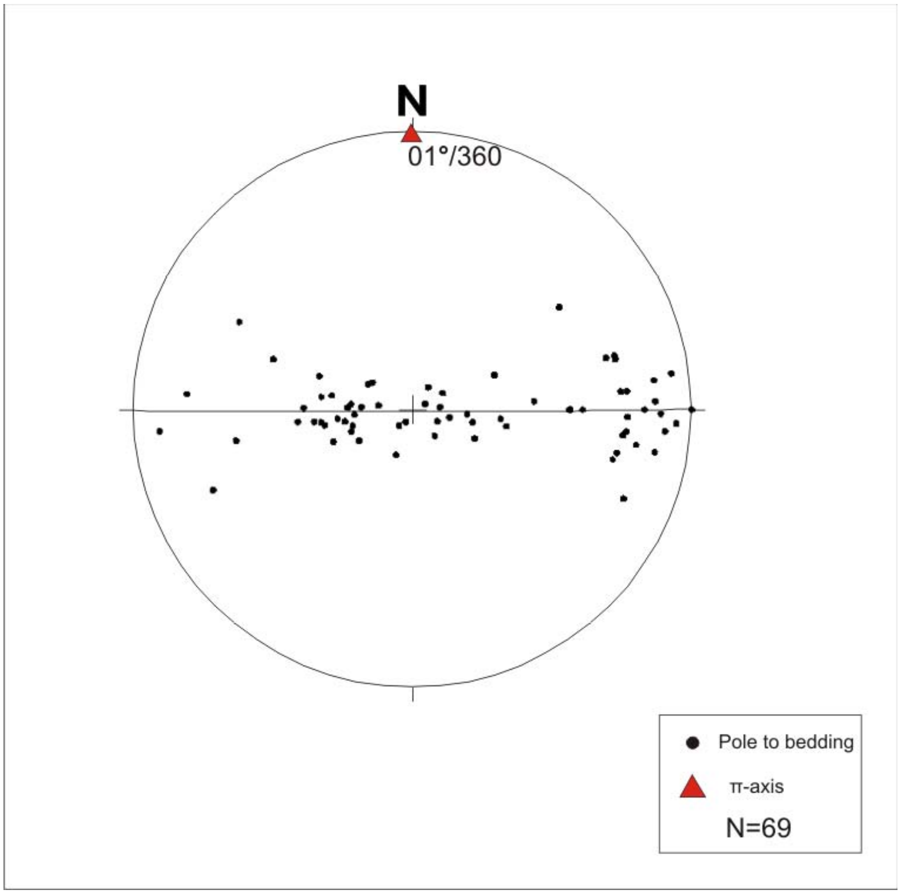

Figure 4.18: π-analysis of Boltaña Anticline pre-growth bedding measurements.

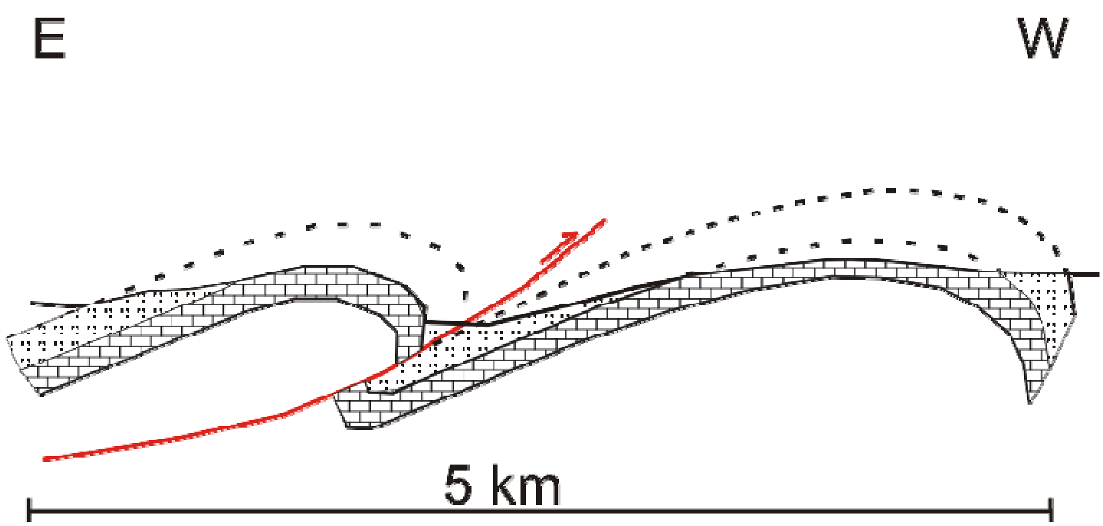

Figure 4.19: Diagram of the Boltaña Anticline in the southern sector. Stippled strata are Morillo limestone sheets. Block strata are Lower Eocene platform carbonates (see Fig. 4.1c or location). No vertical exaggeration.

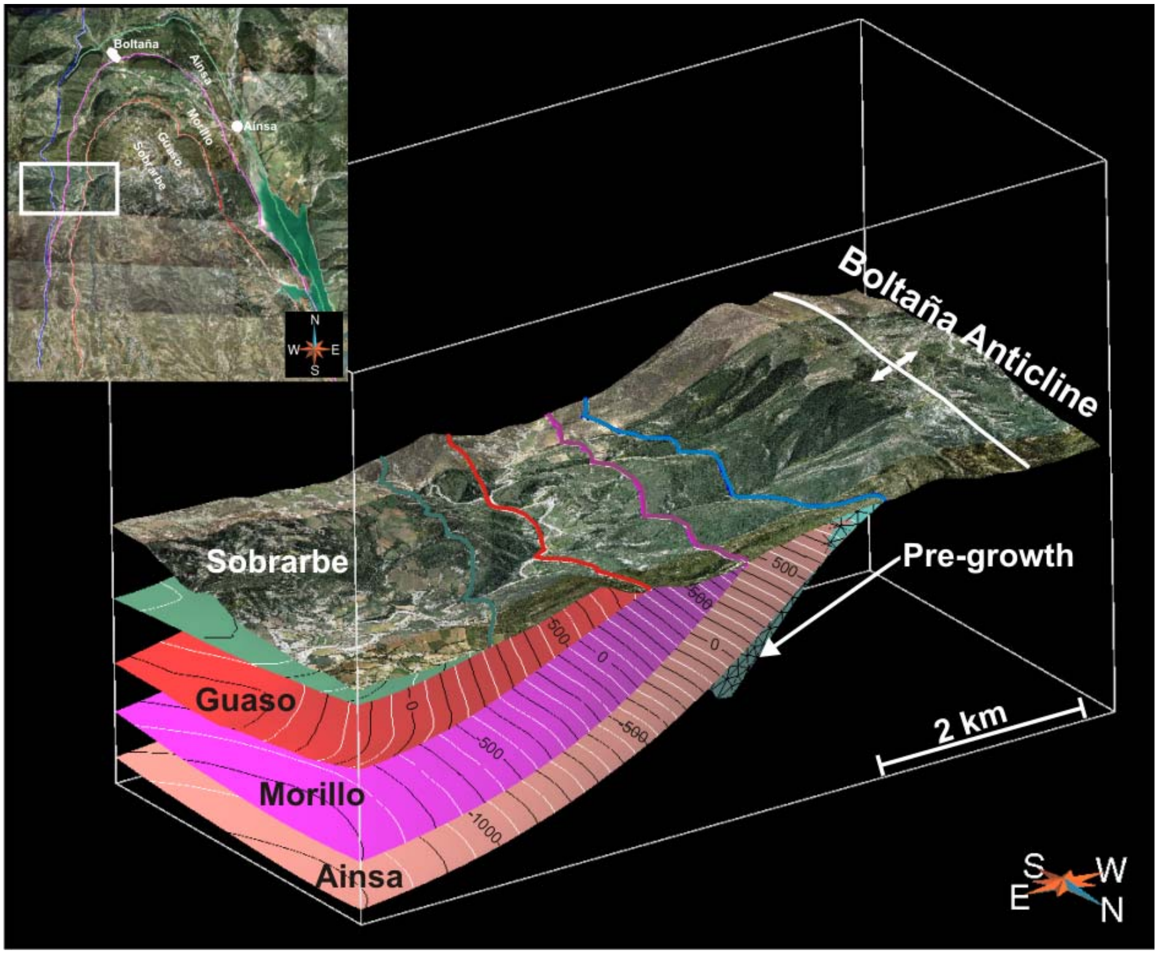

Figure 4.20: Volume extracted from the 3-D structural model showing the relationship between the Ainsa, Morillo, Guaso, and Sobrarbe stratigraphic units and the pre-growth strata of the Boltaña Anticline. Note the thinning to the south and onlap of the base-Ainsa surface onto pre-growth the Lower Eocene carbonates.

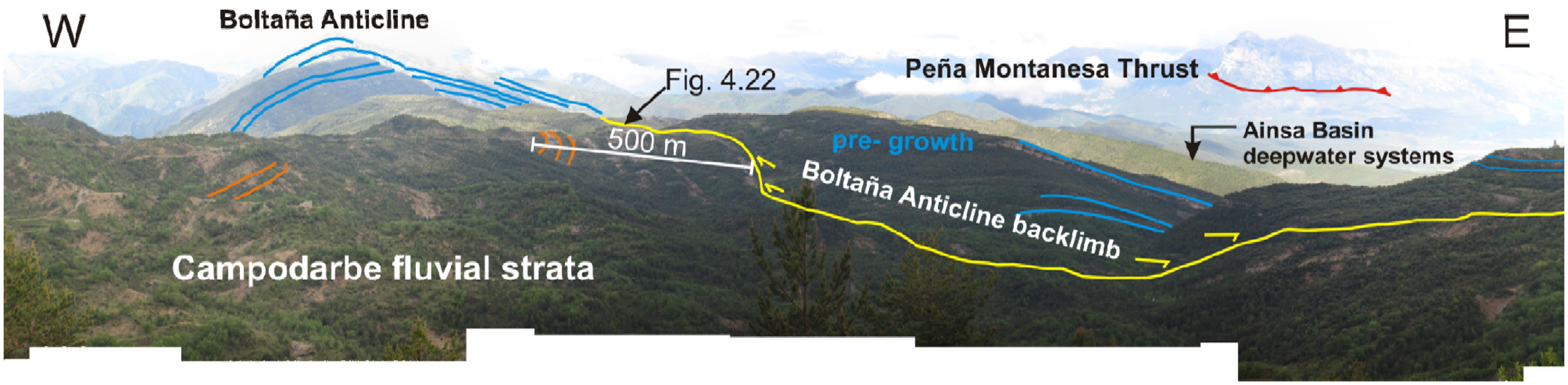

Figure 4.21: A large erosional cut into the fold's western limb that is filled with Late Eocene-Oligocene fluvial strata of the Campodarbe Formation. Yellow arrows mark truncation of pre-growth bedding by the erosional surface.

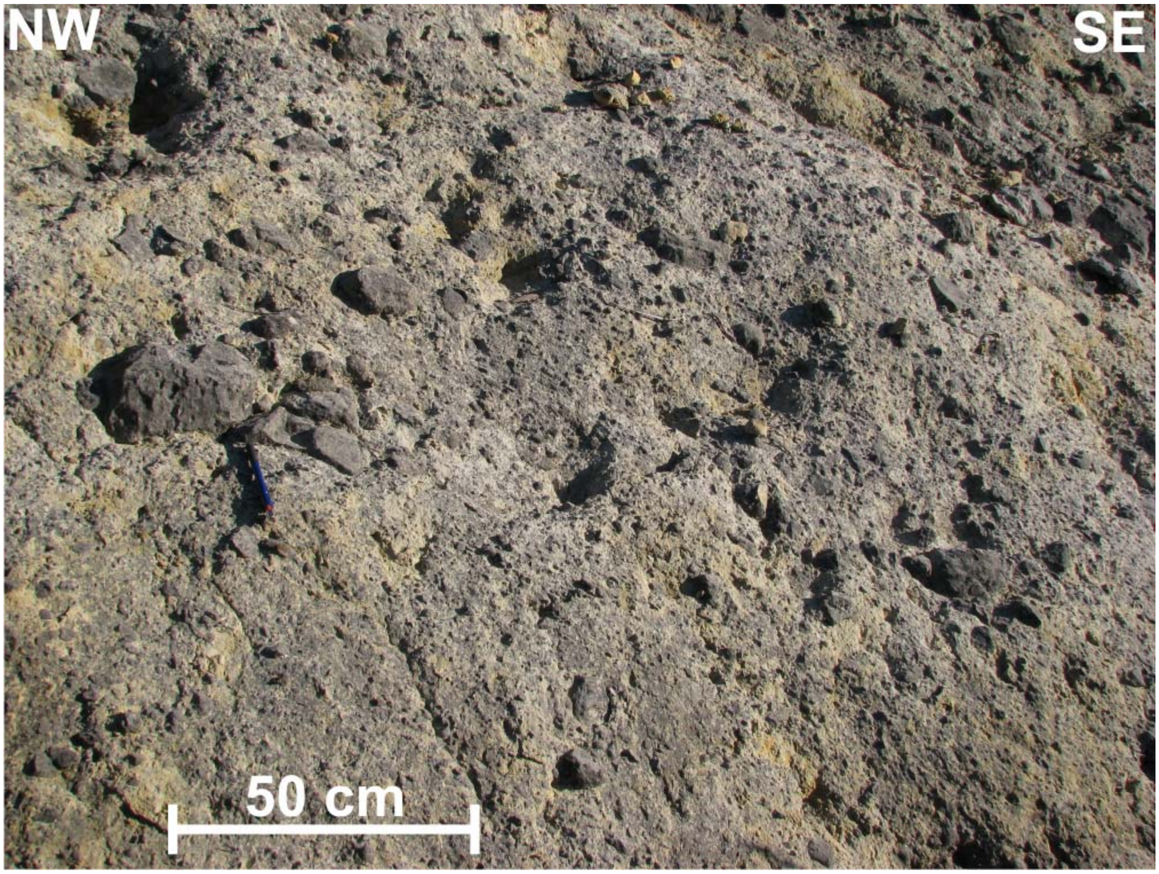

Figure 4.22: Conglomerates rich in cobble-sized carbonate clasts (up to 30 cm in diameter) that crop out along the erosional surface that cuts into the western limb of the Boltaña Anticline.

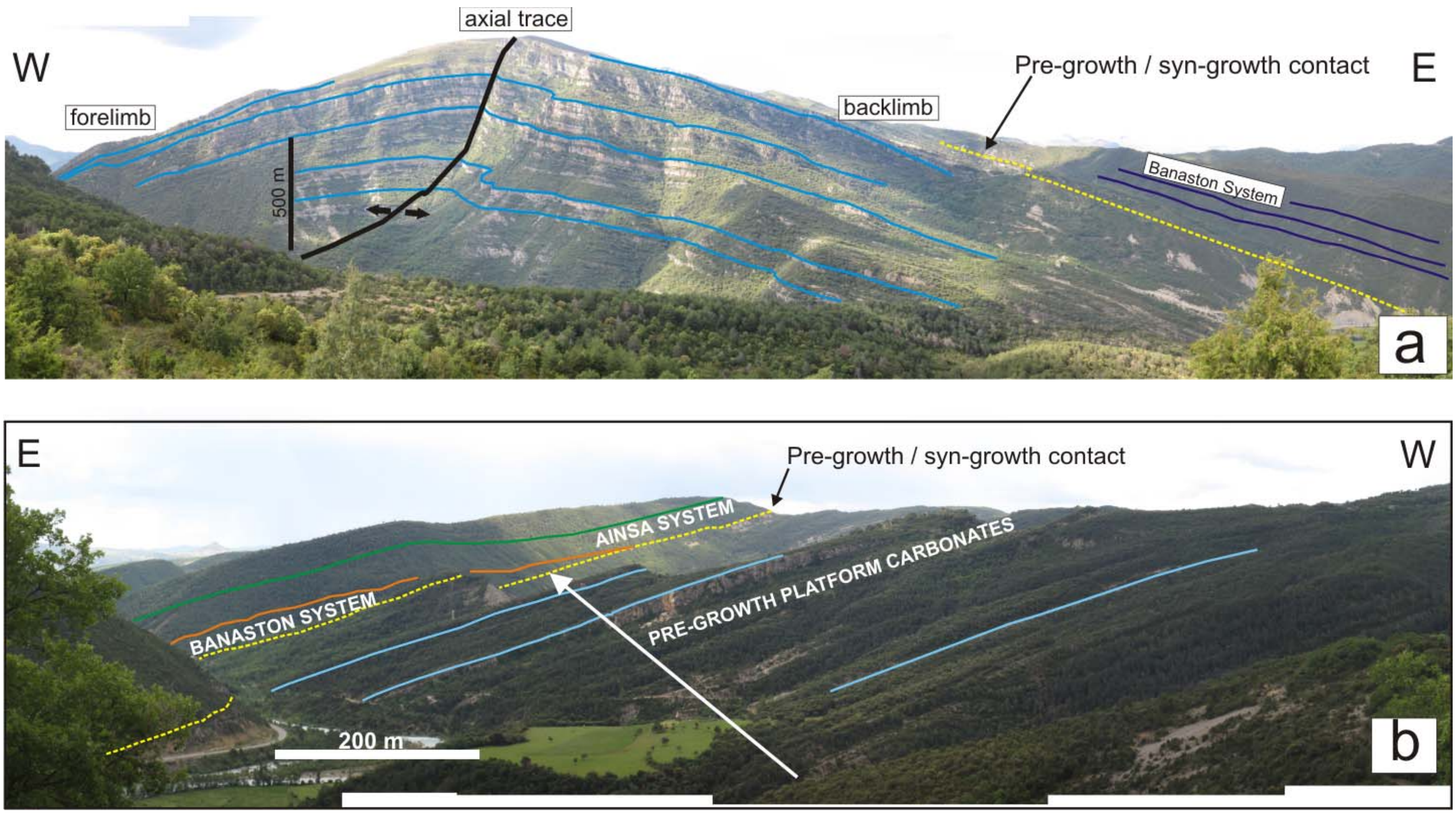

Figure 4.23: Interpreted photopanels of the Boltaña Anticline. a) onlap of the Banaston and Ainsa systems onto the fold's eastern limb. b) Exposure of the pre-growth carbonate within the Boltaña Canyon.

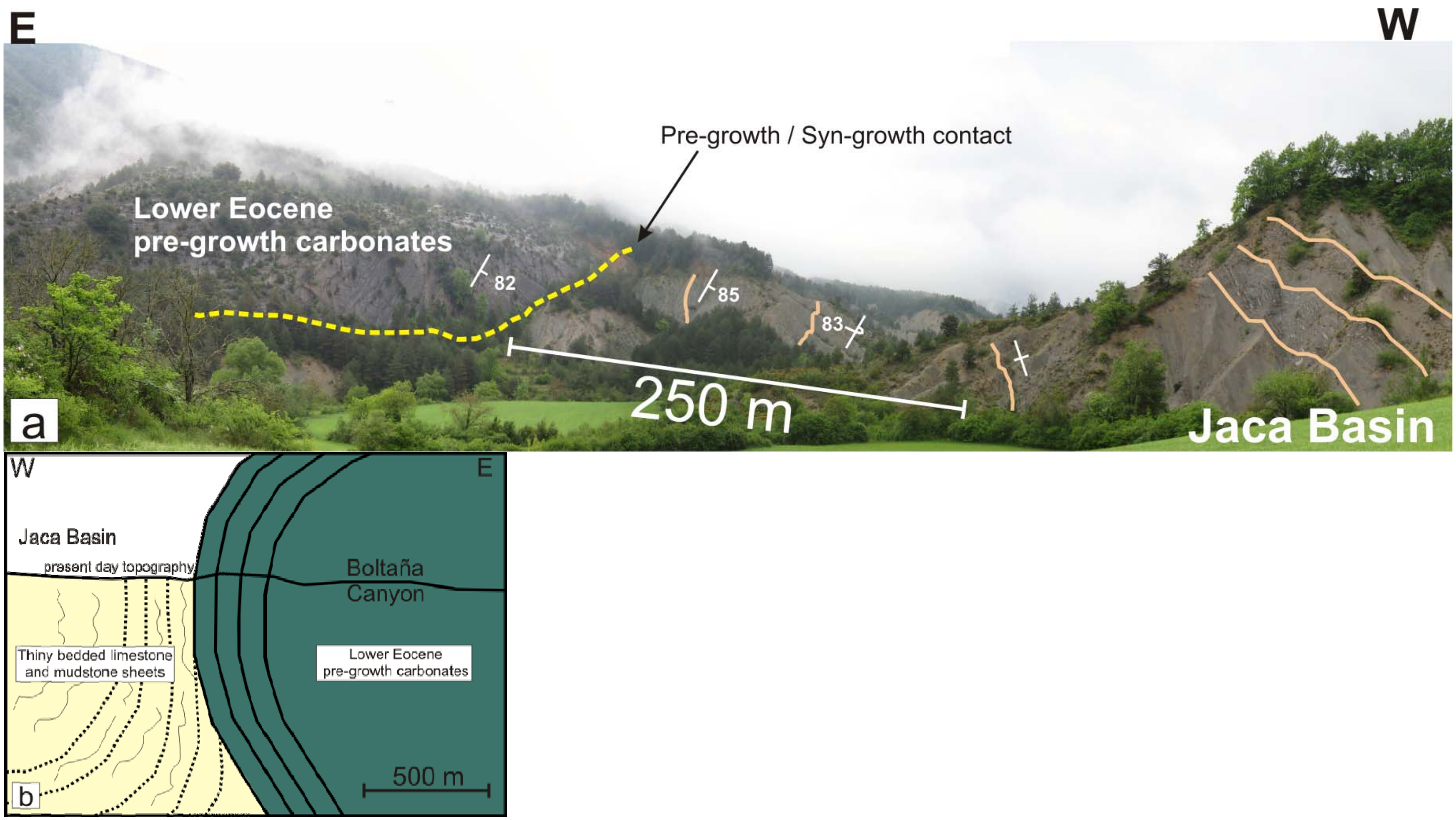

Figure 4.24: Relationship between Lower Eocene pre-growth carbonates and thinly bedded limestone and mudstone sheets of the Jaca Basin in the fold's northern sector. Note the vertical bedding and the undulatory strike within limestone and mudstone sheets to the west (see Fig. 4.6 for location). b) cross section sketch of the pre-growth/syn-growth relationship at this location.

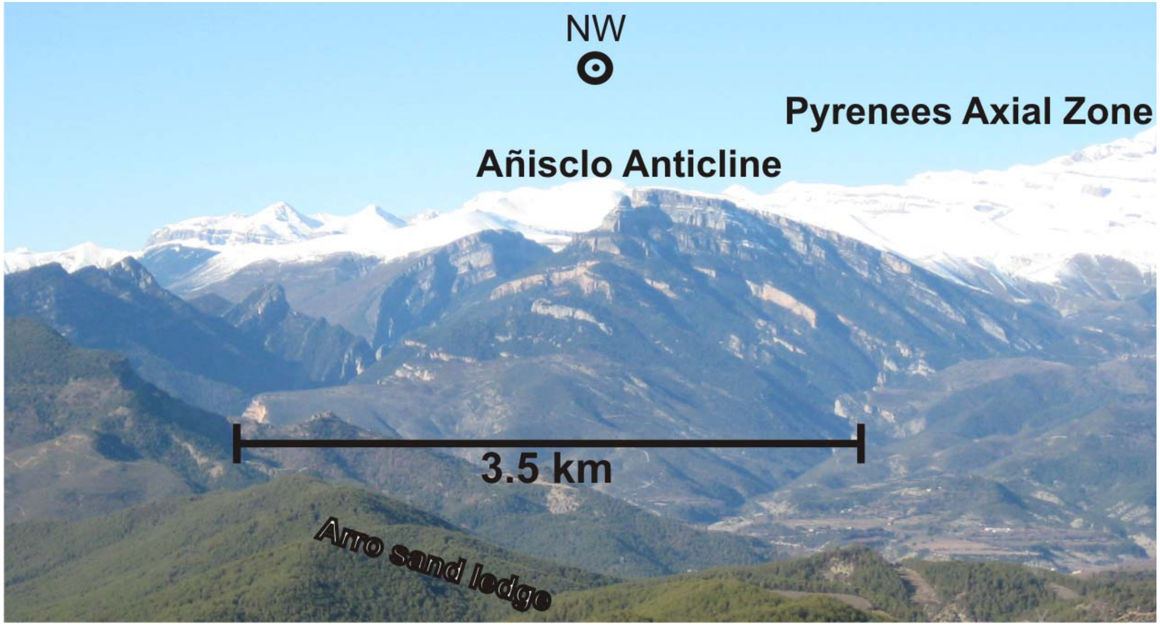

Figure 4.25: Photograph of the Añisclo Anticline. View is to the northwest of the study area.

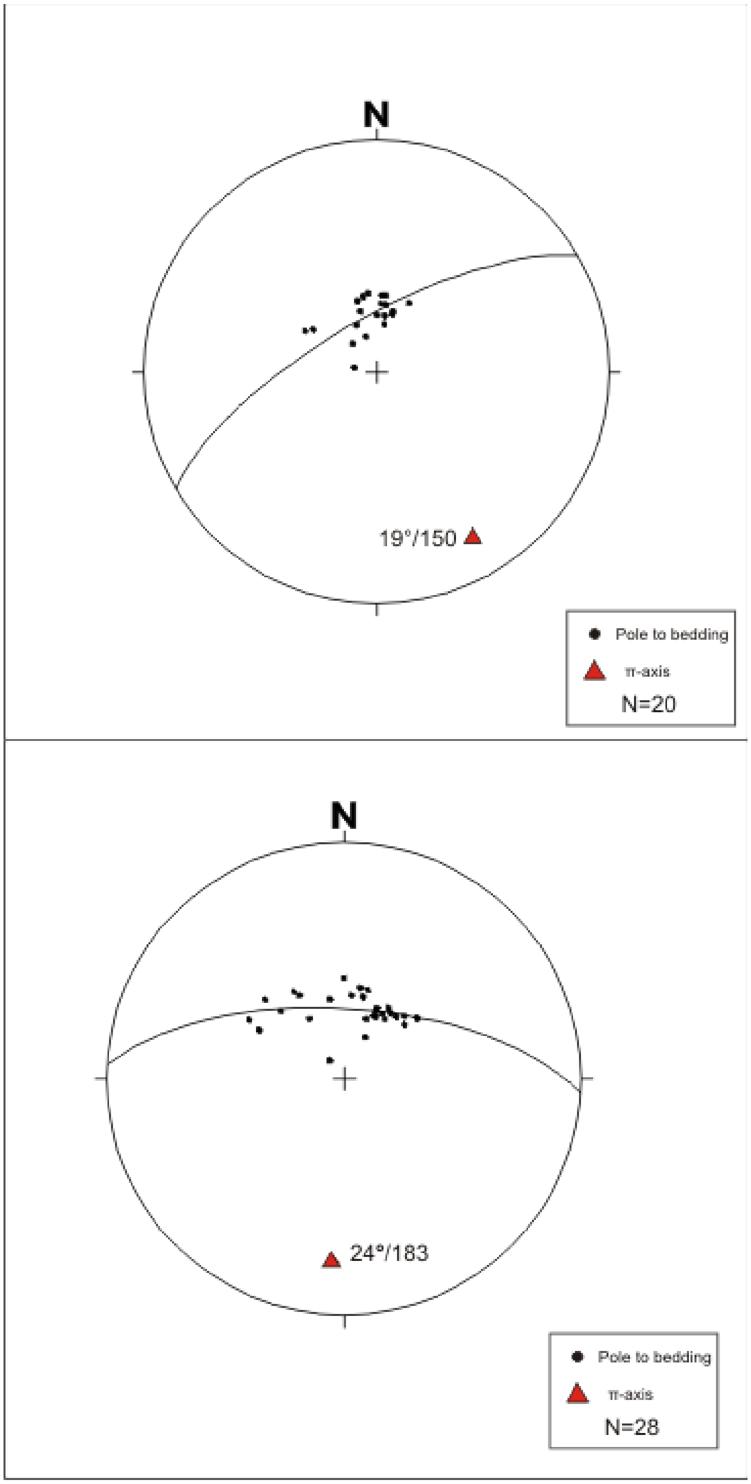

Figure 4.26: π-axis analysis of the Buerba Syncline (a) and the San Vicente Syncline (b). Measurements were acquired within the Ainsa and Banaston stratigraphic units in the northern region of the study area. The data were plotted and fold axes calculated using StereoNet© (Geological Software).

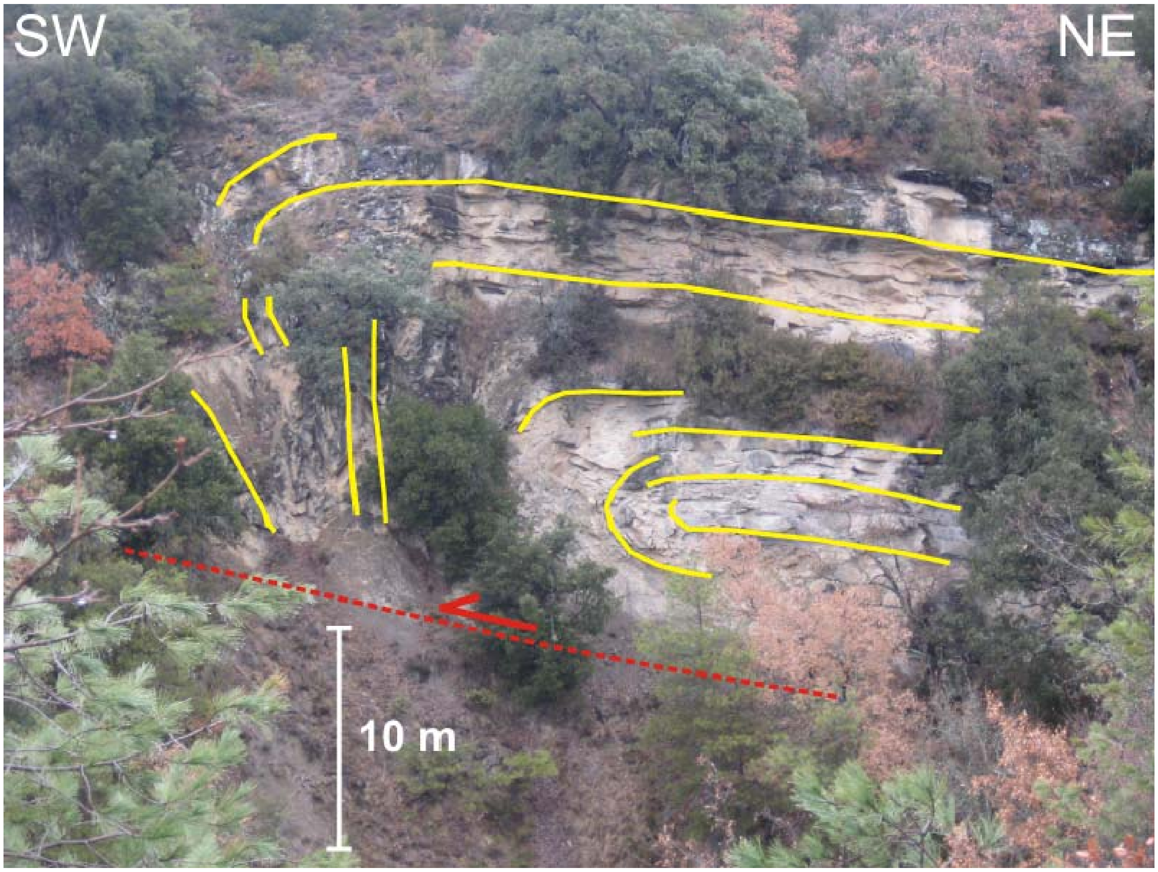

Figure 4.27: Photograph of lower Arro sands within the southwest-verging, recumbent anticline associated with the Las Almazuras Thrust. The red dashed line marks the approximate location of the Las Almazuras Thrust.

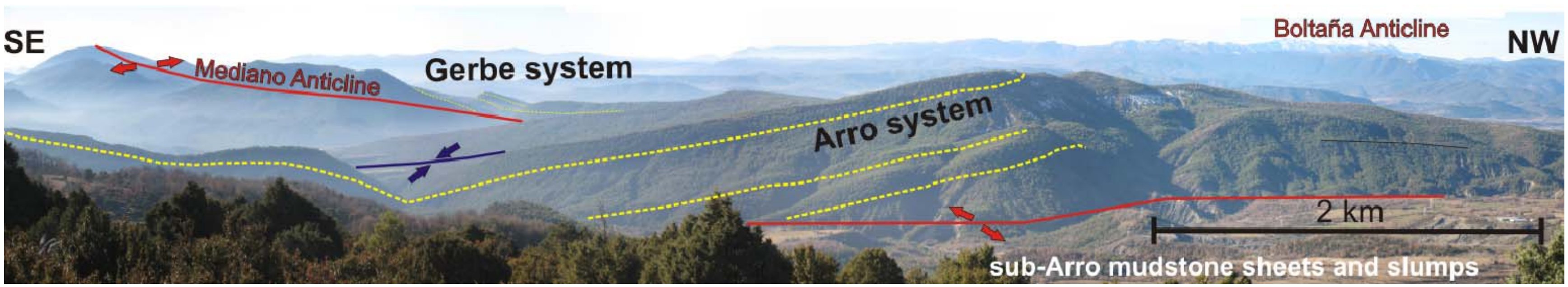

Figure 4.28: View to the southwest from the Peña Montanesa of the Arro and Gerbe deepwater systems and the sub-Arro mudstone sheets and slumps. The Arro ledge is dipping to the southwest and forms the northeastern limb of the syncline immediately adjacent and northeast of the northern termination of the Mediano Anticline.

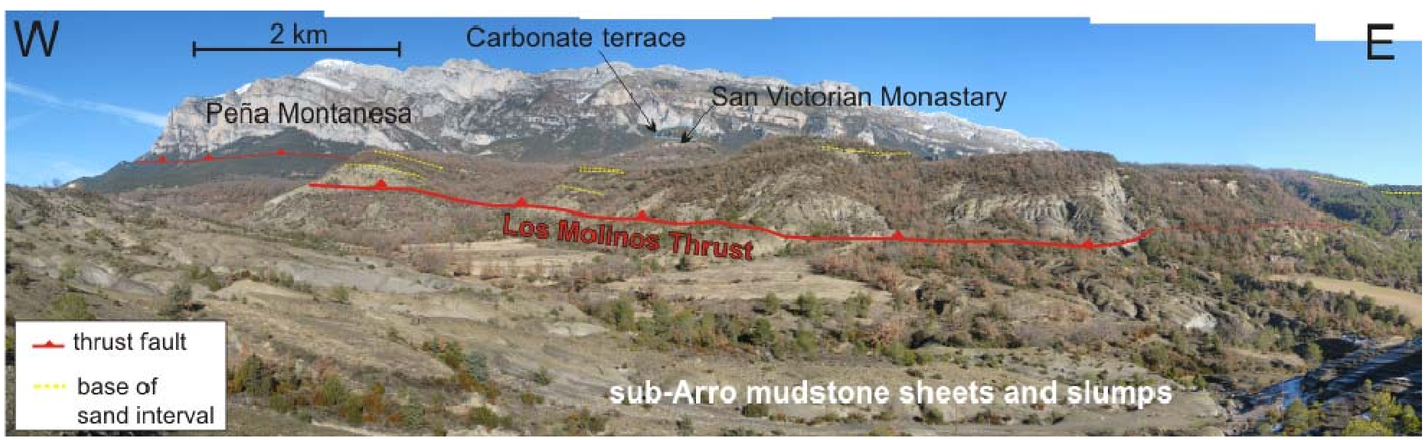

Fig. 4.29: View to the north-northeast from the Arro system ledge. In the foreground are the slump and mudstone dominated sub-Arro strata and the Los Molinos Thrust. Small sand bodies are observed cropping out on the ledges. In the background is the Peña Montanesa and the Peña Montanesa Thrust that mark the northeastern boundary of Ainsa Basin.

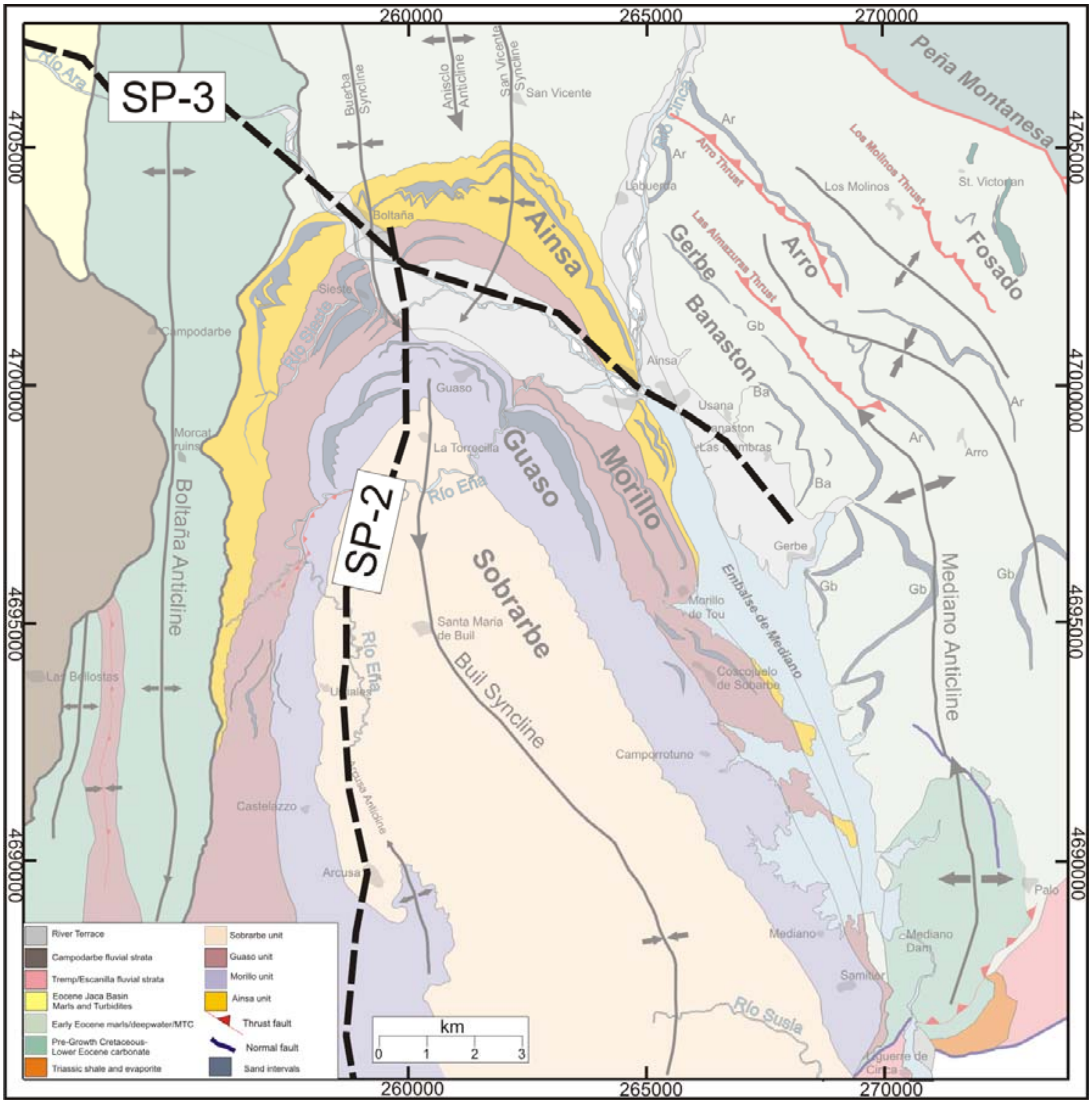

Figure 4.30: Location map of the SP-2 and SP-3 seismic profiles.

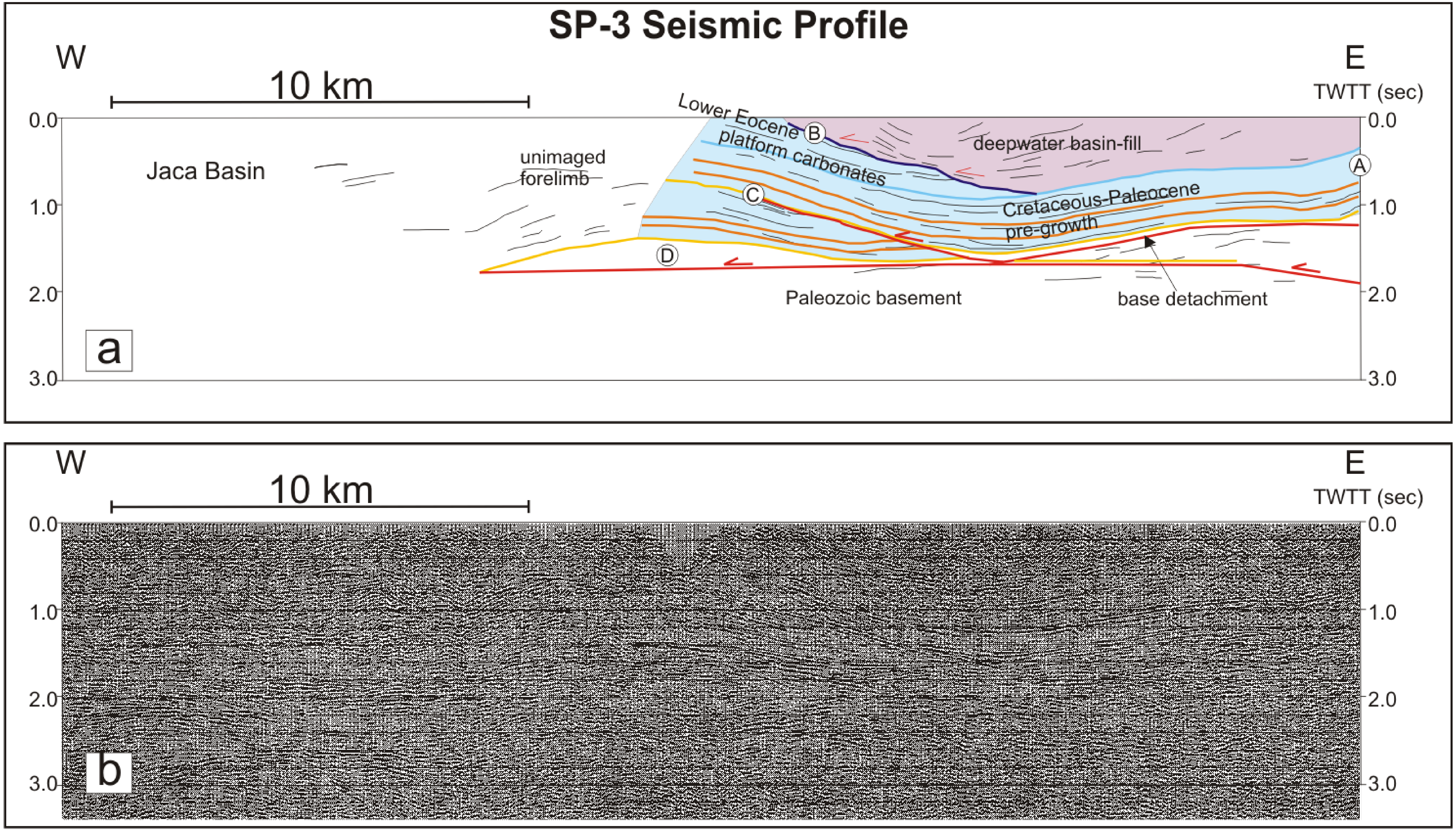

Figure 4.31: Interpretation of the SP-3 seismic profile. a) Line-drawing interpretation. b) Uninterpreted SP-3 time profile. Letters A-D refer to references in the text.

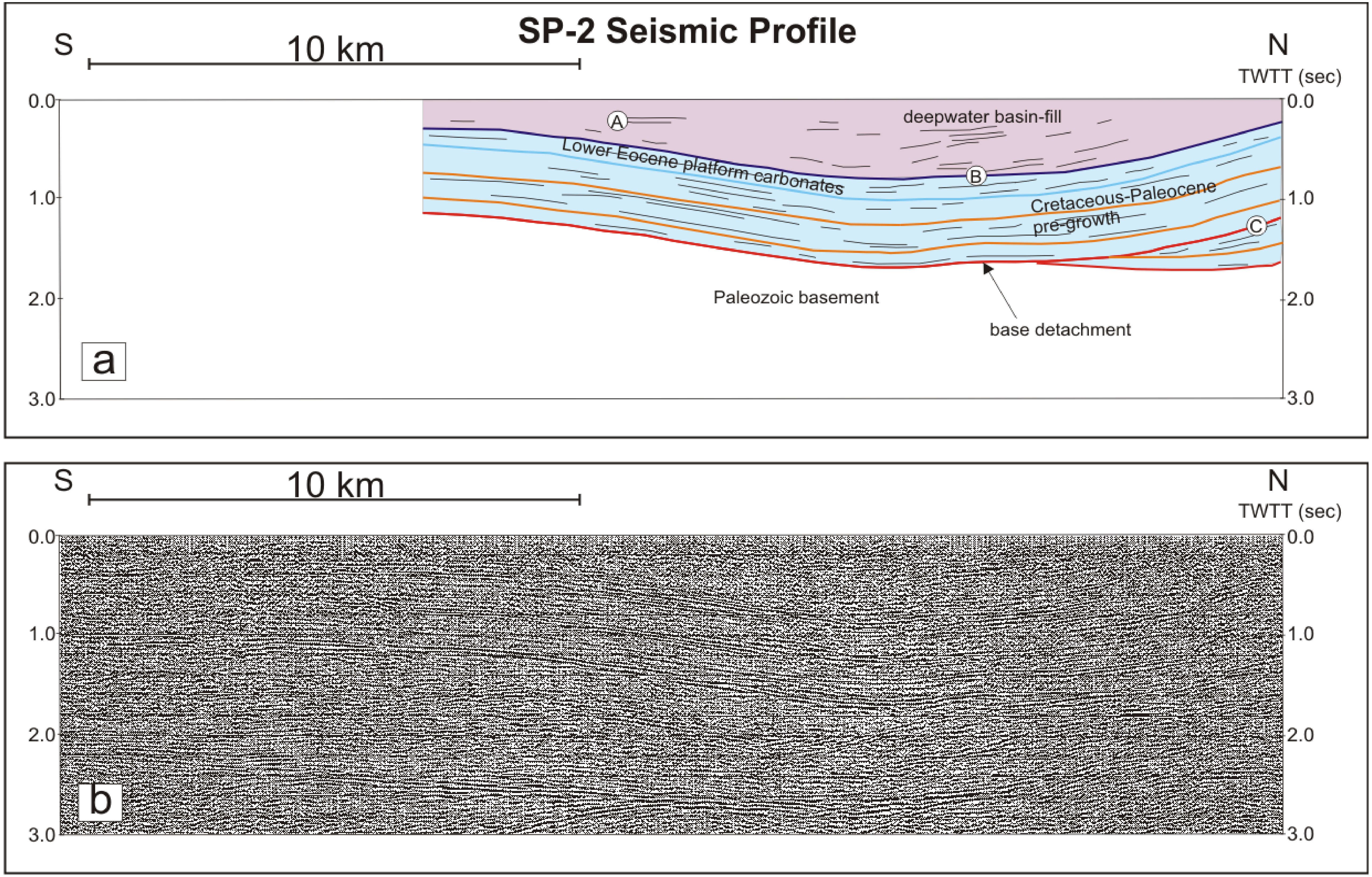

Figure 4.32: Interpretation of the SP-2 seismic profile. a) Line-drawing interpretation. b) Uninterpreted SP-2 time profile. Letters A-C refer to references in the text.

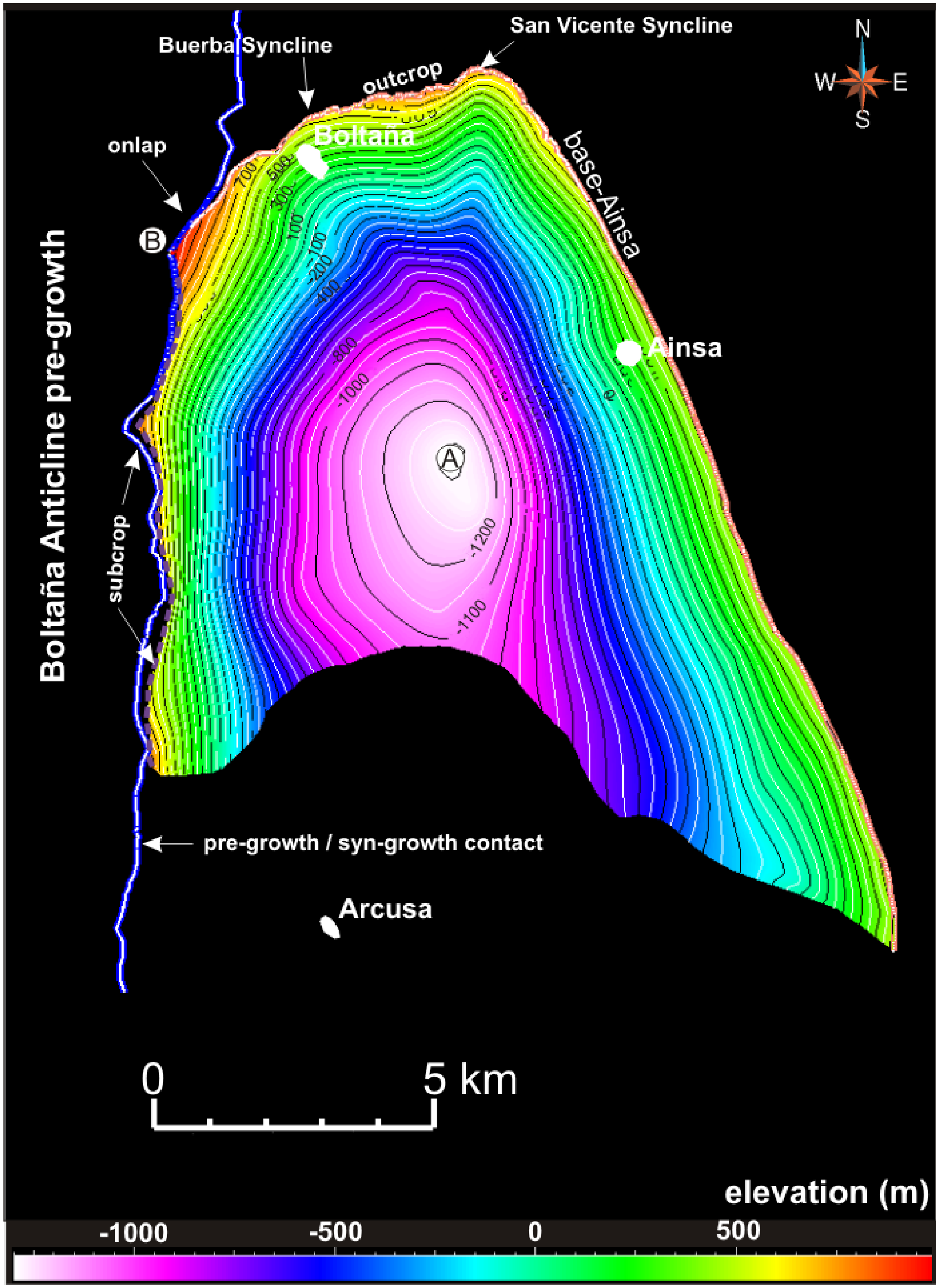

Figure 4.33: Base-Ainsa unit condensed section structural surface. C.I. = 50 m.

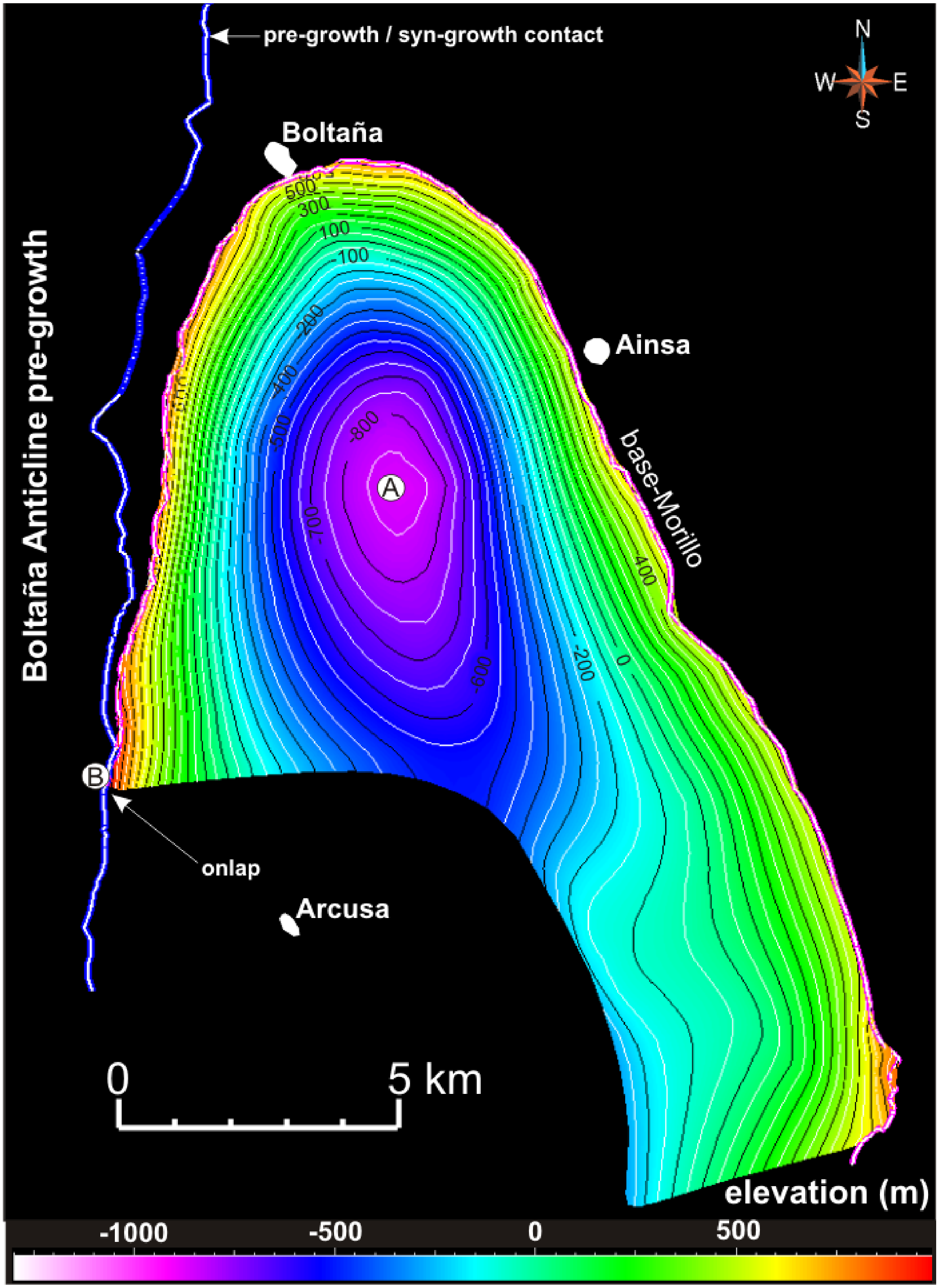

Figure 4.34: Base-Morillo unit condensed section structural surface. C.I. = 50 m.

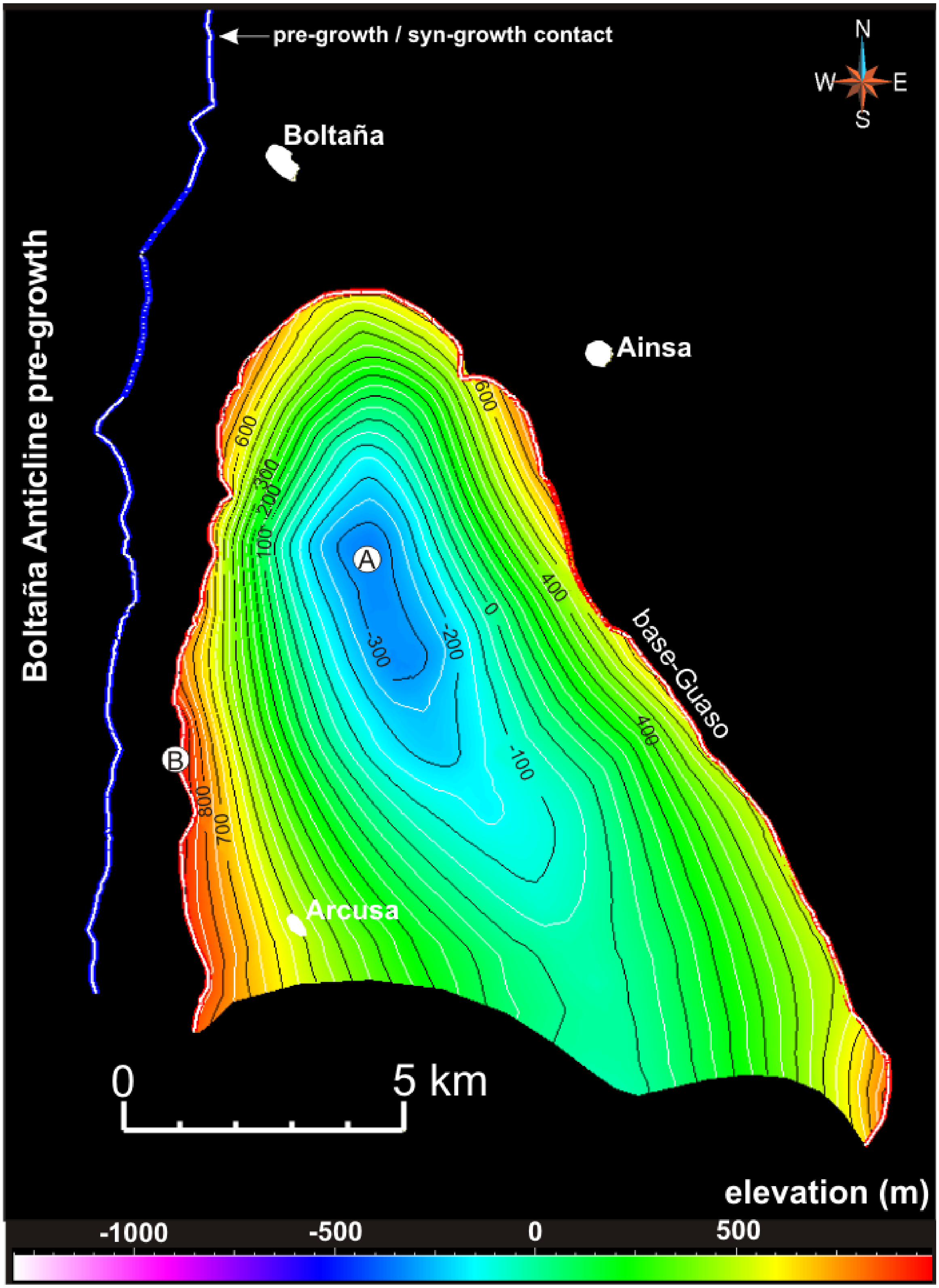

Figure 4.35: Base-Guaso unit condensed section structural surface. C.I. = 50 m.

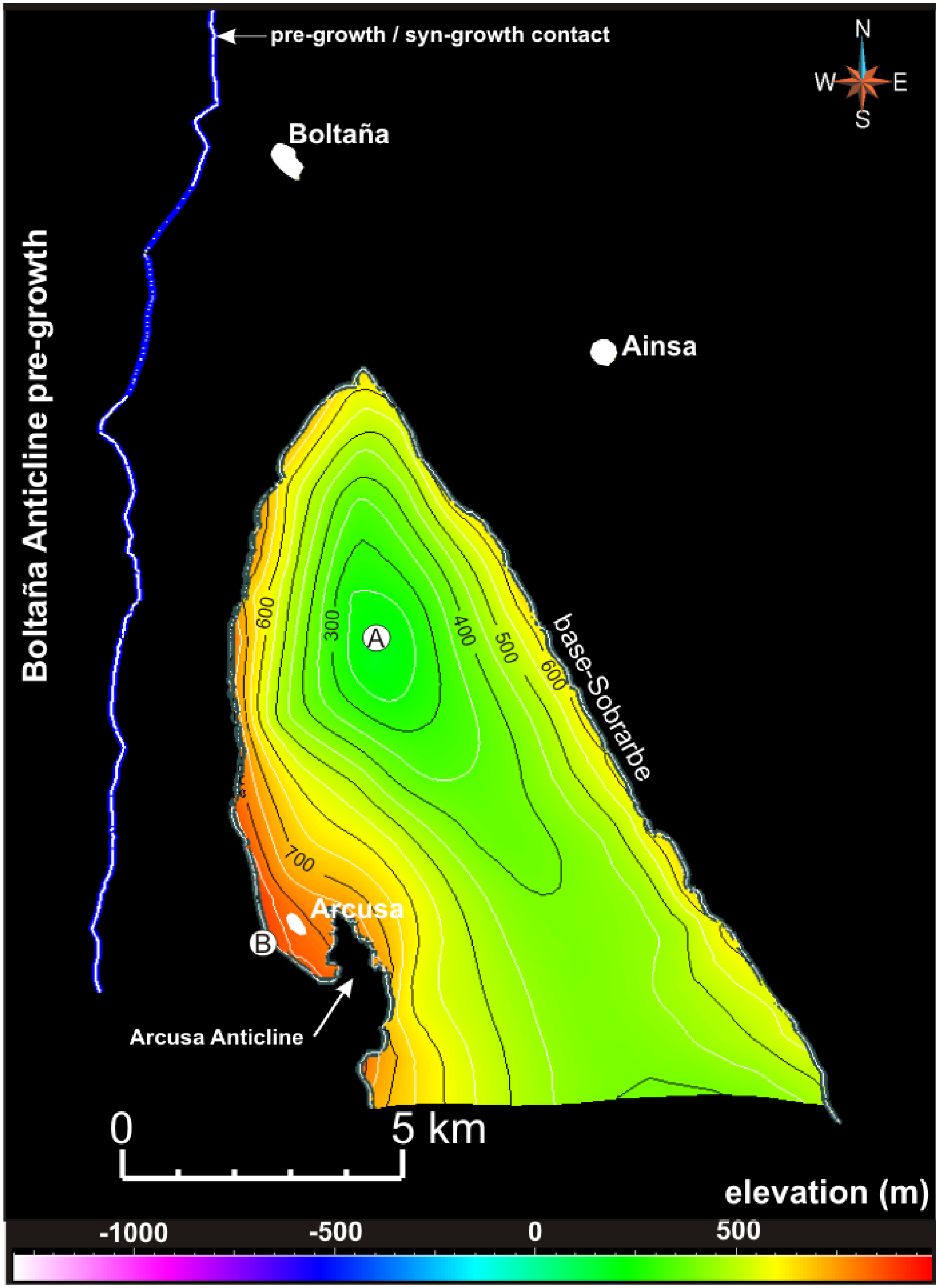

Figure 4.36: Base-Sobrarbe unit condensed section structural surface. C.I. = 50 m.

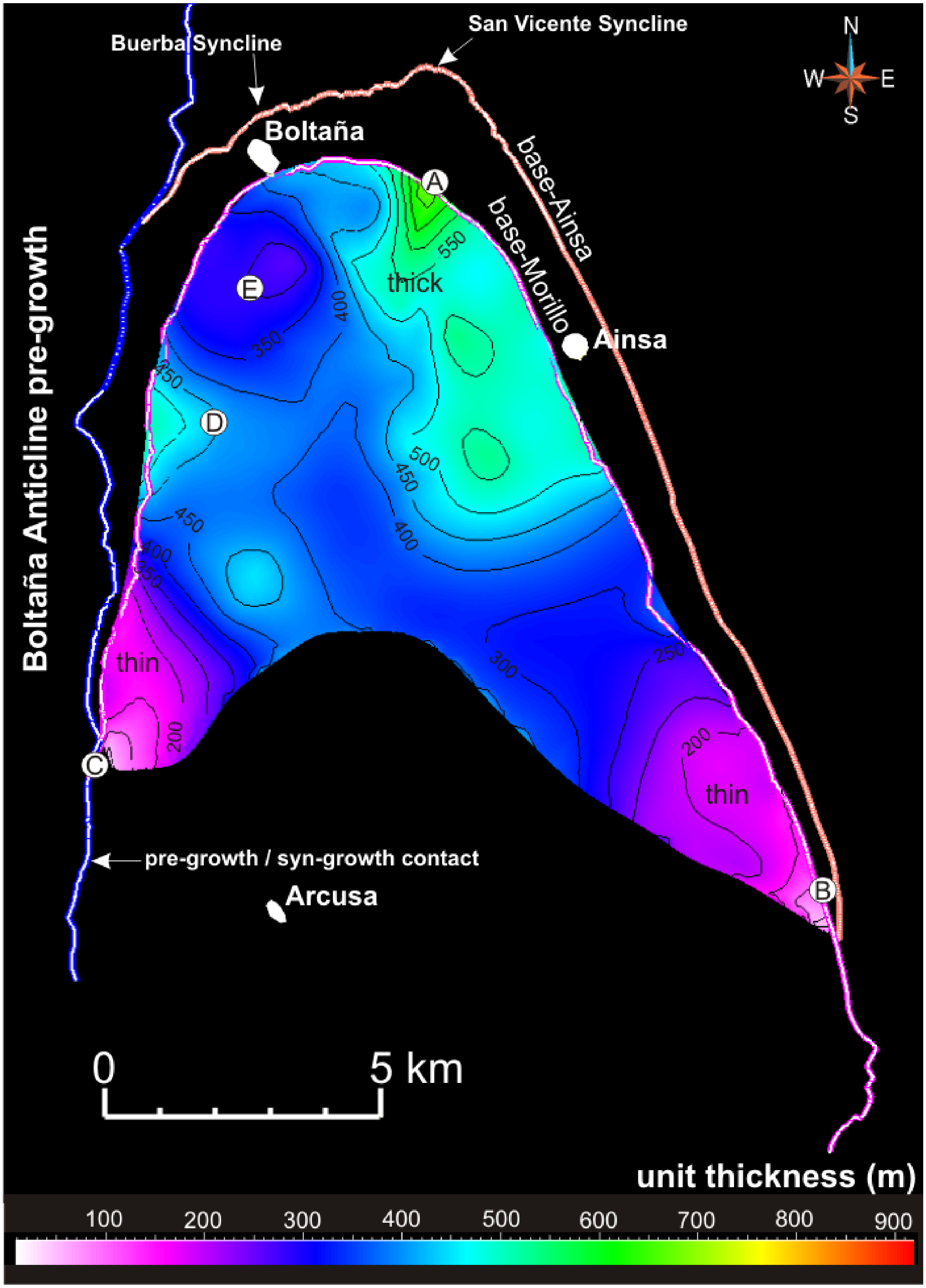

Figure 4.37: Ainsa unit isopach displayed on the base-Morillo structural surface. C.I. = 50 m.

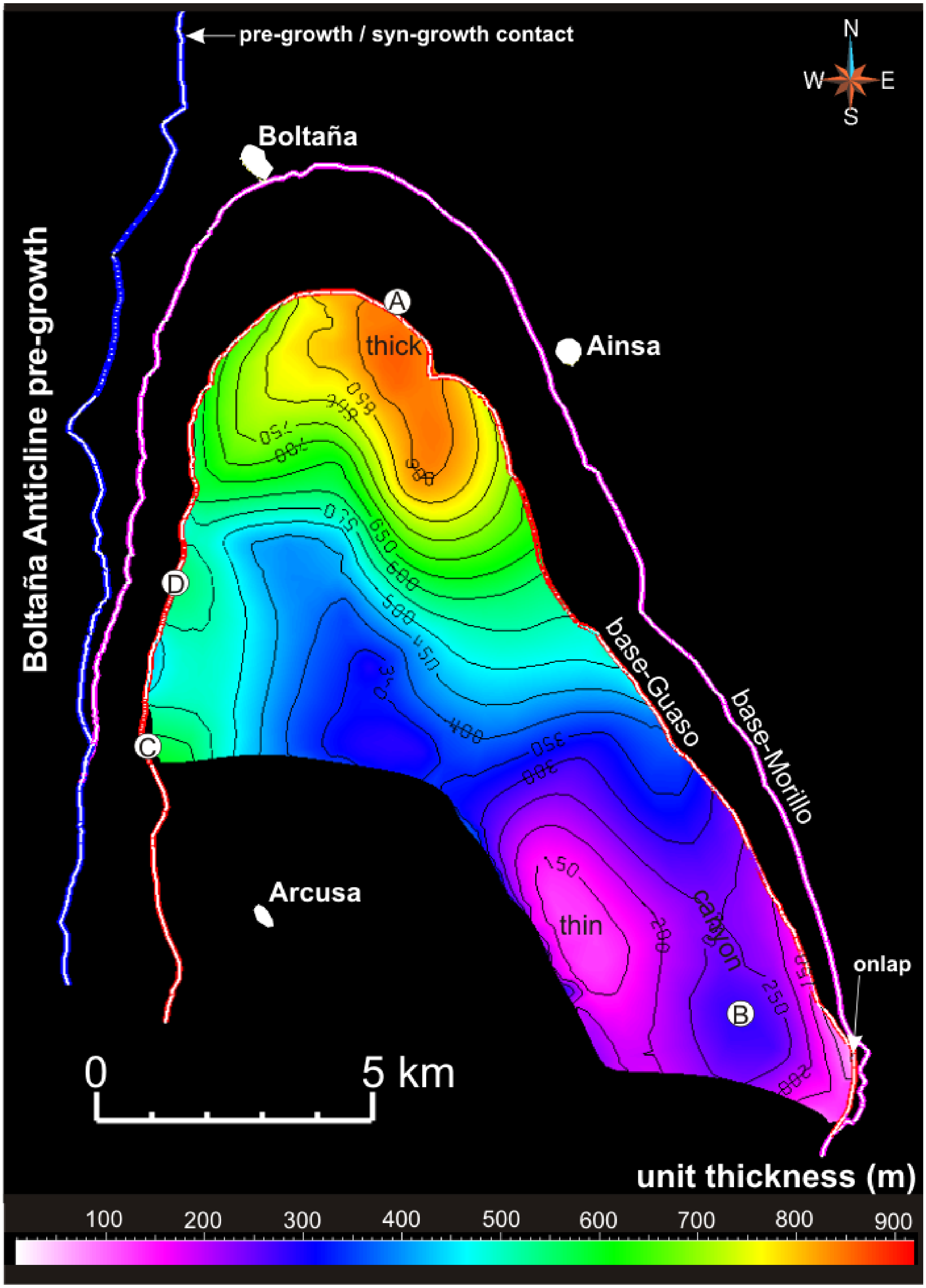

Figure 4.38: Morillo unit isopach displayed on the base-Guaso structural surface. C.I. =50 m.

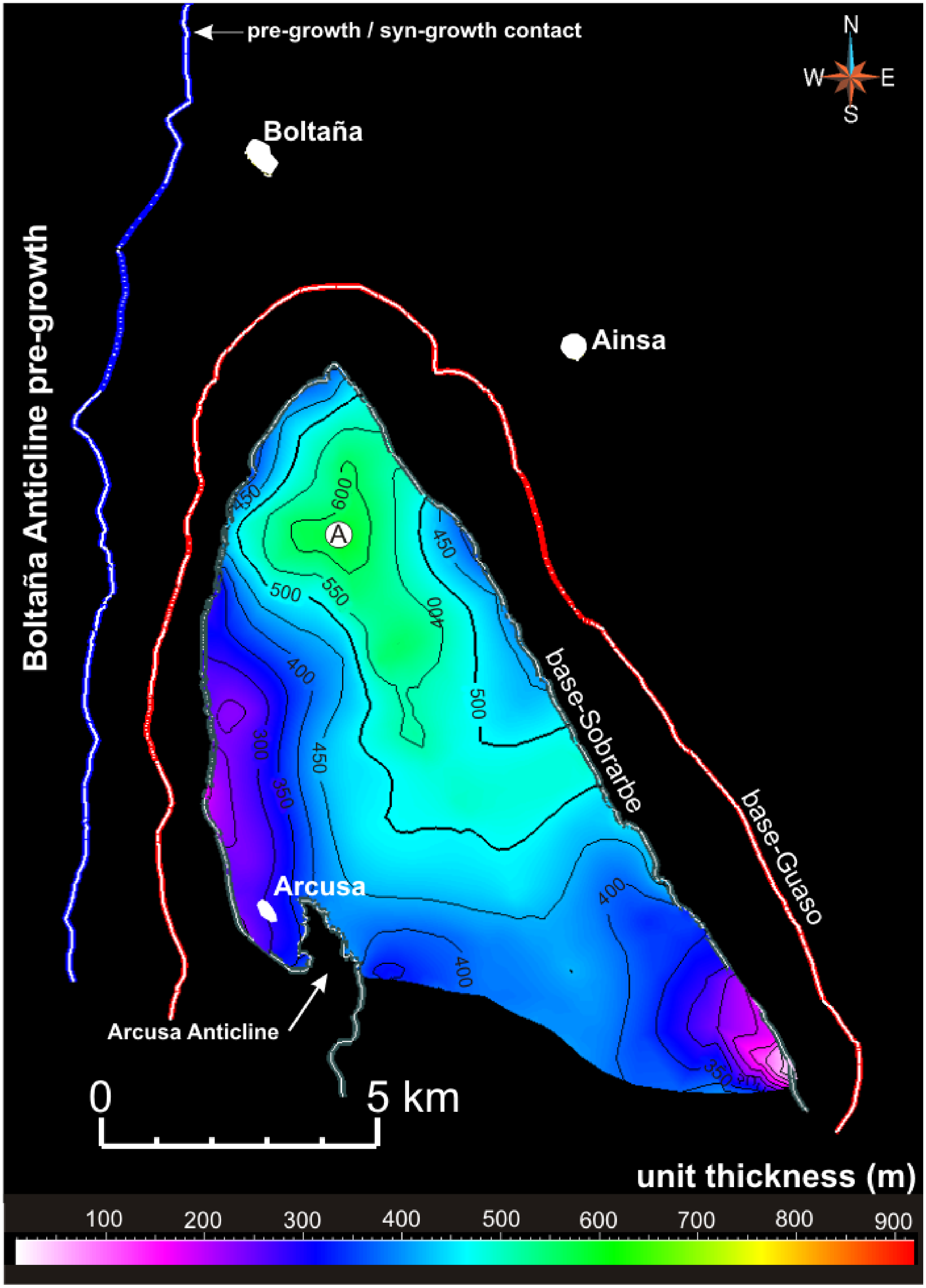

Figure 4.39: Guaso unit isopach displayed on the base-Sobrarbe structural surface. C.I. =50m.

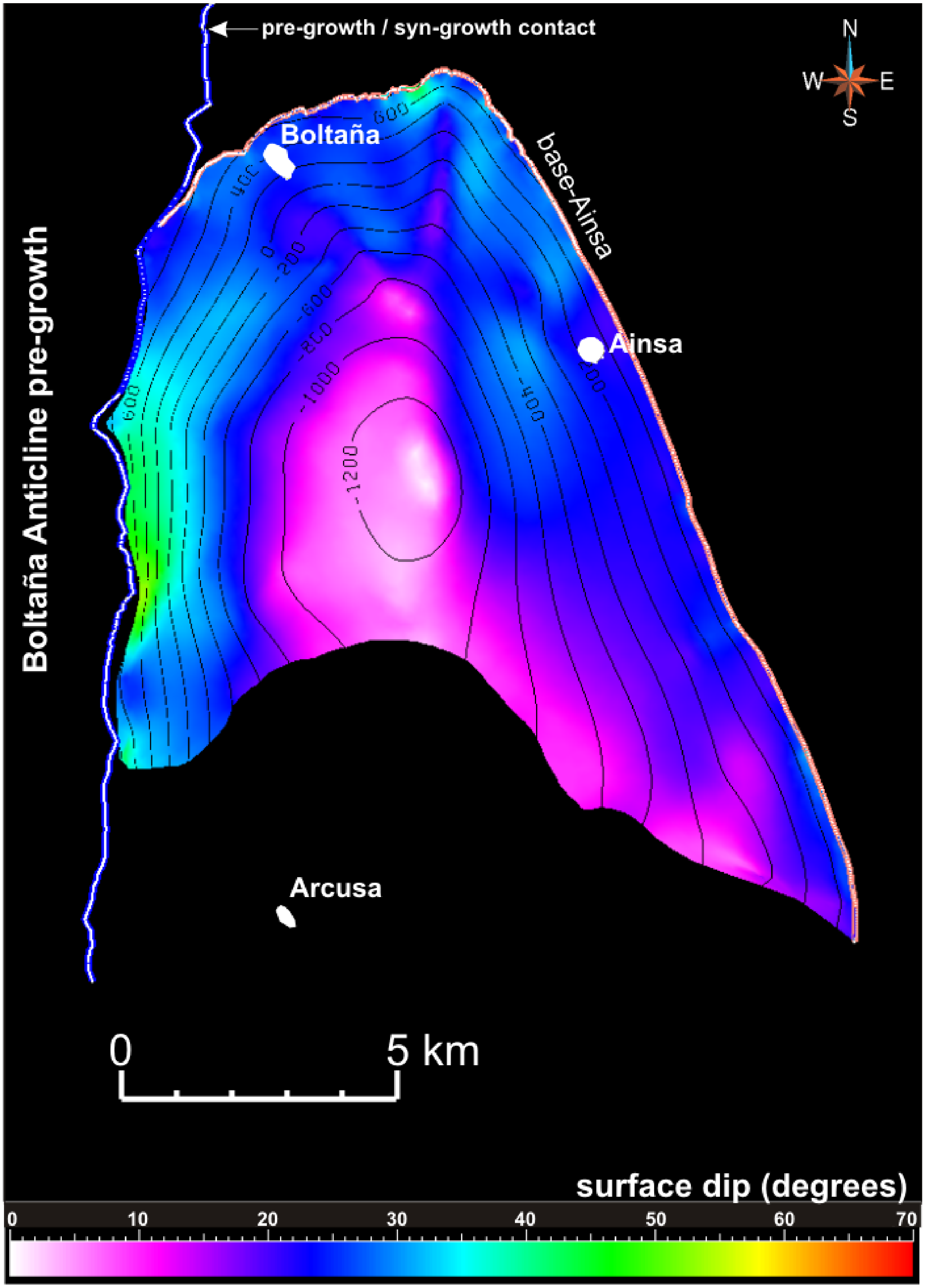

Figure 4.40: Shaded surface dip values of the base-Ainsa structural surface overlain with structure contours. C.I. =200 m

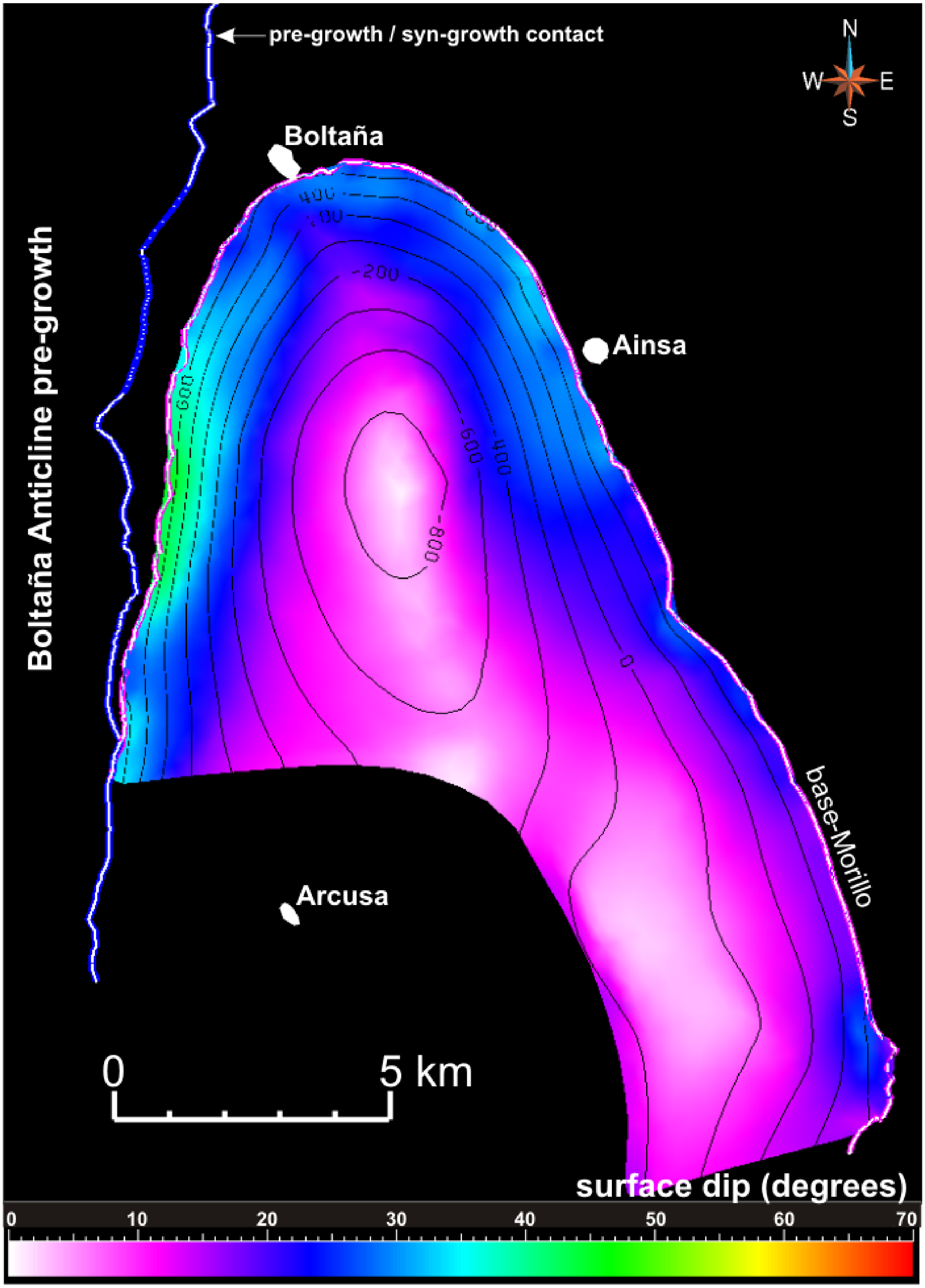

Figure 4.41: Shaded surface dip values of the base-Morillo structural surface overlain with structure contours. C.I. =200 m.

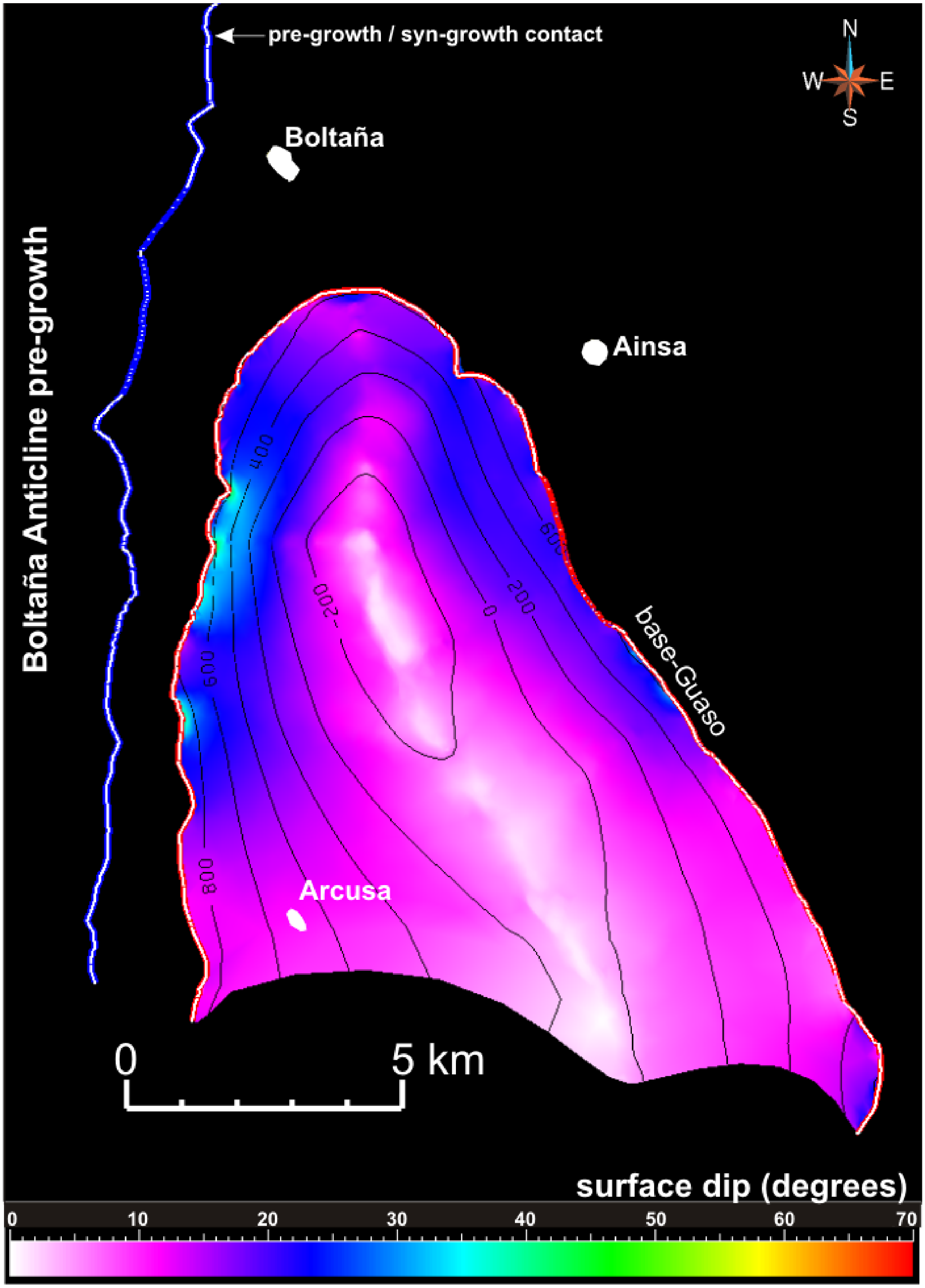

Figure 4.42: Shaded surface dip values of the base-Guaso structural surface overlain with structure contours. C.I. =200 m.

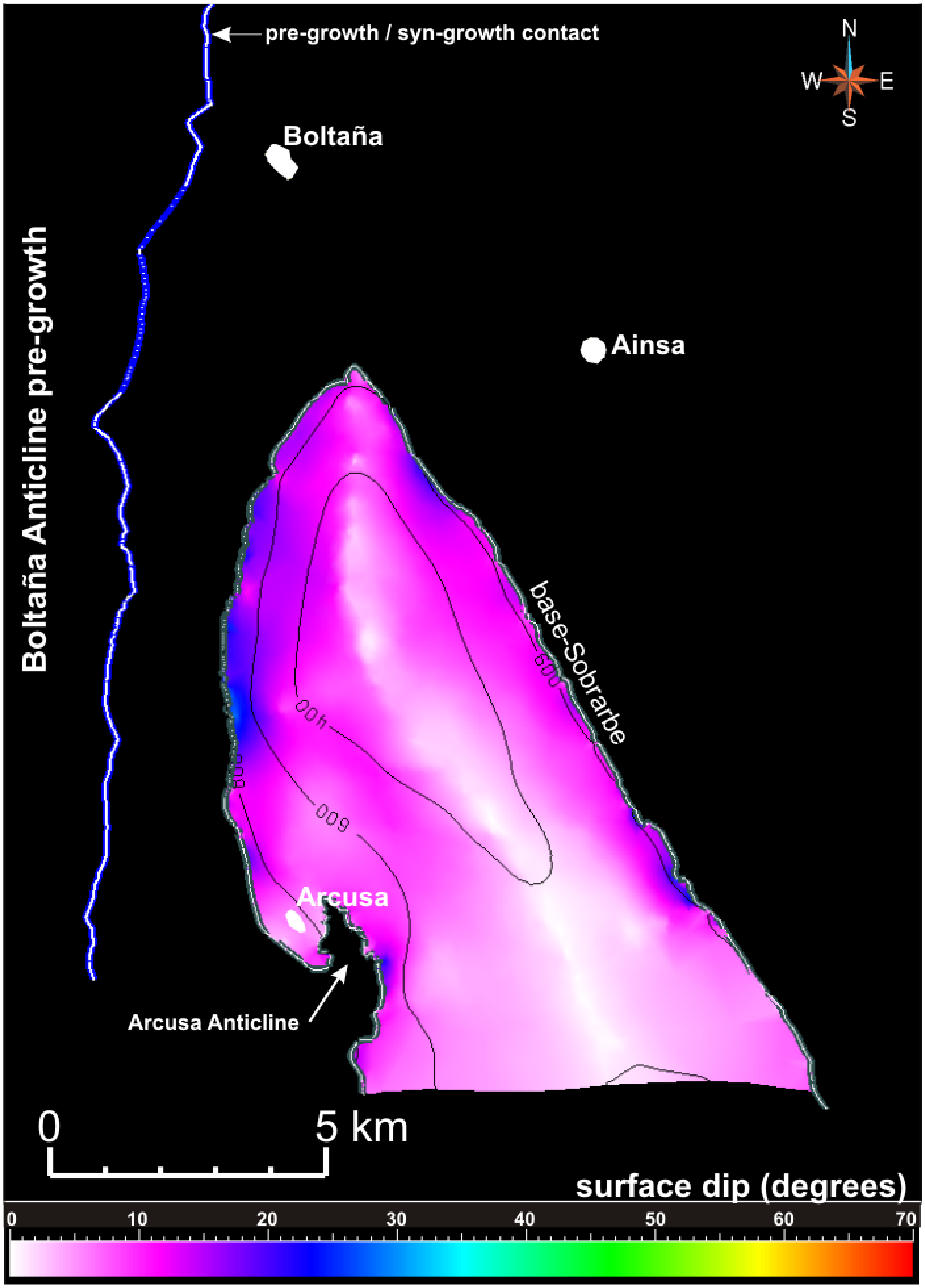

Figure 4.43: Shaded surface dip values of the base-Sobrarbe structural surface overlain with structure contours. C.I. =200 m.

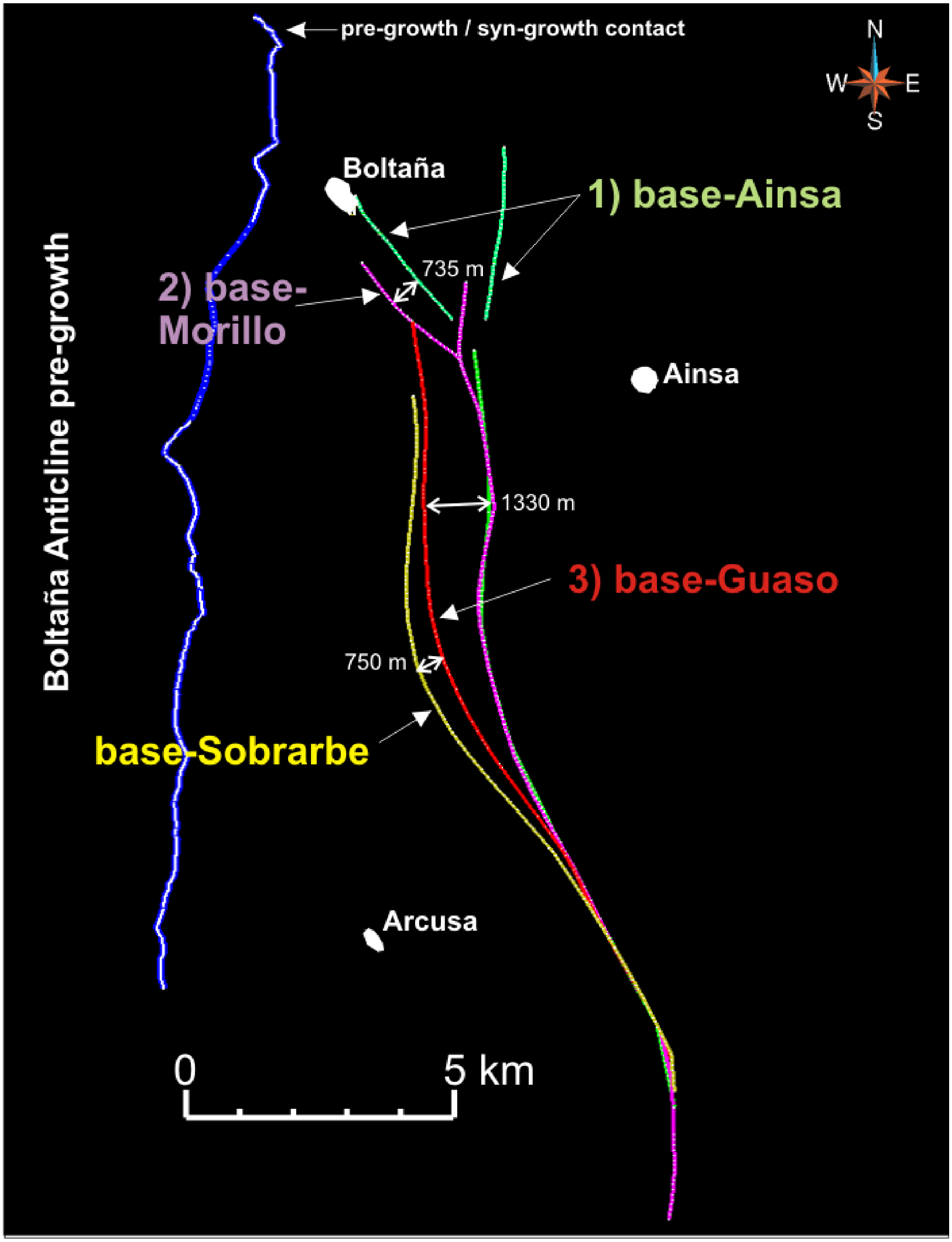

Figure 4.44: Plan-view of the base-Ainsa, base-Morillo, base-Guaso, and base-Sobrarbe constructed system axes.

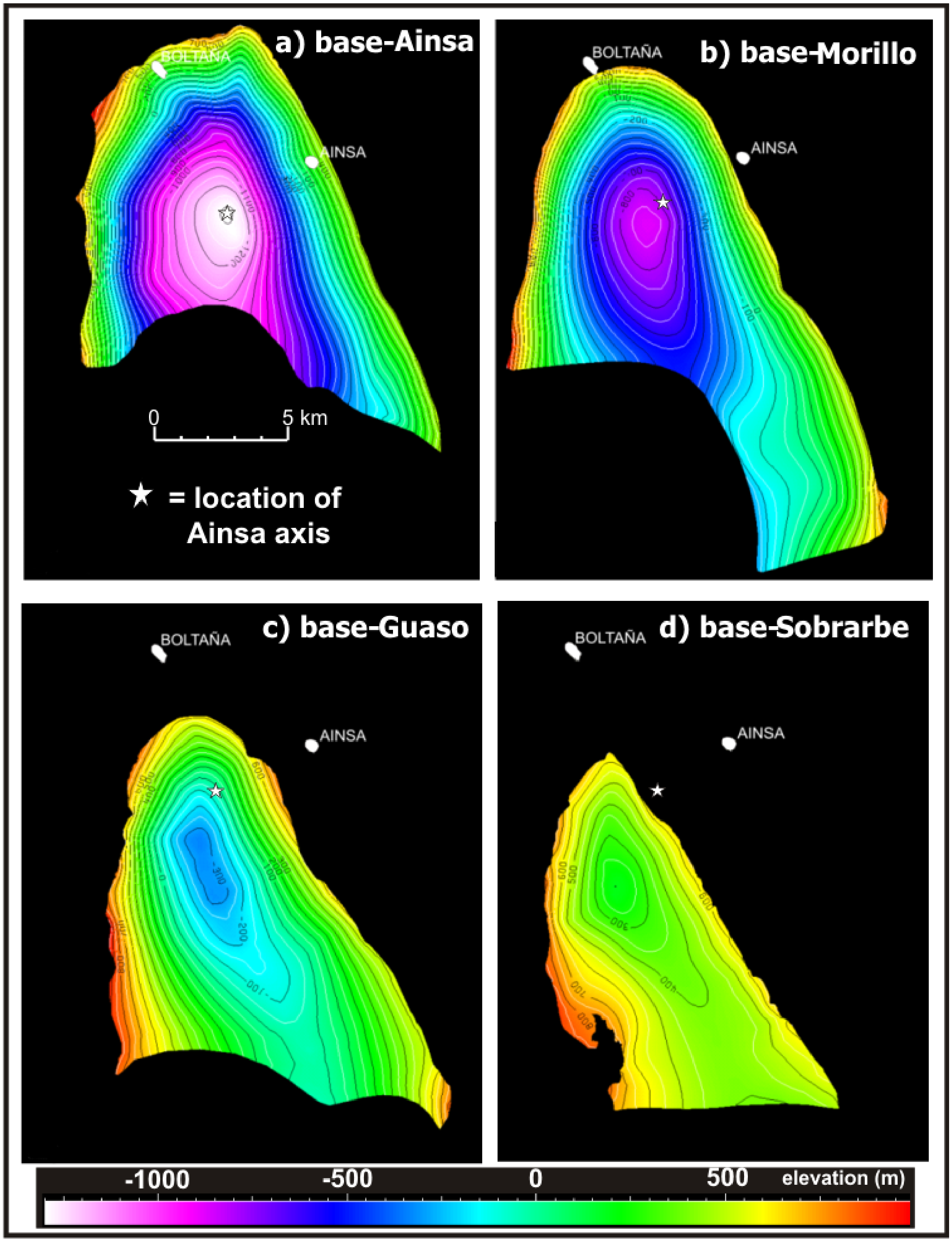

Figure 4.45: Structure maps of the base-Ainsa (a), base-Morillo (b), base-Guaso (c), and base-Sobrarbe (d) shown in relation to the deepest point of the base-Ainsa surface axis (marked by the star).

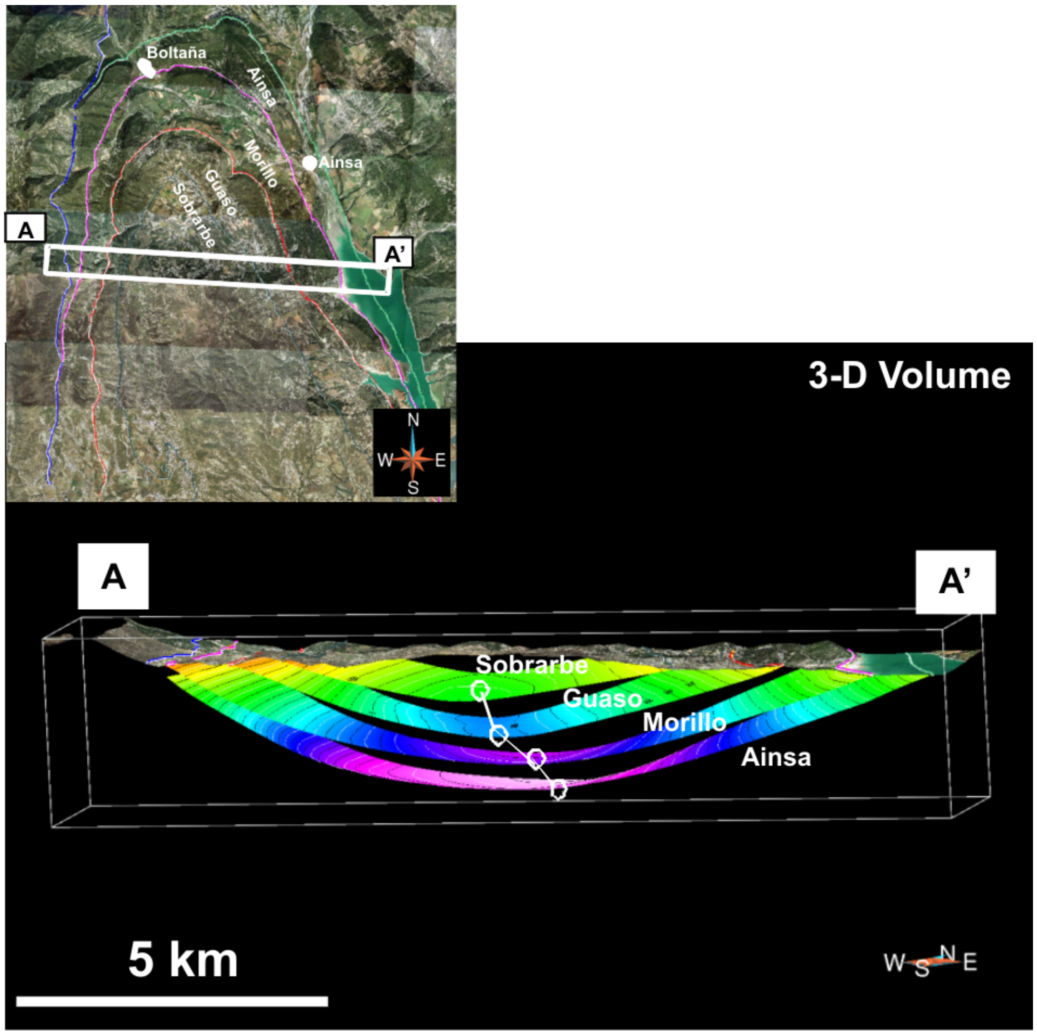

Figure 4.46: 3-D volume extracted from the central portion of Ainsa Basin. Note the western shift of system axes upwards.

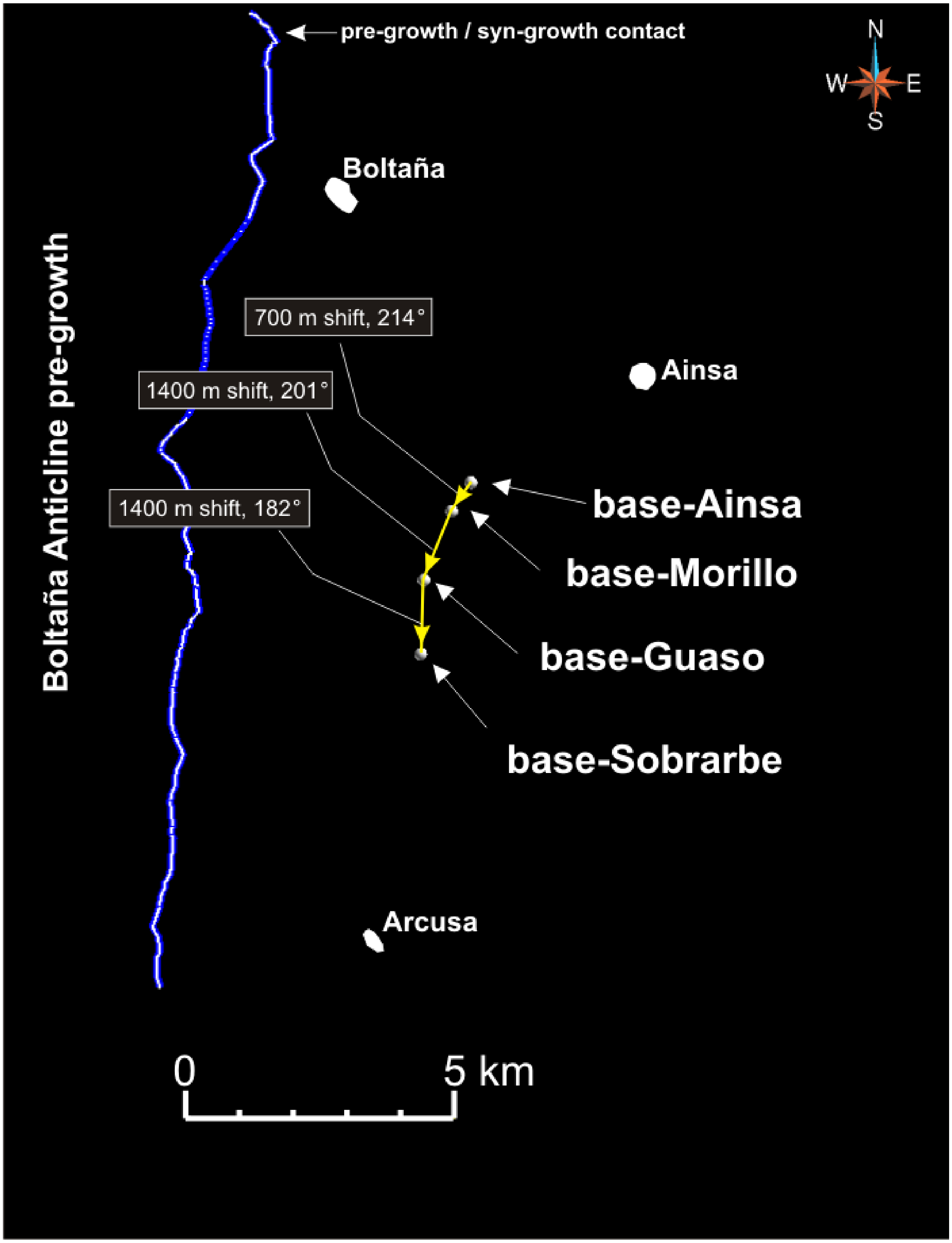

Figure 4.47: Plot of the deepest point on each syn-growth surface axis. The points are connected by a curve. The length and azimuth of each curve segment are listed, which represent the direction and magnitude of each system shift.

CHAPTER 5

DISCUSSION

This chapter describes the geologic interpretations and implications of this study as they relate to the primary research objectives, which are the following:

1) Define the style and timing of deformation on the Ainsa Basin bounding structures.

2) Constrain the 3-D geometries of the syn-growth deepwater systems and the relationship between sand distribution and depocenters through time.

3) Test new techniques in 3-D structural model construction from surface data.

This chapter concludes with a discussion on how the lessons learned in this study can be applied to hydrocarbon exploration and development and a discussion of future work to further explore the concepts addressed in this research.

5.1 Style and Timing of Deformation on the Bounding Anticlines

The style and timing of deformation on the Ainsa Basin structures remains a debate (e.g., Farrell *et al.*, 1983; Muñoz *et al.*, 1994; Poblet *et al.*, 1998; Pickering and Bayliss, 2009). This study outlines a structural history for the basin that unifies new field data and observations with those of prior studies.

In order to constrain the style and timing of deformation in the Ainsa Basin, a cross section (A-A', Fig.5.1) oriented roughly perpendicular to the main structures (Mediano Anticline, Buil Syncline, and Boltaña Anticline) was constructed and restored.

The cross section was constructed using field measurements and the SP-3 seismic profile which trends oblique to A-A' section (Figures 4.31 and 5.1).

A single cross section cannot capture all structural and stratigraphic relationships of a growth basin. Due to the great degree of lateral facies changes, unit thicknesses patterns, and complex 3-D structural geometries, certain key aspects of the basin structures fall outside the plane of the cross section. The location of the cross section captures as many structural elements that are critical in explaining the structural evolution of the basin as possible (Figure 5.1). In addition, the location of the cross section was selected to increase knowledge of structures that were not fully explained in prior studies (e.g., Dreyer *et al.*, 1999; Fernández *et al.*, 2004).

The cross section was constructed by identifying 2-D dip domains from surface data projected onto the A-A' section. A simplified, balanced, and retro-deformable structural model was constructed that fits the surface data and interpreted subsurface geometry. The restored cross section represents 6275 m of shortening (22.8 % total shortening) between the Eocene and Present Day (Fig. 5.2). A total of 3350 m of shortening (13.6% of total shortening) is accommodated in the units above the Triassic detachment. A basement wedge, interpreted beneath the Mediano Anticline, is responsible for transferring slip to the shallow basin structures and requires an additional 2925 m of slip that is not accounted for in the units overlying the detachment. Therefore, this slip must be transferred westward into the Jaca Basin on the regional detachment level. Structural maps of the Jaca Basin (i.e. Teixell and García-Sansegundo, 1995) indicate the presence of compressional structures oriented parallel to the Boltaña and

Mediano Anticlines in the western part of the Jaca Basin. These structures potentially accommodate the additional slip sent by the basement wedge outside of the study area.

The following sections describe the restoration, the shortening each structure accommodates, and the rationale for the structural interpretation.

5.1.1 Structural Interpretation

The following sections describe the interpretation of the basin structures modeled in the structural cross section.

5.1.1.1 Mediano Anticline

The Mediano Anticline is interpreted as a detachment fold, which is consistent with the interpretation of Poblet *et al.*, (1998). These authors demonstrate that the Mediano grew through a combination of limb rotation and limb lengthening, recognized through the identification of a progressive unconformity on the western Mediano Anticline limb. The fold evolution is consistent with the kinematic models of Poblet *et al.*, (1997) for asymmetric detachment folds (Fig. 2.5).

The progressive unconformity identified in the stratigraphic units of Poblet *et al.* (1998) is also apparent in the condensed section unit boundaries used in the present study. The onlap configuration, that is first observed in the Ainsa system and continues through the Guaso system, is evident on the western limb of the southern Mediano Anticline (B, Fig. 4.10). Ainsa and Morillo I stratigraphic units onlap the pre-growth under the Embalse de Mediano (reservoir) and do not crop out to the south where only the Morillo II to Guaso units are observed (B, Fig. 4.10.) (as described in section 4.2.1) and lap onto the progressive unconformity which is highlighted by a canyon cut (Figures 4.17 and B, 4.38).

The A-A' cross section intersects the Mediano Anticline north of the Rio Usia (Figures 4.10 and 4.14) where it exhibits an open and symmetric geometry. The fold at this location is a symmetric detachment fold and is interpreted to sit atop a basement wedge with a simple fault bend fold geometry (A, Fig. 5.2). This wedge is interpreted from the SP-3 seismic profile and accounts for a thickened section of Paleozoic basement below the eastern Buil Syncline limb (Fig. 4.3). The restoration shows that slip from this westward propagating basement wedge is transferred eastwards along its upper surface to the Mediano Anticline. At this location, the Mediano Anticline accommodated 450 m of shortening (1.8% of total shortening) (Fig. 5.2).

5.1.1.2 Boltaña Anticline

The Boltaña Anticline is interpreted as a fault-propagation fold, based on: (1) the recognition of an associated fault ramp on the SP-3 seismic profile that extends upwards from the regional detachment level (C, Fig. 4.31), (2) the absence of a linked upper flat that extends to the west into the Jaca Basin (Teixell and García-Sansegundo, 1995), (3) the fold's pronounced asymmetry defined by a steeply dipping western forelimb and a gentler dipping eastern backlimb, and (4) the fold's vergence in the direction of regional transport (west).

This interpretation is consistent with past structural interpretations of the Boltaña Anticline (i.e. Farrell *et al.*, 1987; Fernández *et al.*, 2004). The cross section of Fernández *et al.* (2004) trends through the Boltaña Canyon (Figures 4.6 and 4.23a), following the SP-3 seismic profile (Fig. 5.1) and interprets forelimb breakthrough of the fault ramp into an upper flat that accommodates a small amount of shortening of the fold to the west. Additionally, Fernández *et al.* (2004) interprets three east-dipping normal faults that exhibit dip-slip values of up to 500 m on the backlimb of the anticline that cut Lower Eocene pre-growth carbonate that crops out in the Boltaña Canyon and extend into the subsurface to the Triassic detachment unit along the associated fault ramp. Figure 4.23a shows an interpreted photopanel through the Lower Eocene pre-growth carbonate exposures in Boltaña Canyon. Extensive field mapping was conducted along the Boltaña Anticline and no east dipping normal faults approaching this magnitude are observed, making the interpretation of Fernández *et al.* (2004) debatable.

The location of the A-A' cross section (Figures 5.1 and 5.2) is 8 km to the south of the SP-3 profile where the Boltaña Anticline (1) exhibits less structural relief than farther north, as it is closer to the fold's southern termination in the southwest corner of the study area, (2) has a backlimb steepened by 15-20° relative to the backlimb dips in the vicinity the SP-3 profile, and (3) has an obscured forelimb as the result of an erosional cut filled with Jaca Basin fluvial strata (Fig. 4.21).

At the location of the A-A' section, the Boltaña Anticline is interpreted to be affected by a deep underlying imbricate detachment fold (B, Fig. 5.2). This detachment fold serves to steepen the Boltaña Anticline fault-propagation fold backlimb to its present day dip of ~40°. The presence of this lower detachment fold is supported by: 1) slightly folded footwall strata below the Boltaña Anticline ramp and above the regional detachment observed on the SP-3 seismic profile (D, Fig. 4.31) (as described in section 4.4.1), 2) the steeper surface dip measurements on the backlimb pre-growth strata in the vicinity of the A-A' section relative to backlimb dips on pre-growth strata along the SP-3 profile (Figures 4.1a and 4.1c), and 3) dip maps of the base-Ainsa and base-Morillo 3-D surfaces that reflect an elongate steepened zone along the strike of the Boltaña Anticline's backlimb (Figures 4.40 and 4.41) The steepened zone on the dip maps reaches a maximum dip at its intersection with the A-A' section, with dips decreasing to the north and south. This zone is interpreted to reflect a slip gradient for the underlying detachment fold that steepens the Boltaña Anticline backlimb along the zone's length.

Alternatives to the interpretation of an imbricate detachment fold include a basement involved structure such as the early stages of a fault-propagation fold or an assembly of basement structures, undefined by the SP-3 seismic profile, with considerable transport out of the plane of section. An imbricate detachment fold was interpreted to account for the symmetrical fold observed in the SP-3 profile that does not appear to be linked to a ramp. However, given the known involvement of Late Eocene basement structures in the region (Farrell et al., 1987; Fernández *et al.*, 2004) and the limited constraint on the deep structural geometry, a basement structure that steepens the backlimb and ramp of the upper fault-propagation fold is both mechanically and temporally viable.

Restoration of the cross section indicates that this lower structure accommodated 550 m of shortening (2.2 % of total shortening) (Fig. 5.2). In contrast, the upper Boltaña anticline fault-propagation fold accommodated 2350 m of shortening (9.5% of total shortening) (Fig. 5.2). The cumulative shortening on the Boltaña Anticline (including deep and shallow structures) is 2900 m (11.7% of total shortening).

5.1.1.3 Añisclo Anticline

The Añislco Anticline lies beyond the study area and was not characterized as part of this study. However the fold's southern termination under the Ainsa Basin is demonstrated to have affected the Ainsa deepwater system, as the base-Ainsa condensed section drapes paleo-lows (San Vincente and Buerba Synclines) associated with Añisclo Anticline growth (Fig. 4.33) (as described in section 4.5.1.1**)**. The implication of this geometry is discussed below.

5.1.2 Timing of Growth

The following section relates the stratigraphic indicators of structural growth documented in this study to phases of growth on the basin structures. Figure 5.3 summarizes the timing of structural activity relative to the deposition of Ainsa Basin fill and evidence supporting this interpretation.

5.1.2.1 Timing of Growth on the Mediano Anticline

Growth of the Mediano Anticline is interpreted to have initiated during Ainsa depositional time, as the Ainsa unit is the oldest unit onlapping and showing thickness change relative to the structure (Poblet *et al.*, 1998). The Mediano pre-growth strata likely experienced minor erosion during Ainsa deposition related to initial uplift of the fold. Evidence of tectonically driven erosion is present within the Morillo II unit in the form of a canyon (Fig. 4.17). This evidence suggests that the Mediano was actively growing during Morillo depositional time. The geometry of this canyon-fill is potentially reflected in the southeast portion of the Morillo isopach map (Fig. 4.38). Additionally, the deposition of reworked platform carbonate in the southern portion of the Mediano Anticline during Morillo and Guaso depositional time indicates that the fold was below sea-level during growth. No karst or evidence of sub-aerial exposure is observed at the apex of the Mediano Anticline (C, Fig. 4.10).

The along strike variation of the Mediano Anticline and its northward plunge can be attributed to a shortening gradient (Poblet *et al.*, 1998). Platform carbonates are only present in the syn-growth stratigraphy (possible Morillo and Guaso age) in the southern region of the fold where the fold exhibits the greatest structural relief and has accommodated the most shortening as evidenced through the tightness of fold geometry and the presence of a backthrust (Figures 4.10 and 4.13) (Poblet *et al.*, 1998). Changes in the along-strike geometry of the fold to the north, away from the region of maximum shortening, can be assumed to reflect stages of fold evolution. The Mediano Anticline propagated northwards through time, developing into the present day symmetrical and open fold geometry observed to the north (Fig. 4.14) (Poblet *et al.*, 1998). This northward propagation is supported by the paleocurrents in the proximal (eastern) outcrops of the Ainsa and Morillo systems (Fig. 4.1a and b). These paleocurrents indicate an eastern source for siliciclastic sediment input into the basin. Ainsa and Morillo channels are oriented orthogonal to the axis of the Mediano Anticline during its earliest stages of growth (Figures 5.4 to 5.7). Paleocurrent measurements and progradational geometries of the younger Guaso and Sobrarbe systems reflect a southern source. This is potentially the result of a heightened stage of growth on the Mediano Anticline that forced the fluvio-deltaic source of Ainsa Basin sedimentation in the Tremp Basin to circumvent the fold to the south.

A general and qualitative indicator of the onset of structural growth in the basin is the change in the color of shales within the upper syn-growth units (Ainsa, Morillo, Guaso, and Sobrarbe). Shales below the Ainsa unit are dark gray to black in color. Shales within and above the Ainsa unit are significantly lighter, ranging from gray to light gray in color, signaling an increased input of carbonaceous sediment into the basin. The known presence of a canyon within the Morillo unit that eroded into pre-growth carbonates on the Mediano Anticline and the presence of platform carbonate coeval with the Morillo and Guaso systems on a Mediano Anticline paleo-high, indicate the onset of a carbonate sediment source to the upper syn-growth systems. This transition in shale color corresponds with the interpreted timing of growth on the Mediano and Boltaña Anticlines. Both structures are cored by carbonates which were actively eroded during deposition of the upper deepwater units and triggered the shale color change.

5.1.2.2 Timing of Growth on the Boltaña Anticline

Constraining the timing of initiation of growth on the Boltaña Anticline fault-propagation fold is not straightforward. The presence of Lower Eocene shallow-water platform carbonate within the Boltaña Anticline indicates that a paleo-high was present at this location, possibly resulting from foreland basin flexure during the Lower Eocene. The Banaston and Ainsa systems are observed onlapping lower Eocene carbonates of the Boltaña Anticline backlimb (Figures 4.6 and 4.23b). Without a 3-D view of this relationship it is difficult to determine whether these systems onlap a true backlimb of a fault-propagation fold or rather against a paleo-high associated with foreland basin flexure.

Nevertheless, stratigraphic indicators within the basin-fill systems provide insight into the timing of periods of growth on the Boltaña fault-propagation fold. Pickering and Bayliss (2009) shows that the paleocurrents in the Banaston system range from 290° to 310° at its westernmost outcrop along the Boltaña Anticline. These paleocurrents are roughly perpendicular to the Boltaña Anticline's axis, indicating that the sediment gravity flows were able to bypass the fold during Banaston depositional time. The same is true for the Ainsa III sands (Pickering and Corregidor, 2000), as the paleocurrents from the westernmost outcrop located along the Boltaña Anticline trend to 320°, in an interception course with Boltaña axis (Fig. 5.6).

The clastic intrusion documented below the Ainsa III sand body along the Boltaña Anticline backlimb is potentially linked to a larger, sub-cropping intrusion network created by high fluid pressures during Ainsa depositional time (Fig. 4.9). These high fluid pressures are potentially generated from a gradient increase associated with early growth on the Boltaña Anticline backlimb during late Ainsa depositional time.

The overlying Morillo system shows clear evidence of interaction with the Boltaña Anticline backlimb. In the proximal position on the eastern Buil Syncline limb, channelized sand intervals stack laterally and exhibit western paleocurrent directions. These channelized sand intervals converge to stack vertically and are deflected northwards in their distal position on the western Buil Syncline limb. The convergence and northward deflection of channels in proximity to the Boltaña Anticline indicate that channel architecture and stacking is directly affected by Boltaña structural growth (Fig. 5.7) (Moody, 2009).

Additional indicators of Boltaña Anticline growth include the frequency and size of MTCs within the Morillo system on the western limb of the Buil Syncline (Fig. 4.7). These MTCs originated from the west (from slump fold axis orientations) and often contain large platform carbonate blocks (up to 70 m long) that were shed from the Boltaña Anticline backlimb (Setiawan, 2009). These strata are interpreted to result from growth on the Boltaña Anticline, which increased gradient and slope instability along the western basin margin that triggered mass failure (MTCs). These same type MTCs are pervasive into the overlying Guaso system, indicating continued fold growth through Guaso depositional time.

Additional data used to constrain the timing of Boltaña Anticline growth is the 3-D structural model. The shift in system axes trends to a more north-south orientation with each successive syn-growth system (Fig. 4.47). This is attributed to the development of the Boltaña Anticline backlimb during late Ainsa depositional time that deflects the southwest shift in system axes to a more southern orientation.

5.1.2.3 Timing of Growth on the Añisclo Anticline

The base-Ainsa structural surface shows the presence of the San Vicente and Buerba Synclines (Fig. 4.37). These two synclines reflect syn-depositional paleo-lows adjacent to the Añisclo Anticline. These trends are not present in the base-Morillo structural surface indicating that these structural lows were filled during Ainsa depositional time. Therefore, the Añisclo Anticline, that bounds the northern margin of the basin, was active during or immediately prior to the earliest stages of the Ainsa unit deposition and ceased during late or early Ainsa depositional time. The base-Ainsa structural surface indicates that the San Vicente syncline was a more pronounced low than the Buerba Syncline during Ainsa deposition. This growth geometry is also reflected in the Ainsa system sand distribution and isopach map, which is discussed later in this chapter.

5.1.2.4 Later Tectonic Events

A final stage of growth in the basin is interpreted to be associated with a regional basement involved thrusting event that took place in the Late Eocene to Early Oligocene (Farrell *et al,*. 1987). This final stage of growth manifests itself in Ainsa Basin in two ways. First, is the development of an imbricate detachment fold beneath the Boltaña Anticline fault-propagation fold. The timing of growth for this deep structure is late as the large erosional cut filled with Eocene-Oligocene age Campodarbe fluvial strata on the Boltaña Anticline forelimb is tilted westward (Fig. 4.21). This fluvial fill above the Boltaña Anticline is interpreted to represent a growth wedge related to the imbricate, deep detachment fold activity. The stratal dip of this wedge is the same as the western limb of the imbricate detachment fold (1, Fig. 5.2). Second, is the development of the Peña Montanesa imbricate thrust system (as described in section 4.3) (Farrell *et al,*. 1987). Low angle, northeast dipping thrusts and associated folds detach within the Tertiary units (not the the regional Triassic layer) and deform the oldest systems of basin-fill in the northeast part of the basin (Fig. 4.1b) (Casas *et al.*, 2002). One of the westernmost structures associated with this event is the Las Almazuras Thrust, which overrides the axis of the Mediano Anticline (Figures 4.1b and 4.27). This cross-cutting relationship supports the conclusion of Farrell *et al.* (1987) that development of the Peña

Montanesa imbricate thrust system occured after deposition of the Ainsa Basin-fill succession and during the regional Late Eocene-Early Oligocene basement involved thrusting event.

5.2 Relationship between Sand Distribution and Depocenter Location in Growth Basins

Another primary goal of this research is to better understand gross sand distribution in deepwater basins in compressional settings, particularly its relationship to depocenter shifts through time. Isopach maps generated in this study illustrate variation within three depositional units (Ainsa, Morillo, and Guaso). These units are defined by condensed sections which are time correlative surfaces that drape basin paleobathymetry. Therefore, isopach maps that indicate thickness variation represent a good proxy for depocenter identification. Isopach maps of the Ainsa, Morillo, and Guaso units are compared to sand distribution maps. The resulting maps show a strong correlation between sand distribution and isopach thicks (Figures 5.4 to 5.8).

It is important to note that the isopach maps are not corrected for decompaction. Thickness values that correlate with sand distribution are likely slightly exaggerated due to the lower compaction values in sandstones relative to shale. In order to constrain the magnitude of change between the decompacted and compacted states for the Ainsa deepwater systems, the Ainsa unit isopach is compared with a decompaction example from the Central Graben of the North Sea (Allen and Allen, 1990) that was used as an analog for past decompaction studies in the Ainsa Basin (Poblet *et al.*, 1998). Allen and Allen (1990) model a decompacted sandstone unit thickness of 800 m to decrease in thickness by 24% to 650 m at a burial depth of ~2 km. A shale unit is also modeled with a decompacted thickness of 850 m decreasing in thickness by 46% to 460 m at a burial depth of ~ 2km. Assuming a 2 km burial of the Ainsa unit, a decompacted shale-dominated thin on the isopach map is compared to a sand-rich thick (~20% N:G) using the same thickness reduction percentages, corrected for relative thickness and N:G of the Ainsa unit, to generally test if isopach thickness trends are maintained in a decompacted state. A shale-dominated point on the isopach with a thickness of 450 m (D, Fig. 4.37) is compared to a sand-rich point (~20% N:G) with a thickness of 700 m (A, Fig. 4.37). In a decompacted state, the shale-dominated point thickness is calculated to be ~657 m (+ 46% from compacted thickness). In a decompacted state, the sand-rich portion (~20% N:G) is calculated to be ~990 m (+41 % from the compacted thickness). This rough calculation illustrates that the isopach trends are likely maintained in a decompacted state, which is largely due to the relatively low overall N:G values for the Ainsa unit, even in locations where major sand intervals are present.

In addition to correction for decompaction, additional uncertainty in the isopach maps is associated with error involved in the surface construction, which is discussed below.

5.2.1 Ainsa Stratigraphic Unit

The Ainsa isopach map is compared individually to the Ainsa I, II, and III sand distribution maps from Pickering and Corregidor (2000). The Ainsa I sand interval is confined to the eastern portion of the map and follows the north-northwest trend present in the Ainsa isopach map thick toward the San Vicente Syncline, where the Ainsa isopach reaches a maximum thickness of 700 m (A, Fig. 5.4). The focusing of the Ainsa

I sands within the San Vicente Syncline is likely a result of channel deflection by the Añisclo Anticline (Pickering and Corregidor, 2000).

The Ainsa II sand distribution follows a similar trend, however shows a westward shift compared to Ainsa I and is not entirely confined to the San Vicente Syncline (Fig. 5.5). This possibly indicates the complete filling of the accommodation space created by the Añisclo Anticline. Therefore, Ainsa II deposition coincides with the cessation of fold growth (as discussed in section 5.1.2.3.).

The Ainsa III sand interval shows a broader distribution across the northwestern portion of the map and does not appear to directly correlate to any isopach trends (Fig. 5.6). Only the Ainsa III sand interval is present over the isopach thin displayed in the northwestern portion of the map (A, Fig. 5.6). This thin corresponds to the western limb of the Buerba Syncline. The presence of Ainsa III sands over this thin indicate that the Buerba Syncline was likely filled by the time of Ainsa III deposition. Overall, the sand intervals that comprise the Ainsa unit show a strong correlation with the N-NW trending isopach thick that extends across the Ainsa isopach map.

5.2.2 Morillo Stratigraphic Unit

The Morillo isopach is compared to a paleobathymetric map showing sand-filled channel and MTC distribution within the Morillo I stratigraphic unit (Moody, 2009). A strong correlation exists between the distribution of channels and the north-northwest trending, broad isopach thick that extends across the northern portion of the map. Also, note the large MTCs in the northwest part of the map that were generated from the backlimb of the Boltaña Anticline and merge with the channel system.

5.2.3 Guaso Stratigraphic Unit

The Guaso isopach map shows a thick in the northern central area that thins onto the Buil Syncline limbs where the Guaso I and II sand intervals are exposed (Fig. 5.8). This sandy strata crops out along the northern portion of the map and indicates a more northward sediment transport direction. The outward thinning geometry possibly reflects an increase in basin structural confinement, creating a ponded Guaso depocenter.

5.2.4 Isopach Geometries and Depocenter Shifts

The Ainsa and Morillo isopach maps display a wedge geometry that opens to the northeast (Figures 4.37 and 4.38). This geometry is consistent with the isopachs for the Ainsa and Morillo units of Fernández *et al.*, 2004. These wedge geometries have been attributed to foreland basin flexure that created a paleo-low that ran parallel to these isopach thickness trends (Fernández *et al.*, 2004). The north-northwest trends of these isopach thicks are approximately orthogonal to the south-southwest shift in system axes through time that was constrained by the dip vector projection method (Figures 4.44 and 4.47). This indicates that tectonically induced foreland flexure potentially played a role of shifting basin depocenters through time, independent of growth on the basin bounding growth structures.

Another potential mechanism to drive the shift in depocenters is the presence of the basement wedge beneath the Mediano Anticline. The restoration demonstrates that as the wedge propagates westward through time, a west dipping forelimb initiates and amplifies within the overlying pre-growth and syn-growth units (Fig. 5.2). The progressive growth of this forelimb potentially drove the westward shift of depocenters, as documented in the 3-D model (Figures 4.44 to 4.47). Movement on the basement wedge out of the plane of the A-A' section can be attributed to southward component of the shifts' trajectories (Fig. 4.47).

This is further evidenced by secondary deformation to the Mediano Anticline and Buil Syncline. The Boltaña Anticline axis maintains a constant north-south trend throughout its length in Ainsa Basin, while the Mediano Anticline and Buil Syncline both experience jogs in their axes from a north-south orientation to a north-northwest to south-southeast orientation (Fig. 4.1). Additionally, the system axes constrained in the 3-D model display shifts in their northern portions, however merge to the south where no shift is evident (Fig. 4.44). This suggests that early propagation of the wedge occurred syn-depositionally with the Ainsa-Sobrarbe systems to cause the depocenter shifts and continued to deform structures post-filling of the basin to create the jogs in the Mediano Anticline and Buil Syncline structural axes. The lack of secondary deformation to Boltaña Anticline axis indicates that the wedge did not propagate into Boltaña Anticline kink bands. This is supported by the cross section, as the wedge is limited to the eastern limb of the Buil Syncline and does not affect kink bands associated with the Boltaña Anticline (1, Fig. 5.2).

5.3 3-D Model Construction

The following sections summarize the implications of the dip vector projection methodology used in the 3-D model construction and the potential sources of error.

5.3.1 Lessons Learned

The 3-D model construction methodology (as described in section 3.3) is specifically developed to model syn-growth surfaces in a growth basin where depositional axes and stratigraphic unit thicknesses vary through time. In the case of the Buil Syncline and associated basin-fill, modeling of a single axial plane and axis for surface construction through the fold creates a subsurface geometry that does not reflect the complexity of the syn-growth units. Through the construction of separate system axes through dip vector projection, the shift in basin-fill depocenters can be constrained.

The Ainsa Basin is unique in that both synclinal axes are well exposed, which is necessary to define the zone of dip vector intersections that constrain the deepwater system axes in three-dimensions (as described in section 3.3.6.1). Additionally, this study benefited from two seismic profiles through the basin that provided insight into the overall subsurface system geometries at the basin-scale and constrained dip magnitude for the constructed axes and surfaces.

A dense data set is required to constrain the system axes with good confidence. Upwards of 100 measurements spread throughout the Buil Syncline axis and limbs were used in the final steps of construction for each surface (Fig. 3.13b). This does not include measurements that were discarded due to inconsistency with surrounding data. Multiple surface measurements taken within proximity of each other help the interpreter distinguish between measurements that reflect true regional bedding orientation and measurements that reflect bedding irregularities. Three-point problem measurements (as described in section 3.3.2) serve to densify the dataset, particularly in inaccessible regions.

The most constrained portion of the surfaces is in the northern region of the study area, where the systems' axes intersect the surface. Dip vectors from both synclinal limbs are in close proximity (<10km apart) and provide a robust control on the subsurface position of the axes and surface geometry. The least constrained portions of the surfaces are in the southern region of the study area, where the syncline broadens and dip vectors are projected to the axes from greater distances (>10 km apart). However, at a minimum the first ~800 m of any surfaces' projection from the contact into the subsurface can be considered well constrained. During the surface interpolation, the first 800 m of dip vector extensions from the contact were set as controls, or curves the surface was forced to fit, ensuring the upper portions of every surface are consistent with the surface data.

5.3.1 Error in Surface Construction

As in any subsurface modeling study, potential sources of error must be accounted for in order to assess the accuracy of surface construction. Fernández *et al.* (2004) estimates the error involved with surface construction using a 3-D dip domain method. Quantifiable sources of error relevant to the present study include: 1) acquisition of surface data (i.e. outcrop strike and dip measurements, 2) positioning of the digital elevation model, 3) seismic depth conversion, and 4) surface construction. Individual strike and dip measurements on average contain an error of 2 to 4°. Positioning of the DEM and aerial photo-drape is estimated to contain a maximum potential error of 20-30 m. An additional error associated with the DEM, not accounted for in Fernández *et al.*, 2004, is the topographic resolution of the map used for field mapping relative to the resolution of the DEM. The topographic maps used in field mapping have contour intervals of 10 m. The 90 m resolution of the DEM does not account for minor variations in the topographic surface that are identifiable on the topographic maps. Therefore, geologic contacts projected onto the DEM may account for surface variability that is absent on the DEM, and lead to inaccurate interactions of the contact with DEM topography. Seismic depth conversion likely contributes the greatest individual source of error. The error associated with seismic interpretation combined with a rough depth conversion unconstrained by well data is estimated to be upwards of 100 m.

It is important to note that no single source of data is relied on individually for the 3-D surface construction. Each set of data serves as one of several constraint on the position of a system axis. Due to the nature of the 3-D construction methodology, quantifying uncertainty beyond the steps taken to acquire and convert data to a usable format is not possible. The actual process of 3-D surface construction from a limited data set is interpretive, and therefore invalid data is able to be recognized and eliminated from the model. For example, in the case of dip vector projection to surface contacts (as described in section 3.3.5), bedding orientation measurements that strike oblique to perpendicular to the contact are eliminated in favor of measurements that exhibit a more parallel strike to the contact. This is particularly important in projecting data to a rugose contact (Fig. 3.12b).

Additionally, error is potentially encountered in the interpretation of the shape of the subsurface syncline geometry. The syncline shape was constrained by the SP-3 seismic profile, which provided a dip section of the fill units and suggests a sub-cylindrical fold geometry (Fig. 4.31). The shape of the surface projection was controlled by the length of the dip vectors projected from the surface contacts as they served as hard controls in surface interpolation. Consistency in syncline geometry can be maintained between surfaces by systematically projecting the vectors to pre-defined lengths.

5.4 Application to Petroleum Geology

The following sections describe the potential applications and the limitations of this research in regard to hydrocarbon exploration and development.

5.4.1 3-D Modeling Application and Limitations

The dip vector projection methodology used in this study has application in future basin exploration and development, particularly in data-poor environments. Three-dimensional geologic surfaces can be constructed from dip-vectors projected from limited datasets, such as seismic data and well dip-meter data, and extrapolated into poorly imaged structures that are difficult to constrain. Additionally, dip vectors created from seismic volumes or profiles can be used to extrapolate surfaces beyond the limits of the data and reconcile them with orientation data from a nearby well.

In an onshore setting, the dip vector projection methodology has the potential to better integrate surface and subsurface structural data. This study illustrates this concept through the identification of a seismic reflection on the SP-3 profile that correlated to the top of pre-growth carbonates on the Boltaña Anticline. Projected dip vectors from the top of the pre-growth surface contact were used to make the correlation between outrcop and seismic reflection and calibrate the seismic depth conversion (Fig. 3.10).

This methodology serves as a quick technique to construct surfaces in three-dimensions and meet all available constraints. The accuracy of the model is dependent both on the interpretation involved with construction (as described in section 5.3.1) and with the reliability and density of available data.

5.4.2 Ainsa Basin as an Analog

This study highlights the relationship between basin depocenters and sand distribution in a deepwater compressional growth basin. Considering the deepwater systems of the Ainsa Basin in a subsurface setting as potential hydrocarbon reservoirs, an increased understanding of basin depocenter location through time would clearly increase the chances of predicting the location of sand intervals. This is demonstrated by the comparison of isopach maps with gross sand distribution for the Ainsa, Morillo, and Guaso units. Basin depocenters are clearly recognized in seismic data (Fig. 5.9), while facies and architectural elements are often below the resolution of the data. Therefore, the ability to predict gross sand distribution at a location relative to its position to the basin depocenter is a powerful tool.

Gross sand distribution does not always correlate with basin depocenters. This is documented in the salt-withdrawal mini-basins of the Brazos-Trinity Slope System in the western Gulf of Mexico (Beaubouef *et al.*, 2003). Two stages of basin-fill are recognized for this system: an early "ponded" stage and a late "perched" stage (Beaubouef *et al.*, 2003). Units associated with the ponded stage of fill consist of sheet complexes that are confined to the deepest portion of the basin and display isopach patterns that are concordant with the basin depocenter. Units associated with the perched stage are highly channelized and display isopach values that are discordant with the basin depocenter. The transition from the ponded to perched stage is attributed to a progressive shallowing of gradient and decrease in basin confinement (Beaubouef *et al.*, 2003). Therefore, knowledge of the stage of fill (perched or ponded) associated with any given stratigraphic unit may be critical in determining whether basin depocenters can serve as a reliable predictor of sand distribution.

While knowledge of the basin depocenter shifts can increase the likelihood of predicting sand distribution, it may not serve as a high resolution predictor of reservoir quality. This is demonstrated for the Morillo system by Moody (2009), where the reservoir quality changes from the proximal to distal position. Highest sand connectivity and greatest potential reservoir volume occurs in the proximal position on the eastern syncline limb where channels stack laterally. While this region of high quality reservoir correlates to the Morillo isopach thick, it represents a portion of a broader Morillo isopach thickness trend that likely contains variable reservoir quality and channel connectivity (Fig. 5.7).

Finally, the model presented for the development of the basin bounding structures can be used as an analog for modeling other fold and thrust systems, as similar structures are observed in other fold and thrust settings (i.e. Canadian Rockies, offshore Brunei, offshore Nigeria, deep Gulf of Mexico). This study demonstrates that understanding the timing of structural growth has major implications for prediction of reservoir distribution in deepwater systems where topographic confinement plays a primary role in sand distribution.

5.5 Future Work

Future work that will serve to improve and expand upon the results of this study includes the following:

1) The addition of key stratigraphic surfaces within the condensed section bound units to the 3-D model (i.e. channel complex boundaries, intra-unit condensed sections) will serve to improve on the understanding of the 3-D stratigraphic architecture of each unit, allowing further development of the deepwater systems as reservoir analogs. The initial condensed section surfaces serve as an initial framework and constraint for further surface construction.

2) 3-D decompaction and backstripping will serve to constrain approximate sediment volumes and produce corrected isopach maps.

3) A detailed comparison of gross sand distribution and depocenter shifts between the Ainsa Basin and subsurface and modern examples will provide further insight into this relationship. Understanding how the relationship between gross sand distribution in the Ainsa Basin compares to other systems will serve to further develop the basin as an analog and also identify other controlling factors that may play role in the relationship between basin depocenters and gross sand distribution.

4) Extending the study area outside of the basin to the south and east of the Mediano Anticline, where a complex zone of deformation cuts the southern Mediano Anticline axis, will provide insight into post-folding structural activity. Additionally, extending the study area to the west into Jaca Basin will enhance the proximal to distal correlations of the deepwater systems and further document structures in the Jaca Basin that are related to Ainsa Basin's bounding structures.

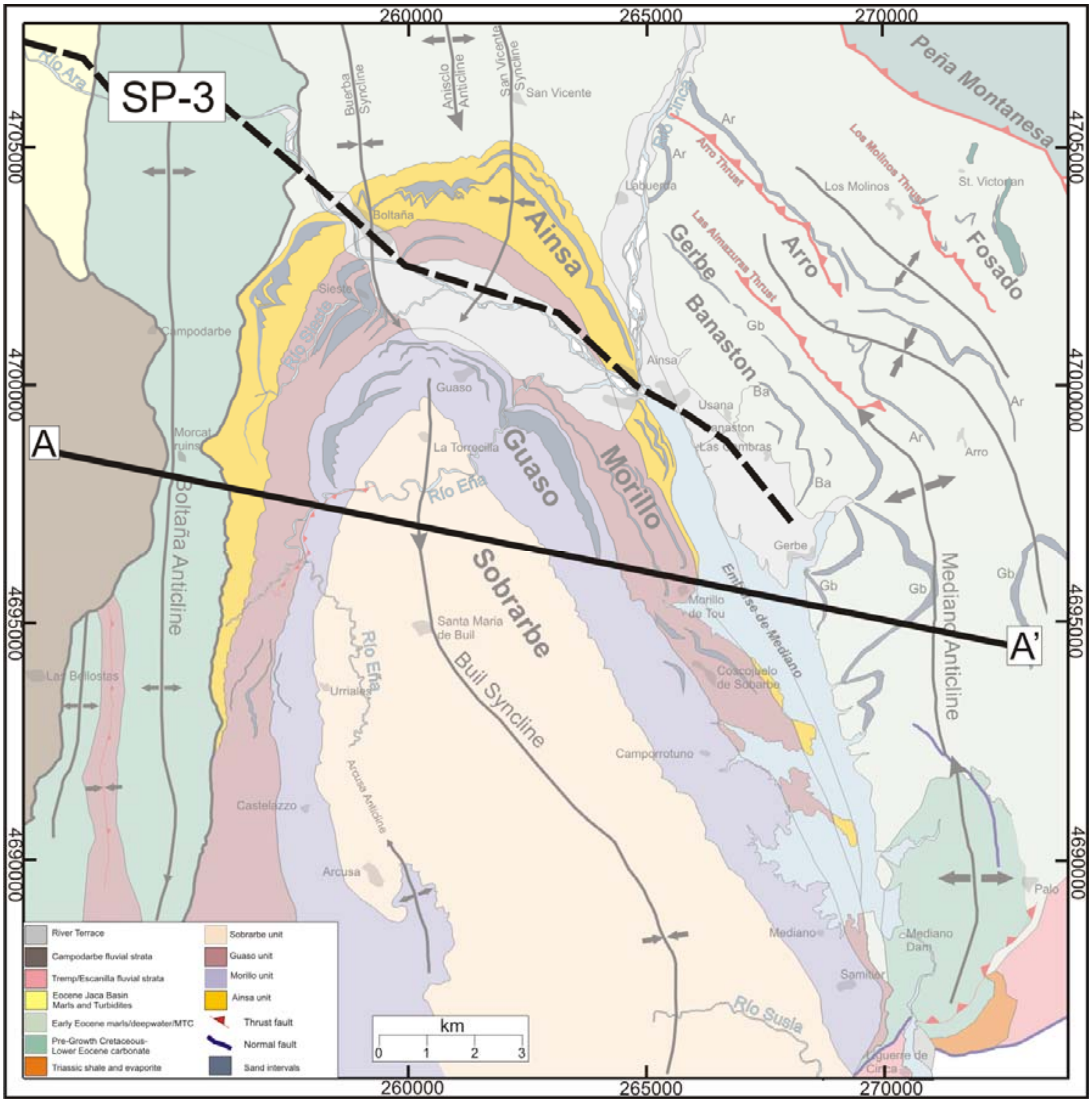

Figure 5.1: Location map of the restored structural cross section (A-A') and the position of the SP-3 seismic profile that was used to constrain the cross section construction.

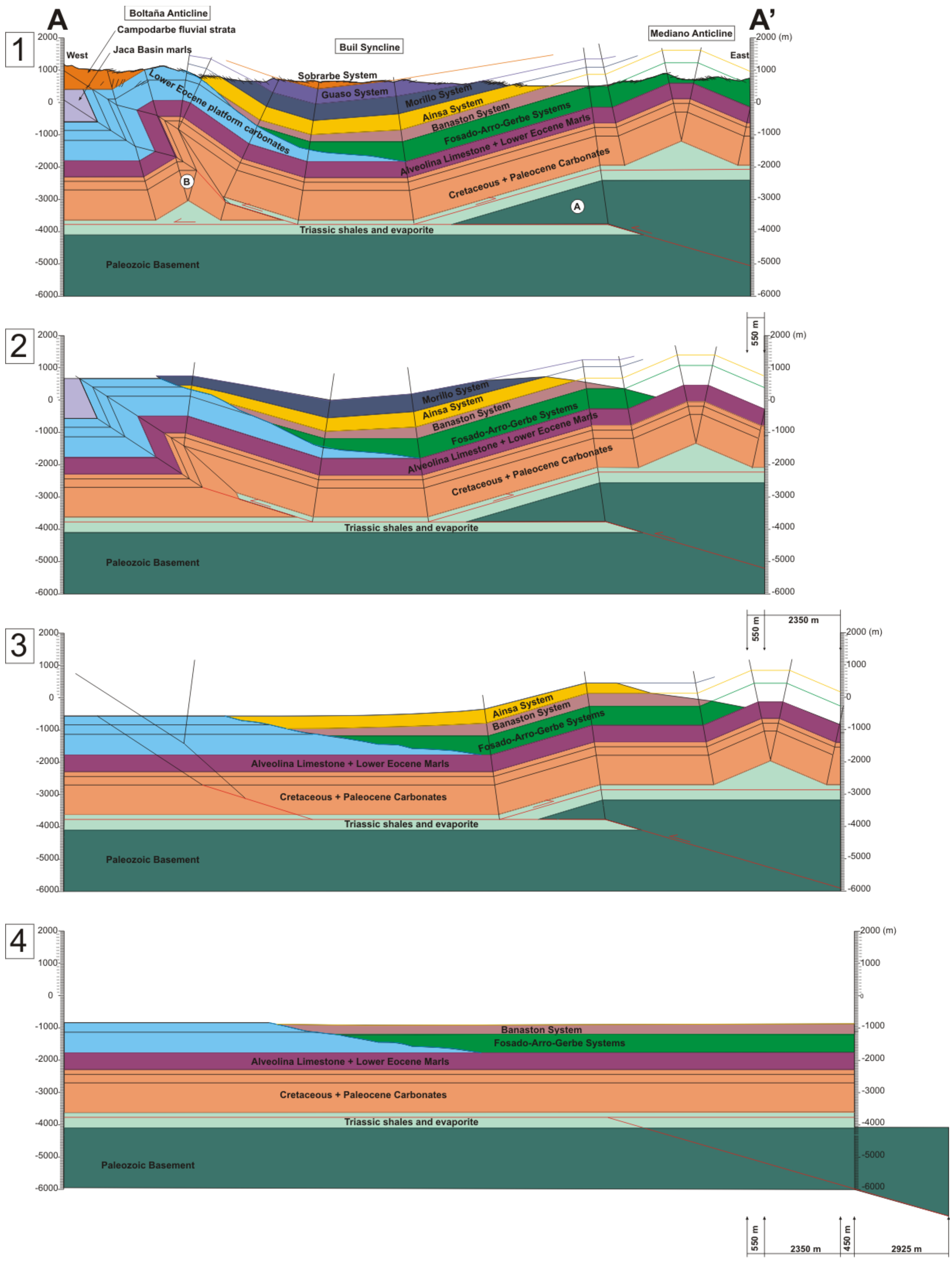

Figure 5.2: Palinspastic restoration of the Ainsa Basin and bounding structures. The restoration is performed in four steps. 1) Present day structural configuration. 2) Restoration of the lower Boltaña imbricate detachment fold. 3) Restoration of the upper Boltaña fault-propagation fold. 4) Restoration of the basement wedge and Mediano Anticline.

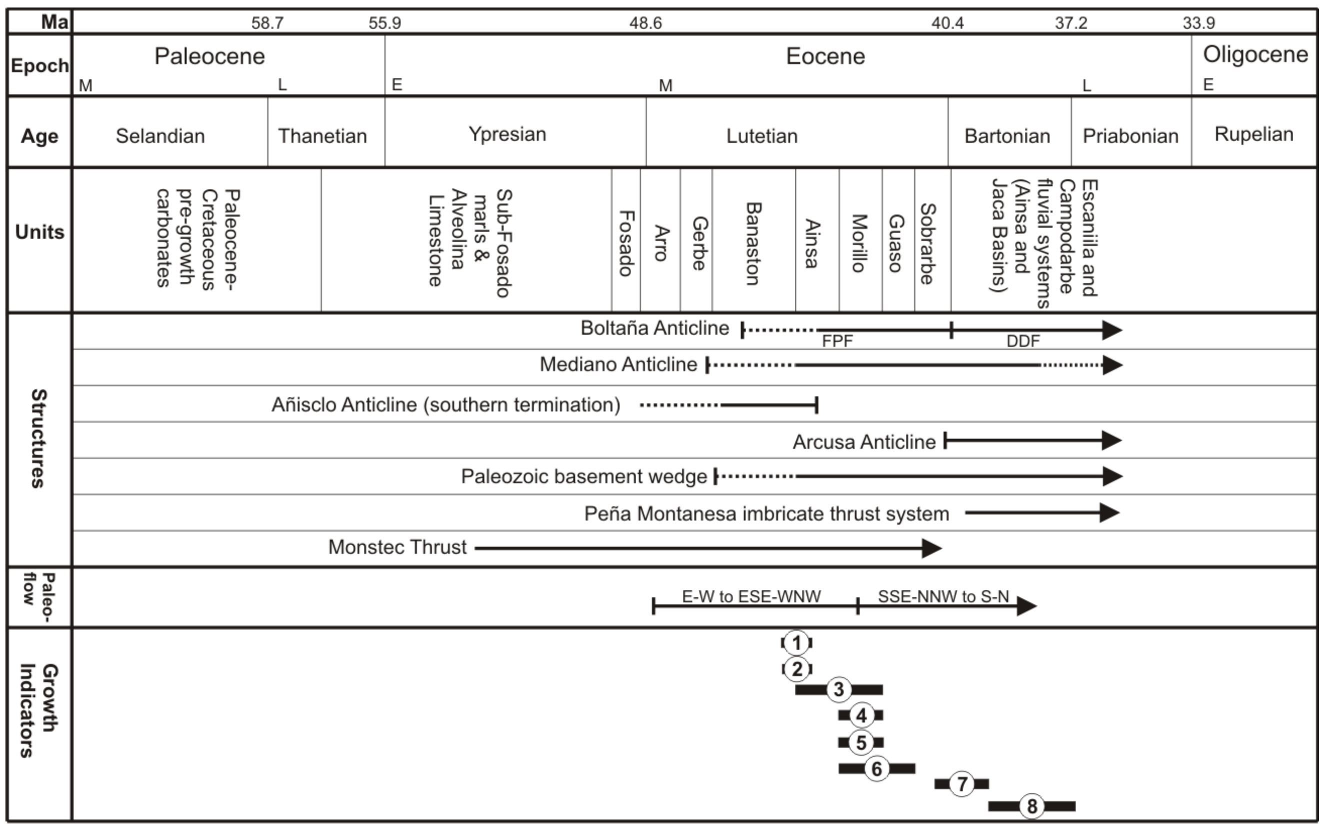

Figure 5.3: Stratigraphic units and structures of the Ainsa Basin compared to the geologic time scale of Gradstein *et al*. (2005). Timing of Ainsa Basin fill is after Pickering and Bayliss (2009). Solid lines next to structure names indicate a known period of growth. Dashed lines denote a period of growth that is either speculative or highly subdued. Paleoflow directions are regional trends in Ainsa Basin. FPF= fault-propagation fold, DDF= deep detachment fold, 1: Ainsa onlap (Mediano), 2: base-Ainsa structural surface (Añisclo), 3: Ainsa and Morillo paleoflow across Mediano axis (Mediano), 4: intra-Morillo canyon (Mediano), 5: Morillo paleocurrent deflection (Boltaña FPF), 6: Morillo and Guaso MTCs (Boltaña FPF), 7: intra-Sobrarbe growth wedge (Arcusa), 8: Campodarbe fluvial strata growth wedge (Boltaña DDF). Growth indicators are discussed in section 5.1.2.

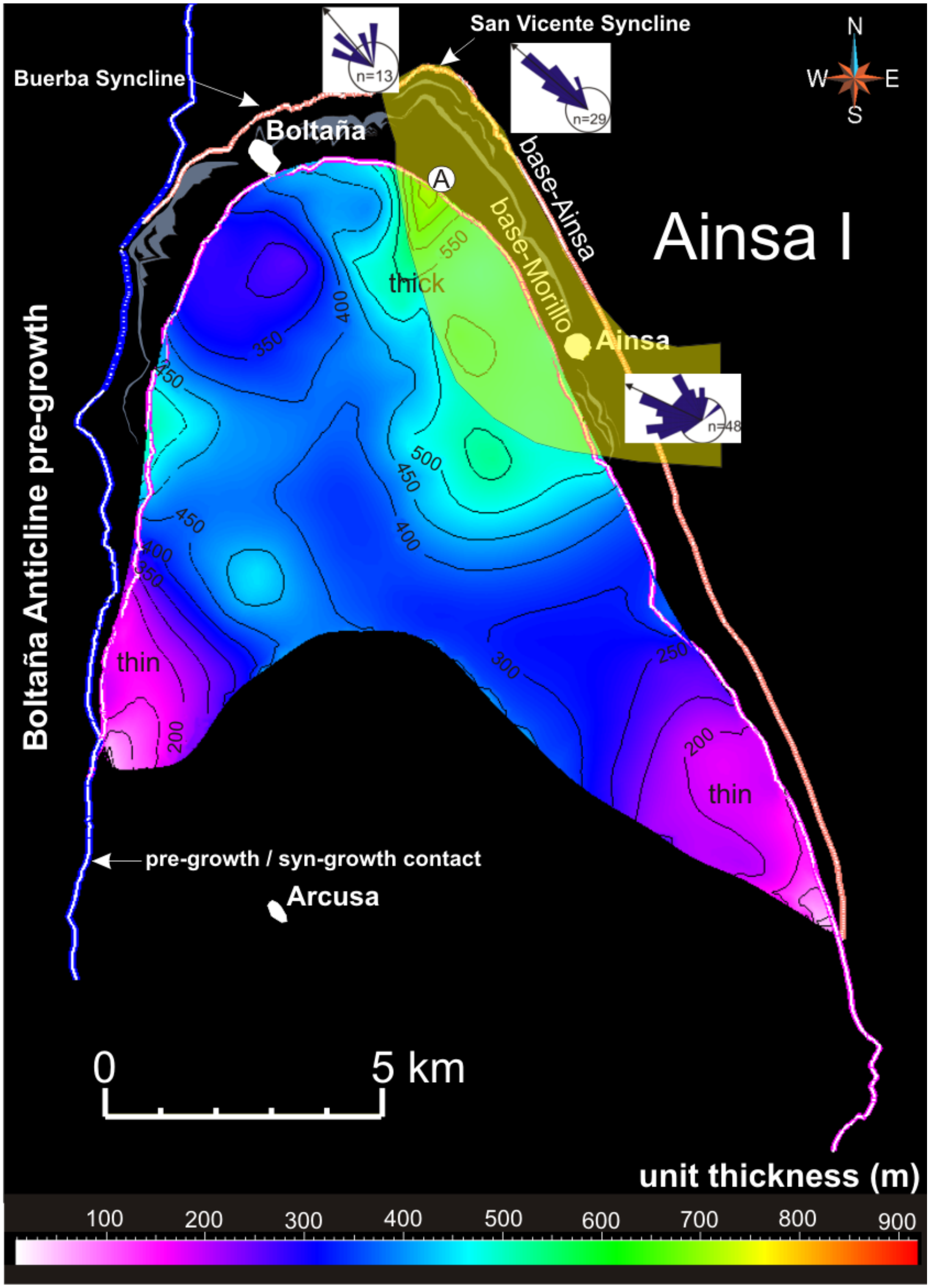

Figure 5.4: Distribution of the Ainsa I sand interval (shaded region) overlain on the Ainsa unit isopach map. Paleocurrents are from Pickering and Corregidor (2005). C.I.= 50 m.

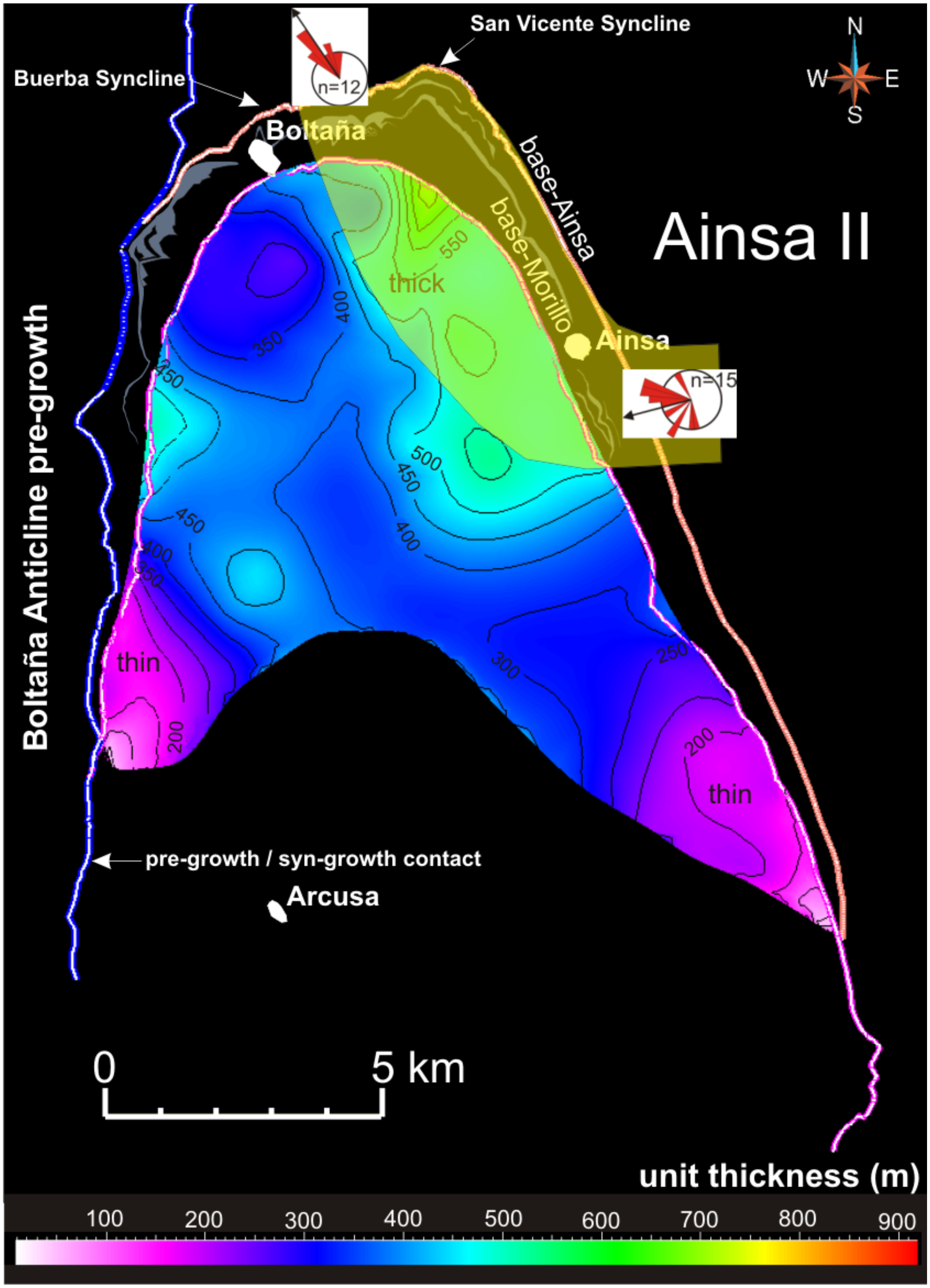

Figure 5.5: Distribution of the Ainsa II sand interval (shaded region) overlain on the Ainsa unit isopach map. Paleocurrents are from Pickering and Corregidor (2000). C.I.= 50 m.

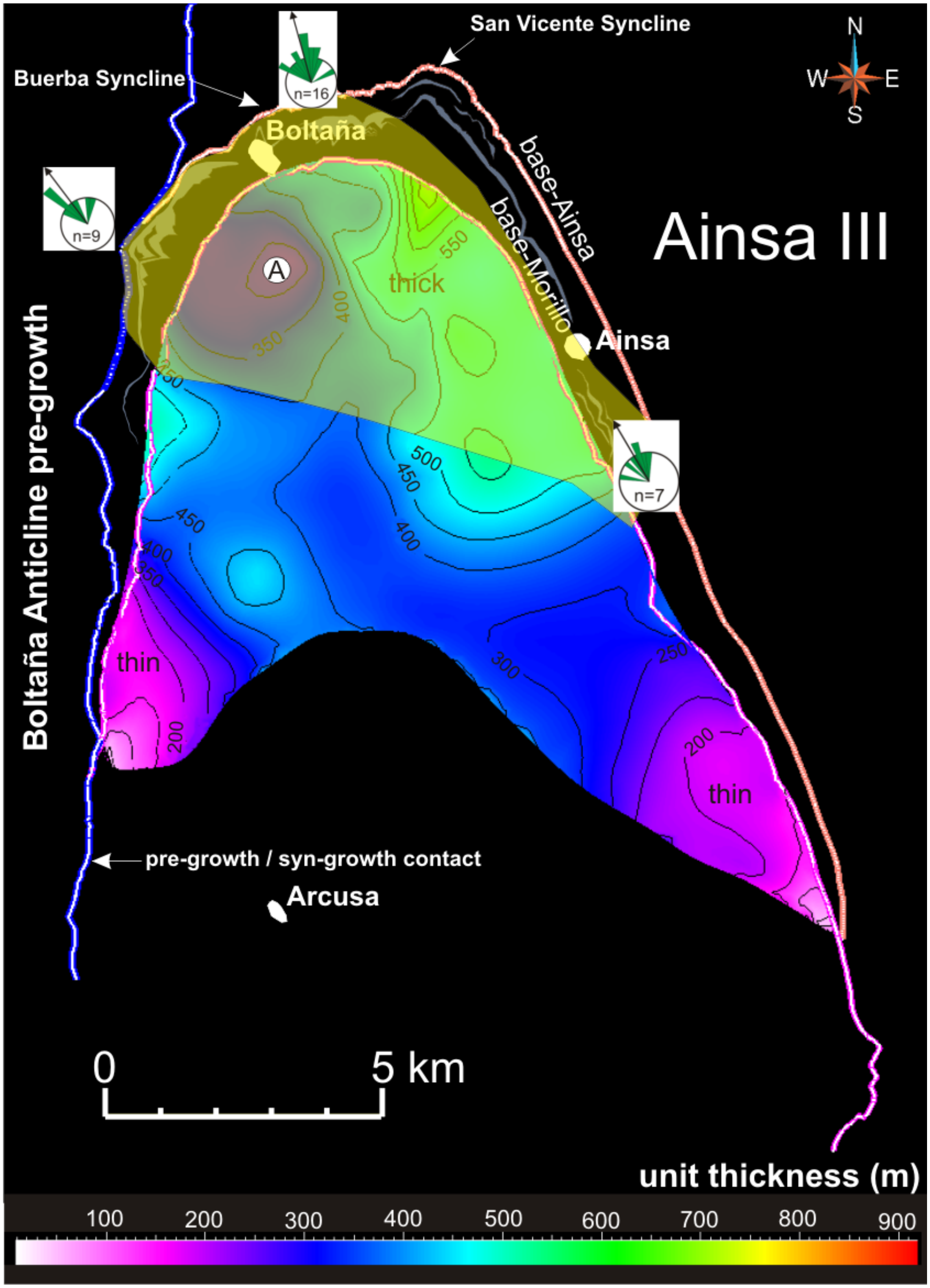

Figure 5.6: Distribution of the Ainsa III sand interval (shaded yellow zone) and overlain on the Ainsa unit isopach map. Paleocurrent measurements are from Pickering and Corregidor (2000). C.I.= 50 m.

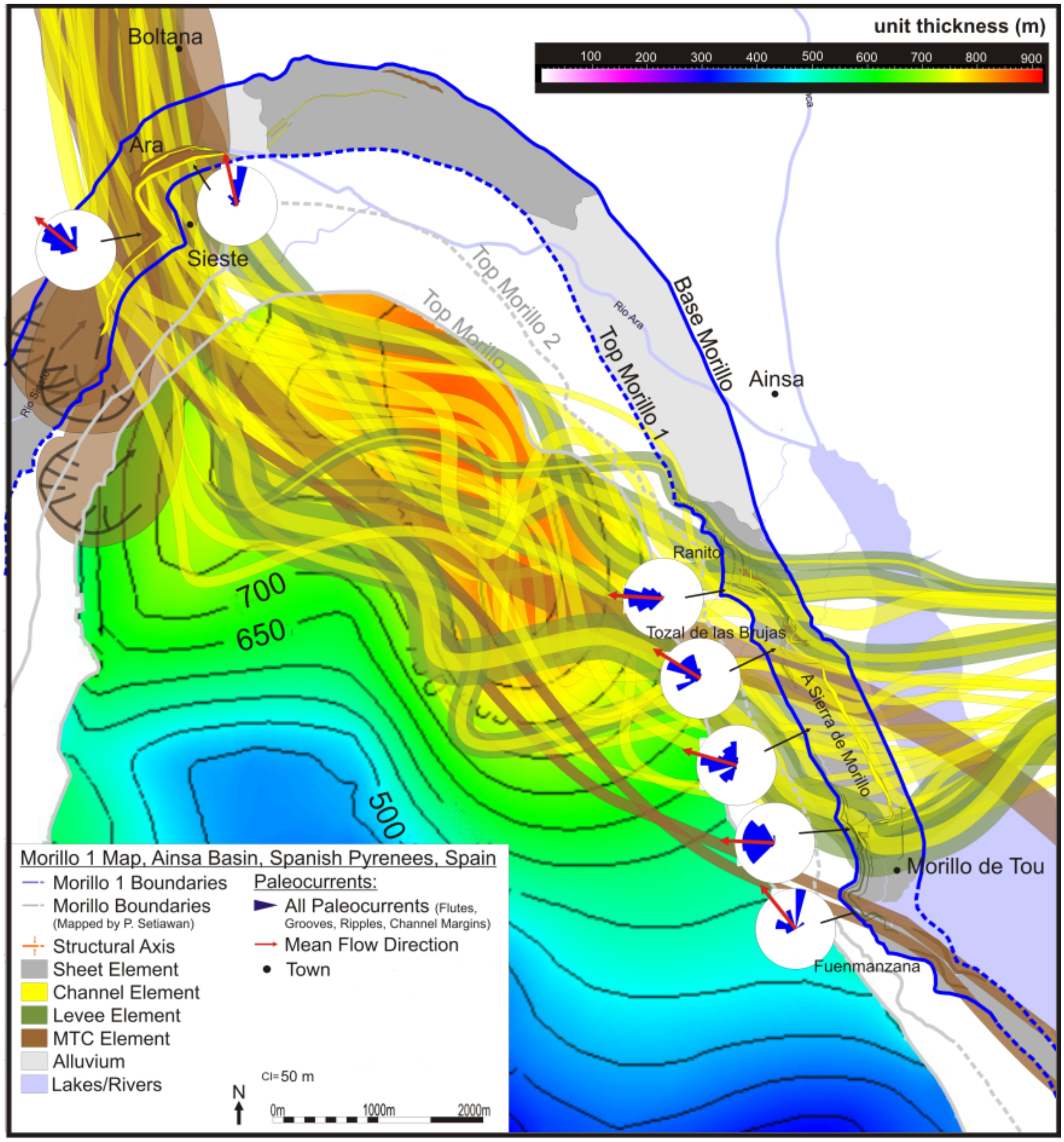

Figure 5.7: Paleogeographic map of the Morillo I stratigraphic unit and Morillo I paleocurrent measurements overlain on the Morillo unit isopach map. C.I.= 50 m (modified from Moody, 2009).

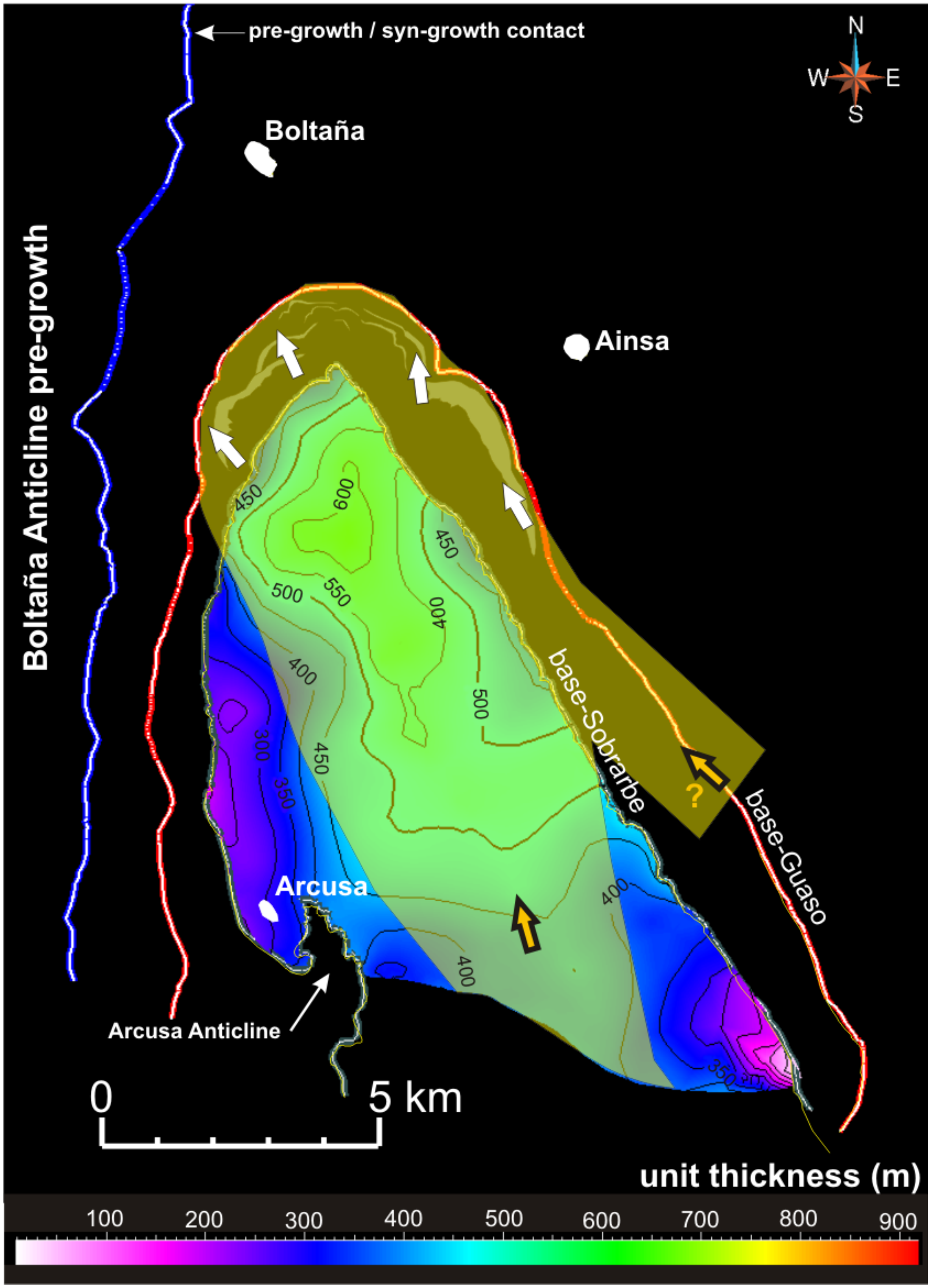

Figure 5.8: Distribution of the Guaso I and II sand intervals (shaded yellow zone) overlain on the Guaso unit isopach. White arrows represent outcrop paleocurrent measurements. Yellow arrows indicate interpreted direction of sediment input. Paleocurrents are from the present study and Sutcliffe and Pickering (2009). C.I.= 50 m.

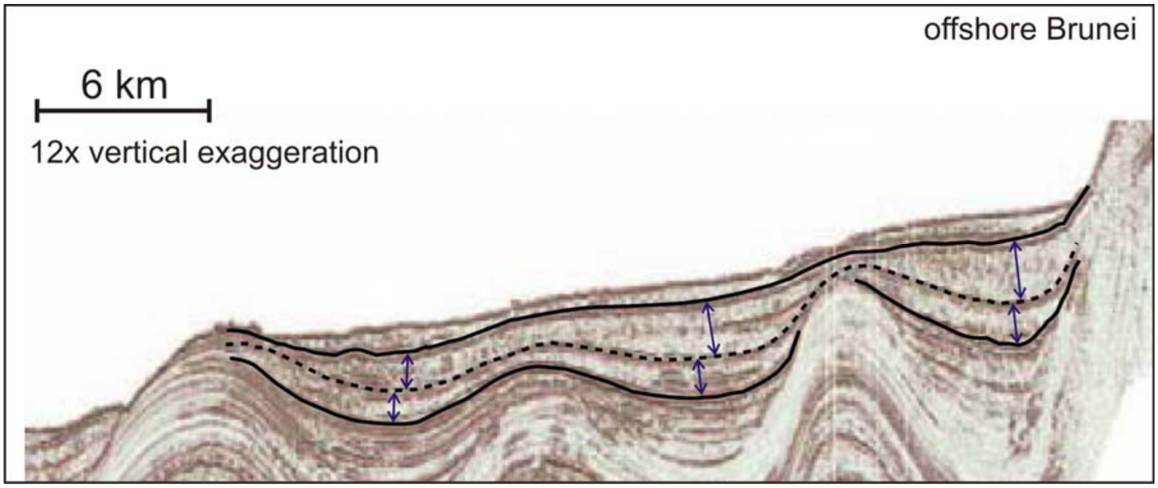

Figure 5.9: Interpreted seismic profile of a piggyback basin from offshore Brunei. Arrows reflect the changes in sub-basin depocenters driven by growth on basin bounding and intra-basinal anticlines. Transparent intervals between the interpreted surfaces represent stacked sediment gravity flows (modified from Morley and Leong, 2008).

CHAPTER 6

CONCLUSIONS

This chapter summarizes the concepts, methods, results, and research applications discussed in this thesis. The main conclusions of this study are the following:

1) This study presents a new approach to mapping the Eocene deepwater systems of the Ainsa Basin fill through the identification of condensed section bounding surfaces, permitting the correlation of syn-growth systems on a chronostratigraphic basis from the basin margins to axis.
2) Restoration of the Ainsa Basin structures indicates that strata above the regional Triassic detachment layer underwent 3350 m of shortening (13.6% shortening). A Paleozoic basement wedge beneath the Mediano Anticline translates slip to the structures overlying the regional Triassic detachment layer.
3) Though the integration of published and newly acquired stratigraphic and structural data, this study suggests a timing scenario for activity on the Ainsa Basin bounding growth structures that is consistent with observed structural geometries and stratigraphic indicators of growth.
4) This study proposes a multi-phase growth history for the Boltaña Anticline: 1) a Middle Eocene stage of growth as a fault-propagation fold, coeval with the Ainsa, Morillo, and Guaso deepwater systems, and 2) a Late Eocene to Early Oligocene stage of growth on a deep, imbricate detachment fold. Mediano Anticline growth initiated during Ainsa deposition and propagated northwards through time. A

5) A northwest-southeast trending wedge that opens to the northeast is present within Ainsa and Morillo units. First identified by Fernandez *et al.* (2004), the wedge is attributed to foreland flexure. This wedge runs perpendicular to the south-southwest shift in system axes that occurs between the Ainsa, Morillo, Guaso, and Sobrarbe units, indicating that foreland flexure is playing a role in the shift of basin depocenters, independent of activity on the basin growth structures.
6) Gross sand distribution within the Ainsa, Morillo, and Guaso units shows a strong correlation to unit isopach thicks, a proxy for basin paleo-depocenters, suggesting that basin depocenters serve as a good predictor for the position of reservoir-quality strata in a growth basin.
7) This study introduces a new dip vector projection methodology for 3-D structural surface construction from surface data. This methodology is particularly applicable to the modeling of syn-growth surfaces in a growth basin where depositional axes and stratigraphic unit thicknesses vary through time.
8) The dip vector projection methodology has application in hydrocarbon exploration and development, particularly in modeling structure in data-poor environments, permitting the extrapolation of three-dimensional surfaces that fit all available data.

9) This study can be used as an analog for complex tectono-stratigraphic settings where syn-depositional structures play a major role in the distribution and evolution of deepwater reservoirs.

REFERENCES CITED

Allen, P. A. and J. R. Allen, 1990, Basin analysis: principles and applications: Oxford, United Kingdom, Blackwell Scientific Publications, 451 p.

Arbués, P., D. Mellere, O. Falivene, O. Fernández, J. A. Muñoz, M. Marzo, and J. M. de Gibert, 2007, Context and architecture of the Ainsa-1-quarry channel complex, Spain, *in* T. H. Nilsen, R. D. Shew, G. S. Steffens, and J. R. J. Studlick, eds., Atlas of deep-water outcrops: American Association of Petroleum Geologists Studies in Geology 56, CD-ROM, 20 p.

Beaubouef, R T, V. Abreu, and J.C. Van Wagoner, 2003, Basin 4 of the Brazos-Trinity slope system, western Gulf of Mexico; the terminal portion of a late Pleistocene lowstand systems tract (abs.): Society of Economic Paleontologists Gulf Coast Section Research Conference, vol. 23, p.45-66.

Boyer, S.E., 1995, Sedimentary basin taper as a factor controlling the geometry and advance of thrust belts: American Journal of Science, v. 295, p. 1220-1254.

Bradley, D., and L. Hanson, 1998, Paleoslope analysis of slump folds in the Devonian Flysch of Maine: The Journal of Geology, v. 106, p. 305-318.

Burbank, D.W., J. Verges, J.A. Muñoz, and P. Bentham, 1992, Coeval hindward- and forward-imbricating thrusting in the south-central Pyrenees, Spain: Timing and rates of shortening and deposition: Geological Society of America Bulletin, v. 104, p. 3-17.

Carminati, E., 2008, Neglected basement ductile deformation in balanced-section restoration: An example from the Central Southern Alps (Northern Italy): Tectonophysics, v. 463, no. 1, p. 161-166.

Casas, A.M., R. Soto, and B. Martinez-Peña, 2002, Geometrical relationships between unconformities and subsequent folding: the Arro fold system (southern Pyrenees): C.R. Geoscience, v. 334, p. 765-772.

Chapple, W.M., 1978, Mechanics of thin-skinned fold and thrust belts: Geological Society of America Bulletin, v. 89, p. 1189-1198.

Clark, J. D. and K. T. Pickering, 1996, Submarine channels: processes and architecture: London, Vail Press, 231 p.

Clayton, C.J., 1993, Deflection versus reflection of sediment gravity flows in the late Llandovery Rhuddant Grits turbidite system, Welsh Basin: Journal of the Geological Society, London, v. 150, p. 819-822.

Clevis, Q., G. de Jager, W. Nijman, and P.L. de Boer, 2004, Stratigraphic signatures of translation of thrust-sheet top basins over low-angle detachment faults: Basin Research, v. 16, p. 145-163.

Cobbold, P.R. and M. Percevault, 1983, Spatial integration of strains using finite elements: Journal of Structural Geology, v. 5, no. 3/4, p. 299-305.

Cobbold, P.R., 1979, Removal of finite deformation using strain trajectories: Journal of Structural Geology, v. 1, no.1, p. 67-72.

Coney, P.J., J.A. Muñoz, K.R. McClay, and C.A. Evenchick, 1996, Syntectonic burial and post-tectonic exhumation of the southern Pyrenees foreland fold-thrust belt: Journal of the Geological Society of London, v. 153, p. 9-14.

Cook H.E., and H.T. Mullins, 1983, Basin margin environment, in: Schole, P.A., Bebout, D.G., and Moore, C.H., eds: Carbonate depositional environments: American Association of Petroleum Geologists Memoir 33, p. 539-618.

Cooper, M.A., 1983, The calculation of bulk strain in oblique and inclined balanced sections: Journal of Structural Geology, v. 5, no. 2, p. 161-165.

Cooper, M.A. and P.M. Trayner, 1986, Thrust-surface geometry: implications for thrust-belt evolution and section balancing techniques: Journal of Structural Geology, v. 8, no. 3/4, p. 305-312

Coward, 1992, Section construction and balanced sections: SAPEC courses, v. 3, p. 3.1-3.23.

Dahlstrom, C.D.A., 1990, Geometric constraints derived from the law of conservation of volume and applied to evolutionary models for detachment folding: American Association of Petroleum Geologists Bulletin, v. 74, no. 3, p. 336-344.

Davis, D., J. Suppe, and F.A. Dahlen, 1983, Mechanics of Fold-and-Thrust Belts and Accretionary Wedges: Journal of Geophysical Research, v. 88, p. 1153-1172.

DeCelles, P.G., and K.A. Giles, 1996, Foreland basin systems: Basin Research, v. 8, p. 105-123.

De Donatis, M., 2001, Three-dimensional visualization of the Neogene structures of an external sector of the northern Apennines, Italy: American Association of Petroleum Geologists Bulletin, v. 85, p. 419–431.

de Kemp, E.A., 1998, Three-dimensional projection of curvilinear geological features through direction cosine interpolation of structural field observations: Computers & Geosciences, v. 24, no. 3, p. 269-284.

de Kemp, E.A., 2000, 3-D visualization of structural field data: examples from the Archaean Caopatina Formation, Abititi greenstone belt, Quebec, Canada: Computers and Geosciences, v. 26, p. 509-530.

Dickinson, W.R., and C.A. Suczek, C.A., 1979, Plate tectonics and sandstone compositions: American Association of Petroleum Geologists Bulletin, v. 63, p. 2164-2182.

Dreyer, T., J. Corredigor, P. Arbués, and C. Puigdefebregas, 1999, Architecture of the tectonically influenced Sobrarbe deltaic complex in the Ainsa Basin, northern Spain: Sedimentary Geology, v. 127, p. 127-169.

Elliott, D., 1983, The construction of balanced cross-sections: Journal of Structural Geology, v. 5, no. 2, p. 101.

Epard, J.L., R.H. Groshong Jr., 1995, Kinematic model of detachment folding including limb rotation, fixed hinges and layer-parallel strain: v. 247, p. 85-103.

Erslev, E.A., 1991, Trishear fault-propagation folding: Geology, v. 19, p. 617-620.

Farrell, S.G., G.D. Williams, and C.D. Atkinson, 1987, Constraints on the age of movement of the Montsech and Cotiella Thrusts, south central Pyrenees, Spain: Journal of the Geological Society, London, v. 144, 1987, p. 907-914.

Fernández, O., J.A. Muñoz, P. Arbués, 2003, Quantifying and correcting errors derived from apparent dip in the construction of dip-domain cross-sections: Journal of Structural Geology, v. 25, p. 35-42.

Fernández, O., J.A. Muñoz, P. Arbués, and M. Marzo, 2004, Three dimensional reconstruction of geological surface: An example of growth strata and turbidite systems from the Ainsa Basin (Pyreness, Spain): American Association of Petroleum Geologists Bulletin, v. 88, no. 8, p. 1049-1068.

Fitzgerald, P.G., J.A. Muñoz, P.J. Coney, and S.L. Baldwin, 1999, Asymmetric exhumation across the Pyrenean Orogen; implications for the tectonic evolution of a collisional orogen: Earth and Planetary Science Letters, v. 173, no. 3, p.157-170.

Freeth, S.J., and K.O. Ladipo, 1986, The development and restoration of syn-sedimentary faults: Earth and Planetary Science Letters, v. 78, p. 411-419.

Gradstein, F.M., J.G. Ogg, and A.G. Smith, 2005, A geologic time scale 2004: Cambridge University Press, p. 610.

Gratier, J., B. Guillier, A. Delorme, and F. Odonn, 1991, Restoration and balance of a folded and faulted surface by best-fitting of finite elements: principle and applications: Journal of Structural Geology, v. 13, no. 1, p. 111-115.

Groshong, R.H., 1999, 3-D Structural Geology: Berlin, Springer-Verlag, 324 p.

Guillaume, B., D. Dhont, and S. Brusset, 2008, Three-dimensional geologic imaging and tectonic control on stratigraphic architecture: Upper Cretaceous of the Tremp Basin (south-central Pyrenees, Spain): American Association of Petroleum Geologists Bulletin, v. 92, no. 2, p. 249-269.

Gupta, S. and P.A. Cowie, 2000, Processes and controls in the stratigraphic development of extensional basins: Basin Research, v. 12, no. 3-4, p.185-447.

Handin, J., R.V. Hager, M. Friedman, and J.N. Feather, 1963, Experimental deformation of sedimentary rocks under confining pressure: pore pressure tests: American Association of Petroleum Geologists Bulletin, v. 47, p. 717-755.

Hennings, P.H., J.E. Olson, and L.B. Thompson, 2000, Combining outcrop data and three-dimensional structural models to characterize fractured reservoirs: an example from Wyoming: American Association of Petroleum Geologists Bulletin, v. 84, no. 6, p. 830-849.

Husson, L., and J. Mugnier, 2003, Three-dimensional horizon construction from outcrop structural data, restoration, and strain field of the Baishai anticline, Western Nepal: Journal of Structural Geology, v. 25, p. 79-90.

Jolly, R.J.H., and L. Lonergan, 2002, Mechanisms and controls on the formation of sand intrusions: Journal of the Geological Society, London, v. 159, p. 605-617.

Labaume, P., E. Mutti, and M. Seguret, 1987, Megeturbidites: A depositional model from the Eocene of the SW-Pyrenean foreland basin, Spain: Geo-Marine Letters 7, p. 91-101

Labourdette, R., P. Cremeyrolle, and E. Remacha, 2008, Characterization of dynamic flow patterns in turbidite reservoirs using 3D outcrops analogues: Example of the Eocene Morillo turbidite system (south-central Pyrenees, Spain): Marine and Petroleum Geology, v. 25, p. 255-270.

Lévy, B. and J.L. Mallet, 1999, Constrained discrete fairing for arbitrary meshes: ALiCE GOCAD consortium.

Kneller, B.C., D. Edwards, W. McCaffrey, R. Moore, 1991, Oblique reflection of turbidity currents: Geology, v. 14, p. 250-252.

Kneller, B.C. and M.J. Branney, 1995, Sustained high-density turbidity currents and the deposition of thick massive sands: Sedimentology, v. 42, p. 607-616.

Maerten, L., D.D. Pollard, and F. Maerten, 2001, Digital mapping of three-dimensional structures of the Chimney Rock fault system, central Utah: Journal of Structural Geology, v. 23, p. 585-592.

Martinsen, O.J., T. Lien, R.G. Walker, and J.D. Collinson, 2003, Facies and sequential organization of a mud-dominated slope and basin floor succession: the Gull Island Formation, Shannon Basin, Western Ireland. Marine and Petroleum Geology, v. 20, p. 789-807.

Millington, J.J. and J.D. Clark, 1995, The Charo/Arro canyon-mouth sheet system, south-central Pyrenees, Spain: A structurally influenced zone of sediment dispersal: Journal of Sedimentary Research, v. B65, no. 4, p. 443-454.

Mitra, S., 1990, Fault-propagation folds: Geometry, kinematic evolution, and hydrocarbon traps: American Association of Petroleum Geologists Bulletin, v. 74, no. 6, p. 921-945.

Moody, J., 2009, Slope channel architecture and reservoir characterization in a growth basin, Eocene Morillo turbidite system (South-Central Pyrenees, Spain): Master's thesis, Colorado School of Mines, Golden, Colorado, (in prep).

Morley, C.K. and L.C. Leong, 2008, Evolution of deep-water synkinematic sedimentation in a piggyback basin, determined from three-dimensional seismic reflection data: Geosphere, v. 4, no. 6, p. 939-962.

Morris, S.A. and J. Alexander, 2003, Changes in flow direction at a point caused by obstacles during passage of a density current: Journal of Sedimentary Research, v. 73, no. 4, p. 621-629.

Moscardelli, L., Wood, L., and P. Mann, 2006, Mass transport complexes and associated processes in the offshore area of Trinidad and Venezuela: American Association of Petroleum Geologists Bulletin, v. 90, no. 7, p. 1059-1088.

Moss-Russell, A.C., 2009, The stratigraphic architecture of a prograding shelf- margin delta in outcrop, the Sobrarbe Formation, Ainsa Basin, Spain: Master's thesis, Colorado School of Mines, Golden, CO, (in prep).

Muñoz, J.A., K. McClay, and J. Poblet, 1994, Synchronous extension and contraction in frontal thrust sheets of the Spanish Pyrenees: Geology, v. 22, p. 921-924.

Muñoz, J. A., P. Arbués, and J. Serra-Kiel, 1998, The Ainsa basin and the Sobrarbe oblique thrust system: sedimentological and tectonic processes controlling slope and platform sequences deposited synchronously with a submarine emergent thrust system, in A. Melendez Hevia and A. R. Soria, eds., Field trip guidebook of the 15th International Association of Sedimentologists International Congress of Sedimentology, p. 213–223.

Mutti, E., 1977, Distinctive thin-bedded turbidite facies and related depositional environments in the Eocene Hecho Group (South-central Pyrenees, Spain): Sedimentology, v. 24, p. 107-131.

Mutti, E., M. Seguret, and M Sgavetti, 1988, Sedimentation and deformation in the Tertiary sequence of the Southern Pyrenees: Field Trip Guide 7, American Association of Petroleum Geologists Mediterranean Basins Conference, Nice, France.

Oertel, G., 1974, Unfolding of an antiform by the reversal of observed strains: Bulletin of the Geological Society of America, v. 85, p. 445-450.

Oertel G, and W.G. Ernst, 1978, Strain and rotation in a multilayered fold: Tectonophysics, v. 48, p.77-106.

Ori, G.G., and P.F. Friend, 1984, Sedimentary basins formed and carried piggyback on active thrust sheets: Geology, v. 12, p. 475-478.

Paton, D., M. Carr, B. Trudgill, H. Ortner, and D.A. Medwedeff, 2007, Alpine-scale 3D geospatial modeling: Applying new techniques to old problems: Geosphere, v. 3, no. 6, p. 527-549.

Poblet, J. and S. Hardy, 1995, Reverse modeling of detachment folds; application to the Pica de1 Aguila anticline in the South Central Pyrenees (Spain): Journal of Structural Geology, v. 17, no. 12, p. 1707-1724.

Poblet, J., K. McClay, F. Storti, and J.A. Muñoz, 1997, Geometries of syntectonic sediments associated with single-layer detachment folds: Journal of Structural Geology, v. 19, no. 3-4, p. 369-381.

Poblet, J., J.A., Munoz, A.Trave, and J.S. Kiel, 1998, Quantifying the kinematics of detachment folds using three dimensional geometry: Application to the Mediano anticline (Pyrenees, Spain): Geological Society of America Bulletin, v.110, no. 1, p. 111-125.

Pickering, K.T., and J. Corregidor, 2000, 3D reservoir-scale study of Eocene confined submarine fans, south-central Spanish Pyrenees (abs.): GCSSEPM Foundation 20th Annual Research Conference.

Pickering, K.T., and J. Corregidor, 2005, Mass-transport complexes (MTCs) and tectonic control on basin-floor submarine fans, Middle Eocene, South Spanish Pyrenees: Journal of Sedimentary Research v. 75, p. 761-783.

Pickering, K.T., and N.J. Bayliss, 2009, Deconvolving tectono-climate signals in deep-marine siliciclastics, Eocene Ainsa basin, Spanish Pyrenees: Seesaw tectonics versus eustasy: Geology, v. 37, no. 3, p. 203-206.

Puigdefábregas, C., J.A. Muñoz, and J. Vergés, 1992, Thrusting and foreland basin evolution in the Southern Pyrenees, in K.R. McClay ed., Thrust Tectonics: London, Chapman and Hall, p. 235-245.

Pyles, D., R. Bouroullec, C. Rourke, J. Clark, F. Harris, M. Sullivan, N. Drinkwater, D. Medwedeff, and C. Guzofski, 2007, Study of deepwater depositional systems at Chevron Center of Research Excellence (CoRE), Colorado School of Mines: Chevron Subsurface Characterization Forum, Houston, Texas.

Pyles, D.R. and R.M. Slatt, 2007, Stratigraphy of the Lewis Shale, Wyoming, USA: Applications to Understanding Shelf-edge to Base-of-slope Changes in Stratigraphic Architecture of Prograding Basin Margins, *in* T. H. Nilsen, R. D. Shew, G. S. Steffens, and J. R. J. Studlick, eds., Atlas of Deepwater Outcrops, American Association of Petroleum Geologists Studies in Geology 56, 504 p.

Pyles, D.R., 2008, Multiscale stratigraphic analysis of a structurally confined submarine fan: Carboniferous Ross Sandstone, Ireland: American Association of Petroleum Geologists Bulletin, v. 92, no. 5, p. 557-587.

Riba, O., 1976, Syntectonic unconformities of the Alto Cardener, Spanish Pyrenees: A genetic interpretation: Sedimentary Geology, v. 15, p. 213-233.

Rowan, M.G., 1997, Three-dimensional geometry and evolution of a segmented detachment fold, Mississippi Fan foldbelt, Gulf Mexico: Journal of Structural Geology, v. 19, no. 3-4, p. 463-480.

Saffar, M.A., 1993, Geometry of fault-propagation folds: methods and application: Tectonophysics, v. 223, 363-380.

Seguret, M., P. Labaume, and R. Madariaga, 1984, Eocene seismicity in the Pyrenees from megaturbidites of the south Pyrenean basin (Spain): Marine Geology, v. 55, p. 117-131.

Setiawan, P., 2009, Architectural elements and facies distribution along an actively growing deepwater basin margin, Eocene Morillo stratigraphic unit, Ainsa Basin, Spain: Master's thesis, Colorado School of Mines, Golden, Colorado, 224 p.

Shaw, J.H., E. Novoa, and C.D. Connors, 2004, Structural controls on growth stratigraphy in contractional fault-related folds, in K.R. McClay eds., Thrust tectonics and hydrocarbon systems: American Association of Petroleum Geologists Memoir, v. 82, p. 400-412.

Shaw, J.H., C.D. Connors, and J. Suppe, 2005, Structural interpretation methods, in Shaw, J.H., C.D. Connors, and J. Suppe, Seismic interpretation of contractional fault-related folds: American Association of Petroleum Geologists Seismic Atlas 53, p. 156.

Sibuet, J.C. Srivastava, and S.P. Spakman, W., 2004, Pyrenean orogeny and plate kinematics: Journal of Geophysical Research, v. 109, p. 1-18.

Silalahi, H.S.M.P., 2009, Stratigraphic architecture of slope deposits associated with prograding margins, Sobrarbe Formation, Ainsa Basin, Spain: Master's Thesis, Colorado School of Mines, Golden, Colorado, 146 p.

Soto, R., A.M. Casas, F. Storti, and C Faccenna, 2002, Role of lateral thickness variations on the development of oblique structures at the Western end of the South Pyrenean Central Unit: Tectonophysics, v. 350, p. 215-235.

Srivastava, S.P., H. Schouten, W.R. Roest, K.D. Klitgord, L.C. Kovacs, J. Verhoef, and R. Macnab, 1990, Iberian plate kinematics: a jumping plate boundary between Eurasia and Africa: Nature, v. 344, p. 756-758.

Storti, F. and J. Poblet, 1997, Growth stratal architectures associated to decollement folds and fault propagation folds. Inferences on fold kinematics: Tectonophysics, v. 282, p. 353-373.

Suppe, J. and D.A. Medwedeff, 1990, Geometry and kinematics of fault-propagation folding: Eclogae geol, no. 3, v. 83, p. 409-454.

Suppe, J., G.T. Chou, and S.C. Hook, 1992, Rates of folding and faulting determined from growth strata, in K.R. McClay ed., Thrust Tectonics: London, Chapman and Hall, p. 105-121.

Süss, M.P. and J.H. Shaw, 2003, P wave seismic velocity structure derived from sonic logs and industry reflection data in the Los Angeles basin, California: Journal of Geophysical Research, v. 108, p. 1-18.

Tavani, S., F. Storti, O. Fernández, J.A. Muñoz, F. Salvini, 2006, 3-D deformation pattern analysis and evolution of the Añisclo anticline, southern Pyrenees: Journal of Structural Geology, v. 28, p. 695-712.

Tavani, S., F. Storti, and F. Salvini, 2007, Modeling growth stratal architectures associated with double-edge fault-propagation folding: Sedimentary Geology, v. 196, p. 119-132.

Teixell, A. and J. García-Sansegundo, 1995, Estructura del sector central de la Cuenca de Jaca (Pirineos meridionales): Revista de la Sociedad Geológica de España, v. 8 no. 3, p. 215-228.

Tripsanas, E.K., W.R. Bryant, and B.A. Phaneuf, 2004, Slope-instability processes caused by salt movements in a complex deep-water environment, Bryant Canyon area, northwest Gulf of Mexico: American Association of Petroleum Geologists Bulletin, v.88, no. 6, p. 801-823.

Vacher, H.L., 2000, Cramer's rule and the three-point problem: Journal of Geoscience Education, v. 48, no. 4, p. 522-532.

Vergés, J., M. Marzo, and J.A. Muñoz, 2002, Growth strata in foreland settings: Sedimentary Geology, v. 146, p. 1-9.

Wallace, W.K., and T.K. Homza, 2004, Detachment folds versus fault-propagation folds, and their truncation by thrust faults: in K.R. McClay, ed., Thrust tectonics and hydrocarbon systems: American Association of Petroleum Geologists Memoir, 82, p. 324-355.

Wickham, J., and G. Moeckel, 1997, Restoration of structural cross-sections: Journal of Structural Geology, v. 19, no. 7, p. 975-986.

Winslow, M.A., 1983, Clastic dike swarm and the structural evolution of the foreland and thrust belt of the Southern Andes: Geological Society of America Bulletin, v. 94, p. 1073–1080.

Zoetemeijer, R., and W. Sassi, 1992, 2-D reconstruction of thrust evolution using the fault-bend fold method, in K.R. McClay ed., Thrust Tectonics: London, Chapman and Hall, p. 133-140.